Studies of aerosol and cloud properties using synergy of lidar and radar measurements

Dongxiang Wang

A doctoral dissertation

prepared at the Institute of Geophysics,

Faculty of Physics, University of Warsaw

Under the supervision of

Dr. hab. Iwona. S. Stachlewska

Reviewer: Prof. dr hab. inż. Zbigniew Bielecki
Reviewer: Prof. dr hab. Zdzisław Kazimierz Błaszczak

Warsaw, 3 July 2020

Submitted to the Faculty of Physics of the University of Warsaw
in fulfilment of the requirements for the degree of Philosophiæ Doctor in Physics

Acknowledgements:

With this PhD thesis about to be completed, I would like to express my gratitude to all those who have helped and supported me during my PhD studies.

My deepest gratitude goes first to my supervisor, Dr. hab. Iwona. S. Stachlewska for giving me opportunity to work in the Remote Sensing Laboratory (RS-Lab) in Warsaw in one of the most known research groups within the lidar community. She offered me a lot of valuable suggestions and guidance in the academic studies. I appreciate her patience, encouragement, professional instructions and guidance a lot, as she taught me how to be a solid researcher during my PhD period. I also would like to thank her for the tips on living in Poland. To be honest, without her help, it would not be possible for me to complete the PhD thesis and my studies. I also would like to thank Dr. Xiaoquan Song who provided me with a lot of good ideas and valuable points for my PhD study projects. I thank Dominika Szczepanik, Łucja Janicka, Olga Zawadzka, Patryk Poczta, and Guangyao Dai for helping me with data analysis, results discussion, and field experiment observation. Special thanks should go to those who put considerable time and effort into their comments on my academic papers, Dr. Birgit Heese, Dr. Anca Nemuc, Dr. Julien Delanoë, Dr. Dragos Ene, and Dr. Dirk Schüttemeyer. I thank Dr. hab. Bogdan Chojnicki for granting me an access to the PolWET site over peatland in Rzecin. I also would like to thank Prof. dr. hab. Szymon P. Malinowski, Dr. hab. Krzysztof Markowicz, Dr. Marta Wacławczyk, Katarzyna Dyl, Dr. Emmanuel Olutayo Akinlabi, Moein Mohammadi and other friendly colleagues who helped me during my PhD studies.

Last but not least, thank you to my family who have been understanding and supporting my academic studies.

This study was supported by the Technical assistance for the Polish Radar and Lidar Mobile Observation System (POLIMOS 4000119961/16/NL/FF/mg) funded by the European Space Agency; Preludium-15 (UMO-2018/29/N/ST10/02628) funded by the National Science Centre Poland; as well as the European Cooperation in Science and Technology (COST) Action for the Profiling of the atmospheric Boundary layer on a European scale (PROBE).

Abstract

The atmospheric boundary layer (ABL) is either directly or indirectly related to different weather and climate phenomena. Aerosol and clouds can affect the Earth's radiation budget and the whole climate system. The study of ABL, atmospheric aerosol, and clouds contributes to the improvement of environmental pollution prediction, weather prediction and climate models.

The main focus of my doctoral thesis was on the study of characteristics of ABL and properties of aerosol and clouds. During my studies, I pursued the following three research goals, which resulted in three papers of which I am the first author and which constitute the main body of this portfolio doctoral thesis. All three goals were successfully achieved.

The first goal was to derive and analyse the atmospheric boundary layer height (ABLH) over the Remote Sensing Laboratory (RS-Lab) in Warsaw (52.21°N, 20.98°E, 54 m a.s.l.), Poland. The collocated measurements of the CHM15k ceilometer (from January 2008 to October 2013) and the PollyXT Raman lidar (from July 2013 to December 2018) were used to derive the ABLH. A large sample of 1841 diurnal cycle ABLH retrievals were derived using the wavelet covariance transform method (WCT). A scaling threshold-based algorithm was proposed to homogenize ceilometer and lidar datasets, which improved the results' coherence significantly. The statistical analysis of these long-term observations indicated pronounced seasonal changes of monthly mean diurnal cycles of ABLH. The annual and seasonal variability of 10 years of ABLH record revealed that it was affected by the change of the climate classification over the region, the global heating (El Niño) and cooling (La Niña), reflected in the changes of surface air temperature. The annual mean well-mixed layer (WML), residual layer (RL), and nocturnal layer (NL) under clear-sky and cloudy conditions were compared, indicating that the cloud cover and the urban heat island played an important role in the ABL processes. Finally, the frequency distribution of ABLH revealed a strong seasonal variability in terms of distribution peak and shape.

The second goal was to investigate optical properties of aerosol within ABL using the PollyXT Raman lidar data in Warsaw in July, August, and September of 2013, 2015, and 2016. Profiles stored in the EARLINET/ACTRIS database were used for statistical analysis. In total, 246 sets of intact profiles were used, each set comprising the following intensive aerosol properties: the particle extinction (α) and backscatter coefficients (β), as well as linear particle depolarization ratios (δ) at 355 nm and 532 nm. From those, other properties were calculated, such as the aerosol optical depth (AOD), the lidar ratio (LR), and the Ångström exponent (ÅE). Interrelations between these different aerosol optical properties derived within boundary layer, as well as relations between them, the ABLH, the particulate matter ($PM_{2.5}$ and PM_{10}) and the relative humidity (RH) at the surface were studied. As a result, the AOD_{ABL} and LR_{ABL}

revealed a positive correlation, the ÅE_{ABL} and LR_{ABL} a negative correlation, whereas the δ_{ABL} with water vapor mixing ratio (WV_{ABL}) and the surface relative humidity (RH) showed negative trends. During the measured period, the aerosol composition within the boundary layer was assessed, which consisted of: urban anthropogenic pollution (~ 61 %) or mixtures of anthropogenic aerosol with biomass burning aerosol (< 14 %), local pollen (< 7 %), or Arctic marine particles (< 5 %). No significant contribution of mineral dust was found within the boundary layer.

The third goal was to assess properties and vertical extent of tropospheric aerosol and clouds using the synergy of active and passive remote sensing instruments. Measurements over the period of June-August 2019 with the ESA's Mobile Raman Polarization and Water Vapor Lidar (EMORAL), the LATMOS Bistatic Doppler Cloud Radar System for Atmospheric Studies (BASTA), and the INOE Scanning Microwave Radiometer (HATPRO-G2) were conducted over the PolWET peatland site in Rzecin (52.75°N, 16.30°E, 54 m a.s.l.), Poland. A new scheme for target classification (aerosol-cloud typing) was developed to determine molecules, aerosol (spherical, non-spherical, fine, coarse), the cloud phase (liquid, ice, supercooled droplets), using data synergetic combination of the three instruments. Different types of scatter targets (boundary layer particles, rain, drizzle, supercooled layer, ice cloud, liquid cloud, mixed-phase cloud, aerosol, and molecules) were successfully classified, which was demonstrated based on a case study in a meteorologically complicated situation.

Streszczenie

Atmosferyczna warstwa graniczna (z ang. *atmospheric bounadry layer* ABL) jest bezpośrednio lub pośrednio związana z różnymi zjawiskami pogodowymi i klimatycznymi. Aerozol atmosferyczny i chmury mogą wpływać na budżet promieniowania Ziemi i system klimatyczny. Badanie właściwości ABL, aerozolu i chmur przyczynia się do poprawy prognozowania zanieczyszczenia środowiska, prognoz pogody i modeli klimatycznych.

Głównym celem mojej pracy doktorskiej było badanie atmosferycznej warstwy granicznej oraz właściwości aerozolu atmosferycznego i chmur. W swoich badaniach wydzieliłem trzy cele szczegółowe, które zaowocowały trzema publikacjami, których byłem pierwszym autorem, i które składają się na niniejsza pracę doktorską. Wszystkie trzy cele zrealizowałem.

Za pierwszy cel wziąłem badanie wysokości warstwy granicznej atmosfery (z ang. *atmospheric boundary layer height* ABLH) na podstawie analizy teledetekcyjnych pomiarów ceilometru CHM15k (od stycznia 2008 r. do października 2013 r.) oraz lidaru PollyXT (od lipca 2013 r. do grudnia 2018 r.) w Laboratorium Pomiarów Zdalnych (z ang. *Remote Senising Laboratory* RS-Lab) w Warszawie (52.21°N, 20.98°E, 54 m a.s.l.). Wykorzystałem je do wyznaczenia ABLH w skali ponad 10 lat. Wysoka próba statystyczna (1841) odzyskanych cykli dobowych ABLH została uzyskana przy użyciu metody transformacji kowariancji falkowej (z ang. *wavelet covariance transform* WCT). Algorytm oparty na wartościach progowych użytych do skalowania wartości ABLH został opracowany w celu ujednolicenia danych ceilometru i lidaru, a wykonane przeze mnie testy algorytmu wykazały znaczną poprawę spójności wyników. Analiza statystyczna długoterminowych obserwacji wykazała wyraźne sezonowe zmiany średnich miesięcznych cykli dobowych ABLH. Roczna i sezonowa zmienność ABLH ujawniła, że wpływ na nią miało globalne ogrzewanie (El Niño) i chłodzenie (La Niña), odzwierciedlone w zmianach temperatury powietrza na powierzchni. Ponadto porównanie średniej rocznej warstwy wymieszanej (z ang. *well-mixed* layer WML), rezydualnej (z ang. *residual layer* RL) i nocnej (z ang. *nocturnal layer* NL) w warunkach czystego nieba i zachmurzenia, wskazało, że pokrywa chmur i miejska wyspa ciepła odgrywały ważną rolę w procesach ABL. Wreszcie rozkład częstotliwości ABLH ujawnił silną zmienność sezonową pod względem maksymalnej amplitudy i kształtu rozkładu.

Drugim celem było zbadanie właściwości optycznych aerozolu atmosferycznego w warstwie granicznej. Wykorzystałem tu dane lidaru PollyXT w Warszawie w lipcu, sierpniu i wrześniu 2013, 2015 i 2016. Profile przechowywane w bazie danych EARLINET / ACTRIS zostały wykorzystane do badań statystycznych. W sumie zastosowano 246 zestawów profili własności optycznych, każdy zawierający współczynniki ekstynkcji (α) i rozproszenia wstecznego (β) na cząstkach aerozoli atmosferycznych, a także liniowe współczynniki depolaryzacji cząstek (δ). Profile te posłużyły mi do wyliczenia kolejnych własności

optycznych: grubości optycznej aerozolu (AOD), ilorazu lidarowego (LR) i wykładnika Ångströma (ÅE). Zbadałem zależności między różnymi właściwościami optycznymi aerozolu w warstwie granicznej oraz relacje między nimi a pyłem zawieszonym ($PM_{2.5}$ i PM_{10}) oraz wilgotnością względną (RH) przy powierzchni. W rezultacie AOD_{ABL} i LR_{ABL} wykazały dodatnią korelację, AE_{ABL} i LR_{ABL} ujemną korelację, a δ_{ABL} ze współczynnikiem mieszania pary wodnej (WV_{ABL}) i RH wykazały ujemne trendy. Kompozycja aerozolu w warstwie granicznej w analizowanym okresie składała się z: antropogenicznych zanieczyszczeń miejskich (~ 61%) lub ich mieszanin z aerozolem pochodzącym ze spalania biomasy (<14%), lokalnym pyłkami biogenicznymi (<7%) lub cząstkami aerozolu transportowanego znad Arktyki (<5%). W warstwie granicznej nie stwierdzono znaczącego udziału pyłu mineralnego.

Jako trzeci cel postawiłem sobie badanie aerozolu i chmurami w troposferze przy użyciu synergii aktywnych i pasywnych pomiarów teledetekcyjnych. Pomiary wykonane w okresie od czerwca do sierpnia 2019 r. z wykorzystaniem mobilnego lidaru ramanowskiego ESA (EMORAL), bistatycznego dopplerowskiego radaru chmurowego LATMOS (BASTA) oraz skaningowego radiometru mikrofalowego INOE (HATPRO-G2) przeprowadzono na torfowisku w Rzecinie (52.75°N, 16.30°E, 54 m a.s.l.). Opracowany nowy schemat klasyfikacji cząstek, aerozolu i stanu fazy chmur na podstawie połączonych danych z trzech instrumentów pozwolił na szczegółową analizę rozproszenia (cząstki aerozolu w warstwie granicznej, aerozol sferyczny i niesferyczny, aerozol drobno i gruboziarnisty, deszcz, mżawka, warstwa przechłodzona, chmura lodowa, ciekłą i fazy mieszanej). Zalety opracowanej metodologii zademonstrowałem dla studium przypadku podczas skomplikowanej sytuacji meteorologicznej.

Contents

Preface

1.1 Introduction

The main topic of my thesis was to study atmospheric aerosol and cloud properties. Such a research goal cannot be realized without basic knowledge on aerosol abundant within the atmospheric boundary layer (ABL), in the free troposphere (FT), and in the lower stratosphere (LST). In order to learn about it, at first, I started to work on the ABL research. The height, structure, and evolution of ABL were investigated over Warsaw, using collocated lidar and ceilometer observations. Measurements of the CHM15k ceilometer (January 2008 to October 2013) and the PollyXT Raman lidar (July 2013 to December 2018) were used to derive the atmospheric boundary layer height (ABLH) over the Remote Sensing Laboratory (RS-Lab) in Warsaw (52.21°N, 20.98°E, 54 m a.s.l.), Poland. After I completed the study on ABL retrievals, I was able to broaden the research – the next step was studying a more dynamic process between the aerosol and clouds within ABL and FT, and their differences. This work resulted in a publication entitled *Variability of the boundary layer over an urban continental site based on 10 years of active remote sensing observations in Warsaw* (Wang et al. 2020a). This study laid a solid base for the following research. For example, the scheme of ABL top height retrieval using a wavelet covariance method that I coded was used in another paper that I co-authored on *Modification of local urban aerosol properties by long-range transport of biomass burning aerosol* (Stachlewska et al. 2018), where it helped to investigate the injection of aerosol particles from FT into ABL.

Apart from investigations of the ABL variability, I had to do more research on aerosol optical properties. This work was done using measurements of the PollyXT Raman lidar during three summer seasons over the RS-Lab in Warsaw. I did not focus on mastering the field of optical properties retrieval via direct calculations, and neither did I focus on the lidar development techniques. Instead, I explored an existing high-quality dataset and learned from it in an efficient way, by conducting a statistical analysis. The final period chosen for this study covered a subset of measurements in July-September of 2013, 2015, and 2016, as they had the highest number of profiles available. I used the quality checked aerosol optical properties profiles (particle backscattering and extinction coefficients, as well as the particle depolarization ratio) stored in the EARLINET / ACTRIS Database, in order to derive mean aerosol optical properties within ABL. This work resulted in the second publication entitled *Interrelations between surface, boundary layer, and columnar aerosol properties derived in summer and early autumn over a continental urban site in Warsaw, Poland* (Wang et al. 2019). The knowledge on relations between the different aerosol optical properties within ABL was extremely useful for expanding further work. For example, I used this knowledge recently when I participated in the near real time (NRT) campaign for studying changes in the atmosphere during the COVID-19 lockdown. Comprehensive information on the atmospheric structure, its dynamics, and optical properties of aerosol within ABL and FT were derived from lidar measurements thanks to their high temporal and vertical resolutions. I compared the profiles for different observational sites (e.g. Warsaw, Barcelona, Leipzig) to assess their variability during the COVID-19 lockdown and beforehand. A report on this study that I co-author is published as *EARLINET/ACTRIS analysis of aerosol profiles during the COVID-19 lock-down and relaxation period. A preliminary study on aerosol properties in the low and high troposphere* (Nicolae et al. 2020). Another example is an analysis of aerosol particles in the very high troposphere and low stratosphere. This work resulted in co-authoring of a paper entitled *The unprecedented 2017–2018 stratospheric smoke event: decay phase and aerosol properties observed with the EARLINET* (Baars et al. 2019) that reports and discusses the geometrical and optical aerosol properties in the stratosphere (13-25 km) for twenty-eight European lidar stations, among others RS-Lab in Warsaw, the datasets of which I co-evaluated. This research encouraged me to deal with the most challenging topic and to make the final step of the doctoral work, namely investigate jointly aerosol and clouds properties.

I conducted a study on feasibility of aerosol and cloud typing, from the synergy of three remote sensing instruments within the framework of the ESA funded POLIMOS and RAMOS campaigns. Measurements over the period of June-August 2019 with the ESA's Mobile Raman Polarization and Water Vapor Lidar (EMORAL), the LATMOS Bistatic Doppler Cloud Radar System for Atmospheric Studies (BASTA), and the INOE Scanning Microwave Radiometer (HATPRO-G2) were conducted over the peatland site in Rzecin (52.75°N, 16.30°E, 54 m a.s.l.), Poland. The core question was how to distinguish, in a meteorologically complicated situation, between spherical and non-spherical, fine and coarse sizes of aerosol, and how to discriminate liquid particles, ice cloud, supercooled droplets and precipitation. The main goal of my work was to develop an algorithm for complex aerosol-cloud typing, which would be a base for future studies on aerosol and cloud optical and microphysical properties. Data products from lidar, cloud radar and microwave radiometer were needed. I was aware of the lidar capabilities, so I mainly focused on performing and exploiting lidar observations, including an extensive data inversion (including retrieval of the attenuated backscatter signals, volume depolarization ratio, atmospheric boundary layer height, range of aerosol optical properties, and backward scattering ratio). I also explored, in a statistical way, the cloud radar data provided by a partner institution (LATMOS, France) that provided level-1 products (reflectivity, Doppler velocity) and level-2 products (rain, drizzle, ice cloud, and liquid particles) and the microwave radiometer data provided by another partner institution (INOE, Romania) delivering profiles of temperature and relative humidity. Next, an extensive study was conducted on different methodologies of using the standard data available from the cloud radar and microwave radiometer. Finally, it was possible to design a concept in the aerosol and cloud classification, come up with a new algorithm and code it. Based on this work, a new achievement in aerosol and cloud categorization was made, which resulted in publishing the paper on *Spatio-temporal discrimination of molecular, aerosol and cloud scattering and polarization using a combination of Raman lidar, Doppler cloud radar and microwave radiometer* (Wang et al. 2020b). A unique method to characterize molecules, aerosol particles and clouds within the range of the whole troposphere with high temporal and spatial resolution was developed. The molecules, aerosol (spherical, non-spherical, fine, coarse), the cloud phase (liquid, ice, supercooled droplets) and precipitation (drizzle, rain) were discriminated using the method.

This portfolio PhD thesis is a summary of the three published papers, which I am the first author of (Wang et al. 2019, 2020a, 2020b). An overview of the instrumentation used is reported in Chapter 2. The methodology is presented in Chapter 3. In Chapters 4 (boundary layer structure), 5 (aerosol properties within boundary layer) and 6 (aerosol and cloud properties within troposphere), I summarize the main content and added value of each published paper. The three papers are an integral part of this thesis and a published version of each paper is included in the respective Chapters. The outlook and future plans are given in Chapter 7.

1.2 Significance of the research

The atmospheric boundary layer height (ABLH) plays a crucial role in boundary layer processes. The dispersion of anthropogenic pollutants (direction, altitude, and distance of transport) and resulting concentrations can interplay with and be influenced by the boundary layer structure and diurnal evolution (Gerbig et al., 2008). Thus, the atmospheric boundary layer height and its cycle are important parameters that can control air pollution by affecting the pollutants dispersion (Geiß et al., 2017). Accurate estimates of the boundary layer height are also important in climate modelling, as the boundary layer height and processes therein influence the output of models (Barlage et al., 2016).

Atmospheric aerosol of natural (e.g. volcanic ash, forest fire smoke) and anthropogenic origin (e.g. urban pollution), suspended within the boundary layer, in the free troposphere and low stratosphere, affects the Earth’s radiation budget. Aerosol particles, dependently on their properties, interact with the incoming solar short-wave radiation and the outgoing terrestrial long-wave radiation (Kaufman et al., 2002). Depending on the aerosol type, they can scatter or absorb radiation, thus causing warming or cooling of the atmosphere locally, at the surface and at the top of the atmosphere (Seinfeld et al., 2016).

Anthropogenic activity has led to an increase in aerosol particle concentrations globally, and thus, increase of particles that act as cloud condensation nuclei and ice nucleating particles (Marinou et al., 2019). In addition, aerosol can lead to changes in cloud microphysics and atmospheric stability, which can further influence development of clouds and precipitation (Li et al., 2011). Clouds play a key role in Earth's radiation budget and climate system. The effect of the change of atmospheric aerosol concentrations on the distribution and radiative properties of Earth's clouds is the most uncertain component of the overall global radiative forcing. This uncertainty severely hampers future predictions of climate change (Hasekamp, 2010). A better understanding of aerosol and cloud properties and processes of their interaction is necessary to address uncertainties regarding climate change estimates (Seinfeld et al., 2016).

Knowledge on aerosol and clouds can help better assessment of their direct and indirect effects on the radiation transfer and the balance of the Earth-Atmosphere system. Therefore, measurements of boundary layer characteristics, as well as aerosol and cloud properties, are important for improving environmental pollution prediction and parameterization in weather and climate models. This PhD thesis deals with the atmospheric boundary layer, aerosol and clouds, strongly contributing to the aforementioned research field.

1.3 Initial research hypothesis

Several scientific questions were posed within this PhD thesis:

1. Is there an evident seasonal change in the diurnal cycle of the atmospheric boundary layer height over a continental urban site?
2. Are there significant differences in seasonal boundary layer height distributions at night-time and daytime over a continental urban site?
3. Does global atmospheric heating and cooling influence the variability of atmospheric boundary layer height over a continental urban site?
4. How clouds forming close to the top of the boundary layer affect its retrieval?
5. What are typical aerosol compositions in the atmospheric boundary layer over Warsaw?
6. Is it possible to find clear relations between different aerosol optical properties and meteorological parameters?
7. What are the limits of using synergy of ground-based remote sensing in providing high quality categorization of the atmospheric aerosol, clouds and precipitation?

References

Barlage, M., Miao, S., Chen, F.: Impact of physics parameterizations on high-resolution weather prediction over two Chinese megacities. *J. Geophys. Res.* 2016, 121, 4487–4498. https://doi.org/10.1002/2015JD024450.

Geiß, A., Wiegner, M., Bonn, B., Schäfer, K., Forkel, R., von Schneidemesser, E., Münkel, C., Chan, K. L., and Nothard, R.: Mixing layer height as an indicator for urban air quality? *Atmos. Meas. Tech*. 2017, 10, 2969–2988. https://doi.org/10.5194/amt-10-2969-2017.

Gerbig, C., Körner, S., and Lin, J. C.: Vertical mixing in atmospheric tracer transport models: error characterization and propagation. *Atmos. Chem. Phys*. 2008, 8, 591–602. https://doi.org/10.5194/acp-8-591-2008.

Hasekamp, O. P.: Capability of multi-viewing-angle photo-polarimetric measurements for the simultaneous retrieval of aerosol and cloud properties. *Atmos. Meas. Tech*. 2010, 3, 839–851, https://doi.org/10.5194/amt-3-839-2010.

Kaufman, Y. J., Tanré, D., and Boucher, O.: A satellite view of aerosol in the climate system. *Nature*. 2002, 419, 215–223. https://doi.org/10.1038/nature01091.

Li, Z., Niu, F., Fan, J., Liu, Y., Rosenfeld, D., and D. Ding, Y., Long-term impacts of aerosols on the vertical development of clouds and precipitation. *Nature Geosci*. 2011, 4(12), 888-894. https://doi.org/10.1038/ngeo1313.

Marinou, E., Tesche, M., Nenes, A., Ansmann, A., Schrod, J., Mamali, D., Tsekeri, A., Pikridas, M., Baars, H., Engelmann, R., Voudouri, K.-A., Solomos, S., Sciare, J., Groß, S., Ewald, F., and Amiridis, V.: Retrieval of ice-nucleating particle concentrations from lidar observations and comparison with UAV in situ measurement. *Atmos. Chem. Phys*. 2019, 19, 11315–11342. https://doi.org/10.5194/acp-19-11315-2019.

Seinfeld, J. H., Bretherton, C., Carslaw, K. S., Coe, H., DeMott, P. J., Dunlea, E. J., Feingold, G., Ghan, S., Guenther, A. B., Kahn, R., Kraucunas, I., Kreidenweis, S. M., Molina, M. J., Nenes, A., Penner, J. E., Prather, K. A., Ramanathan, V., Ramaswamy, V., Rasch, P. J., Ravishankara, A. R., Rosenfeld, D., Stephens, G., and Wood, R.: Improving our fundamental understanding of the role of aerosol–cloud interactions in the climate system. *P. Natl. Acad. Sci*. 2016, 113, 5781–5790, https://doi.org/10.1073/pnas.1514043113.

Chapter 2 Instrumentation

In order to complete this study, several instruments were utilized to perform atmospheric observations. The core instruments are CHM15k ceilometer, PollyXT lidar, Mobile Raman Lidar, Doppler cloud radar, and microwave radiometer. All instruments were operated in a mode of quasi-continuous 24/7 observations, providing profiles covering almost the entire troposphere. Hence, observations of the characteristics of the boundary layer, and the properties of aerosol and cloud could be obtained in an exceptional height-time scale. The details of these instruments are described below:

The CHM 15k ceilometer (JenOptik/Lufft, Germany) was continuously operated in Warsaw from 1 January 2008 to 31 October 2013. It was installed on the roof-platform of the Remote Sensing Laboratory (RS-Lab) of the Institute of Geophysics at the Faculty of Physics of the University of Warsaw (21 m a.g.l.). The data was acquired with a temporal resolution of 30 s and a spatial resolution of 15 m, with the maximum signal range of 15.36 km (corresponding to 1024 range-bins). The ceilometer is a custom designed unit with optimized field-of-view (Stachlewska et al., 2012). It comprises a diode-pumped Nd:YAG solid-state laser, which emits low-energy laser pulses (8 µJ), at a high frequency (5-7 kHz), at a wavelength of 1064 nm. The lowermost level of the overlap between the emitted laser beam and the receiver lens is at approximately 180 m and the full overlap is completed at approximately 800 m (Stachlewska et al., 2012). The data products that can be calculated comprise at the level-1, the attenuated backscatter signals (Wiegner et al., 2014) and at the level-2, the atmospheric boundary layer height (Wang et al.2020a), and the estimated backscattering coefficient profiles (Wiegner et al., 2014).

The PollyXT lidar was built in a scientific collaboration of the Institute of Geophysics at the Faculty of Physics of the University of Warsaw (UW, Warsaw, Poland) and the Leibniz Institute of Tropospheric Research (TROPOS, Leipzig, Germany). It was installed at the RS-Lab in Warsaw in June 2013. After an extensive test-phase, the lidar started operation on 1 July

2013 and has performed quasi-continuous observations ever since. The lidar emits high-energy laser pulses of 180 mJ at 1064 nm, 110 mJ at 532 nm, and 60 mJ at 355 nm with a repetition rate of 20 Hz. The measurements are performed at 8-channels, using a large telescope and at 4-channels, using a small telescope. The 8-channels detection unit (so-called $2\alpha + 3\beta + 2\delta +$ WV) enables the determination of the extinction coefficient profiles at 532 nm and 355 nm, the backscatter coefficient at 1064 nm, 532 nm and 355 nm, the depolarization ratio at 532 nm and 355 nm, and water vapor mixing ratio. The 4-channels detection unit (so-called $2\alpha + 2\beta$) is designated for obtaining the extinction and backscatter coefficient profiles at 532 nm and 355 nm. The signals are recorded up to 48 km. The data of all channels is obtained with a standard 7.5 m vertical resolution in temporal steps of 30 s. The overlapping range of the laser beam and the large and small telescope is completed at roughly 400 m and 120 m, respectively (Engelmann et al., 2016, Stachlewska et al., 2018a).

The ESA Mobile Raman Lidar (EMORAL) uses the Nd-YAG laser (SpitLight 400, InnoLas, Germany) as a radiation source, operating at 1064 nm (112 mJ), 532 nm (103 mJ) and 355 nm (128 mJ). The laser emits all three wavelengths to the atmosphere simultaneously and collinearly, with a repetition rate of 10 Hz and pulse lengths of 5-7 ns. The backward scattered radiation is collected with a Cassegrain telescope (primary mirror of 300 mm, adjustable field of view of 2-3.6 mrad), then separated and filtered to detect 8 channels: 3 elastic channels (1064 nm, 532 nm, and 355 nm), 3 vibrational Raman channels (for nitrogen at 387 nm, 607 nm and for water vapour at 407 nm), and 2 depolarization channels at 532 nm and 355 nm. All signals are recorded with an analogue and photon-counting mode, using the 16-bits transient recorders (TR40-160, Licel, Germany), except for 1064 nm (only analogue). The raw signal height resolution is 3.75 m and the time resolution is adjustable (from 2 s to 1 min). The full overlap height is at 400 m (Wang et al., 2020b).

From both lidars, different level data products can be calculated. The level-1 products comprise attenuated backscatter signals and the volume depolarization ratio (Stachlewska et al., 2017). The level-2 products are the water vapour mixing ratio, the atmospheric boundary layer height, the range of aerosol optical properties, and the scattering ratio (Stachlewska et al., 2018b). The level-3 products comprise microphysical parameters (Janicka et al., 2017).

The Bistatic Radar System for Atmospheric Studies (BASTA) is a semi-operational 95 GHz Doppler cloud radar, which uses the frequency-modulated continuous wave (FMCW) technique. The technique can be highly sensitive with much less power than traditional pulsed systems, there are some advantages and some disadvantages of using it. It provides real time 24/7 vertical observations of the cloud vertical structure and vertical distributions of cloud properties (such as cloud fraction, cloud phase, cloud water content, etc). It uses a specific signal processing technique in such a way that the radar can challenge expensive radars and provide high-quality measurements of cloud and fog. The main products are reflectivity and Doppler velocity (level-1), obtained with 12.5 m, 25 m and 100 m vertical resolution and 3 s time resolution. The lower limit is 125 m for 3 modes. The 12.5-m mode is limited to 6 km.

The 25-m resolution mode covers the range up to 12 km. The 100 m resolution mode covers the range up to 18 km. The integration time is set to 3 s for each mode, and 9 s for 3 modes combined. The level-2 products (rain, drizzle, ice cloud and liquid particles and droplets) and the level-3 products (microphysical cloud properties) can also be obtained. The BASTA radar currently uses three successive modes for specific applications: the 12.5 m vertical resolution mode is dedicated to fog and low clouds, the 25 m mode is for liquid and ice mid-tropospheric clouds, and the 100 m is ideal for optically thin, high-level ice clouds (Delanoë et al., 2016).

The microwave radiometer (HATPRO-G2, Radiometer Physics GmbH) consists of two working bands at 22–31 and 51–58 GHz, each with seven channels. The vertical resolution is coarser than that for the other two instruments. Measurements with a temporal resolution of 15 s and a height-dependent vertical resolution: 200 m from 0 to 2 km, 400 m from 2 to 5 km, and > 500 m for the heights above 5 km. The level-1 products are brightness temperatures. The level-2 products are integrated water vapour, the liquid water path, and the vertical profiles of absolute and relative humidity, water vapor, and temperature (Fragkos et al., 2019).

Apart from the above-mentioned core instruments, auxiliary sensors were used, e.g. the air monitoring station and weather station were used to obtain the particulate matters ($PM_{2.5}$ and PM_{10}) and surface relative humidity, respectively.

Particulate matter concentrations for particles with an aerodynamic diameter of less than 2.5 and 10 µm (referred to as $PM_{2.5}$ and PM_{10}, respectively) were measured at the air quality monitoring site of the Warsaw Regional Inspectorate for Environmental Protection (WIOS) in Ursynow, Warsaw, located 6.5 km from the RS-Lab. The data measurements conducted at the State Environmental Monitoring stations are gathered in the JPOAT 2.0 air quality database of the National Chief Inspectorate for Environmental Protection (GIOS). These official, calibrated datasets with daily and hourly averaged $PM_{2.5}$ and PM_{10} are accessible at http://powietrze.gios.gov.pl/pjp/archives (last access: 02 July 2020). The measurement uncertainty is below 30 % for the hourly concentrations.

The relative humidity at the surface was measured by the WXT510 (Vaisala, Finland) weather transmitter mounted on the roof platform of the RS-Lab at 21 m above the ground's surface. The atmospheric temperature, and relative humidity profiles were obtained from the RS92 (Vaisala, Finland) radiosonde launched at two World Meteorological Organization sites located in Poland: WMO 12374 station in Legionowo (52.40°N, 20.96°E, 96 m a.s.l., circa 25 km north of Warsaw).

References

Delanoë, J., Protat, A., Vinson, J.P., Brett, W., Caudoux, C., Bertrand, F., Parent du Chatelet, J., Hallali, R., Barthes, L., Haeffelin, M. and Dupont, J.C.: BASTA: A 95-GHz FMCW Doppler radar for cloud and fog studies. J. Atmos. Ocean. Tech. 2016, 33(5), 1023-1038. https://doi.org/10.1175/JTECH-D-15-0104.1.

Engelmann, R., Kanitz, T., Baars, H., Heese, B., Althausen, D., Skupin, A., Wandinger, U., Komppula, M., Stachlewska, I. S., Amiridis, V., Marinou, E., Mattis, I., Linné, H., and Ansmann, A.: The automated multiwavelength Raman polarization and water-vapor lidar PollyXT: The next generation. *Atmos. Meas. Tech*. 2016, 9, 1767–1784. https://doi.org/10.5194/amt-9-1767-2016.

Fragkos, K., Antonescu, B., Giles, D. M., Ene, D., Boldeanu, M., Efstathiou, G. A., Belegante, L., Nicolae, D.: Assessment of the total precipitable water from a sun photometer, microwave radiometer and radiosondes at a continental site in southeastern Europe. Atmos. Meas. Tech. 2019, 12(3), 1979–1997. https://doi.org/10.5194/amt-12-1979-2019.

Janicka, L., Stachlewska, I. S., Veselovskii, I., and Baars, H.: Temporal variations in optical and microphysical properties of mineral dust and biomass burning aerosol derived from daytime Raman lidar observations over Warsaw, Poland. *Atmos. Environ*. 2017, 169, 162–174. https://doi.org/10.1016/j.atmosenv.2017.09.022.

Stachlewska, I.S., Piadłowski, M., Migacz, S., Szkop, A., Zielinska, A., Swaczyna, P.: Ceilometer observations of the boundary layer over Warsaw, Poland. *Acta Geophys*. 2012, 60, 1386–1412. https://doi.org/10.2478/s11600-012-0054-4.

Stachlewska, I.S., Zawadzka, O., and Engelmann, R.: Effect of Heat Wave Conditions on Aerosol Optical Properties Derived from Satellite and Ground-Based Remote Sensing over Poland. *Remote Sens*. 2017, 9, 1199. https://doi.org/10.3390/rs9111199.

Stachlewska I.S., Ritter C., Böckmann C. and Engelmann R.: Properties of arctic haze aerosol from lidar observations during iarea 2015 campaign on spitsbergen. *EPJ Web of Conferences*. 2018a, 176, 05024. https://doi.org/10.1051/epjconf/201817605024.

Stachlewska, I. S., Samson, M., Zawadzka, O., Harenda, K. M., Janicka, L., Poczta, P., Szczepanik, D., Heese, B., Wang, D., and Borek, K. Tetoni, E., Proestakis, E., Siomos, N., Nemuc, A., Chojnicki, B. H., Markowicz, K. M., Pietruczuk, A., Szkop, A., Althausen, D., Stebel, K., Schüttemeyer, D., and Zehner, C.: Modification of local urban aerosol properties by long-Range transport of biomass burning aerosol. *Remote Sens*. 2018b, 10, 412. https://doi.org/10.3390/rs10030412.

Wiegner, M., Madonna, F., Binietoglou, I., Forkel, R., Gasteiger, J., Geiß, A., Pappalardo, G., Schäfer, K., and Thomas, W.: What is the benefit of ceilometers for aerosol remote sensing? An answer from EARLINET. *Atmos. Meas. Tech*. 2014, 7, 1979–1997. https://doi.org/10.5194/amt-7-1979-2014.

Chapter 3 Methodology

This chapter is giving a theoretical bases for studies that I have conducted within my PhD thesis. I focused here on highlighting the most important equations governing the physical processes used in extensive analysis of remote sensing measurements and derived properties.

3.1 Theoretical background

Remote Sensing means acquisition of information about an object or phenomenon without making physical contact with it. It can be used for detecting and monitoring the physical characteristics of atmospheric area (defined in terms of space-time resolution) by measuring radiation interacting with atmospheric constituents at a distance. Active remote sensors have their own source of energy (e.g. laser radiation), which they emit in the direction of the target area, then the sensors detect the radiation that is either reflected or scattered by the particles present in that area (typically backward scattering is measured) or that is absorbed and reemitted. Passive remote sensors do not have their own source of energy, they usually measure radiation emitted by natural sources (e.g. sunlight) that may be reflected, scattered or absorbed by the target (Campbell et al., 2011). In my work, I used active remote sensing with lidar, ceilometer, and cloud radar and passive remote sensing with microwave radiometer.

For the lidar, the backscatter signal *P* collected by the telescope can be described with the following equation (Klett, 1981):

$$P = C\,\frac{O}{R^2}(\beta_p + \beta_m)\,\exp\left\{-2\int_0^R(\alpha_p + \alpha_m)dr\right\} \tag{1}$$

where *C* is the instrumental constant, *R* is the range of the lidar signal, *O* is the overlap function that equals 1 at the complete overlap between the laser beam and the full field of view of the telescope, β_p is the particle backscatter coefficient, β_m is the molecular backscatter coefficient, α_p is the particle extinction coefficient, α_m is the molecular extinction coefficient. The aerosol optical and microphysical properties and the boundary layer height can be derived from the lidar observations.

For the cloud radar, the signal of a power P_r returning to the receiving antenna (Skolnik, 1980) is given by the following equation (2):

$$P_r = \frac{P_t G_t A_t \sigma F^4}{(4\pi)^2 R^4} \quad (2)$$

where P_t is the transmitter power, G_t is the gain of the transmitting antenna. A_r is the effective aperture of the receiving antenna, σ is the radar cross section, F is the pattern propagation factor, and R is the range. The properties of clouds and precipitation and the boundary layer height can be obtained from the cloud radar.

When it comes to the microwave radiometer (MWR), the temperature (T) and relative humidity (RH) profiles can be used to provide an important reference for the separation of aerosol layers and cloud types in a dry and wet environment.

3.2 The calculations method of atmospheric boundary layer height and aerosol optical properties

The atmospheric boundary layer height (ABLH) can be derived from the lidar backscatter signal, relying on aerosol load within the boundary layer that is higher than in the free troposphere (Stull, 1988). For ABLH retrieval, the most optimal is the wavelet covariance transform method (WCT) (Brooks, 2003). As for the WCT method applied in my studies, the covariance transform W_f of the Haar wavelet function h was used, defined as in the Equation (3):

$$W_f(a,b) = \frac{1}{a}\int_{z_1}^{z_2} P(z)h\left(\frac{z-b}{a}\right)dz, \qquad h\left(\frac{z-b}{a}\right) = \begin{cases} +1 & b-\frac{a}{2} \le z \le b \\ +1 & b \le z \le b+\frac{a}{2} \\ 0 & elsewhere \end{cases} \quad (3)$$

where $P(z)$ is the lidar backscatter signal, z_1 and z_2 are the lower and upper limits of the signal, z is the altitude, then a is the dilation and b is the centre of the Haar wavelet function.

Aerosol optical properties can be derived in different ways. In this thesis, the particle extinction coefficient profiles at 355 and 532 nm were calculated from the so-called Raman lidar equation (Ansmann et al., 1990) using the Rayleigh law for molecules and the Ångström law (usually with ÅE=1) for aerosol particles (Ångström, 1929). The particle extinction coefficient (α_p) was derived as in the Equation (4):

$$\alpha_p = \frac{\frac{d}{dz}\left(\ln\left(\frac{N}{P_N z^2}\right)\right) - \alpha_{\lambda_0}^m - \alpha_{\lambda_N}^m}{1+\left(\frac{\lambda_0}{\lambda_N}\right)^k} \tag{4}$$

where N denotes the molecular number density of the nitrogen, λ_0 is the emitted wavelength (355 or 532 nm), λ_N is the wavelength of the nitrogen channel (387 or 607 nm, respectively), P_N is the Raman signal at the nitrogen channel, z is the distance from the lidar, $\alpha_{\lambda i}{}^m$ (i=0, N) is the molecular extinction coefficient at the emitted or the nitrogen wavelength, and k is the wavelength dependence of the particle.

The particle backscatter coefficient profiles (β_p) at 355, 532 and 1064 nm were derived with the use of the obtained particle extinction coefficient profiles at 355 nm and 532 nm and calibrated at the height range free of aerosol.

The particle lidar ratio (LR) is defined as the ratio of α_p and β_p.

The linear particle depolarization ratio (δ_p) was derived as the ratio of the cross channel and the corresponding total channel at the same wavelength, using the Equation (5):

$$\delta_p = \frac{(1+\delta_m)\delta_v\left(1+\frac{\beta_p}{\beta_m}\right)-(1+\delta_v)\delta_m}{(1+\delta_m)\left(1+\frac{\beta_p}{\beta_m}\right)-(1+\delta_v)} \tag{5}$$

where, δ_v is the linear volume depolarization ratio, δ_m is the linear depolarization ratio of air molecules and β_m is the molecule backscatter coefficient.

The vertical distribution of the Ångström exponent $ÅE$ (355/532) was computed by using the profiles of aerosol extinction coefficient (α_p) at 355 and 532 nm using the Equation (6):

$$ÅE = -\frac{\ln\left(\frac{\alpha_p\,(\lambda_1)}{\alpha_p\,(\lambda_2)}\right)}{\ln\left(\frac{\lambda_1}{\lambda_2}\right)} \tag{6}$$

The aerosol optical depth within the boundary layer (AOD_{ABL}) was calculated by integrating the extrapolated (to the ground) aerosol extinction profiles at 355 and 532 nm, from the height of Z_1=0 to the height of the boundary layer top Z_2=ABLH, as in the Equation (7):

$$AOD_{ABL} = \int_{Z_1}^{Z_2} \alpha_p dz \tag{7}$$

The water vapour mixing ratio (WV) was obtained as the ratio of the Raman water vapour channel at 407 nm and the Raman nitrogen channel at 387 nm, using the Equation (8):

$$WV = C\,\frac{P_{H_2O}}{P_{\mathrm{N}}}\exp\left(-\left(\alpha\left(\lambda_{H_2O}\right)-\alpha(\lambda_N)\right)\right) \tag{8}$$

where P_N is the Raman backscatter signal at the nitrogen channel wavelength λ_N, P_{H2O} is the Raman backscatter signal at the water vapour channel wavelength λ_{H2O}.

3.3 The aerosol optical properties retrievals for the target classification scheme

The continuous lidar, cloud radar and microwave radiometer measurements are needed for the 24/7 target classification scheme. From those measurements, profiles of physical quantities related to aerosol, clouds and precipitating particles, as well as profiles of meteorological parameters have to be obtained in with high spatio-temporal resolution. This is challenging for all three instruments.

For lidar, the described in Subchapter 3.2, Raman method (Ansmann et al., 1990) has its limitations in measured height, particularly during the daytime. Hence, the Raman method was considered as not sufficiently consistent in terms of quality and performance to provide products to be used in the 24/7 classification scheme. Instead, the Klett-Fernald method (Klett, 1981; Fernald, 1984) was chosen to obtain the particle backscatter (β_p) coefficient profiles. The elastic lidar signals were evaluated by solving the Bernoulli equation with the assumption of the height independent particle lidar ratio (*LR*), then they were calibrated at a certain height-range of the atmosphere, where only molecular scattering occurs. It is of course difficult to choose the appropriate lidar ratio and the calibration range in the presence of low-level clouds or when aerosol load is high.

Therefore, as a first step the attenuated backscatter coefficient (β_a) was calculated (Baars et al., 2017), as defined in the Equation (9):

$$\beta_a = \frac{PR^2}{C} \tag{9}$$

with the *C* calculated as in the Equation (10):

$$C = \frac{PR^2}{(\beta_p+\beta_m)\ O} \exp\left\{2\int_0^R (\alpha_p + \alpha_m) dr\right\} \tag{10}$$

The *C* is generally stable in a day-to-day scale or longer, thus it can be calculated once per day during the clear sky observation period. If there is no clear sky on the observational day, the *C* calculated on adjacent days with a clear sky period can be used. The β_p profiles used for the *C* calculation are computed with the Klett-Fernald approach and the β_m is calculated using the atmospheric profiles of the 1976 US standard atmosphere (note that also rawinsondes can be used, if available close to the observational site). The particle lidar ratio (*LR*) of 55 sr was used, being a reference applied at several European continental sites for long-term statistical studies. Finally, the instrumental constant *C* is calculated as the mean value of the height between 1 and 2 km in the equation (10).

As the next step, the determination of the quasi-particle backscatter coefficient profiles (${}^{quasi}\beta_p$) is done (Baars et al., 2017). This comprises a 2-step procedure, where the equation (11) gives the first guess of ${}^{quasi}*\beta_p$ (indicated with *) that is used to obtain the quasi-particle extinction coefficient (${}^{quasi}\alpha_p$), as in the equation (12). Then, the equation (13) is used to calculate the final quasi-particle backscatter coefficient profile (${}^{quasi}\beta_p$) that is proportional to the particle backscatter coefficient profile (β_p).

$$ {}^{quasi*}\beta_p = \beta_a \, exp\left\{2\int_0^R \alpha_m dr\right\} - \beta_m \tag{11} $$

$$ {}^{quasi}\,\alpha_p = {}^{quasi*}\,\beta_p \, LR_p \tag{12} $$

$$ \beta_p \approx {}^{quasi}\,\beta_p = \beta_a \, exp\left\{2\int_0^R ({}^{quasi}\,\alpha_p + \alpha_m) dr\right\} - \beta_m \tag{13} $$

In the final step, the scattering ratio (*SR*) defined as the ratio of the quasi-total backscatter coefficient (${}^{quasi}\beta$) and the molecular backscatter coefficient is calculated, as in the Equation (14) and then directly used in the classification scheme.

$$ SR = \frac{{}^{quasi}\,\beta}{\beta_m} = \frac{({}^{quasi}\,\beta_p + \beta_m)}{\beta_m} \tag{14} $$

There is also the second parameter directly used in the classification scheme, namely the backscatter colour ratio (*CR*), which is defined as the ratio of the quasi particle backscatter coefficient at 532 nm and 1064 nm, as in the Equation (15):

$$ CR\ (532/1064) = \frac{{}^{quasi}\,\beta_{p_{532}}}{{}^{quasi}\,\beta_{p_{1064}}} \tag{15} $$

References

Ångström, A.: On the atmospheric transmission of sun radiation and on dust in the air. *Geogr. Ann*. 1929, 12, 156–166. https://doi.org/10.1080/20014422.1929.11880498.

Ansmann, A., M. Riebesell, and C. Weitkamp.: Measurement of atmospheric aerosol extinction profiles with a Raman lidar. *Opt. Lett*. 1990, 15, 746–748. https://doi.org/10.1364/OL.15.000746.

Brooks, I.M. Finding boundary layer top: Application of a wavelet covariance transform to lidar backscatter profiles. J. *Atmos. Ocean. Tech*. 2003, 20, 1092–1105. https://doi.org/10.1175/1520-0426(2003)020<1092:FBLTAO>2.0.CO;2.

Baars, H., Seifert, P., Engelmann, R., and Wandinger, U.: Target categorization of aerosol and clouds by continuous multiwavelength-polarization lidar measurements, *Atmos. Meas. Tech.* 2017, 10, 3175–3201. https://doi.org/10.5194/amt-10-3175-2017.

Campbell, James B., and Randolph H. Wynne. Introduction to remote sensing. Guilford Press, 2011.

Fernald, F. G.: Analysis of atmospheric lidar observations: some comments. *Appl. Opt*. 1984, 23, 652–653. https://doi.org/10.1364/AO.23.000652.

Klett, J. D.: Stable analytical inversion solution for processing lidar returns. *Appl. Opt*. 1981, 20(2), 211–220. https://doi.org/10.1364/AO.20.000211.

Skolnik, M. I. Introduction to radar systems. Vol. 3. New York: McGraw-hill, 1980.

Stull, R. B.: An Introduction to Boundary Layer Meteorology, Kluwer Academic Publishers, Dordrecht, the Netherlands, 1988.

Chapter 4 Variability of the atmospheric boundary layer in Warsaw

4.1 Value-added of the PhD research

Lidar and ceilometer signals collected during 24/7 measurements were used to derive the atmospheric boundary layer height (ABLH) based on a dataset of 10 years of observations in Warsaw (Wang et al., 2020a). The bias of the ABLH calculation caused by the differences in each instrument set-up parameters was reduced. For this purpose, a scaling, threshold-based algorithm for homogenizing both datasets was developed and extensively tested. As a result, the correlation coefficient of ABLH derived from the collocated lidar and ceilometer measurements using the wavelet covariance transform method was strongly improved, from 0.94 to 0.99. This result demonstrated that the methodology is reliable and can be used to provide coherent results for both datasets. The homogenization method workflow is given in Figure 1.

Based on the long-term observations, the diurnal, seasonal, and annual cycles of homogenized ABLH were calculated from lidar and ceilometer signals at the urban continental site in Warsaw. The structure and evolution of ABLH under clear-sky and cloudy conditions were analysed. The monthly mean diurnal cycles of ABLH showed pronounced changes for consecutive months. A clear prolongation of the summer season, and a somewhat smooth transition from late autumn to the winter season were captured. These phenomena were related to meteorological and climate conditions at the Warsaw site. A flattened-shape cycle of early winter months due to the urban heat island effect was observed. In addition, the effect of the global atmospheric heating (El Niño) and cooling (La Niña) that can influence the monthly and yearly variability of ABLHs in Warsaw was discerned.

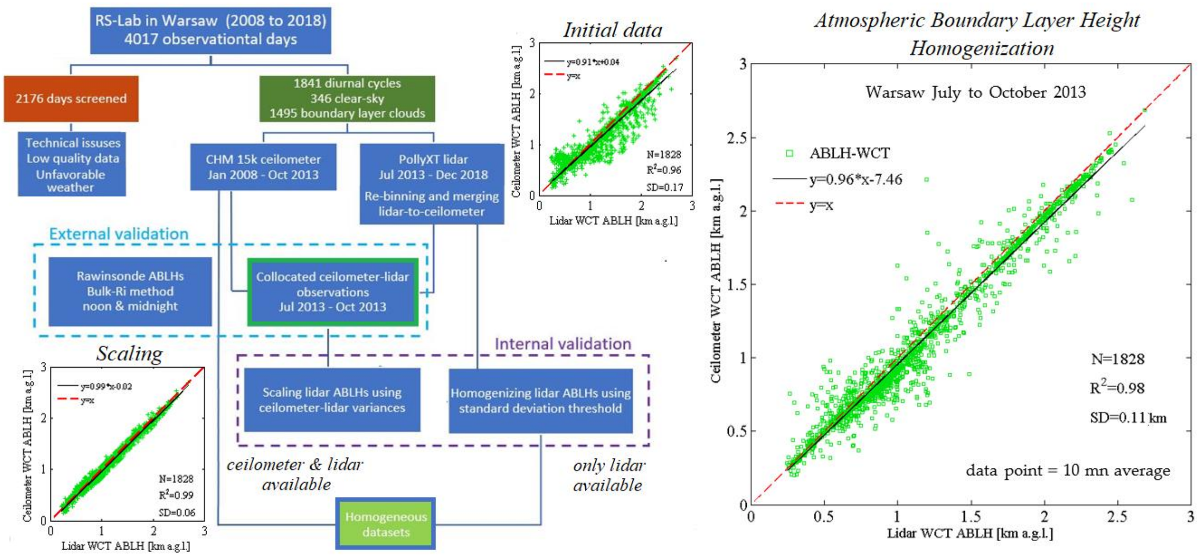

Figure 1. The ABLH data evaluation workflow allowing for the derivation of homogenized datasets from the PollyXT lidar and the CHM15k ceilometer observations in Warsaw; *adapted after Wang et al. 2020a*.

In order to study ABLH in more detail, the nocturnal, residual and well-mixed layers were analysed and discussed separately. The results showed that ABLH characteristics can be affected by local surface conditions (resulting from differences in heat sources, heat capacities, surface roughness) and regional atmospheric structures (resulting in differences in the cloud cover and aerosol load).

A strong seasonal variability of the ABLH distribution (in height and shape) during daytime and night-time was observed. The ABLH night-time and daytime distributions for spring and summer seasons were similar in shape with a peak at 0.8–1.0 km. The autumn distributions have a characteristic plateau between 0.2–1.0 km. In winter, a strong peak at 0.2–0.6 km was revealed. Regardless of the time of the day, the ABLHs above 1.6 km were most frequent in the summer.

Although long-term observations of the characteristics of the atmospheric boundary layer are highly needed in the scientific community, especially in urban environments, such information is scarce. Hence, the 10-year dataset obtained for Warsaw is very valuable. The assessment of temporal variations at different scales gives new, important insights. This work contributes to a better understanding of the ABLH evolution at an urban continental site in the Central Europe region and provides a set of important parameters and references that can be potentially used for improvements of weather prediction and climate models.

Currently, I am working on the analyses of the ABLH at four different sites in Poland. In this study, codes developed within my PhD research are vital.

4.2 Paper 1

Published paper title: Variability of the boundary layer over an urban continental site based on 10 years of active remote sensing observations in Warsaw.
Authors: Dongxiang Wang, Iwona S. Stachlewska, Xiaoquan Song, Birgit Heese, and Anca Nemuc.
Bibliographic record: Remote Sensing, 12(2), 340, 2020.
Link: https://doi.org/10.3390/rs12020340.
Author Contributions (Stated explicitly in the published paper):

D.W. and I.S.S. jointly wrote the paper, prepared the figures and made an extensive literature review. I.S.S. designed the holistic study concept and lead this work, contributed to the development of both remote sensors, took care of the measurement quality assurance and data control and curation, developed the algorithm for homogenizing the lidar-to-ceilometer ABLHs. D.W. contributed with the development of numerical codes for retrieval of ceilometer and lidar data products and prepared statistics of ABLH. X.S. contributed with the ABLH algorithm development. B.H. contributed with lidar hardware and software developments. A.N. contributed with validation of the numerical codes. All authors contributed with interpretation and discussion of results and conducted merit paper revisions. All authors have read and agree to the published version of the manuscript.

remote sensing

MDPI

Article

Variability of the Boundary Layer Over an Urban Continental Site Based on 10 Years of Active Remote Sensing Observations in Warsaw

Dongxiang Wang [1], Iwona S. Stachlewska [1,*], Xiaoquan Song [2,3], Birgit Heese [4] and Anca Nemuc [5]

1 Faculty of Physics, Institute of Geophysics, University of Warsaw, 00-927 Warsaw, Poland; dongxiang.wang@fuw.edu.pl
2 Department of Marine Technology, College of Information Science and Engineering, Ocean University of China, Qingdao 266100, China; songxq@ouc.edu.cn
3 Laboratory for Regional Oceanography and Numerical Modelling, Pilot National Laboratory for Marine Science and Technology (Qingdao), Qingdao 266237, China
4 Leibniz Institute of Tropospheric Research, 04318 Leipzig, Germany; birgit.heese@tropos.de
5 National Institute of Research and Development for Optoelectronics INOE 2000, Remote Sensing Department, 07712 Magurele-Bucharest, Romania; anca@inoe.ro
* Correspondence: iwona.stachlewska@fuw.edu.pl

Received: 19 November 2019; Accepted: 14 January 2020; Published: 20 January 2020

check for updates

Abstract: Atmospheric boundary layer height (ABLH) was observed by the CHM15k ceilometer (January 2008 to October 2013) and the PollyXT lidar (July 2013 to December 2018) over the European Aerosol Research LIdar NETwork to Establish an Aerosol Climatology (EARLINET) site at the Remote Sensing Laboratory (RS-Lab) in Warsaw, Poland. Out of a maximum number of 4017 observational days within this period, a subset of quasi-continuous measurements conducted with these instruments at the same wavelength (1064 nm) was carefully chosen. This provided a data sample of 1841 diurnal cycle ABLH observations. The ABLHs were derived from ceilometer and lidar signals using the wavelet covariance transform method (WCT), gradient method (GDT), and standard deviation method (STD). For comparisons, the rawinsondes of the World Meteorological Organization (WMO 12374 site in Legionowo, 25 km distance to the RS-Lab) were used. The ABLHs derived from rawinsondes by the skew-T-log-p method and the bulk Richardson (bulk-Ri) method had a linear correlation coefficient (R^2) of 0.9 and standard deviation (SD) of 0.32 km. A comparison of the ABLHs obtained for different methods and instruments indicated a relatively good agreement. The ABLHs estimated from the rawinsondes with the bulk-Ri method had the highest correlations, R^2 of 0.80 and 0.70 with the ABLHs determined using the WCT method on ceilometer and lidar signals, respectively. The three methods applied to the simultaneous, collocated lidar, and ceilometer observations (July to October 2013) showed good agreement, especially for the WCT method (R^2 of 0.94, SD of 0.19 km). A scaling threshold-based algorithm was proposed to homogenize ceilometer and lidar datasets, which were applied on the lidar data, and significantly improved the coherence of the results (R^2 of 0.98, SD of 0.11 km). The difference of ABLH between clear-sky and cloudy conditions was on average below 230 m for the ceilometer and below 70 m for the lidar retrievals. The statistical analysis of the long-term observations indicated that the monthly mean ABLHs varied throughout the year between 0.6 and 1.8 km. The seasonal mean ABLH was of 1.16 ± 0.16 km in spring, 1.34 ± 0.15 km in summer, 0.99 ± 0.11 km in autumn, and 0.73 ± 0.08 km in winter. In spring and summer, the daytime and nighttime ABLHs appeared mainly in a frequency distribution range of 0.6 to 1.0 km. In winter, the distribution was common between 0.2 and 0.6 km. In autumn, it was relatively balanced between 0.2 and 1.2 km. The annual mean ABLHs maintained between 0.77 and 1.16 km, whereby the mean heights of the well-mixed, residual, and nocturnal layer were 1.14 ± 0.11, 1.27 ± 0.09, and 0.71 ± 0.06 km, respectively (for clear-sky conditions). For the whole observation period, the ABLHs

Remote Sens. **2020**, *12*, 340; doi:10.3390/rs12020340 www.mdpi.com/journal/remotesensing

below 1 km constituted more than 60% of the retrievals. A strong seasonal change of the monthly mean ABLH diurnal cycle was evident; a mild weakly defined autumn diurnal cycle, followed by a somewhat flat winter diurnal cycle, then a sharp transition to a spring diurnal cycle, and a high bell-like summer diurnal cycle. A prolonged summertime was manifested by the September cycle being more similar to the summer than autumn cycles.

Keywords: scattering lidar; ceilometer; rawinsonde; radiosonde; atmospheric boundary layer cycle; boundary layer height distribution; gradient method; standard deviation method; wavelet covariance transform method

1. Introduction

Different weather and climate phenomena, such as air pollution episodes of smog, severe precipitation, hurricanes, and heat waves, can affect the daily life of human beings, which may cause loss and/or harm to their property. These phenomena are directly or indirectly related to the atmospheric boundary layer (ABL), being the lowest layer of the troposphere directly influenced by the Earth's surface and reacting quickly (within less than an hour) to surface forcing, such as frictional drag, heat transfer, terrain-produced air flows, evaporation, and transpiration [1–3]. On the other hand, there are also global-scale phenomena that can affect the boundary layer. The El Niño Southern Oscillation (ENSO; [4]) is known to accumulate heat in the atmosphere, and thus generates high temperatures [5], affecting indirectly surface conditions even at a global scale [6,7]. The El Niño-related increase of temperatures can cause heat waves [8], and thus affect the variability of the atmospheric boundary layer (the opposite for La Niña) [9].

The atmospheric boundary layer height (ABLH) is one of the most vital parameters, playing a crucial role in boundary layer processes. The dispersion of anthropogenic pollutants, resulting concentrations, and the direction, altitude, and distance of transported pollutants can interplay with and be influenced by the boundary layer structure and diurnal evolution [10,11]. Thus, ABLH is one of the important parameters in studies related to air pollution and pollutant emissions [12]. The boundary layer characteristics and its dynamics are related to adverse ambient conditions, and therefore their knowledge is helpful to model and predict mechanisms that matter in weather forecasting and climate change studies [13]. The efficacy of the climate forcing processes is determined by the effective heat capacity of the atmosphere, which for a cold and dry climate is defined by the depth of the atmospheric boundary layer [14,15]. Therefore, studies of monthly, seasonal, and annual variability of ABLH are of interest for climate assessments. For the forecast of daily weather, as well as the impact of human activity on future climates, the boundary layer must be diagnosed. However, the processes governing the boundary layer evolution are still poorly resolved and/or often not represented in the current forecast models. Especially, continuous observations of changes in the ABLH with high spatial and temporal resolution are desirable to support weather and air quality prediction [16].

Various techniques designed to derive ABLH from various instruments have been compared [17,18]. Rawinsondes onboard meteorological balloons were first employed to estimate ABLHs based on proxies for the mixing process of temperature inversion, relative humidity change, and wind speed and direction variation, parameters considered to be the most reliable reference by many previous studies [19–21]. However, the rawinsondes launches (although usually set for regular observations) are relatively sparse. Moreover, a lack of temporal profiling continuity accompanies the limited vertical resolution, which is influenced by the rawinsonde balloons' size, as well as the wind speed and direction [21]. The ABLH can also be estimated by a wide range of remote sensing techniques, such as sound and radio detection and ranging techniques (sodar/radar), a radio acoustic sounding system (RASS), as well as microwave radiometers or wind profilers [22–24]. Each of these approaches has its limitations regarding the measurement range and accuracy, spatial and temporal resolution, and weather conditions (clouds, fog, and precipitation). The ABLH measurement range and accuracy issues were solved to a large extent with the development of the light detection and ranging technology, e.g., by using next-generation high-power lidars [25–27] or low-power lidars and ceilometers [28–31]. The latter are recognized worldwide as efficient and affordable ground-based instruments for profiling of the atmosphere [32]. A vast number of ceilometers have been deployed in Europe to offer services to airports, meteorological agencies, and research institutions. Many of them operate within the E-PROFILE network (https://e-profile.eu, last access: 11 December 2019) of automatic lidars and ceilometers (ALCs) and radar wind profilers (RWPs) in the framework of the Network of European Meteorological Services EUMETNET (https://www.eumetnet.eu, last access: 11 December 2019). The ceilometers are primarily used for cloud and boundary layer height observations [33,34]. The quick-looks of these ceilometer data are accessible via the German Weather Service (DWD) website (https://www.dwd.de/ceilomap, last access: 11 December 2019).

The determination of ABLH from ceilometer and lidar is based on using the elastic backscatter signals, whereby the ABLH is derived by relying on a higher aerosol load within the boundary layer than in the free troposphere. Several algorithms based on the aerosol load difference have emerged, to name just a few: The first or second derivative methods [35,36], logarithm gradient of the backscatter signal method [22,29,37], backscatter threshold determination [29,38], temporal analysis of the return signal of the standard deviation or variance [39], idealized backscatter fitting [40], and wavelet covariance transform [25,27,41]. In some approaches, a combination of those is applied [12,42–45]. In the STRucture of ATmosphere STRAT algorithm, a combination of the wavelet transform and the range-corrected signal ratio thresholding is used to identify particle regions in lidar profiles. Then, the output of the molecular layer module and the particle layer module is used to help to distinguish the low-altitude clouds from the boundary layer below them [42]. A COBOLT method was compared with the results from three versions of the proprietary software BL-VIEW of the Vaisala CL51 ceilometer designed to retrieve ABLH. Then, the main advantage of the COBOLT is the continuous detection of the MLH with a temporal resolution of 10 min and a lower number of cases when the residual layer is misinterpreted as the mixing layer [12]. The PathfinderTURB algorithm that was developed for the real-time detection of ABLH from CHM15k ceilometer signals uses combined gradient- and variance-based methods to achieve better layer attribution considering the temporal variability of aerosol distribution [45]. For all of the mentioned methods, the basis mainly relies on two principles: The gradient that is related to the signal intensity change, due to the variable vertical distribution of aerosols, and the variance that tracks fluctuations in the temporal distribution of aerosols [25–50]. All approaches have benefits and limitations, which were discussed recently in an extensive review paper on the ABLH retrieval techniques; still, no completely robust and reliable method has been established [18].

Most of the studies reported in the literature focus on ABLH retrieval during the daytime and for fair-weather conditions [24,28,34,37–40] while retrievals during complex weather situations, as well as during the sunrise/sunset and at nighttime, have been performed less often [27,29,31,46]. The most complex boundary layer and aerosol conditions often form at night, which is regarded as an important part of the diurnal changes within the ABL, and thus the nocturnal boundary layer should not be excluded from the ABLH statistical analysis. Moreover, research studies based on continuous long-term monitoring of the ABLH are seldom available [25,29,44], particularly datasets acquired for longer than 5 years, and high temporal and spatial resolution retrievals are rare [30]. In general, the knowledge of the long-term daytime and nighttime boundary layer variability is still rather limited [51]. Added to this, the long-term seasonal and annual statistics at particular places of interest are seldom in existing studies [29,44], especially their combination with other parameters related to the air quality or the optical properties of the atmosphere [11,12,16,52]. Additionally, boundary layer clouds, being a part of ABL, play an important role in the ABL variability [53,54]. However, they often tend to be screened [25,37,55], resulting in the clear-sky bias of the retrieval.

For the work reported within this paper, a combination of lidar and ceilometer observations in Warsaw were analyzed in terms of a unique sample, allowing derivation of the diurnal, seasonal, and annual cycles of ABLH based on 1841 daily evolution measurements. Firstly, through the exploration of these data, the analysis of a statistically significant probe of the ABLHs allowed for an assessment of the performance of the PollyXT lidar and the CHM15k ceilometer. Secondly, the height, structure, and evolution of the Warsaw ABLH for a decade of remote observations obtained by combining the data of both instruments are presented. Also, the characteristics of ABLH in Warsaw under clear-sky and cloudy conditions are discussed. This work contributes to a better understanding of the ABLH evolution at an urban continental site in the central Europe region and provides a set of important parameters and references that can be potentially used for improvements of weather prediction and climate models.

The paper is organized as follows. In Section 2, the remote sensing instruments are described. Section 3 details the methodology for calculating ABLHs from lidar, ceilometer, and rawinsonde measurements. In Section 4, the ABLHs estimated from 4 months of simultaneous lidar and ceilometer data using different retrieval methods were inter-compared. The most suitable method for ABLH retrieval for both sensors was found by comparing the results with the ABLH derived from rawinsondes. In Section 5, the scaling threshold-based method is proposed to decrease the bias of the ABLHs derived with lidar and ceilometer, therefore allowing both datasets to be homogenized. In Section 6, the monthly, seasonal, and yearly variability of the ABLH over Warsaw, including the frequency distribution of altitude occurrence during daytime and nighttime for the entire observational period, are reported. Finally, the paper is concluded in Section 7.

2. Instrumentation

Within this study, two ground-based active remote sensors were utilized: The custom-designed ceilometer (CHM15k model, Lufft/JenOptik, Germany) and the multiwavelength-Raman-polarization lidar PollyXT (collaborative in-house development). Both instruments were operated at the Remote Sensing Laboratory (RS-Lab) of the Institute of Geophysics at the Faculty of Physics of the University of Warsaw, located in Warsaw city center (52.2109°N, 20.9826°E, 112 m a.s.l.). The RS-Lab is equipped with several instruments that were used in this study as auxiliary (locations indicated in Figure 1) or not at all (https://www.igf.fuw.edu.pl/en/instruments/, last access: 11 December 2019). The RS-Lab regularly provides data to several networks: The Polish Aerosol Research Network (PolandAOD-NET, http://www.polandaod.pl, last access: 11 December 2019), the EARLINET (https://www.earlinet.org, last access: 11 December 2019), and the worldwide lidar network Polly-NET (http://polly.rsd.tropos.de, last access: 11 December 2019).

The CHM15k ceilometer was continuously operated in Warsaw from 1 January 2008 to 31 October 2013. It was installed on the roof-platform of the RS-Lab (21 m a.g.l.). The data was acquired with a temporal resolution of 30 s and a spatial resolution of 15 m, with the maximum signal range of 15.36 km (corresponding to 1024 range-bins). The ceilometer comprises a diode-pumped Nd:YAG solid-state laser, which emits low-energy laser pulses (8 µJ), at a high frequency (5–7 kHz), at a wavelength of 1064 nm. The optical design is based on a refracting telescope; the lens has a 100 mm diameter. The lowermost level of the overlap between the emitted laser beam and the receiver lens is at approximately 180 m and the full overlap is completed at approximately 800 m. The CHM15k instrument at the RS-Lab has a custom field of view (FOV, i.e., 0.9 mrad), which results in an optimal overlap and signal-to-noise ratio (SNR) being achieved [29]. For comparison, the standard CHM15k has a narrower FOV (but issues with high overlap) and the CHM15kx has a wider FOV (but issues with background radiation), as discussed in detail by [32]. The automatic manufacturer overlap correction is applied to the ceilometer signals. The standard CHM15k can suffer from the fact that the amplitude of the overlap correction is temperature dependent, this being larger for higher temperatures [56]. The study of the overlap function and the instrumental constant dependence on the internal temperature changes was also done for the RS-Lab CHM15k. From 30 April to 2 May 2012, the ceilometer was installed

Remote Sens. **2020**, *12*, 340

at the St. Jacob the Apostle Parish located in the small, sparsely populated and spacious rural town of Głowno (51.9645°N, 19.7249°E) in the Central Polish Lowlands. Unique horizontal measurements were taken over the Mrożyczka Reservoir, and thus calculations were done within the range where no local traffic influence was possible. The results showed that for the RS-Lab version of the CHM15k, the temperature effects are negligible. The overlap function was determined from several horizontal measurements to assess the signal quality at ranges near the ceilometer. The closest range-bin for which the signal variability was significant (i.e., $>3\sigma$ at daytime and $>1\sigma$ at night) was at the range-bin 12, translating to 180 m. Since November 2013, the ceilometer measurements have been conducted at the SolarAOT Observatory in Strzyzow within the PolandAOD-NET activities. Further details on this particular version of the custom-designed ceilometer are described in [29] and the differences of various versions of the CHM15k and CHM15kx ceilometers are discussed in [32].

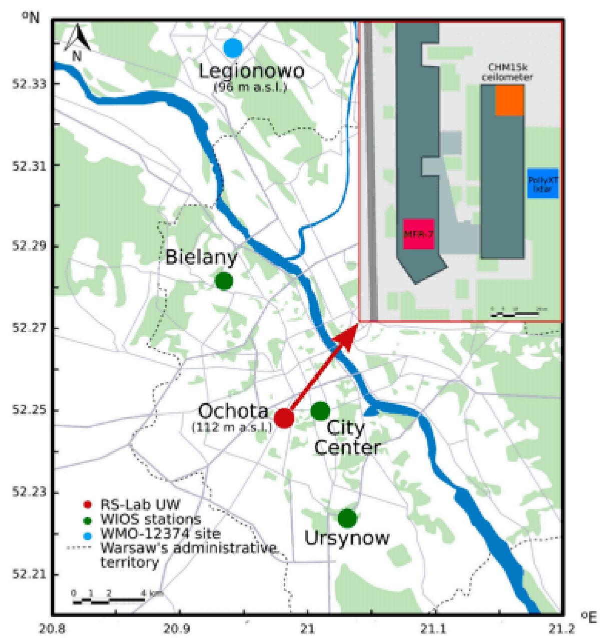

Figure 1. Location of the Remote Sensing Laboratory (RS-Lab) at the Ochota Campus of the University of Warsaw in the city center (in red), the World Meteorological Organization site (WMO-12374) in the small town Legionowo (in blue), and the Chief Inspectorate for Environmental Protection of Poland (WIOS) $PM_{2.5}$ and PM_{10} monitoring stations (in green). The locations of the PollyXT lidar, the CHM15k ceilometer, and the MFR-7 shadowband radiometer at the RS-Lab at ground-based station and two roof-platforms are indicated (map provided by Olga Zawadzka-Mańko).

The PollyXT lidar was built in a scientific collaboration of the Institute of Geophysics at the Faculty of Physics of the University of Warsaw (IGFUW, Warsaw, Poland) and the Leibniz Institute of Tropospheric Research (TROPOS, Leipzig, Germany). It was installed at the RS-Lab in Warsaw in June 2013. After an extensive test phase, the lidar started operation on 1 July 2013 and has performed quasi-continuous observations ever since. The lidar emits high-energy laser pulses of 180 mJ at 1064 nm, 110 mJ at 532 nm, and 60 mJ at 355 nm, with a repetition rate of 20 Hz. The initial laser beam is expanded to a 45 mm diameter, providing a low beam divergence of 0.2 mrad. The signals are received by two reflecting telescopes: The narrow field of view (1 mrad) large-sized telescope (300 mm diameter) and the wide field of view (2.5 mrad) small-sized telescope (50 mm diameter). The later was installed in April 2016, with the aim of improving the lidar detection range at altitudes close to the ground (<1 km). The measurements are performed at 8-channels, using the large telescope, and at 4-channels, using the small telescope. The 8-channel detection unit (so-called $2\alpha + 3\beta + 2\delta + WV$) enables the determination of the extinction coefficient profiles at 532 and 355 nm; the backscatter coefficient at 1064, 532, and 355 nm; the depolarization ratio at 532 and 355 nm; and the water vapor mixing ratio. The 4-channel detection unit (so-called $2\alpha + 2\beta$) is designated for obtaining the extinction and backscatter coefficient profiles at 532 and 355 nm. The signals are recorded up to 48 km (with a pretrigger length of 250 range-bins). The data of all channels is obtained with a standard 7.5 m vertical resolution in temporal steps of 30 s. The overlapping range of the laser beam and the large and the small telescopes is completed at roughly 400 and 120 m, respectively. No overlap correction was applied to the lidar data in this paper. The overlap function of lidar is monitored as the ratio of the signal collected with the small telescope to the signal collected at the large telescope, and thus for two elastic (355 and 532 nm) and two Raman (387 and 607 nm) channels. Additionally, we monitored the stability of the overlap with a camera, the laser pulse energy with a power meter, and the temperature inside the lidar cabinet. The inspection of the monitored parameters shows that typically, the temperature-dependent differences in the overlap are very low (<15 m) and the stability of the lidar signal is high (>98%), which is due to the use of an insulated cabinet equipped with an efficient heating–cooling system. More technical information on PollyXT-type lidars can be found in [57]. The aerosol optical properties retrieval schemes are introduced in [11,58,59]. The aerosol microphysical properties' retrieval is described in [60] and the water vapor derivation methodology in [61].

Concerning the overlap region of the two sensors, the lowest possible height of ABLH that can be unambiguously detected with the ceilometer and lidar (large telescope) is at 195 m a.g.l. Note that the lidar range resolution is reduced to merge the ceilometer range resolution of 15 m, whereby the lidar initial range-bins 4th and 5th correspond to the ceilometer 1st range-bin.

Note that for both instruments described here, the signal-to-noise ratio depends on the solar background illumination and the presence of molecules and particles suspended in the atmosphere, whereby it decreases rapidly when the optical depth of the atmosphere declines. The SNR was calculated using the approach described in [62].

The auxiliary instrumentation of the RS-Lab that was used in this paper comprises the sensors installed at two roof platforms (Figure 1), i.e., the weather transmitter WXT510 (Vaisala), the disdrometer OTT (Parsivel), the passive multi-filter rotating shadowband radiometer on a solar tracker MFR-7 (Yankee Environmental Systems), and the sun photometer CE318 (CIMEL Electronique); the latter has been operated since 1 January 2018.

3. Methodology

3.1. Atmospheric Boundary Layer Heights from Lidar and Ceilometer

As already described in the introduction, several studies have demonstrated that the PollyXT lidars and CHM15k ceilometers are reliable in detecting atmospheric aerosol structure and evolution. The first automated ABLH retrieval for one year of the PollyXT lidar data was reported by [25]. The annual ABLH cycles derived from 4-year CHM15k ceilometer observations were reported by [29]. In the current paper, the ABLH datasets derived from these two instruments were obtained using an automated routine and utilized to derive the decadal coverage of the ABLH variability over Warsaw.

The auxiliary instrumentation was used for identifying the fog/smog and precipitation, as well as for distinguishing clear-sky from cloudy days.

The fog/smog and precipitation conditions were identified using of the following information: The RS-Lab roof platform measurements of the metrological data with the WXT510 (Vaisala) weather transmitter and the OTT disdrometer, the aerosol optical depth (AOD) derived from the MFR-7 and CE318 sun photometer, as well as the particulate matter, $PM_{2.5}$ and PM_{10}, concentrations measured by the air quality monitoring WIOS stations (Figure 1). The WIOS data are publicly available via the Archive of the Chief Inspectorate for Environmental Protection of Poland (http://powietrze.gios.gov.pl/pjp/archives, last access: 11 December 2019).

The clearness index of the sky can be quantified with the use of the instantaneous extraterrestrial solar fluxes reaching Earth's surface [63], which are a good indicator for distinguishing clear from cloudy days at daytime. At the RS-Lab roof platform, the MFR-7 radiometer measures the global and diffuse fluxes and the pyranometer the hemispheric solar radiation flux density. The fluxes are obtained only in daytime, and thus another method is needed to estimate the sky clearness at nighttime. Therefore, for both day and night observations, the state-of-the-art cloud screening procedure of EARLINET is applied [64]. This procedure is used by the so-called Single Calculus Chain (SCC) software developments (https://scc-documentation.readthedocs.io, last access: 16 December 2019). Note that in this paper, the clear-sky definition includes the cloudless scenarios, as well as the scenarios for which Cirrus clouds occur above 8 km over the measurement site.

The specific aim was to derive the diurnal cycles of the ABLH, defined as starting at night, with the nocturnal boundary layer (NL), characterized by stable air with sporadic turbulence, followed (after sunrise) by a development of the well-mixed layer (WML) during the day, and after sunset, the residual layer (RL) in place of the mixed layer, and/or the stable boundary layer near the ground [1–3]. The boundary layer heights derived from the lidar and ceilometer data are related to the aerosol load present in the lowermost atmosphere, and therefore they do not precisely correspond to the atmospheric boundary layer height as defined therein. In comparison with the idealized definitions, the lidar and ceilometer ABLHs are derived based on an apparent aerosol load change, which occurs between the atmospheric boundary layer and the free troposphere. However, even if this relation is not simple, in this paper, it was assumed that they are proportional. The ABLH derived around sunrise and sunset was defined as the transition layer (TL). As the WML, TL, RL, and NL are related to certain times of the day, which depends on the season; their definitions are given in Table 1.

Table 1. The definitions of the time duration for the boundary layer per season used in this study. The given times were assessed as corresponding to the listed periods in different seasons and do not represent the mean values. Times are given in UTC.

	Spring (MAM) Autumn (SON)	**Summer (JJA)**	**Winter (DJF)**
Daytime	05:00–17:00	04:00–19:00	06:00–15:00
Nighttime	19:00–04:00	20:00–03:00	16:00–06:00
Well-mixed layer (WML)	12:00–16:00	12:00–17:00	12:00–14:00
Transition layer (TL) sunrise	05:00–11:00	03:00–11:00	06:00–11:00
Transition layer (TL) sunset	17:00–19:00	16:00–20:00	15:00–16:00
Nocturnal and residual layer (NL, RL)	20:00–04:00	21:00–02:00	17:00–05:00

From the individual diurnal cycle data, the monthly mean diurnal cycles and the annual cycles of the ABLH, the seasonal mean ABLHs, and the annual mean NL, WML, and RL heights, as well as the daytime and nighttime ABLH frequency distribution, were derived. The time duration of daytime and nighttime per season used in this study are specified in Table 1. For comparison, the exact sunrise and sunset times are available via https://www.timeanddate.com/sun/poland/warsaw. Warsaw is located in the Central European Summer Time zone, i.e., CEST = UTC/GMT + 2 h. The daylight-saving time starts on 31 March with 1 hour forward and ends on 27 October with 1 hour back. The local time is divided to LT = UTC + 2 h (so-called local summertime) or, LT = UTC + 1 h (so-called local wintertime).

More information can be found at https://www.timeanddate.com/worldclock/poland/warsaw (last access: 11 December 2019). Note that all analyses were performed in local time, but in this paper, the values are given in UTC.

The elastically backscattered 1064 nm lidar and ceilometer signals were used for the boundary layer detection. The range resolution of the two instruments was merged to ceilometer resolution (15 m). Thus, the re-binning was applied before the data processing. The 4th and 5th range-bins of the lidar (block average) corresponding to 33.75 m a.g.l. was merged to the 1st range-bin of the ceilometer (on the roof platform) corresponding to 36 m a.g.l. The resulting difference was regarded as negligible.

The lidar and ceilometer signals were collected with a 30 s resolution but the ABLH detection was performed on the 10 min averaged range-corrected backscatter signals. Then, the sliding average in time was applied, thus one 10 min average signal was provided every 30 s. Three different algorithms were used on these signals to estimate the ABLH. In the gradient method (hereafter GDT), the first derivative of the signal logarithm (with height) is used and the strongest negative gradient marks the ABLH. The second method is based on investigating a standard deviation of the signals (hereafter STD). The standard deviation of the averaged signals (after the sliding average) is calculated over the 10 min window, and then the altitude at which the standard deviation is maximal marks the ABLH. The wavelet covariance transform method (hereafter WCT) comprises analysis of the vertical signal gradient and fast temporal changes in the signal time series, as a function of the height. On the one hand, the advantage of the WCT method is that it is less affected by the signal-to-noise ratio than the two other methods [25,41]. On the other hand, the main challenge of this method is to find an appropriate value of the dilation, a. In this paper, the dilation defined as 4 times the range resolution of 15 m was used, based on a sensitivity study conducted to optimize the choice of dilation. Smaller dilation values resulted in numerous local minima and prevented unambiguous detection of ABLH. Thus, the height window of 60 m was used for the time window of 10 min (for both instruments).

In order to reduce the impact of the overlap-affected range of the remote sensing measurements [65] and the middle-level clouds [53], the lower and the upper limit for the derived ABLH was defined. Within the blind region of the incomplete overlap range of each instrument, the received signal is extremely weak and dominated by noise, thus it is difficult to obtain a valid ABLH, except for particular conditions, such as very low clouds, fog, or smog (even then, the accuracy of the retrieval is low). Above the blind region, when the laser beam begins to enter the telescope's field of view, the signal increases and the SNR improves. In the range of the completed overlap, the SNR is entirely driven by the scattering and absorption by molecules and particles suspended in the atmosphere. Thus, both instruments need a defined lowest level height (concerning the blind region of the incomplete overlap) to maintain high-quality calculations [62].

The cloud bottom heights (CBHs) derived within the 3-km altitude were regarded as marking the top of the boundary layer. The CBH was detected by the strongest positive change in the range-corrected backscatter signal of the lidar or ceilometer measurement. Generally, clouds influence short-wave and long-wave radiation, as well as latent and sensible heat flux, thus consequently, the boundary layer diurnal cycle. They can form either at the top of the daytime mixed boundary layer or at the base of the stable (usually nocturnal) boundary layer. Their occurrence is closely connected to thermodynamics within the boundary layer. Low-level clouds (cloud bottom heights < 2 km) are a frequent phenomenon in the boundary layer, especially cumulus and stratocumulus that often occur at the top of the boundary layer (a so-called boundary layer cloud). Therefore, the upper limit of the ABLH retrieval was set to 3 km. This is in accordance with the mixing layer heights reported for other continental sites as being below this altitude [17,25,26,29,66–68]. Note that, in general a ceilometer signal is less powerful compared to that of lidar, and therefore the excellent ability of ceilometers to detect aerosols is practically limited up to approximately a 3 km height [62,65,69]. For the cases when the algorithm chooses the cloud as the top of ABL, when such a cloud is at the altitude of 3 to 6 km (i.e., middle-level clouds), it is not used as marking the ABLH, as it is considered to be detached from the boundary layer [1–3].

3.2. Atmospheric Boundary Layer Heights from Rawinsondes

Balloon soundings are frequently done with the use of radiosondes that measure atmospheric pressure, temperature, and humidity. When the radiosonde position is tracked to also provide the wind speed and direction it is called a rawinsonde. Rawinsondes launches at the World Meteorological Organization site closest to Warsaw were used. The WMO-12374 site in a small town Legionowo

(52.40°N, 20.96°E, 96 m a.s.l.) is located 25 km north of the RS-Lab. Note that Warsaw and Legionowo are characterized by a flat orography, with a maximum elevation difference below 40 m a.g.l. between the two measurement sites (an elevation map of the 50 km^2 area is available at https://en-us.topographic-map.com/maps/tlmm/Warsaw, last access: 11 December 2019).

The RS92 rawinsondes (Vaisala, Finland) are launched twice a day at 00:00 and 12:00 UTC. They provide vertical profiles of, amongst others, the atmospheric pressure, temperature, dew point temperature, relative humidity, and wind speed. These parameters were used in our study for different retrievals. The ABLH was identified in the rawinsonde profiles using two methods. The first one was based on identifying the height of a sharp change in the temperature (or dew point temperature) and the relative humidity profiles on the skew-T-log-p diagram used frequently for radiosondes [70]. The second one was the bulk Richardson (bulk-Ri) method [71], which is known to be favorable for ABLH retrieval in both stable and convective conditions [51], whereby this method requires rawinsondes. The bulk-Ri method uses the ratio of the turbulence associated with buoyancy to that associated with mechanical shear, and the ABLH is defined as the lowest height at which Ri matches the critical value of 0.25 [71].

Rawinsondes' data were obtained from the Upper Air Data website of the University of Wyoming (http://weather.uwyo.edu/upperair/sounding.html, last access: 11 December 2019).

The diagrams of rawinsondes for the discussed measurement period of 2008 to 2018 are depicted as quick-looks at the PolandAOD-NET Website (http://www.Polandaod.pl, last access: 16 December 2019).

4. Results of Boundary Layer Height Retrieval Comparison

The ABLH values derived from lidar and ceilometer signals were compared against the ABLHs derived independently from the rawinsondes meteorological profiles. The direct lidar–ceilometer comparison was performed as well. This analysis was done for the 4 months when the ceilometer and lidar performed simultaneous observations from 1 July to 31 October 2013. The observations conducted under clear-sky and cloudy weather were analyzed while those collected in fog/smog and precipitation were not used.

4.1. ABLH Comparisons for Lidar, Ceilometer, and Rawinsondes Data

Within the time window of 1 July to 31 October 2013, all lidar and ceilometer measurements in Warsaw that were coincident with the rawinsondes' launches at 00:00 and 12:00 UTC in Legionowo were compared. Due to the limited availability of the coincident data (mainly due to lidar), only 84 profiles were available for comparison. As for the rawinsonde evaluated with the skew-T-log-p method, five profiles with no significant inversion in the temperature or the dew point temperature profile were screened. The inversion threshold was defined as the difference in the value of the two adjacent temperature points exhibiting a sharp gradient of at least 3 °C. Lidar and ceilometer profiles for which the ABLH was >3 km in altitude (three cases) were screened [70,72]. The data points where the ABLHs difference between the rawinsonde lidar or rawinsonde ceilometer was >2 km (four cases) were screened, as in those cases each instrument clearly measured a different air mass [60,61,69].

The ABLHs derived from active remote sensors using the GDT, STD, and WCT methods, separated to clear-sky and cloudy conditions, for both pairs of instruments (lidar rawinsonde and ceilometer rawinsonde) are shown in corresponding scatter plots in Figure 2 (for brevity, only results for the bulk-Ri method are shown). For all plots, a linear fit to 72 data points was made. In general, the fitted lines indicate a better correspondence of ceilometer than lidar to the rawinsonde. Note that the Pearson correlation coefficients in this paper were calculated to assess the linear relationship between the two variables (ABLH values) derived with the different methods. When the significance level was $p \leq 0.05$, then the correlation coefficient was considered statistically significant. All correlations reported in this paper were found to be statistically significant, unless explicitly stated otherwise. The correlation coefficients are denoted as R^2 and the corresponding standard deviation as SD.

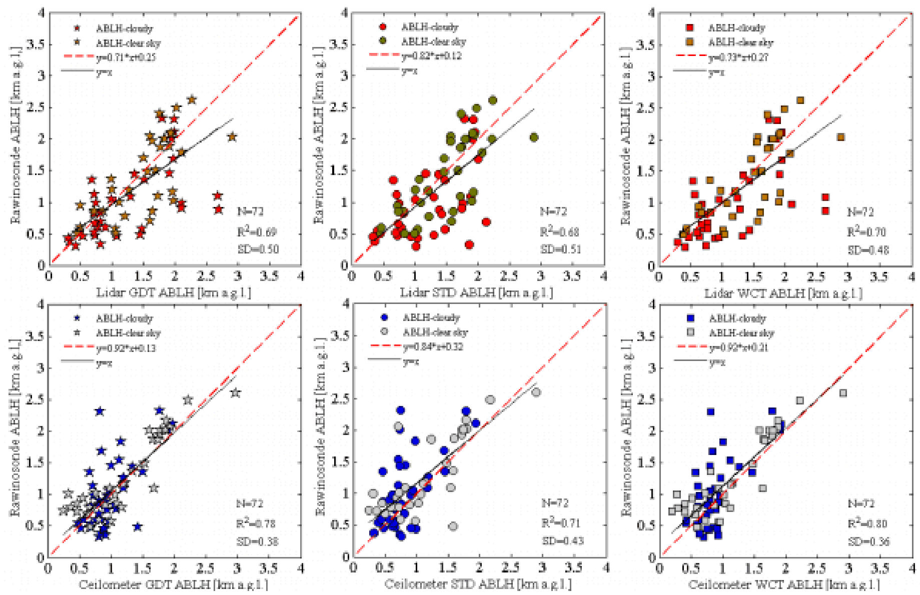

Figure 2. Correlation plots of the atmospheric boundary layer height (ABLH) derived from rawinsondes (bulk Richardson method) at 00:00 and 12:00 UTC in Legionowo versus those derived using the gradient method GDT (left, stars), standard deviation method STD (middle, circles), and wavelet covariance transform WCT (right, squares) algorithms applied to the PollyXT lidar (top) and the CHM15k ceilometer (bottom) in Warsaw. The period of July to October 2013 is covered. In brown/gray, the ABLHs derived in clear-sky conditions and in red/blue for boundary layer cloud conditions.

In Table 2, the results regarding the lidar and ceilometer ABLHs comparisons with the two rawinsonde retrieval methods are listed. In Figure 3, the correlation plot of ABLHs calculated using the skew-T-log-p method versus the bulk-Ri method for daytime and nighttime rawinsonde launches are plotted.

Table 2. The correlation coefficient (R^2) and the standard deviation (SD) of the ABLHs derived from lidar and ceilometer by using the GDT, STD, and WCT methods versus the ABLHs derived from rawinsonde by using the skew-T-log-p and the bulk-Ri methods. Results obtained during clear-sky and cloudy conditions from July to October 2013.

July to October 2013	Lidar			Ceilometer		
	GDT	STD	WCT	GDT	STD	WCT
Bulk Richardson method						
All measurements N = 72	R^2 = 0.69 SD = 0.50 km	R^2 = 0.68 SD = 0.51 km	R^2 = 0.70 SD = 0.48 km	R^2 = 0.78 SD = 0.38 km	R^2 = 0.70 SD = 0.43 km	R^2 = 0.80 SD = 0.36 km
Clear-sky conditions N = 34	R^2 = 0.70 SD = 0.61 km	R^2 = 0.72 SD = 0.46 km	R^2 = 0.74 SD = 0.42 km	R^2 = 0.88 SD = 0.30 km	R^2 = 0.78 SD = 0.45 km	R^2 = 0.90 SD = 0.29 km
Cloudy conditions N = 38	R^2 = 0.66 SD = 0.56 km	R^2 = 0.55 SD = 0.53 km	R^2 = 0.60 SD = 0.54 km	R^2 = 0.73 SD = 0.47 km	R^2 = 0.59 SD = 0.53 km	R^2 = 0.75 SD = 0.43 km
Skew-T-log-p method						
All measurements N = 72	R^2 = 0.62 SD = 0.60 km	R^2 = 0.59 SD = 0.61 km	R^2 = 0.63 SD = 0.59 km	R^2 = 0.75 SD = 0.44 km	R^2 = 0.64 SD = 0.52 km	R^2 = 0.76 SD = 0.43 km
Clear-sky conditions N = 34	R^2 = 0.64 SD = 0.55 km	R^2 = 0.61 SD = 0.57 km	R^2 = 0.65 SD = 0.53 km	R^2 = 0.82 SD = 0.36 km	R^2 = 0.72 SD = 0.48 km	R^2 = 0.83 SD = 0.36 km
Cloudy conditions N = 38	R^2 = 0.62 SD = 0.62 km	R^2 = 0.52 SD = 0.58 km	R^2 = 0.56 SD = 0.62 km	R^2 = 0.64 SD = 0.49 km	R^2 = 0.49 SD = 0.55 km	R^2 = 0.68 SD = 0.47 km

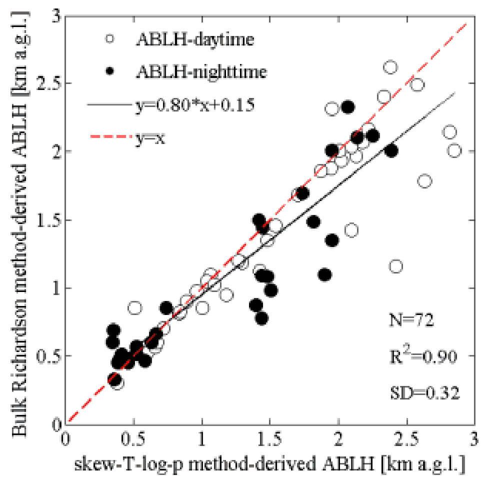

Figure 3. Correlation plots of ABLHs calculated using the skew-T-log-p method and the bulk Richardson method from rawinsonde at 00:00 and 12:00 UTC in Legionowo within the period of July to October 2013 for N = 72 data points coinciding with the data points depicted in Figure 2.

The scatter plot of the lidar-rawinsondes ABLHs is given in Figure 2, top row. Regardless of the applied retrieval method, the correlation coefficients were found to be positive and relatively high, although accompanied by a significant standard deviation. The differences in the correlation coefficients were negligible within the obtained range of the standard deviations. The best agreement of the lidar-derived ABLHs was obtained for the WCT method (R^2 of 0.70 and SD of 480 m), then for the GDT method (0.69 and 500 m), and the STD method (0.68 and 510 m), when compared to the rawinsonde.

The comparison results for the ceilometer-rawinsonde ABLHs are given in Figure 2, bottom row. The positive correlation coefficients obtained for ceilometer versus rawinsonde were somewhat higher than those derived for lidar versus rawinsondes, being the highest for the WCT (R^2 of 0.80 with SD of 360 m), then the GDT method (0.78 and 380 m), and the STD method (0.71 and 430 m). An underestimation of the ceilometer ABLHs (regardless of the derivation method and altitude range), concerning the rawinsonde ABLHs, was clearly discernible.

The ABLHs shown in Figure 3 for direct comparison of the skew-T-log-p method and the bulk-Ri method have an R^2 of 0.9 and SD of 0.32 km. Note that the daytime and nighttime rawinsondes are plotted separately. For many data points, the skew-T-log-p method retrievals are overestimated, which (as expected) favors the bulk-Ri method, as the latter considers both buoyancy-produced and mechanically produced turbulence [51]. One can see that in the samples of daytime (related to WML; N = 39) and nighttime (NL, N = 33) measurements over Legionowo, there are some ABLH values derived within the range 1.5–2.5 km at nighttime. This gives confidence that a few such high ABLH values obtained for NL from lidar/ceilometer are not an artifact.

Advected residual or lofted aerosol can sometimes be observed at nighttime in Warsaw and its vicinity, and it can lead to ABLH > 2 km. This agrees with observations under heat wave conditions reported in [11], where semi-persistent growth of ABLH values to extreme levels is discussed as being due to an injection of long-range transported pollution from Germany into the urban boundary layer over Warsaw. Several high ABLHs at nighttime are also reported for statistical analyses of the boundary layer optical properties by [52], where one of the possible reasons discussed is aerosol bursts [73]. As shown in Figure 3, ABLHs derived in Legionowo confirm the possible existence of such high NL in the vicinity of Warsaw city. Therefore, the values are in relation to the true boundary layer top variability.

Comparison studies for the collocated rawinsonde-lidar ABLHs revealed high correlation coefficients of 0.91 for stable and 0.96 for unstable environments [21]. For the collocated rawinsonde-ceilometer AHLHs, the correlation coefficients of 0.9 in convective conditions and 0.8 for stable conditions were reported [34]. The ABLH correlation coefficients of 0.85, 0.82, and 0.89 were reported for using, respectively, the gradient method, cluster method, and wavelet method applied to ceilometer data, as compared to rawinsonde-derived ABLHs [70]. Therefore, this kind of comparison was regarded as an appropriate approach to verify the accuracy of the ABLHs derived from the lidar and ceilometer. However, in the current study, the difference in the location of the rawinsonde and the location of the lidar and ceilometer resulted in somewhat lower correlation coefficients concerning the values reported in the literature. The low number of samples and the method applied for rawinsonde ABLH retrievals can play a role in such a comparative study [17,44]. This cannot be excluded also in our case, which is visible in Table 2, whereby the performance of one of the methods is indeed better.

The lidar-rawinsonde and ceilometer-rawinsonde ABLHs for clear-sky and cloudy conditions for the period from July to October 2013 are listed in Table 2. For both lidar and ceilometer, the best results in terms of the highest correlation coefficient and the lowest standard deviation were obtained in clear-sky conditions (WCT method) and the worst in cloudy conditions (STD method). Comparisons of the rawinsonde bulk-Ri method retrievals with the lidar/ceilometer GDT, STD, and WCT retrievals shows that (regardless of the weather conditions) the standard deviation is higher for the rawinsonde versus lidar (420–540 m) than for the rawinsonde versus ceilometer (290–430 m), whereby the highest standard deviations were obtained for the STD method.

The correlation coefficients were in the range 0.55–0.74 for the lidar rawinsonde and 0.59–0.90 for the ceilometer rawinsonde. As for comparisons of the skew-T-log-p with the lidar/ceilometer retrievals, they show consistent results with the bulk-Ri comparisons, with somewhat lower R^2 and SD. Based on the values given in Table 2, the WCT method performed the best, except for one case (the GDT for lidar in cloudy conditions). As for the analyses of the differences between the clear days and the cloudy days shown in Table 2, it must be mentioned that although they are present, they are not statistically significant.

The discrepancies found between the ABLHs derived from the three different instruments must be at least partly attributed to the differences in the measurement technique (the active remote sensing versus the in-situ sounding) as well as to the retrieval algorithms and their physical definition (the tracking of sharp changes in the aerosol load versus the marking of the top of the mixing process, with respect to the thermodynamic principle). The differences are expected also due to the atmospheric conditions, so when complex aerosol layers or boundary layer clouds appear within 3 km, different results between the rawinsonde and lidar/ceilometer ABLH retrieval can be expected [21,70]. Therefore, the higher correlation coefficients are expected to be obtained for the typical clear-sky-biased analyses [34,37,39]. Thus, in the case of occurrence of very local phenomena, such as fog or smog at one of the sites, data points should not be used for comparative analyses. The differences attributed to the distance (25 km), the elevation altitudes (112 versus 96 m a.s.l., and the near-surface conditions (city center versus semi-rural) at the two sites can be considered, especially in the lowermost atmosphere. The elevation altitude differences mentioned here are not related to retrieval uncertainties but the physical features in the atmosphere above each measurement site.

The impact of the distance, local surroundings, and the near-surface conditions was reported as not significant for the relative humidity profiles' comparison at the two sites in Warsaw and Legionowo [61]. For these cities, more of a concern was the large-scale circulation [11,59] and the air-mass inflow with a related height-dependent tropospheric wind direction change at each site [60,61]. Therefore, for certain meteorological conditions, higher correlations can be expected, e.g., for the air-mass transport within less than 1 h along the north–south transect between the two cities [60].

The comparison study of the mixing height (calculated using the gradient method combined with the wind speed threshold method) between Wien Hohe Warte (suburban) and Obersiebenbrunn (rural) located at a distance of roughly 30 km, with an elevation difference of above 70 m between the two sites, revealed that local conditions could give rise to occasional large differences in the mixing height [74]. The frequency distribution analysis of the ABLH differences among Pairs (urban metropolitan), Palaiseau (suburban), and Trainou (rural), located at a distance of 20 km from each other, with even more significant differences in elevation (28 m to 159 m), revealed the urban ABLH was higher than the rural ABLH during daytime and higher that of the suburban during nighttime [75]. In our case, no clear conclusion was drawn on the ABLH difference between the two sites in Warsaw and Legionowo, as related to urban versus rural effects.

4.2. Comparison of ABLH Derived by Lidar and Ceilometer under Different Conditions

Further comparison of the ABLHs derived from lidar and ceilometer measurements under certain conditions, i.e., day versus nighttime and clear-sky versus boundary layer clouds, were performed. The results of these direct comparisons obtained with the three methods (GDT, STD, and WCT) showed consistent results, and therefore, only the results of WCT method comparison are shown in Figure 4 for brevity.

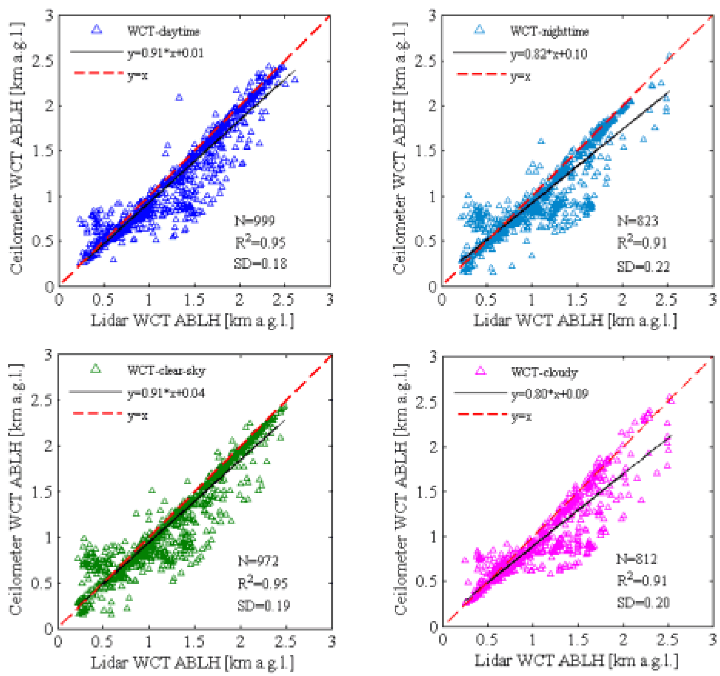

Figure 4. Correlation plots of the ABLHs derived from the PollyXT lidar and the CHM15k ceilometer using the wavelet covariance transform (WCT) algorithm for the collocated measurements from July to October 2013 in Warsaw. In blue, measurements at daytime; and in light blue, at night. In green, measurements in clear sky; and in pink, for boundary layer clouds. Each data point represents the 10 min average.

The WCT method was found to have the highest correlation coefficient with the lowest standard deviation for all conditions. Only for the cloudy conditions did the GDT method (not shown) perform slightly better. In Figure 4, top, the comparison in daytime conditions (999 data points) indicated a higher performance (R^2 of 0.95 and SD of 180 m) than that for the nighttime conditions (823 data points, 0.91 and 220 m, respectively). In Figure 4, bottom, the comparison of the clear-sky conditions (defined as lacking any clouds except Cirrus; 972 data points) showed a better performance, with an R^2 of 0.95 and SD of 190 m, than the cloudy conditions (boundary layer low clouds; 812 data points, 0.91 and 200 m, respectively).

Note that the comparisons of the rawinsondes-lidar and the rawinsondes-ceilometer ABLHs shown in Figure 2 and listed in Table 2 had significantly higher standard deviations (two to three times) and lower correlation coefficients than the direct comparisons of the lidar-ceilometer ABLHs shown in Figure 4.

5. Scaling Threshold-Based Method for Consistent Lidar and Ceilometer ABLH Retrieval

The direct comparison of the ABLHs derived from the collocated lidar and ceilometer measurements using the three methods (GDT, STD, and WCT) is shown in Figure 5. From July to October 2013, the data sample of 1828 measurements (each data point represents the 10 min average) was compared. In Figure 5, top subfigures, the lidar and ceilometer data are not merged (i.e., they were obtained for initial resolutions of 7.5 m for lidar and 15 m for ceilometer, and the difference in each instrument elevation height was not considered). The correlation coefficients obtained for each of the three methods are high ($0.93 < R^2 < 0.94$) with the standard deviation in a range that corresponds to the initial bias (300 m) of the lidar-ceilometer measurements ($0.19 < SD < 0.2$ km). Generally, below the altitude of 0.7 km, the lidar-derived ABLHs are slightly lower in comparison to the ceilometer-derived values while above the altitude of 1 km, the opposite tendency is observed (this is also evident in Figure 4). In Figure 5, middle subfigures, one can see that lidar-to-ceilometer signal re-binning and merging (as in Section 3.1) slightly improved the data correlation ($0.94 < R^2 < 0.96$) and decreased the standard deviation (0.17–0.19 km), resulting in reduced bias (200 m).

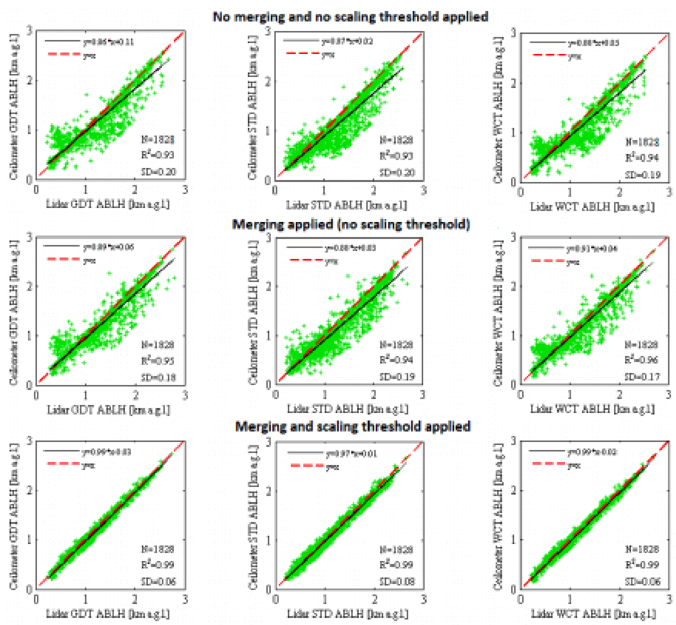

Figure 5. Correlation plots of ABLH obtained from the PollyXT lidar and the CHM15k ceilometer observations in Warsaw derived using the gradient method GDT (left), standard deviation method STD (middle), and wavelet covariance transform WCT (right) algorithms, within the period of July to October 2013 (each data point represents the 10 min average). Top: comparisons for initial resolution datasets; Middle: comparison after lidar-to-ceilometer signal merging (range resolution and height of the first range-bin); Bottom: comparison after lidar-to-ceilometer signal merging and scaling of the lidar ABLHs with the thresholds defined in Equations (1) and (2).

In order to further reduce the bias in the lidar-ceilometer ABLH retrievals, the threshold-based scaling method was developed and applied to the merged data. In this paper, the choice to scale the lidar-to-ceilometer ABLHs was made for two reasons. Firstly, there are much more low-power ceilometers over Europe than complex high-power lidars, and therefore the ceilometers can be regarded as reference instruments for ABLH retrieval. Secondly, it was considered that the results of the comparisons of the lidar-rawindsonde and the ceilometer-rawindsonde ABLH values (discussed in Section 4.1) showed more consistent results for the latter.

The working principle of the threshold-based scaling algorithm is given below.

Let us denote SD as the standard deviation obtained for the direct comparison of the ceilometer-derived ABLH (denoted CH) and the merged lidar-derived ABLH (denoted LH) collected during the collocated side-by-side measurements. Then, the scaled LH_{new} can be obtained as in Equations (1) and (2):

$$LH_{new} = \begin{cases} LH, 0 \leq Y1 < 2SD \\ LH - 1.5SD, 2SD \leq Y1 < 3SD \\ LH - 2.5SD, 3SD \leq Y1 < 4SD \\ LH - 3.5SD, Y1 \geq 4SD \end{cases}, \tag{1}$$

where $Y1 = (LH - CH)$.

$$LH_{new} = \begin{cases} LH, 0 \leq Y2 < 2SD \\ LH + 1.5SD, 2SD \leq Y2 < 3SD \\ LH + 2.5SD, 3SD \leq Y2 < 4SD \\ LH + 3.5SD, Y2 \geq 4SD \end{cases}, \tag{2}$$

where $Y2 = (CH - LH)$.

The scaling Equations (1) and (2) are not directly based on any physical process. Still, indirectly, they have a physical basis, which is exposed in the standard deviation of the initially derived ABLHs. Two instruments are available, each sensing the atmosphere with the identical principle but using a different technological solution for the light source and the detection system.

Hence, discrepancies can be expected in the derived ABLH, which are due to differences in the initial sensitivity to atmospheric aerosol and molecules sensed by the ceilometer and/or the lidar (due to the different signal intensities). Consequently, the proposed scaling method assumes that those differences are visible in the standard deviation. Note that this approach cannot be treated as the data correcting procedure but instead as the scaling approach to homogenize the datasets obtained by the two instruments. Also, this has nothing to do with any judgment of which instrument is better or worse.

In Figure 6, bottom subfigures, the improvement of the comparison results due to an application of the proposed scaling scheme is depicted by lowering the bias significantly, i.e., to only 60 m for the GDT and WCT methods, and only slightly higher at 80 m for the STD method. The correlation coefficients are very high (0.99) for all the tested ABLH retrieval methods.

Note that the Equations (1) and (2) can be applied only for the days when the collocated lidar and ceilometer measurements are available. However, from 1 November 2013, the measurements in Warsaw were conducted only with the PollyXT lidar. When only lidar measurements are available, the calculation of the standard deviation of lidar-ceilometer ABLHs is not possible, and hence, the universal method is needed to solve this issue. As a solution, the standard deviation of the lidar-derived ABLH was examined to provide a possible indication on the inadequacies of the retrieval. The standard deviation of the lidar-derived ABLHs (denoted SD_L) was obtained within every 10 min average and used as an independent threshold. Then, the lidar-derived ABLH (denoted LH) was scaled to the new value (LH_{new}) to homogenize the datasets, as given in Equation (3):

$$LH_{new} = \begin{cases} LH, LH \le 0.7\text{ km} \wedge SD_L < 0.10\text{ km} \\ LH + 1.5SD_L, LH \le 0.7\text{ km} \wedge SD_L > 0.10\text{ km} \\ \\ LH, 0.7\text{ km} < LH \le 1.5\text{ km} \wedge SD_L < 0.15\text{ km} \\ LH - 1.5SD_L, 0.7\text{ km} < LH \le 1.5\text{ km} \wedge SD_L > 0.15\text{ km} \\ \\ LH, 1.5\text{ km} < LH \le 3.0\text{ km} \wedge SD_L < 0.20\text{ km} \\ LH - 3.5SD_L, 1.5\text{ km} < LH \le 3.0\text{ km} \wedge SD_L > 0.20\text{ km} \end{cases} \quad (3)$$

In Figure 6, the ceilometer-derived ABLHs are used to test the lidar-derived ABLHs obtained by applying the homogenization algorithm as in Equation (3). The resulting correlation coefficient of the two instruments is an R^2 of 0.98, and an SD of 0.11 km was obtained. Similarly, high numbers were also obtained for the clear-sky versus cloudy conditions and the daytime (well mixed) versus nighttime (stable) (not shown for brevity). This demonstrates that the proposed method is reliable and can provide coherent results for both datasets. Therefore, it was applied to all lidar-derived ABLHs from 1 November 2013 to 31 December 2018.

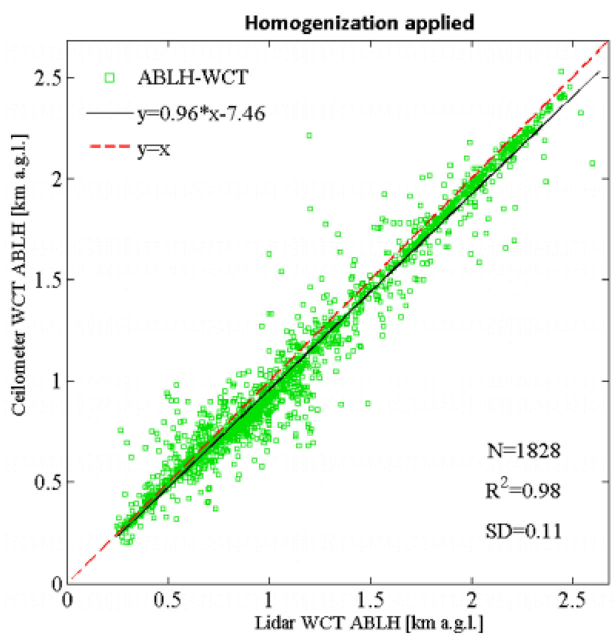

Figure 6. Correlation plots of ABLH derived from the PollyXT lidar and the CHM15k ceilometer collocated observations in Warsaw from July to October 2013. Each data point represents the 10 min average. The WCT algorithm was applied for the ABLH retrieval. The lidar-derived ABLHs' homogenization was done using the thresholds defined in Equation (3).

Overall, the correlation of ABLHs obtained from the lidar and ceilometer measurements (Figures 4 and 5) are high ($R^2 > 0.91$, with SD < 0.22 km) for all performed comparison tests. Therefore, after applying the homogenization, a good continuity of the observations is expected during the whole period of interest (2008–2018). The WCT method applied on the merged signals for the scaled datasets (Figure 5, bottom subfigures, and Figure 6) was identified as the best option for conducting further analyses of the decadal datasets, combining the lidar and ceilometer observations in Warsaw.

The homogenization algorithm workflow is given in Figure 7.

Remote Sens. **2020**, *12*, 340

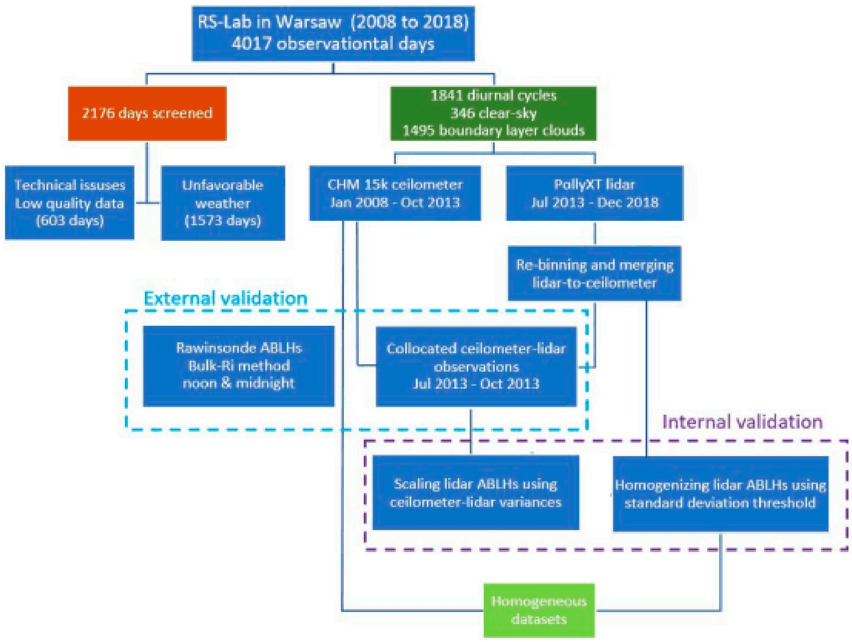

Figure 7. The ABLH data evaluation workflow allowing for the derivation of homogenized datasets from the PollyXT lidar and the CHM15k ceilometer observations in Warsaw.

6. Statistical Analyses of a Decade of ABLH Measurements in Warsaw

A decade of long-term observations of CHM15k ceilometer and PollyXT lidar performed in Warsaw from 2008 to 2018 were used for the statistical analyses. The ceilometer measurements from 1 January 2008 to 31 October 2013 and the lidar measurements from 1 November 2013 until 31 December 2018 were homogenized and combined.

A total number of 1841 daily evolution measurements were obtained, whereby the valid observation day was defined as providing data for at least 12 h on that day (with a minimum of 6 h per day and per night). The observation day was regarded as a clear sky if no cloud occurred within at least 12 h (except Cirrus > 8 km). The separation methodology for the clear-sky and the cloudy days is detailed in Section 4.

For further analyses, the following are defined as providing representative values:

The diurnal cycle: More than 12 h/day of measurements, with a minimum of 6 h per day and per night;

The annual cycle: More than six monthly mean values per year; and

The monthly mean: At least 3 days, each with more than 12 h/day of measurements, with a minimum of 6 h per day and per night;

The seasonal mean: At least 10 days, each with more than 12 h/day of measurements, with a minimum of 6 h per day and per night, within the 3-month-long season in each year; and

The yearly mean: At least 3 days, each with more than 12 h/day of measurements, with a minimum of 6 h per day and per night, for at least 8 months in each year.

Within the subset of the 1841 daily evolution observations, the daytime/nighttime and the cloudy/clear-sky coverage do not significantly influence the data sample. There is no bias towards any of those conditions due to the well-defined subsample focused on capturing the diurnal cycle.

The number of valid observational days for each year under the analyses is listed in Table 3, where next to the total number of observational days, a subset of 346 observational days regarded as being taken under clear-sky conditions is indicated. Note that a clear sky does not mean pollution-free conditions. For reference, in Warsaw, the PollyXT lidar-derived aerosol optical depth at 532 nm $AOD_{ABL}(532)$ of 0.11 ± 0.06 was reported as a mean background value within the boundary layer, whereby the lowermost values as low as 0.03 were measured under extremely clean urban conditions after precipitation [52]. In the case of the long-range transport over the site, the columnar measurements with the MFR-7 radiometer at 550 nm can easily increase by an order of magnitude or more ($AOD_{CL}(550)$ even up to 0.7 reported by [60]), with a mean $AOD_{CL}(550)$ of 0.26 reported by [76].

Table 3. The number of lidar/ceilometer-derived diurnal cycles of the atmospheric boundary layer over Warsaw, for the years 2008 to 2018. The number of the available clear-sky cycles is given in brackets. The percentage of clear-sky data to the total number of observations is indicated for each year and each month. Note that before 31 October 2013, the ceilometer data were used, and after that date, the lidar data were used (denoted with *).

	Jan	Feb	Mar	Apr	May	Jun	Jul	Aug	Sep	Oct	Nov	Dec	Total	%
2008	8(1)	8(0)	10(1)	8(2)	9(2)	7(3)	4(2)	9(3)	9(1)	12(2)	9(2)	31(6)	124(25)	20
2009	29(7)	6(0)	15(2)	18(11)	8(1)	17(0)	18(0)	9(3)	5(1)	10(1)	9(2)	7(0)	151(28)	19
2010	15(4)	7(0)	21(2)	20(3)	28(0)	24(5)	28(9)	14(1)	7(1)	16(8)	9(1)	6(2)	195(36)	18
2011	7(0)	13(5)	31(9)	30(7)	29(4)	29(3)	24(2)	9(1)	30(7)	31(8)	30(8)	31(0)	294(54)	18
2012	31(4)	29(5)	31(7)	27(3)	23(4)	21(0)	10(4)	16(1)	16(3)	0	0	11(0)	215(31)	14
2013	31(1)	28(0)	31(9)	30(3)	31(3)	30(3)	31(4)	31(5)	30(4)	18(3)	* 9(0)	0	300(35)	12
2014	0	0	0	4(1)	12(2)	7(1)	12(2)	13(0)	0	0	0	2(0)	50(6)	12
2015	0	0	12(4)	7(2)	0	0	8(0)	20(19)	2(1)	0	0	5(0)	53(26)	49
2016	0	5(0)	10(0)	6(0)	8(0)	21(3)	22(1)	28(6)	24(13)	10(0)	3(2)	11(1)	148(26)	18
2017	15(2)	0	3(0)	0	12(3)	29(3)	20(1)	6(0)	17(2)	21(3)	0	0	123(14)	12
2018	0	18(3)	17(4)	23(6)	12(7)	21(6)	14(6)	19(9)	11(6)	23(10)	20(6)	10(2)	188(65)	35
Total	136(19)	114(13)	181(38)	173(38)	172(26)	206(27)	191(31)	174(48)	151(39)	141(35)	89(21)	113(11)	1841(346)	19
%	14	11	21	22	15	13	16	28	26	25	24	10	19	

As for the monthly representativeness within the total number of days, the highest number of observations was achieved for June and July (>190 days, each) and the lowest in November (<90 days). However, for the clear-sky data subset, the highest number of observations were conducted in August (48 days) and the lowest in December and February (<15 days, each). As for the yearly representativeness for the total number of days, the highest number of observations was for the years 2011 and 2013 (circa 300 days, each) and the lowest for the years 2014 and 2015 (circa 50 days, each). Within the clear-sky data subset, the year 2018 had the highest number of observations (65 days). The clear-sky occurrence within the total sample was highest in the year 2015 (49%) and in the month of August (28%, whereby the majority of these measurements were taken in 2015).

The missing data comprise in total 2176 days (1 January 2008 to 31 December 2018).

Due to purely technical issues, 542 days of lidar data and 61 days of ceilometer data were missing. In October and November 2012, there was a ceilometer computer failure. From December 2013 until March 2014 and from September until November 2014, the lidar laser head failure inhibited observations. In the years 2015 and 2017, there were several breakdowns of the lidar laser cooling system. Additionally, in the years 2014 and 2015, a new research facility was built next to the lidar, disabling any observations during the tower crane stock operation.

The missing days are also attributed to unfavorable weather conditions, as affected by the ground precipitation and/or the fog/smog conditions (refer to Section 4). Ceilometer measurements are performed continuously but ABLH cannot be derived in the aforementioned conditions. Consequently, there were 1270 valid days from 1 January 2008 to 31 October 2013. For precipitation of snow or rain, the continuous lidar measurements stop automatically and restart after the event passed, which resulted in 571 valid days (from 1 November 2013 to 31 December 2018).

The analyzed data sample contained all days listed in Table 3, including the overcast weather days (here, boundary layer clouds <3 km) and the clear-sky days (here, cloudless or with Cirrus >8 km), i.e., not only the aerosol signatures but also the boundary layer clouds in the lidar and ceilometer signals were used as a marker to track the ABLHs.

6.1. Monthly Variability of the Average Diurnal Cycles of the Boundary Layer Height

The monthly average diurnal cycles of ABLH were derived for a subset of the clear-sky diurnal cycle data listed in brackets in Table 3. They were calculated separately for the ABLH values obtained as the NL, TL, and WML versus the RL, TL, and WML (definition in Table 1) to assess the differences related to the nocturnal and the residual boundary layer. As expected, the diurnal cycles that included the nocturnal layer information, shown in Figure 8, were more pronounced than the diurnal cycles including information on the residual layer (the latter not shown for brevity). The ABLH maximum values in each cycle for 12 months were mainly distributed from 12:00 until 15:00 UTC, except for the winter months. The significantly higher nocturnal boundary layer in August than December can be attributed to the solar position and zenith angle, which leads to an earlier sunrise and a late sunset in the summer months. Thus, it affects the solar radiation reaching the surface, and hence, the surface temperature, causing a higher boundary layer in summer than in winter. In Warsaw, nighttime in summer lasts about 7 h (or less) and in winter about 14 h (or more), so that in summer, one cannot expect a strong cooling effect at night. Therefore, the difference of 500 to 700 m in the ABLH derived at night in summer and winter is plausible.

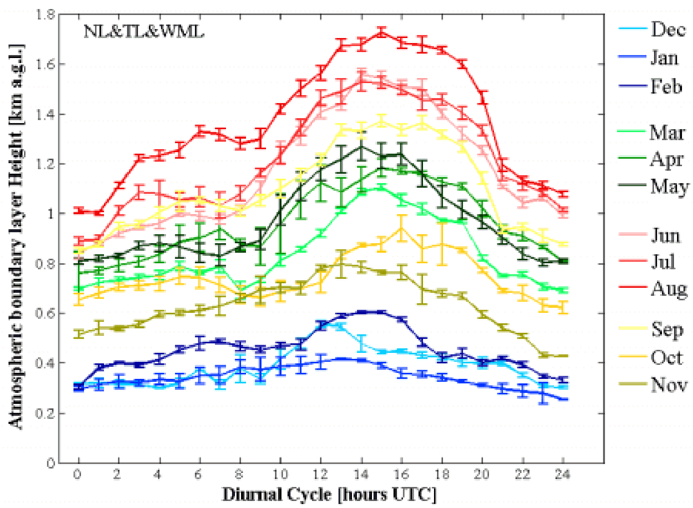

Figure 8. The average monthly diurnal cycles of the boundary layer height obtained from a subset of 346 clear-sky 24 h/day observations of the nocturnal layer (NL), transition layer (TL), and well- mixed layer (WML), in the years 2008–2018 in the city center of Warsaw, Poland. The ABLHs were obtained from the PollyXT lidar and CHM15k ceilometer signals using the wavelet covariance transform method (WCT). Merging and homogenization were applied to lidar data from November 2013 to December 2018. The months of each season are indicated in green for spring, in red for summer, in yellow for autumn, and in blue for winter. Temporal definitions of each season are given in Table 1.

The monthly average diurnal cycles indicated strong seasonal changes. The most spectacular was the abrupt change of the winter boundary layer cycle shape and height (Figure 8, in blue), which maintained a very low diurnal variability in December, January, and February. A well-pronounced diurnal cycle of the following spring months is depicted (in green). This sharp winter-to-spring cycle change was related to a well-pronounced pre-spring season (discussed below).

The diurnal cycles obtained for spring and summer indicated a smooth and mild month-to-month transition to higher ABLH values, with an increase of the heights during both the day and nighttime. The diurnal cycle for August (Figure 8, in red) was found to be the highest; it stands out from the others in terms of the ABLH values but not the shape. The August diurnal cycle remained practically unaffected by the uneven data sampling—the highest probe for August 2015 (48/19 cases). Excluding the August 2015 data from the diurnal cycle of August (not shown for brevity) revealed only a slightly flattened shape (30 to 90 m lower ABLH values between 12:00 and 20:00 UTC).

The autumn diurnal cycle of September (Figure 8, in beige) resembled the summer cycles of June and July (Figure 8, in pink and red), which indicates a prolongation of the summer season at the cost of autumn. The similarity of the September cycle to the summer cycles is naturally related to the meteorological conditions being more like those in summer. The prolongation of summer in Poland that is manifested in the derived diurnal mean cycles of 2008 to 2018 was reported in other studies (e.g., [77]). The remaining autumn cycles (Figure 8, in yellow) were significantly lower, not only from the September cycle, but generally from all spring and summer cycles. This indicates a somewhat smooth transition to the winter season. Still, the October and November diurnal cycles have distinctly different shapes from all winter cycles.

The much higher spring cycles than the winter cycles and the well-separated height in the autumn cycles from the winter cycles indicate a very short and well-defined winter season. The January cycle has a flat shape. Taking into account the equal representatives of the data for the hour of day (the majority of samples obtained for ceilometer observations in 2008 to 2013), this can be explained by the urban heat island effect.

The urban heat island (UHI) means that the temperature within the urban area is significantly warmer than in the surrounding rural areas [76]. The effect is due to both human activities in the city (traffic, combustion, etc.) and the differences between the land surfaces in the city and the rural areas [78]. At night, the absence of solar heating (no strong atmospheric convection) normally leads to the stable boundary layer [1–3]. During UHI conditions, the inversion traps the urban air near the surface and keeps it warm from the urban surfaces. This results in warmer nighttime air temperatures that prevent a strong decrease of the urban boundary layer height after sunset [79]. The mean yearly intensity of the UHI index (difference of the minimum daily temperature for the urban area to the value of the minimum daily temperature for the suburb area) reaches over 2 °C in the city center over Warsaw. The very center of the city is warmer in the night by 2.5 °C compared to the outskirts [78]. The UHI is most effective and intensive in wintertime, at night or before dawn [78]. The wintertime diurnal cycles may also be affected by biases due to an occurrence of the nocturnal layers below the detection range of the ceilometer or lidar (195 m), although this is expected to have a minor effect on the retrievals in comparison with the heat island effect.

In general, the diurnal cycles showed an increase during the transition from the spring months (0.7–1.2 km) to reach their highest values in the summer months (0.9–1.7 km). Thereafter, in autumn, a decline of the mean monthly ABLHs was observed (0.6–1.3 km). The lowest mean values (≤0.6 km) occurred, as expected, in the winter months. This is, in general, in agreement with the average ABLH summer and winter values of, respectively, 1.5 and 0.7 km reported previously for Warsaw [29,52].

According to the Koeppen–Geiger climate classification system (maps available at http://koeppen-geiger.vu-wien.ac.at), the climate over Poland has changed. In 1951 to 1975, western Poland was under the Cfb climate (defined as warm temperate humid with warm summer) and eastern Poland was under the Dwd climate (defined as boreal extremely continental with dry winter). In the following decade, the Cfb climate was already over the whole of Poland [80]. Traditionally, the climatic and astronomical seasons are not identically defined for Poland, as there are two additional pre-seasons regarded as being present in Poland's climate: The pre-winter, with significant cooling in November, and the pre-spring, with significant warming at the turn of February and March [77]. In the obtained monthly mean diurnal cycles, the pre-spring season was evident (exceptionally high March cycle; Figure 8, in light green). The autumn diurnal cycle of November was not very low, as expected as representing the pre-winter season (Figure 8, in dark yellow). The change of the climate seasonality of Poland [80] is in accordance with the ABLH cycles resembling the very warm spring [77], as well as the prolonged summer into the month of September.

6.2. Annual Variability of the Monthly and Seasonal Mean Boundary Layer Height

The monthly mean ABLH values with standard deviations were calculated from the 1841 daily evolution cycles obtained in all-weather conditions. Note that the obtained temporal variations may be affected by data availability (Table 3). The annual variability of the monthly mean ABLH values from 2008 to 2018 was plotted in Figure 9, separated into the RL, TL, and WML average (in red) and the NL, TL, and WML average (in blue). Because the residual layers can be valuable for the interpretation of pollution concentrations observed within the ABL [55,59], such a separation can be useful for future studies. As expected, the heights of the NL, TL, and WML were lower, but the trend of both was similar. The monthly annual changes from 2008 to 2011 were observed for all months, whereas after 2011, for some months the mean values could not be obtained. In general, the monthly mean ABLHs showed a slight increase from the spring months (MAM) to the summer months (JJA), where the mean ABLH increased to its highest values, with the mean exceeding 1 km. The lowest mean ABLH values appeared mainly during the winter months (DJF), with mean values of less than 1 km for all years. For the autumn months (SON), a similarity with either the winter or spring months was captured. From 2008 to 2013, the fluctuations of ABLHs generally remain around 1 km. In 2014 and 2015, high monthly mean ABLHs (>1.5 km) were derived, which can be partly attributed to the most missing data in these two years (a total of about 50 days per year).

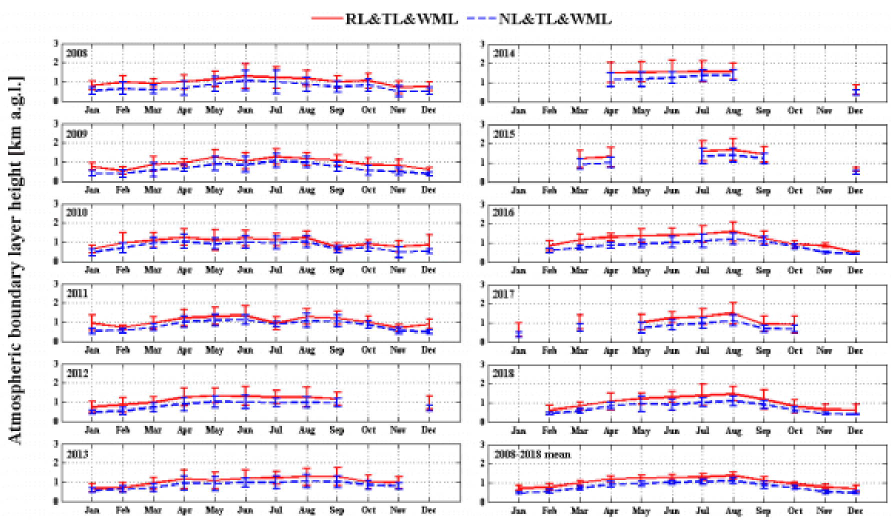

Figure 9. The monthly mean variability of the ABLHs obtained by using the wavelet covariance transform (WCT) method for the PollyXT lidar and the CHM15k ceilometer observations in cloudy and clear-sky conditions over Warsaw, within the period of 2008 to 2018. Merging and homogenization were applied to the lidar data from November 2013 to December 2018.

The year-to-year monthly mean ABLHs were the lowest for the winter of 2016 and 2018, and the highest for the springs and summers of 2014, 2015, and 2016. This should be at least partly attributed to the decadal activity of the ENSO, resulting in global atmospheric heating (El Niño) or cooling (La Niña). The monthly mean ABLHs are in accordance with the moderate-to-strong El Niño in 2014–2016 and the moderate La Niña in 2010–2012, both reported by the NOAA Oceanic Niño Index (available via http://origin.cpc.ncep.noaa.gov/products/analysis_monitoring/ensostuff/ONI_v5.php, last access: 11 December 2019). The strong El Niño can result in highly increased temperatures and droughts in Europe [81,82]. At the same time, the resulting prolonged increase of the surface temperature due to droughts and heat waves can cause a higher boundary layer [8–11].

These effects can be seen on the scale of the annual cycle (Figure 9). The extreme summer heat wave was observed over Europe during July 2015 and resembled exceptionally high values for the two following months [82–84]. A European heat wave event was also reported for September 2016 [11]. The surface air temperature monthly means with anomalies (relative to the monthly average calculated for the period 1981–2010) are provided from September 2015 until the present month by the ERA-Interim ECMWF Copernicus Climate Change Service (maps available via https://climate.copernicus.eu/resources/data-analysis/average-surface-air-temperature-analysis, last access: 11 December 2019). The monthly mean ABLHs depicted in Figure 9 are in accordance with the surface air temperature monthly anomalies, and also the observed variability of the monthly mean ABLHs are related to the average surface air monthly temperature, reported therein.

In Table 4, the variability of the seasonal mean ABLH values in each year, (winter months (DJF), spring (MAM), summer (JJA), and autumn (SON) for the years of 2008 to 2018 is given. In autumn and winter of 2014 and 2015, the values indicated in brackets cannot be regarded as representative of the seasonal mean (defined as at least 10 days within the 3-month-long season of each year, with at least 6 h at daytime and 6 h at night). Still, these values are given to provide rough information but not as a seasonal mean. The decadal seasonal mean ABLH reached its largest values in the summertime, with an altitude of 1.34 km, and the lowest values in the wintertime of 0.73 km. The mean spring and autumn ABLHs were 1.16 and 0.99 km, respectively.

Table 4. The seasonal mean ABLH values obtained from the PollyXT lidar and the CHM15k ceilometer data using the wavelet covariance transform (WCT) method for observations conducted in all-weather conditions over Warsaw, within the period from 2008 to 2018. Mean values for seasons with less than 10 measurement cycles are indicated in italics, being regarded as statistically not representative. Merging and homogenization were applied to lidar data from November 2013 to December 2018.

	Spring (MAM) Mean ± std [km]	Summer (JJA) Mean ± std [km]	Autumn (SON) Mean ± std [km]	Winter (DJF) Mean ± std [km]
2008	1.02 ± 0.58	1.24 ± 0.72	0.96 ± 0.61	0.81 ± 0.50
2009	1.00 ± 0.56	1.16 ± 0.64	0.96 ± 0.56	0.72 ± 0.43
2010	1.15 ± 0.69	1.17 ± 0.60	0.83 ± 0.50	0.75 ± 0.59
2011	1.16 ± 0.65	1.18 ± 0.68	0.98 ± 0.58	0.85 ± 0.49
2012	1.18 ± 0.63	1.28 ± 0.69	1.17 ± 0.58	0.83 ± 0.58
2013	1.06 ± 0.64	1.24 ± 0.64	1.11 ± 0.57	0.70 ± 0.41
2014	1.54 ± 0.57	1.58 ± 0.60	× *(0)*	× *(0.65)*
2015	1.24 ± 0.48	1.61 ± 0.51	× *(1.30)*	× *(0.61)*
2016	1.29 ± 0.59	1.46 ± 0.60	1.09 ± 0.49	0.67 ± 0.34
2017	1.01 ± 0.43	1.35 ± 0.57	0.92 ± 0.41	0.65 ± 0.36
2018	1.09 ± 0.41	1.40 ± 0.53	0.85 ± 0.45	0.63 ± 0.25
Total	**1.16 ± 0.16**	**1.34 ± 0.15**	**0.99 ± 0.11**	**0.73 ± 0.08**

The seasonal mean ABLHs, listed in Table 4, indicate for most of the years that for spring and summer the values were above 1.1 km, for autumn below 1.1 km, and during winter below 0.8 km. However, after 2014, the mean height in the spring and the summer seasons was notably higher (200–300 m) than those of the previous years while for the winter season, it was further decreased (of about 200 m). For the years 2008–2013 and 2017–2018, the differences in the seasonal mean ABLH values were relatively small and remained within 400 m, but for 2014–2016, those differences were about twice larger, which should not be solely attributed to the absence of data in 2014 and 2015. The 10-year mean seasonal ABLH was 1.16 ± 0.16 km for spring, 1.34 ± 0.15 km for summer, 0.99 ± 0.11 km for autumn, and 0.73 ± 0.08 km for winter.

If any sampling biases were to critically affect the year-to-year variation of all mean ABLHs in the four seasons for the years 2014–2018 (derived with lidar only), they would be expected to reveal higher values than those of 2008–2012 (derived from ceilometer only), as a systematic error. This is not the case, as, e.g., the results for the winters of 2013–2018 and springs and autumns of 2017–2018 are lower than those derived from 2008 to 2012. As for the decadal mean seasonal variability of ABLH, they are least affected by biases and these values can be used as a reference.

6.3. Variability of Yearly Mean Well-Mixed, Nocturnal, and Residual Boundary Layer Height

The box and whisker plots depicted in Figure 10 summarize the variability in the annual mean ABLH values derived for the subset of the clear-sky data (346 days). In this figure, the solid lines indicate the annual mean ABLH obtained for each year, except for the years 2014 and 2015, for which calculation of the annual mean was not possible (too low data availability in autumn and winter months; Table 3). The annual mean ABLHs (Figure 10, in green) were the highest in 2016 and 2018. Overall, the annual mean ABLHs were between 0.8 and 1.3 km.

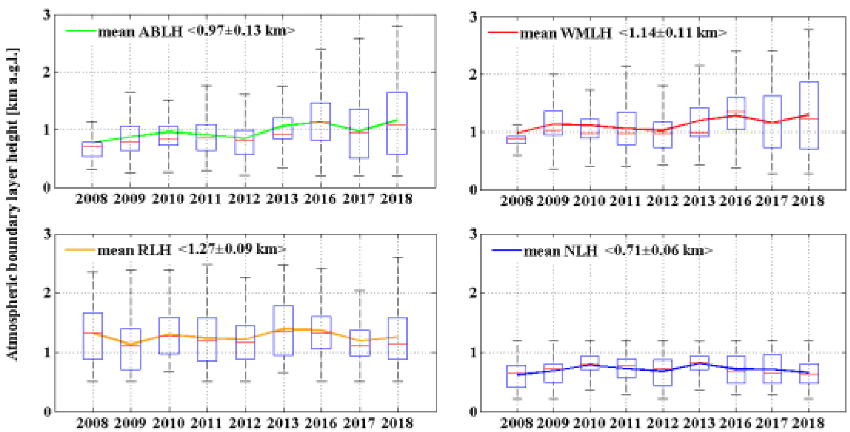

Figure 10. Box plot showing the annual mean ABLH values (solid lines) calculated using the WCT method applied to the PollyXT lidar and the CHM15k ceilometer signals. Calculations in clear-sky conditions over Warsaw from 2008 to 2018. The boxes show the median, 25th, and 75th percentiles. In green, the annual mean ABLH for all derived atmospheric boundary layer (ABL, i.e., the mean of RL or NL, TL, and WML); in red, for the well-mixed layer height (WMLH); in blue, for the nocturnal layer height (NLH); in orange, for the residual layer height (RLH). The lack of data for 2014 and 2015 is due to their underrepresentation for the annual mean. Merging and homogenization were applied to the lidar data from November 2013 to December 2018.

The annual mean WML, NL, and RL in Figure 10 show that the mean annual WML values have strong similarities with the mean annual ABLHs, with the peaks in 2016 and 2018. The mean annual NL and RL values followed different trends with no distinct peaks; the NL below 0.83 km and the RL between 1.13 and 1.39 km. Lower residual layer heights, being in the range 0.7–1.4 km, were reported for Paris, France and in the range 0.5–0.9 km for Moscow, Russia [85]. Over Houston, Texas, the nocturnal boundary layer height was reported at 0.25 km throughout the year while the convective boundary layer heights were at 1.1 km in winter and 2 km in summer [55]. Such differences are not unexpected and can be attributed to the diverse climatic conditions at these sites. Two of them have a temperate climate (1980–2016), i.e., Houston (Cfa) and Paris (Cfb). The two others have a continental climate (1980–2016), i.e., Warsaw (Dfb) and Moscow (Dfc) [80]. As for the derivation of the nocturnal boundary layer in Warsaw, the lower detection limit at 195 m could have led to a slight overestimation of the derived values. However, even for scanning lidars, where the overlap is claimed to play a negligible role due to the measurement geometry, heights of the boundary layer between 0.5 and 2.4 km were reported for August to October over Slovenia [86], considered a continental climate of the Dfb type, such as Warsaw [80].

The mean yearly ABLH, WML, RL, and NL values were obtained for the total number of available data (1841 diurnal cycles) as well as for the subset of clear-sky data (346 diurnal cycles). This was done to assess expected differences between those two samples, whereby the temporal separation of the data was taken into account. The bias of the ABLH retrieval performed in the clear-sky and boundary layer clouds is related to clouds forming directly above the boundary layer itself (e.g., in the entrainment zone, <3 km [1–3]). The other types of clouds, e.g., generated by the mesoscale frontal weather systems, were not considered (they have been screened, as, in the majority of situations, they are detached from the boundary layer). Therefore, the difference of the annual mean ABLH derived for the all-weather conditions and the clear-sky conditions represents this bias. In Figure 11, right subfigure, the bias is below 230 m for the ceilometer (2008–2012) and 70 m for the lidar (2016–2018). For the annual mean values of the WML, RL, and NL, the bias is below 250 m for both instruments. Measurements with each instrument indicate different cloud effects, which can be partly attributed to the difference in their design and partly to various atmospheric conditions. The signal-to-noise ratio is lower for the ceilometer than lidar due to the lower laser power, resulting also in a shorter range of the ceilometer signals [38,62,69]. Therefore, lidar is more sensitive for the aerosol and cloud detection. On the other hand, the differences seen for the cloudy conditions in Figure 11, also have to do with the captured annual variations in the atmospheric conditions for the all-weather data depicted in Figure 9.

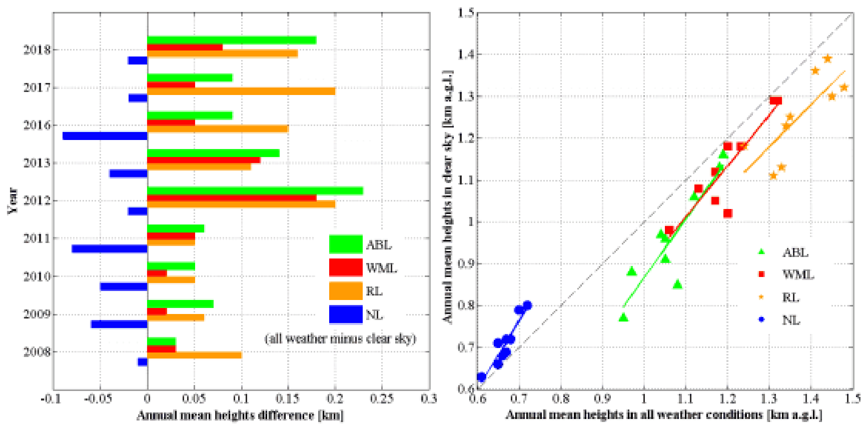

Figure 11. The difference of the annual mean boundary layer heights obtained in all-weather and clear-sky conditions (left subfigure). The comparisons of the mean annual boundary layer heights in both conditions (right subfigure). Notation: the atmospheric boundary layer (ABL), the well-mixed layer (WML), the nocturnal layer (NL), and the residual layer (RL). Data derived by the CHM15k ceilometer and the PollyXT lidar over Warsaw within the period of 2008 to 2018. A lack of data points due to the underrepresentation of the annual mean for 2014 and 2015. Merging and homogenization were applied to lidar data from November 2013 to December 2018.

In general, with an increase of the annual mean ABLH, increased heights of the WML, RL, and NL were observed (Figure 11, left subfigure). The heights of the ABL, WML, and RL were higher for the all-weather conditions than on the clear-sky days. Conversely, the height of the NL under the all-weather conditions was found to be lower compared to its height in the clear-sky days (Figure 11, right subfigure). Both, an increase in the cloud cover at night and an urban heat island under clear-sky conditions can lead to a deeper ABLH at night. For the data sample collected and analyzed in this paper, the second process seems to be more efficient in Warsaw.

The ABLH under the UHI is the result of processes driven not only by the local surface conditions but also by the regional atmospheric structures [87]. In the literature, there are some idealized realizations of boundary layers, such as, e.g., in [1–3]. Reality is more complicated due to differences in the heat sources, heat capacities, and surface roughness, e.g., the classic evolution of a daytime convective boundary layer distribution as affected by advection of dry air and gravity waves was reported by [88]. In the current paper, not all those regimes were studied.

Several studies reported in the literature are limited to the clear-sky daytime conditions and provide only the maximum ABLH. For instance, for an urban continental site in Leipzig, Germany, the afternoon ABLHs corresponding to the well-mixed layer height were reported, with a maximum value at approximately 1.4 km in spring, 1.8 km in summer, 1.2 km in autumn, and 0.8 km in winter, as derived from single-year observations [25]. The maximum ABLHs in the current study were found even beyond 2 km in Warsaw, Poland. The mean ABLHs in Warsaw, calculated for the different seasons and years, are reported as being in the range of circa 250 m lower than the maximum values reported for Leipzig [25]. The annual cycle of convective boundary layer heights in summer and winter reported above the Swiss Plateau [44] had values far from those derived for Warsaw and Leipzig. Over Neuchâtel, Switzerland, the nighttime residual heights detected with lidar were reported as changing from 0.5 to 1.5 km [21]. In Barcelona, Spain, the well-mixed boundary layer was reported between 0.3 and 1.45 km in summer and between 0.39 and 1.42 km in winter, showing almost no seasonal difference, unlike in Warsaw [37]. The discrepancies of the values reported within the current study and the mentioned publications are attributed to the differences in the localization of cities/regions (coastal, plateau, inland). Also, the distinct climatological conditions add to these differences.

It has been reported that the aerosol optical properties derived within the boundary layer (divided to the different temporal regimes: WML, TL, NL, and RL) show significant differences in Warsaw, especially for the diurnal variation [52]. Thus, high-quality retrieval of the ALBH at daytime and nighttime is crucial. Note that the analysis of Figure 11 relies on cloud characteristics (cloud cover, cloud base height, cloud type), therefore its interpretation is not straightforward.

The dependence of the temperature on cloud cover is strong in the middle latitudes [89]. During the daytime, an increase in cloud cover can restrict the incoming solar radiation, and thus, decrease surface temperatures. However, at night, an increase in the cloud cover is expected to reduce the long-wave cooling (i.e., warmer surface temperatures), and thus lead to a deeper ABLH at night (e.g., in [14]). The cloud cover and type influence the boundary layer characteristics; the mixed layer height may vary distinctly depending on the frequency and cloud types present [53]. Moreover, the global temperature rise, reinforced in urbanized areas by the anthropogenic heat flux, leads to an intensified convection process and increased precipitation (especially torrential rain), causing thermal and hydrological hazards in large conurbations. The areas currently exposed to thermal and urban flood hazards in Warsaw were identified and assessed in the recent work of [83].

6.4. Frequency Distribution of Daytime and Nighttime Boundary Layer Height

In order to indicate on the total distribution of ABLH within 2008–2018 over Warsaw, the histogram of the frequency distribution of the ABLH derived for the 1841 diurnal cycles is depicted in Figure 12. All hours were used, hence there is no bias for any particular time of day.

The asymmetric positive skew distribution with the right tail significantly longer and with the mean value higher than the median was obtained. The ABLH values up to 1 km had a frequency of more than 60% of the entire data sample. The ABLH distribution was dominated with the values between 0.6 and 1 km (the class 0.6–0.8 km was the most frequent, with the percentage of 18.15%, followed by the class 0.8–1 km, with a frequency of 17.67%). Then, the values between 0.2 and 0.6 km were significantly frequent (class 0.4–0.6 km (12.07%), followed by the class 0.2–0.4 km (12.05%).

For higher altitudes (>1 km), as the ABLH increased, their occurrence gradually decreased. Rarely, the ABLH values reached altitudes of 2.4 to 3 km, which accounts for only 4.76% of the whole data sample. The obtained frequency distribution can be used as a reference for comparison with other measurement sites, e.g., as in [74], whereby a distinction can be made between, e.g., the daytime and nighttime distributions.

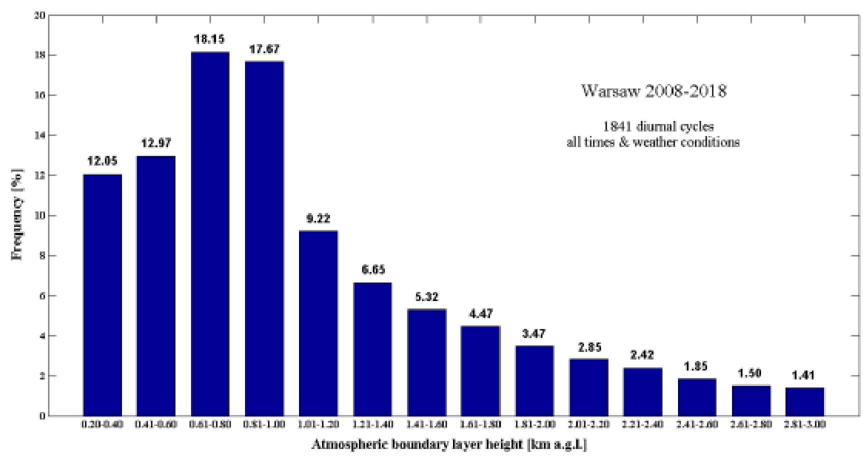

Figure 12. Frequency distribution of ABLH calculated from the PollyXT lidar and the CHM15k ceilometer observations in Warsaw from 2008 to 2018. The ABLH values are separated into classes of 200 m. The merging and the homogenization were applied to lidar data from November 2013 to December 2018.

Additionally, a detailed investigation of the ABLH frequency distribution was performed with respect to the time of day and for the different seasons of the year. The frequency distribution histograms are plotted in Figure 13, where the daytime frequencies are given in grey and nighttime in black.

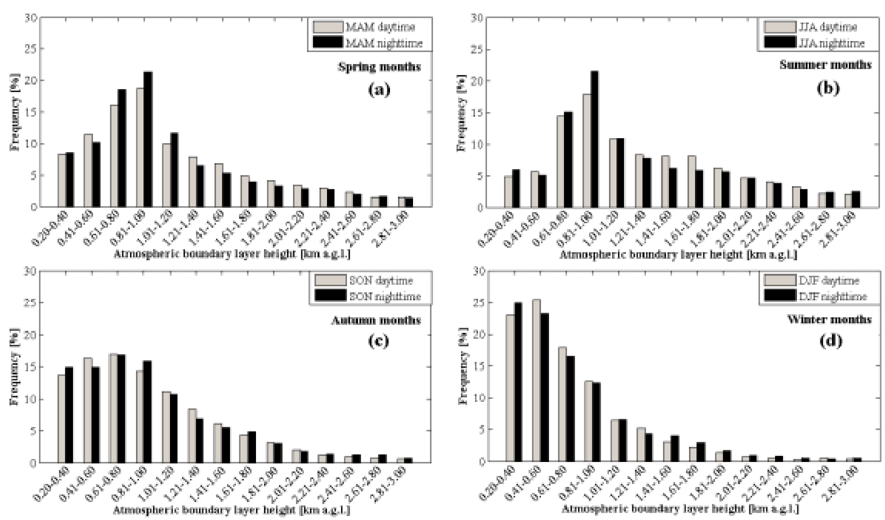

Figure 13. Frequency distribution of ABLHs calculated from the PollyXT lidar and the CHM15k ceilometer observations in Warsaw, for the period from 2008 to 2018, as separated into spring (**a**), summer (**b**), autumn (**c**), and winter (**d**) seasons, as well as daytime (in grey) and nighttime (in black). The ABLH values are separated into classes of 200 m. Merging and homogenization were applied to lidar data from November 2013 to December 2018.

In spring and summer (Figure 13a,b), the ABLHs were most often within the range of 0.6 to 1 km; this being a distinct maximum of the occurrence frequency of 30% to 40%. In general, at the ranges up to 1.2 km, the ABLH occurrence at nighttime was practically always slightly higher than at daytime (expect for winter); above this height, an opposite trend occurred. For winter and autumn, no such trends are observed. In the summer months (Figure 13b), a visibly higher frequency of ABLHs over 1.4 km was observed, as compared to the other seasons. This is consistent with the fact that in summer, more solar radiation is expected to be absorbed by both land and atmosphere, which is then attributed to a stronger variation of the heat flux, turbulence, and more active energy exchange. Consequently, this leads to a lofted ABLH during the summer months. On the contrary, most of the ABLH values during the winter season (Figure 13d) occurred within the range between 0.2 and 0.6 km (~50%, at both, day and night). In winter, the occurrence of ABLH above 1.8 km is negligible (<5%). During the autumn months (Figure 13c), the distribution of the ABLH values within 0.2 and 1 km was well balanced, with frequencies between 14% to 16% (in total ~60%), at both, day and night.

Notably, a few ABLHs above 2.8 km were found in all four seasons, regardless of during the daytime or nighttime. A reasonable explanation for such observations at daytime may be stronger turbulent mixing and exchange processes between the surface and the free troposphere, which contribute to a relatively high ABLH between noon and the late afternoon (e.g., [52,75]). As for an ABLH above 2.8 km during the night, it may be attributed to at least to two reasons. Either there were aerosols remaining after sunset, which developed a residual layer when the temperatures declined during the course of the night (e.g., an extremely high boundary layer (up to 3 km), driven by a severe heat wave conditions, discussed in detail in [11]). Or the tested boundary layer retrieval methods (GDT, STD, and WCT) were, to some extent, influenced by the atmospheric stratification (particularly in complex advection-pronounced conditions), as these algorithms always find the largest signal change. These factors, each alone or in interplay, may have led to a higher ABLH during the nighttime. The ABLH values found above 2.8 km in autumn and winter are considered as limitations of the applied methodology. Note that no passing clouds appeared for the ABLHs found at the range 2.8–3 km.

As expected for an urban continental site in Central–East Europe, a strong seasonal variability of the ABLH distribution (in height and shape) was observed. The spring distribution (Figure 13a) clearly dominated the total distribution (Figure 12). The ABLH distribution peak and shape varied strongly with the seasons. The peak of ABLHs between 0.6 and 1 km was observed in spring, then it became sharper (0.8–1 km) in summer, just to flatten in autumn as an equal spread between 0.2 and 1 km, and finally to peak in winter at 0.2 to 0.6 km. The study of the boundary layer height over Europe, derived based on the bulk-Ri number from the rawinsondes, revealed that 50% of all ABLH values at daytime are generally <1 km and at nighttime <0.5 km [51]. The seasonal patterns for the daytime and nighttime can significantly differ; daytime heights larger in summer than in winter, but the nighttime heights larger in winter, were reported by [45]. These variability trends obtained over Europe are similar to the results for Warsaw. The differences are therefore due to the physical basis for instruments'/algorithms' working principles as well as the specific weather or air quality-related episodes.

7. Conclusions

Measurements conducted at the same wavelength (1064 nm) using the CHM15k ceilometer (2008 to 2013) and the PollyXT lidar (2013 to 2018) were homogenized, combined, and deployed to determine the atmospheric boundary layer characteristics. The height, structure, and evolution of ABLH were obtained for 1841 observations of diurnal cycles over the city center of Warsaw, Poland. For comparative study, 4 months of collocated ceilometer and lidar measurements (July–October 2013) were chosen. For this period, the ABLH was determined also from the WMO rawinsondes launched at noon and midnight in Legionowo (25 km, North).

The bulk Richardson (bulk-Ri) method was found more favorable than the skew-T-log-P for ABLH detection from rawinsondes. The lidar and ceilometer ABLHs in Warsaw, obtained with the gradient method (GDT), standard deviation method (STD), and wavelet covariance transform method (WCT), exhibited relatively high correlations (R^2 of 0.68–0.80 with SD of 360–510 m), in comparison with the rawinsondes ABLHs obtained by using the bulk-Ri method. The WCT results indicated an ability to detect ABLHs more accurately than the GDT and the STD methods. The ceilometer-derived ABLHs were assessed as more reliable (more similar to the rawinsondes' retrievals).

The lidar–ceilometer direct comparisons revealed significantly higher correlations (R^2 of 0.93–0.94 with SD of 190–200 m). The algorithms developed for homogenization of the ceilometer and lidar datasets reduced this bias to only 110 m. The WCT method performed well at day and nighttime in different conditions. The bias of ABLH retrieval in the clear-sky to the cloudy-conditions was <230 m for ceilometer and <70 m for lidar. Currently, this bias cannot be corrected.

The statistical analysis of the long-term datasets (2008–2018, 1841 diurnal cycles) revealed that the annual cycles of the monthly mean ABLHs (calculated for all days; clear sky and with boundary layer clouds) in Warsaw ranged from approximately 0.6 to 1.8 km, throughout the years. The lowest monthly mean ABLHs were derived for the winters of 2016 and 2018, and the highest for the springs and summers of 2014, 2015, and 2016.

The average monthly diurnal cycles of ABLH derived for clear-sky data showed pronounced changes: (i) A gradual transition from spring months (0.7–1.2 km) to summer months (0.9–1.7 km) with maximum values in August; (ii) the cycle for September (autumn) strongly resembled the cycles of June and July, indicating prolongation of the summer season; (iii) a decline of mean monthly ABLHs in mid-autumn (0.6–0.9 km) and a smooth transition to winter; (iv) the lowest mean values (below 0.6 km) in the winter months with spectacular flattening of the January cycle shape; and v) the abrupt change between the winter and spring season due to the regional climate change.

The annual mean ABLH in clear-sky conditions over Warsaw was obtained for the years from 2008 to 2018, except for 2014 and 2015 (significant absence of measurements in autumn and winter months). The annual mean ABLHs were maintained between 0.77 and 1.16 km, whereby the annual mean well-mixed boundary height ranged from 0.98 to 1.29 km, the annual mean residual layer from 1.13 to 1.39 km, and the annual mean nocturnal layer from 0.62 to 0.81 km. The seasonal mean ABLH was 1.16 ± 0.16 km in spring, 1.34 ± 0.15 km in summer, 0.99 ± 0.11 km in autumn, and 0.73 ± 0.08 km in winter.

The frequency distribution revealed ABLHs occurring below 1 km as constituting more than 60% of the total data. A strong seasonal variability of the ABLH distribution was observed (the spring distribution clearly dominated the total distribution). ABLHs between 0.6 and 1 km were most frequent during spring and summer (>35% and >30% of all data, respectively). In autumn, the distribution flattened (60% of data equally spread between 0.2 and 1 km). In winter, the distribution peak was between 0.2 and 0.8 km (~70% of data) to fall quasi-exponentially above 0.8 km.

The nighttime and daytime ABLH distribution revealed significant differences; heights reaching beyond 1.2 km were more often observed at daytime in all seasons (except winter). An opposite trend was observed below 1.2 km. Regardless of the time of day, the ABLHs above 1.2 km are more frequent in summer than during the other seasons while the ABLHs below 0.6 km account for the main part of the observations during the winter and autumn months. Due to the occurrence of residual lofted aerosols, the ABLHs exceeding 2.8 km were observed sporadically regardless of the season (<5% summer, <1% winter).

Recently, available methods for the ABLH retrieval from the lidar and ceilometer observations were summarized in a review paper [18], which concludes that although many techniques have been proposed in the literature, it is still impossible to recommend a technique that is suitable in all atmospheric scenarios. In the current paper, an approach of scaling the lidar-derived ABLH to homogenize them with the ceilometer-derived ABLH was proposed and was applied with success, providing comparable products from both instruments.

Author Contributions: D.W. and I.S.S. jointly wrote the paper, prepared the figures and made an extensive literature review. I.S.S. designed the holistic study concept and lead this work, contributed to the development of both remote sensors, took care of the measurement quality assurance and data control and curation, developed the

algorithm for homogenizing the lidar-to-ceilometer ABLHs. D.W. contributed with the development of numerical codes for retrieval of ceilometer and lidar data products and prepared statistics of ABLH. X.S. contributed with the ABLH algorithm development. B.H. contributed with lidar hardware and software developments. A.N. contributed with validation of the numerical codes. All authors contributed with interpretation and discussion of results and conducted merit paper revisions. All authors have read and agree to the published version of the manuscript.

Funding: This research was funded by the European Space Agency (ESA-ESTEC), grant no. 4000119961/16/NL/FF/mg (POLIMOS); the National Key Research and Development Program of China, grant no. 2016YFC1400905 and 2018YFC0213101; the Ministry of Science and Higher Education of Poland, grants no. PBS-19/ACC/2007/01 and KBN-1283/B/P01/2010/38; the Polish Foundation of Science and Technology, grant no. 519/FNITP/115/2010; the Polish National Science Centre, grant no. UMO-2018/29/N/ST10/02628; the Ministry of Research and Innovation of Romania, Program I - Development of the national research-development system, Subprogram 1.2 - Institutional Performance - Projects of Excellence Financing in RDI, grant no. 19PFE/17.10.2018; the Romanian National Core Program, grant no. 18N/2019; the European Commission, grants no. 262254 (ACTRIS), no. 654109 (ACTRIS-2), and no. 739530 (ACTRIS PPP). The APC was funded by the Polish National Science Centre grant no. UMO-2018/29/N/ST10/02628.

Acknowledgments: The development of the algorithms and codes used in this research has been done within the ESA-ESTEC Technical assistance for Polish Radar and Lidar Mobile Observation System (POLIMOS) and the National Key Research and Development Program of China. The PollyXT lidar was developed in a scientific collaboration of the Faculty of Physics, University of Warsaw (FUW) with the Institute of Tropospheric Research (TROPOS), whereby this development was financed by the Polish Foundation of Science and Technology. The purchase of the CHM15k ceilometer and the horizontal measurements campaign was funded by the Ministry of Science and Higher Education of Poland. The lidar ABLH retrievals and statistical analyses were financed by the Polish National Science Centre. The validation of the developed codes was funded by the Ministry of Research and Innovation of Romania and by the Romanian National Core Program. The quasi-continuous lidar measurements at the RS-Lab in Warsaw were performed within the European Aerosol Research LIdar NETwork to Establish an Aerosol Climatology (EARLINET) being a part of the European Research Infrastructure for the observation of Aerosol, Clouds and Trace Gases (ACTRIS). We are thankful to Ks. kan. dr Stanisław Banach for granting access to the spacious terrace of the St. Jacob the Apostle Parish in Głowno, from which unique horizontal ceilometer measurements were conducted over Mrożyczka Reservoir. We acknowledge Artur Szkop and Rafał Fortuna for conducting the measurements in Głowno, Wojciech Kumala for the technical support in operating the RS-Lab instruments in Warsaw, Krzysztof Markowicz for generating quick-looks available at the website of the Polish Aerosol Research Network (PolandAOD-NET). Olga Zawadzka-Mańko generated the map of the measurement scene used in this paper (Figure 1). We acknowledge Alison Smuts-Simons for proof reading of this paper.

Conflicts of Interest: The authors declare no conflict of interest.

References

1. Sorbjan, Z. *Structure of the Atmospheric Boundary Layer*; Prentice Hall: Englewood Cliffs, NJ, USA, 1989.
2. Garratt, J.R. *The Atmospheric Boundary Layer*; Cambridge University Press: Cambridge, UK, 1992.
3. Stull, R.B. *An Introduction to Boundary Layer Meteorology*; Springer Science & Business Media: Berlin, Germany, 2012; Volume 13.
4. Climate Prediction Center/NCEP, ENSO: Recent Evolution, Current Status and Predictions. 16 December 2019. Available online: https://www.cpc.noaa.gov/products/analysis_monitoring/lanina/enso_evolutionstatus-fcsts-web.pdf (accessed on 11 December 2019).
5. Sungsu, P.; Clara, D.; Michael, A.A. Estimation of the Surface Heat Flux Response to Sea Surface Temperature Anomalies over the Global Oceans. *J. Clim.* **2005**, *18*, 4582–4599.
6. Park, S.; Alexander, M.A.; Deser, C. The Impact of Cloud Radiative Feedback, Remote ENSO Forcing, and Entrainment on the Persistence of North Pacific Sea Surface Temperature Anomalies. *J. Clim.* **2006**, *19*, 6243–6261. [CrossRef]
7. Stuecker, M.F.; Jin, F.-F.; Timmermann, A.; McGregor, S. Combination mode dynamics of the anomalous northwest Pacific anticyclone. *J. Clim.* **2015**, *28*, 1093–1111. [CrossRef]
8. Loughran, T.F.; Pitman, A.J.; Perkins-Kirkpatrick, S.E. The El Niño–Southern Oscillation's effect on summer heatwave development mechanisms in Australia. *J. Clim.* **2019**, *52*, 6279–6300. [CrossRef]
9. Carneiro, R.G.; Fisch, G. Observational analysis of the daily cycle of the planetary boundary layer in the central amazon during a typical year and under the influence of the ENSO (GoAmazon project 2014/5). *Atmos. Chem. Phys. Discuss.* **2019**, in review.
10. Gerbig, C.; Körner, S.; Lin, J. Vertical mixing in atmospheric tracer transport models: Error characterization and propagation. *Atmos. Chem. Phys.* **2008**, *8*, 591–602. [CrossRef]

11. Stachlewska, I.S.; Zawadzka, O.; Engelmann, R. Effect of Heat Wave Conditions on Aerosol Optical Properties Derived from Satellite and Ground-Based Remote Sensing over Poland. *Remote Sens.* **2017**, *9*, 1199. [CrossRef]
12. Geiß, A.; Wiegner, M.; Bonn, B.; Schäfer, K.; Forkel, R.; von Schneidemesser, E.; Münkel, C.; Chan, K.L.; Nothard, R. Mixing layer height as an indicator for urban air quality? *Atmos. Meas. Tech.* **2017**, *10*, 2969–2988. [CrossRef]
13. Barlage, M.; Miao, S.; Chen, F. Impact of physics parameterizations on high-resolution weather prediction over two Chinese megacities. *J. Geophys. Res.* **2016**, *121*, 4487–4498. [CrossRef]
14. Davy, R.; Esau, I. Differences in the efficacy of climate forcings explained by variations in atmospheric boundary layer depth. *Nat. Commun.* **2016**, *7*, 11690. [CrossRef] [PubMed]
15. Esau, I.; Zilitinkevich, S. On the role of the planetary boundary layer depth in the climate system. *Adv. Sci. Res.* **2010**, *4*, 63–69. [CrossRef]
16. Qu, Y.; Han, Y.; Wu, Y.; Gao, P.; Wang, T. Study of PBLH and Its Correlation with Particulate Matter from One-Year Observation over Nanjing, Southeast China. *Remote Sens.* **2017**, *9*, 668. [CrossRef]
17. Seibert, P.; Beyrich, F.; Gryning, S.-E.; Joffre, S.; Rasmussen, A.; Tercier, P. Review and intercomparison of operational methods for the determination of the mixing height. *Atmos. Environ.* **2000**, *34*, 1001–1027. [CrossRef]
18. Dang, R.; Yang, Y.; Hu, X.; Wang, Z.; Zhang, S. A Review of Techniques for Diagnosing the Atmospheric Boundary Layer Height (ABLH) Using Aerosol Lidar Data. *Remote Sens.* **2019**, *11*, 1590. [CrossRef]
19. Lokoshchenko, M.A. Long-Term Sodar Observations in Moscow and a New Approach to Potential Mixing Determination by Rawinsondes Data. *J. Atmos. Ocean. Technol.* **2002**, *19*, 1151–1162. [CrossRef]
20. O'Connor, E.J.; Illingworth, A.J.; Brooks, I.M.; Westbrook, C.D.; Hogan, R.J.; Davies, F.; Brooks, B.J. A method for estimating the turbulent kinetic energy dissipation rate from a vertically pointing Doppler lidar, and independent evaluation from balloon-borne in situ measurements. *J. Atmos. Ocean. Tech.* **2010**, *27*, 1652–1664. [CrossRef]
21. Martucci, G.; Matthey, R.; Mitev, V.; Richner, H. Comparison between backscatter lidar and rawinsondes measurements of the diurnal and nocturnal stratification in the lower troposphere. *J. Atmos. Ocean. Tech.* **2007**, *24*, 1231–1244. [CrossRef]
22. Senff, C.; Bösenberg, J.; Peters, G.; Schaberl, T. Remote sensing of turbulent ozone fluxes and the ozone budget in the convective boundary layer with DIAL and Radar-RASS: A case study. *Beitr. Phys. Atmos.* **1996**, *69*, 161–176.
23. Emeis, S.; Münkel, C.; Vogt, S.; Müller, W.J.; Schäfer, K. Atmospheric boundary-layer structure from simultaneous SODAR, RASS, and ceilometer measurements. *Atmos. Environ.* **2004**, *38*, 273–286. [CrossRef]
24. Schween, J.; Hirsikko, A.; Löhnert, U.; Crewell, S. Mixing-layer height retrieval with ceilometer and Doppler lidar: From case studies to long-term assessment. *Atmos. Meas. Tech.* **2014**, *7*, 3685–3704. [CrossRef]
25. Baars, H.; Ansmann, A.; Engelmann, R.; Althausen, D. Continuous monitoring of the boundary-layer top with lidar. *Atmos. Chem. Phys.* **2008**, *8*, 7281–7296. [CrossRef]
26. Haeffelin, M.; Angelini, F.; Morille, Y.; Martucci, G.; Frey, S.; Gobbi, G.; Lolli, S.; O'Dowd, C.; Sauvage, L.; Xueref-Rémy, I. Evaluation of mixing-height retrievals from automatic profiling lidars and ceilometers in view of future integrated networks in Europe. *Bound. Layer Meteorol.* **2012**, *143*, 49–75. [CrossRef]
27. Nakoudi, K.; Giannakaki, E.; Dandou, A.; Tombrou, M.; Komppula, M. Planetary boundary layer height by means of lidar and numerical simulations over New Delhi, India. *Atmos. Meas. Tech.* **2019**, *12*, 2595–2610. [CrossRef]
28. Eresmaa, N.; Karppinen, A.; Joffre, S.; Räsänen, J.; Talvitie, H. Mixing height determination by ceilometer. *Atmos. Chem. Phys.* **2006**, *6*, 1485–1493. [CrossRef]
29. Stachlewska, I.; Piądłowski, M.; Migacz, S.; Szkop, A.; Zielińska, A.; Swaczyna, P. Ceilometer observations of the boundary layer over Warsaw, Poland. *Acta Geophys.* **2012**, *60*, 1386–1412. [CrossRef]
30. Wiegner, M.; Geiß, A. Aerosol profiling with the JenOptik Ceilometer CHM15kx. *Atmos. Meas. Tech.* **2012**, *5*, 1953. [CrossRef]
31. Dang, R.; Yang, Y.; Li, H.; Hu, X.-M.; Wang, Z.; Huang, Z.; Zhou, T.; Zhang, T. Atmosphere Boundary Layer Height (ABLH) Determination under Multiple-Layer Conditions Using Micro-Pulse Lidar. *Remote Sens.* **2019**, *11*, 263. [CrossRef]

32. Wiegner, M.; Madonna, F.; Binietoglou, I.; Forkel, R.; Gasteiger, J.; Geiß, A.; Pappalardo, G.; Schäfer, K.; Thomas, W. What is the benefit of ceilometers for aerosol remote sensing? An answer from EARLINET. *Atmos. Meas. Tech.* **2014**, *7*, 1979–1997. [CrossRef]
33. Martucci, G.; Milroy, C.; O'Dowd, C.D. Detection of cloud-base height using JenOptik CHM15k and Vaisala CL31 ceilometers. *J. Atmos. Ocean. Tech.* **2010**, *27*, 305–318. [CrossRef]
34. Münkel, C.; Eresmaa, N.; Räsänen, J.; Karppinen, A. Retrieval of mixing height and dust concentration with lidar ceilometer. *Bound. Layer Meteorol.* **2007**, *124*, 117–128. [CrossRef]
35. Flamant, C.; Pelon, J.; Flamant, P.H.; Durand, P. Lidar determination of the entrainment zone thickness at the top of the unstable marine atmospheric boundary layer. *Bound. Layer Meteorol.* **1997**, *83*, 247–284. [CrossRef]
36. Menut, L.; Flamant, C.; Pelon, J.; Flamant, P.H. Urban boundary-layer height determination from lidar measurements over the Paris area. *Appl. Opt.* **1999**, *38*, 945–954. [CrossRef]
37. Sicard, M.; Pérez, C.; Rocadenbosch, F.; Baldasano, J.; García-Vizcaino, D. Mixed-layer depth determination in the Barcelona coastal area from regular lidar measurements: Methods, results and limitations. *Bound. Layer Meteorol.* **2006**, *119*, 135–157. [CrossRef]
38. Sokół, P.; Stachlewska, I.S.; Ungureanu, I.; Stefan, S. Evaluation of the Boundary Layer Morning Transition Using the CL-31 Ceilometer Signals. *Acta Geophys.* **2014**, *62*, 367–380. [CrossRef]
39. Lammert, A.; Bösenberg, J. Determination of the convective boundary-layer height with laser remote sensing. *Bound. Layer Meteorol.* **2006**, *119*, 159–170. [CrossRef]
40. Steyn, D.G.; Baldi, M.; Hoff, R. The detection of mixed layer depth and entrainment zone thickness from lidar backscatter profiles. *J. Atmos. Ocean. Tech.* **1999**, *16*, 953–959. [CrossRef]
41. Brooks, I.M. Finding boundary layer top: Application of a wavelet covariance transform to lidar backscatter profiles. *J. Atmos. Ocean. Tech.* **2003**, *20*, 1092–1105. [CrossRef]
42. Morille, Y.; Haeffelin, M.; Drobinski, P.; Pelon, J. STRAT. an automated algorithm to retrieve the vertical structure of the atmosphere from single-channel lidar data. *J. Atmos. Ocean. Tech.* **2007**, *24*, 761–775. [CrossRef]
43. Di Giuseppe, F.; Riccio, A.; Caporaso, L.; Bonafé, G.; Gobbi, G.P.; Angelini, F. Automatic detection of atmospheric boundary layer height using ceilometer backscatter data assisted by a boundary layer model. *Q. J. R. Meteorol. Soc.* **2012**, *138*, 649–663. [CrossRef]
44. Collaud, C.M.; Praz, C.; Haefele, A.; Ruffieux, D.; Kaufmann, P.; Calpini, B. Determination and climatology of the planetary boundary layer height above the Swiss Plateau by in situ and remote sensing measurements as well as by the COSMO-2 model. *Atmos. Chem. Phys.* **2014**, *14*, 13205–13221. [CrossRef]
45. Poltera, Y.; Martucci, G.; Coen, M.C.; Hervo, M.; Emmenegger, L.; Henne, S.; Brunner, D.; Haefele, A. PathfinderTURB: An automatic boundary layer algorithm. Development, validation and application to study the impact on in situ measurements at the Jungfraujoch. *Atmos. Chem. Phys.* **2017**, *17*, 10051. [CrossRef]
46. Martucci, G.; Matthey, R.; Mitev, V.; Richner, H. Frequency of boundary-layer-top fluctuations in convective and stable conditions using laser remote sensing. *Bound. Layer Meteorol.* **2010**, *135*, 313–331. [CrossRef]
47. Eresmaa, N.; Härkönen, J.; Joffre, S.M.; Schultz, D.M.; Karppinen, A.; Kukkonen, J. A three-step method for estimating the mixing height using ceilometer data from the Helsinki testbed. *J. Appl. Meteorol. Climatol.* **2012**, *51*, 2172–2187. [CrossRef]
48. Kotthaus, S.; O'Connor, E.; Münkel, C.; Charlton-Perez, C.; Haeffelin, M.; Gabey, A.M.; Grimmond, C.S.B. Recommendations for processing atmospheric attenuated backscatter profiles from Vaisala CL31 ceilometers. *Atmos. Meas. Tech.* **2016**, *9*, 3769–3791. [CrossRef]
49. Kotthaus, S.; Halios, C.H.; Barlow, J.F.; Grimmond, C. Volume for pollution dispersion: London's atmospheric boundary layer during ClearfLo observed with two ground-based lidar types. *Atmos. Environ.* **2018**, *190*, 401–414. [CrossRef]
50. Chiriaco, M.; Dupont, J.-C.; Bastin, S.; Badosa, J.; Lopez, J.; Haeffelin, M.; Chepfer, H.; Guzman, R. ReOBS a new approach to synthesize long-term multi-variable dataset and application to the SIRTA supersite. *Earth Syst. Sci. Data* **2018**, *10*, 919–940. [CrossRef]
51. Seidel, D.J.; Zhang, Y.; Beljaars, A.; Golaz, J.C.; Jacobson, A.R.; Medeiros, B. Climatology of the planetary boundary layer over the continental United States and Europe. *J. Geophys. Res.* **2012**, *117*. [CrossRef]
52. Wang, D.; Szczepanik, D.; Stachlewska, I.S. Interrelations between surface, boundary layer, and columnar aerosol properties over a continental urban site. *Atmos. Chem. Phys.* **2019**, *19*, 13097–13128. [CrossRef]

53. Kotthaus, S.; Grimmond, C.S.B. Atmospheric boundary-layer characteristics from ceilometer measurements. Part 1: A new method to track mixed layer height and classify clouds. *Q. J. R. Meteorol. Soc.* **2018**, *144*, 1525–1538. [CrossRef]
54. Kotthaus, S.; Grimmond, C.S.B. Atmospheric boundary layer characteristics from ceilometer measurements. Part 2: Application to London's urban boundary. *Q. J. R. Meteorol. Soc.* **2018**, *144*, 1511–1524. [CrossRef]
55. Haman, C.L.; Lefer, B.; Morris, G.A. Seasonal variability in the diurnal evolution of the boundary layer in a near-coastal urban environment. *J. Atmos. Ocean. Tech.* **2012**, *29*, 697–710. [CrossRef]
56. Hervo, M.; Poltera, Y.; Haefele, A. An empirical method to correct for temperature-dependent variations in the overlap function of CHM15k ceilometers. *Atmos. Meas. Tech.* **2016**, *9*, 2947–2959. [CrossRef]
57. Engelmann, R.; Kanitz, T.; Baars, H.; Heese, B.; Althausen, D.; Skupin, A.; Wandinger, U.; Komppula, M.; Stachlewska, I.S.; Amiridis, V.; et al. The automated multiwavelength Raman polarization and water-vapor lidar PollyXT: The next generation. *Atmos. Meas. Tech.* **2016**, *9*, 1767–1784. [CrossRef]
58. Baars, H.; Kanitz, T.; Engelmann, R.; Althausen, D.; Heese, B.; Komppula, M.; Preißler, J.; Tesche, M.; Ansmann, A.; Wandinger, U.; et al. An overview of the first decade of PollyNET: An emerging network of automated Raman-polarization lidars for continuous aerosol profiling. *Atmos. Chem. Phys.* **2016**, *16*, 5111–5137. [CrossRef]
59. Stachlewska, I.S.; Samson, M.; Zawadzka, O.; Harenda, K.M.; Janicka, L.; Poczta, P.; Szczepanik, D.; Heese, B.; Wang, D.; Borek, K.; et al. Modification of Local Urban Aerosol Properties by Long-Range Transport of Biomass Burning Aerosol. *Remote Sens.* **2018**, *10*, 412. [CrossRef]
60. Janicka, L.; Stachlewska, I.S.; Veselovskii, I.; Baars, H. Temporal variations in optical and microphysical properties of mineral dust and biomass burning aerosol derived from daytime Raman lidar observations over Warsaw, Poland. *Atmos. Environ.* **2017**, *169*, 162–174. [CrossRef]
61. Stachlewska, I.S.; Costa-Surós, M.; Althausen, D. Raman lidar water vapor profiling over Warsaw, Poland. *Atmos. Res.* **2017**, *194*, 258–267. [CrossRef]
62. Heese, B.; Flentje, H.; Althausen, D.; Ansmann, A.; Frey, S. Ceilometer lidar comparison: Backscatter coefficient retrieval and signal-to-noise ratio determination. *Atmos. Meas. Tech.* **2010**, *3*, 1763–1770. [CrossRef]
63. Whiteman, C.D.; Allwine, K.J. Extraterrestrial solar radiation on inclined surfaces. *Environ. Softw.* **1986**, *1*, 164–169. [CrossRef]
64. Binietoglou, I.; Giuseppe, D.; Baars, H.; Belegante, L.; Marinou, E. A methodology for cloud masking uncalibrated lidar signals. *EPJ Web Conf.* **2018**, *176*, 05048. [CrossRef]
65. Pal, S. Monitoring Depth of Shallow Atmospheric Boundary Layer to Complement LiDAR Measurements Affected by Partial Overlap. *Remote Sens.* **2014**, *6*, 8468–8493. [CrossRef]
66. Matthias, V.; Balis, D.; Bösenberg, J.; Eixmann, R.; Iarlori, M.; Komguem, L.; Mattis, I.; Papayannis, A.; Pappalardo, G.; Perrone, M.R.; et al. Vertical aerosol distribution over Europe: Statistical analysis of Raman lidar data from 10 European Aerosol Research Lidar Network (EARLINET) stations. *J. Geophys. Res.* **2004**, *109*, D18201. [CrossRef]
67. Zhang, Y.; Seidel, D.J.; Zhang, S. Trends in planetary boundary layer height over Europe. *J. Clim.* **2013**, *26*, 10071–10076. [CrossRef]
68. Piringer, M.; Joffre, S.; Baklanov, A.; Christen, A.; Deserti, M.; De Ridder, K.; Emeis, S.; Mestayer, P.; Tombrou, M.; Middleton, D. The surface energy balance and the mixing height in urban areas—activities and recommendations of Cost-Action 715. *Bound. Layer Meteorol.* **2007**, *124*, 3–24. [CrossRef]
69. Tsaknakis, G.; Papayannis, A.; Kokkalis, P.; Amiridis, V.; Kambezidis, H.D.; Mamouri, R.E.; Georgoussis, G.; Avdikos, G. Inter-comparison of lidar and ceilometer retrievals for aerosol and planetary boundary layer profiling over Athens, Greece. *Atmos. Meas. Tech.* **2011**, *4*, 1261–1273. [CrossRef]
70. Caicedo, V.; Rappenglück, B.; Lefer, B.; Morris, G.; Toledo, D.; Delgado, R. Comparison of aerosol lidar retrieval methods for boundary layer height detection using ceilometer aerosol backscatter data. *Atmos. Meas. Tech.* **2017**, *10*, 1609. [CrossRef]
71. Vogelezang, D.H.P.; Holtslag, A.A.M. Evaluation and model impacts of alternative boundary–layer height formulations. *Bound. Layer Meteorol.* **1996**, *81*, 245–269. [CrossRef]
72. Dong, X.; Kennedy, A. A 19-month record of marine aerosol–cloud–radiation properties derived from DOE ARM mobile facility deployment at the Azores. Part I: Cloud fraction and single-layered MBL cloud properties. *J. Clim.* **2014**, *27*, 3665–3682. [CrossRef]

73. Béghein, C.; Allery, C.; Wacławczyk, C.; Pozorski, J. Application of POD-based dynamical systems to dispersion and deposition of particles in turbulent channel flow. *Int. J. Multiphase Flow.* **2014**, *58*, 97–113. [CrossRef]
74. Lotteraner, C.; Piringer, M. Mixing-Height Time Series from Operational Ceilometer Aerosol-Layer Heights. *Bound. Layer Meteorol.* **2016**, *161*, 265–287. [CrossRef]
75. Pal, S.; Xueref-Remy, I.; Ammoura, L.; Chazette, P.; Gibert, F.; Royer, P.; Dieudonn, E.; Dupont, J.-C.; Haeffelin, M.; Lac, C.; et al. Spatio-temporal variability of the atmospheric boundary layer depth over the Paris agglomeration: An assessment of the impact of the urban heat island intensity. *Atmos. Environ.* **2012**, *63*, 261–275. [CrossRef]
76. Czerwińska, A.E.; Krzyścin, J.W.; Jarosławski, J.; Posyniak, M. Effects of urban agglomeration on surface-UV doses: A comparison of Brewer measurements in Warsaw and Belsk, Poland, for the period 2013–2015. *Atmos. Chem. Phys.* **2016**, *16*, 13641–13651. [CrossRef]
77. Kożuchowski, K.; Degirmendžić, J.; Fortuniak, K.; Wibig, J. Trends to changes in seasonal aspects of the climate in Poland. *Geogr. Pol.* **2000**, *73*, 7–24.
78. Błażejczyk, K.; Kuchcik, M.; Dudek, W.; Kręcisz, B.; Błażejczyk, A.; Milewski, P.; Szmyd, J.; Pałczyński, C. Urban Heat Island and Bioclimatic Comfort in Warsaw. In *Counteracting Urban Heat Island Effects in a Global Climate Change Scenario*; Musco, F., Ed.; Springer: Cham, Switzerland, 2016; pp. 305–321.
79. Oke, T.R. The heat island of the urban boundary layer: Characteristics, causes and effects. *Nat. Adv. Sci. Inst. Ser.* **1995**, *277*, 81–107.
80. Rubel, F.; Kottek, M. Observed and projected climate shifts 1901-2100 depicted by world maps of the Köppen-Geiger climate classification. *Meteorol. Z.* **2010**, *19*, 135–141. [CrossRef]
81. Brönnimann, S. The impact of El Nino–Southern Oscillation on European climate. *Rev. Geophys.* **2007**, *45*, RG3003. [CrossRef]
82. Scaife, A.A. Impact of ENSO on European Climate. In Proceedings of the ECMWF Seminar on Predictability in the European and Atlantic regions, Reading, UK, 6–9 September 2010; pp. 83–91.
83. Żmudzka, E.; Kulesza, K.; Lenartowicz, M.; Leziak, K.; Magnuszewski, A. Assessment of modern hydro-meteorological hazards in a big city–identification for Warsaw. *Meteorol. Appl.* **2019**, *26*, 500–510. [CrossRef]
84. Zhai, P.; Yu, R.; Guo, Y.; Li, O.; Ren, X.; Wang, Y.; Xu, W.; Liu, Y.; Ding, Y. The strong El Niño of 2015/16 and its dominant impacts on global and China's climate. *J. Meteorol. Res.* **2016**, *30*, 283–297. [CrossRef]
85. Dieudonné, E.; Chazette, P.; Marnas, F.; Totems, J.; Shang, X. Raman Lidar Observations of Aerosol Optical Properties in 11 Cities from France to Siberia. *Remote Sens.* **2017**, *9*, 978. [CrossRef]
86. Gao, F.; Stanič, S.; Bergant, K.; Li, Y.; Li, S.; Hua, D.; Wang, L. Application of the Ultraviolet Scanning Elastic Backscatter LiDAR for the Investigation of Aerosol Variability. *Remote Sens.* **2015**, *7*, 6320–6335. [CrossRef]
87. Barlow, J.F.; Halios, C.H.; Lane, S.E.; Wood, C.R. Observations of urban boundary layer structure during a strong urban heat island event. *Environ. Fluid Mech.* **2014**, *15*, 1–26. [CrossRef]
88. Bennett, L.J.; Weckwerth, T.; Blyth, A.M.; Geerts, B.; Miao, Q.; Richardson, Y. Observations of the evolution of the nocturnal and convective boundary layers and the structure of open-celled convection on 14 June 2002. *Mon. Weather Rev.* **2010**, *138*, 2589–2607. [CrossRef]
89. Tang, Q.; Leng, G. Damped summer warming accompanied with cloud cover increase over Eurasia from 1982 to 2009. *Environ. Res. Lett.* **2012**, *7*, 014004. [CrossRef]

Chapter 5 Interrelations between aerosol optical properties in Warsaw

5.1 Value-added of the PhD research

A statistical analysis of aerosol optical properties derived within the atmospheric boundary layer from lidar long-term observations at the urban continental site in Warsaw was done for the subset of measurements conducted in July, August, and September of 2013, 2015, and 2016 (Wang et al., 2019). The interrelations within the lidar-derived properties were established for different periods: the entire day (ET); at night-time, with respect to the nocturnal (NL) and residual boundary layers (RL); at sunrise, with respect to the morning transition layer (MTL); and from late afternoon until sunset, with respect to the well-mixed boundary layer (WML). Moreover, the relations between the aerosol optical properties within atmospheric boundary layer (ABL), the particulate matter ($PM_{2.5}$ and PM_{10}), and the relative humidity (RH) were investigated.

The aerosol optical depth (AOD_{ABL}), lidar ratio (LR_{ABL}), particle depolarization ratio (δ_{ABL}) and Ångström exponent ($ÅE_{ABL}$) derived at 355 and 532 nm within ABL, and the fine-to-coarse mass ratio (FCMR, defined as $PM_{2.5}$ /(PM_{10} - $PM_{2.5}$)) derived from surface $PM_{2.5}$ and PM_{10} measurements for the entire, nocturnal, and sunrise/sunset periods were calculated. The differences in wavelength-dependent properties were attributed to the different aerosol composition within ABL, that consisted mainly of the following aerosol types:

(i) Urban anthropogenic pollution of local origin or pollution transported from areas over the Czech Republic via Silesia and/or Germany (61 %),

or its mixtures with

(ii) grass and peatland biomass burning aerosol transported from Russia, Ukraine, and Belarus (14 %),

(iii) pollen emissions of strictly local origin from Warsaw's semi-natural green parks (7 %),

(iv) marine particles transported mainly from the Arctic over the Baltic Sea (5 %).

(v) For the remaining cases, the aerosol composition was regarded as being due to a mixture of more than two subcomponents (13 %).

(vi) No significant contribution of mineral dust was found within the boundary layer.

The relations of different parameters are shown in Figure 2. The lidar-derived ABLH and AOD_{ABL} exhibited a positive correlation. The LR_{ABL} showed a negative correlation with $ÅE_{ABL}$. A negative trend for δ_{ABL} with water vapour mixing ratio (WV_{ABL}) and surface relative humidity (RH) were observed. The FCMR and surface RH showed a positive correlation. A weak negative correlation of the FCMR and δ_{ABL} was discernible. Most interestingly, smaller particles with a high $ÅE_{ABL}$ and lower LR_{ABL} and AOD_{ABL} were observed under wetter conditions in the morning transition boundary layer, while larger particles with a lower $ÅE_{ABL}$ and higher LR_{ABL} and AOD_{ABL} were observed in the well-mixed boundary layer under drier conditions.

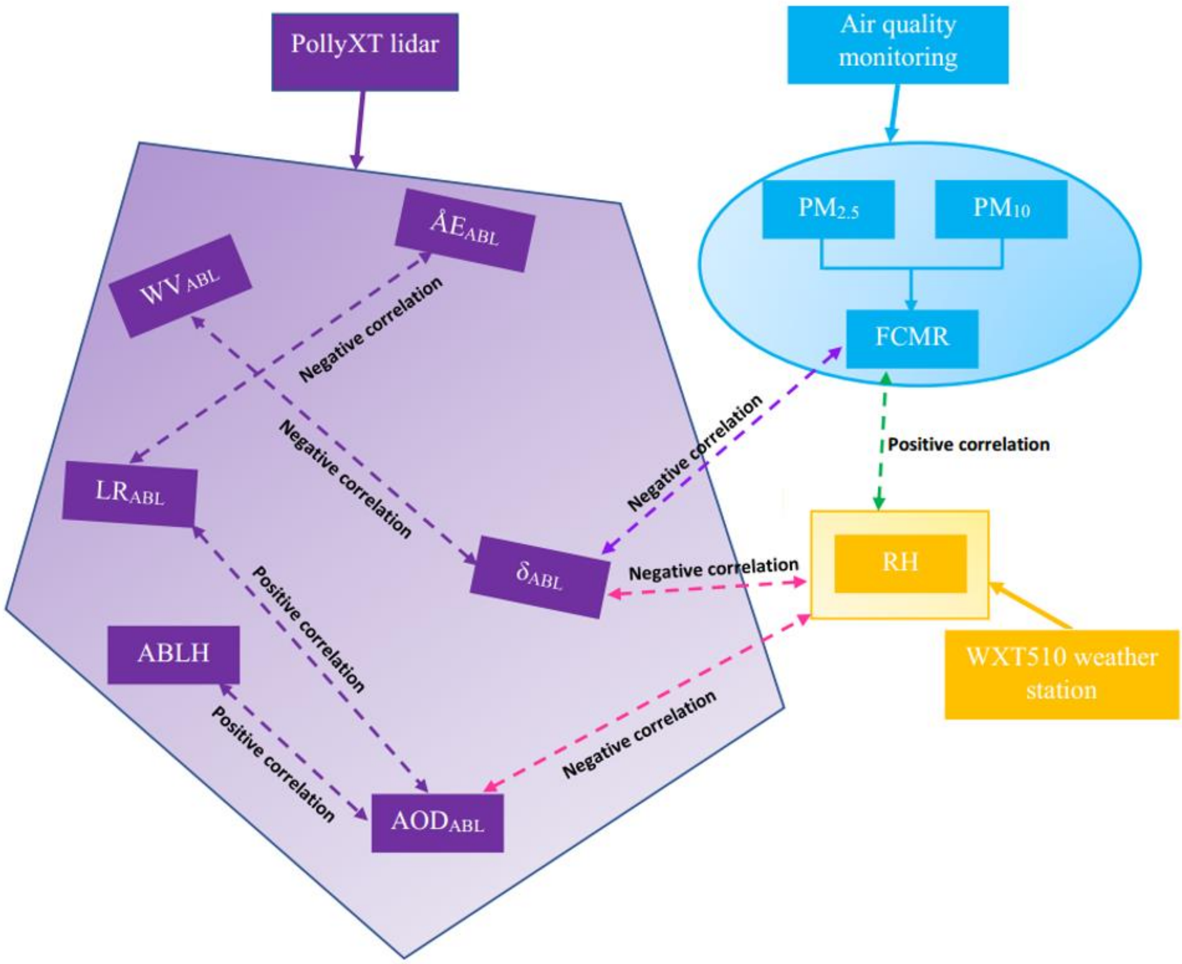

Figure 2. The relations of the aerosol optical properties derived within the atmospheric boundary layer, and particulate matter ($PM_{2.5}$ and PM_{10}), and the relative humidity in Warsaw for the period of July–September of 2013, 2015, and 2016, *based on the results in Wang et al. 2019.*

This work is very important for the scientific community. Most of studies reported in literature so far are limited to the analysis of either AOD and/or LR values in the ABL. Comprehensive investigations of interrelations of aerosol optical properties in such an extensive range of various properties as done within my PhD work have not been reported so far, except for my own research (Wang et al. 2019). The provided characteristic parameters can well be used for future studies of boundary layer meteorology. The derived aerosol optical properties can be used to verify aerosol transport models. Furthermore, they can be used in the estimation of the aerosol radiative forcing in radiative transfer modelling, as well as for the validation of spaceborne lidar data, as e.g. in work I co-authored (Stachlewska et al. 2018).

Currently, I am involved in a research study that is using the obtained dataset to compare it with satellite measurements of CALIPSO and CATS lidars.

5.2 Paper 2

Published paper title: Interrelations between surface, boundary layer, and columnar aerosol properties derived in summer and early autumn over a continental urban site in Warsaw, Poland.
Authors: Dongxiang Wang, Dominika Szczepanik, and Iwona S. Stachlewska.
Bibliographic record: Atmospheric Chemistry and Physics, 19, 13097–13128, 2019.
Link: https://doi.org/10.5194/acp-19-13097-2019.
Author Contributions (Stated explicitly in the published paper):

Author contributions. I.S.S. wrote the paper, obtained funding for the research, came up with the study approach, designed the methodology, performed the experiment, contributed to the development of the PollyXT lidar (Warsaw) and the lidar evaluation algorithms, took care of the quality assurance of lidar measurements and data products, and holistically interpreted the lidar results with respect to other data sources' results (AERONET, PolandAOD-NET, and WIOS Monitoring Network). D.S. was responsible for the calculation of the aerosol optical property profiles (α, β, and δ) and their categorization for the EARLINET/ACTRIS database. D.W. was responsible for an extensive literature review, wrote the codes for the ABLH and the WV retrieval algorithms, and performed statistical analysis of the optical properties (ÅE, LR, δ, and WV). All authors contributed to revisions of the paper.

Atmos. Chem. Phys., 19, 13097–13128, 2019
https://doi.org/10.5194/acp-19-13097-2019

Atmospheric Chemistry and Physics
Open Access
EGU

Interrelations between surface, boundary layer, and columnar aerosol properties derived in summer and early autumn over a continental urban site in Warsaw, Poland

Dongxiang Wang, Dominika Szczepanik, and Iwona S. Stachlewska

Institute of Geophysics, Faculty of Physics, University of Warsaw, 02-093, Warsaw, Poland

Correspondence: Iwona S. Stachlewska (iwona.stachlewska@fuw.edu.pl)

Received: 21 November 2018 – Discussion started: 30 November 2018
Revised: 25 September 2019 – Accepted: 30 September 2019 – Published: 23 October 2019

Abstract. PollyXT Raman polarization lidar observations were performed at the Remote Sensing Laboratory (RS-Lab) in Warsaw (52.2109° N, 20.9826° E), Poland, in the framework of the European Aerosol Research Lidar Network (EARLINET) and the Aerosol, Clouds, and Trace gases Research Infrastructure (ACTRIS) projects. Data collected in July, August, and September of 2013, 2015, and 2016 were analysed using the classical Raman approach. In total, 246 sets of intact profiles, each set comprising particle extinction (α) and backscatter coefficients (β) as well as linear particle depolarization ratios (δ) at 355 nm and 532 nm, were derived for statistical investigations and stored in the EARLINET/ACTRIS database. The main analysis was focused on intensive optical properties obtained within the atmospheric boundary layer (ABL). Their interrelations were discussed for different periods: the entire day; nighttime, with respect to the nocturnal boundary layer (NL) and the residual boundary layer (RL); at sunrise, with respect to the morning transition boundary layer (MTL); and from late afternoon until sunset, with respect to the well-mixed boundary layer (WML). Within the boundary layer, the lidar-derived optical properties (entire day, 246 sets) revealed a mean aerosol optical depth (AOD_{ABL}) of 0.20 ± 0.10 at 355 nm and 0.11 ± 0.06 at 532 nm; a mean Ångström exponent ($ÅE_{ABL}$) of 1.54 ± 0.37; a mean lidar ratio (LR_{ABL}) of 48 ± 17 sr at 355 nm and 41 ± 15 sr at 532 nm; a mean linear particle depolarization ratio (δ_{ABL}) of 0.02 ± 0.01 at 355 nm and 0.05 ± 0.01 at 532 nm; and a mean water vapour mixing ratio (WV_{ABL}) of $8.28\pm2.46\,g\,kg^{-1}$. In addition, the lidar-derived daytime boundary layer optical properties (for the MTL and WML) were compared with the corresponding daytime columnar aerosol properties derived from the multi-filter rotating shadowband radiometer (MFR-7) measuring within the National Aerosol Research Network (PolandAOD-NET) and the CE318 sun photometer of the Aerosol Robotic NETwork (AERONET). A high linear correlation of the columnar aerosol optical depth values from the two latter instruments was obtained in Warsaw (a correlation coefficient of 0.98 with a standard deviation of 0.02). The contribution of the aerosol load in the summer and early-autumn free troposphere can result in an AOD_{CL} value that is twice as high as the AOD_{ABL} over Warsaw. The occurrence of a turbulence-driven aerosol burst from the boundary layer into the free troposphere can further increase this difference. Aerosol within the ABL and in the free troposphere was interpreted based on comparisons of the properties derived at different altitudes with values reported in the literature, which were characteristic for different aerosol types, in combination with backward trajectory calculations, satellite data, and model outputs. Within the boundary layer, the aerosol consisted of either urban anthropogenic pollution (~61 %) or mixtures of anthropogenic aerosol with biomass-burning aerosol (< 14 %), local pollen (< 7 %), or Arctic marine particles (< 5 %). No significant contribution of mineral dust was found in the boundary layer. The lidar-derived atmospheric boundary layer height (ABLH) and the AOD_{ABL} exhibited a positive correlation (R of 0.76), associated with the local anthropogenic pollution (most pronounced for the RL and WML). A positive correlation of the AOD_{ABL} and LR_{ABL} and a negative correlation of the $ÅE_{ABL}$ and LR_{ABL}, as well as the expected negative trends for the WV_{ABL} (and surface relative humidity, RH) and δ_{ABL}, were observed. Relations of the lidar-derived aerosol properties within the ABL and the surface in situ measurements of particulate matter

Published by Copernicus Publications on behalf of the European Geosciences Union.

with an aerodynamic diameter less than 10 µm (PM_{10}) and less than 2.5 µm ($PM_{2.5}$) measured by the Warsaw Regional Inspectorate for Environmental Protection (WIOS) network, and the fine-to-coarse mass ratio (FCMR) were investigated. The FCMR and surface RH showed a positive correlation even at nighttime (R of 0.71 for the MTL, 0.63 for the WML, and 0.6 for the NL), which generally lacked statistically significant relations. A weak negative correlation of the FCMR and δ_{ABL} (more pronounced at 532 nm at nighttime) and no casual relation between the FCMR and $ÅE_{ABL}$ were found. Most interestingly, distinct differences were observed for the morning transition layer (MTL) and the well-mixed layer (WML). The MTL ranged up to 0.6–1 km, and was characterized by a lower AOD_{ABL} (< 0.12), wetter conditions (RH 50–80 %), smaller particles ($ÅE_{ABL}$ of 1–2.2; FCMR from 0.5 to 3), and a low LR_{ABL} of between 20 and 40 sr. The WML ranged up to 1–2.5 km and exhibited a higher AOD_{ABL} (reaching up to 0.45), drier conditions (RH 25–60 %), larger particles ($ÅE_{ABL}$ of 0.8–1.7; FCMR of 0.2–1.5), and a higher LR_{ABL} of up to 90 sr.

1 Introduction

Atmospheric aerosol can impact climate (e.g. Feingold et al., 2016; Seinfeld et al., 2016), weather (e.g. Fan et al., 2016; Gayatri et al., 2017), air quality (e.g. Fuzzi et al., 2015), and human health (e.g. Zheng et al., 2015; Trippetta et al., 2016). Aerosol particles affect the Earth's radiative budget, as they interact with the incoming solar short-wave radiation and the outgoing terrestrial long-wave radiation. Depending on the aerosol type, they can scatter and/or absorb the radiation, causing local warming or cooling of the atmosphere, at the surface and at the top of atmosphere (Kaufman et al., 2002). The variety of aerosol sources, those of natural and anthropogenic origin, as well as the influence of diverse meteorological conditions on aerosol characteristics and transport, lead to strongly variable aerosol contents within the troposphere. Aerosol optical properties, size, and composition are important for aerosol–cloud–radiation interaction studies (Seinfeld et al., 2016) and for radiative transfer modelling (Lolli et al., 2018).

The Intergovernmental Panel on Climate Change (IPCC) reported that the sparse and/or poorly-known information on the aerosol temporal and spatial variability causes high uncertainty in the assessment of their influence on the global radiation budget (Stocker et al., 2013). The latest IPCC report indicates that the reduction of uncertainties is still necessary, as it can improve the ability to accurately forecast global climate change (Masson-Delmotte et al., 2018). Several past studies have been dedicated to investigating and improving the above-mentioned uncertainties. Pan et al. (2015) identified the major discrepancies between the state-of-the-art global aerosol models and observations with respect to simulating aerosol loading over South Asia, thereby providing directions for future model improvements in this important region. Ghan et al. (2016) found that uncertainty regarding anthropogenic aerosol effects on cloud radiative forcing arises from uncertainty in several relationships, including the choice of parameter values and numerical integration methods. Koffi et al. (2016) provided further spatial and temporal details on the state-of-the-art AeroCom II global aerosol models and investigated the reasons for the model discrepancies and diversity, which provided a good foundation for further evaluation of the models' performance at a global scale. Kipling et al. (2016) investigated the impact of a wide range of processes (emission, transport, deposition, and microphysical and chemical processes) on aerosol vertical distribution in the aerosol–climate model via a series of limiting case process-based sensitivity tests; they showed that the processes that have the greatest impact on the vertical distribution vary both between different aerosol components and over the particle size spectrum. Seinfeld et al. (2016) provided strategies for improving estimates of aerosol–cloud relationships in climate models, for new remote sensing and in situ measurements, and for quantifying and reducing the model uncertainties.

Air pollution is one of the major environmental issues in metropolitan areas due to its adverse effects on human health (e.g. Chen et al., 2008; Lelieveld et al., 2015). Juda-Rezler et al. (2012) reported that air quality is related to anthropogenic emissions and natural emissions and that a change in temperature, water vapour, precipitation, wind speed, and wind direction can affect atmospheric chemical reactions, atmospheric transport, and deposition processes, as well as the rate of pollutant transport from urban environments to global-scale environments. The emission of pollutants changes the chemical composition of the atmosphere, which in turn has a feedback effect on the regional and global climate (Juda-Rezler et al., 2012). Strong emissions, e.g. from traffic, industry, or heating, can drastically decrease air quality, particularly when meteorological conditions prevent an exchange of polluted and clean air, (Juda-Rezler et al., 2011). In Europe, surface particulate matter (with an aerodynamic diameter below 10 µm, PM_{10}, and 2.5 µm, $PM_{2.5}$) is one of the most serious air quality problems (e.g. De Leeuw et al., 2001; Wolff and Perry, 2010). As atmospheric aerosol can affect air quality, health, and the environment, joint studies of the aerosol optical property measurements in combination with surface observations of PM_{10} (e.g. Guo et al., 2009, 2017; Stachlewska et al., 2017b; Popovici et al., 2018), $PM_{2.5}$ (e.g. Schaap et al., 2009; Stachlewska et al., 2017b, 2018), and PM_1 (e.g. Qin et al., 2018) concentrations can improve our knowledge of the atmospheric environment.

The atmospheric boundary layer (ABL) can affect the dispersion of pollutants within the mixing layer (Wałaszek et al., 2018). The knowledge of ABL characteristics and ABL dynamics, both related to ambient meteorological conditions, is helpful to model and predict mechanisms of importance in weather forecasting, air pollution, and climate change studies (Barlage et al., 2016). Therefore, it is meaningful to acquire knowledge of the ABL top height distribution along with the aerosol optical properties within the ABL.

Lidar techniques seem to be an optimal tool to provide height-resolved aerosol data products. Several lidar techniques suitable for aerosol studies have recently matured. In the last 10 years, rapid progress in laser technology, measurement techniques, and data acquisition systems has contributed to a much wider use of these techniques for aerosol monitoring, ranging from simple elastic backscatter lidar/ceilometer networks (Flentje et al., 2010; Lolli and Di Girolamo, 2015) to advanced multi-wavelength Raman lidar system networks (Baars et al., 2016). The European Aerosol Research Lidar Network (EARLINET; https://www.earlinet.orglast access: 15 October 2019) conducts lidar observations and provides relevant sets of lidar data products on the aerosol distribution over Europe, which are stored in a comprehensive, quantitative, and statistically significant database (Pappalardo et al., 2014). A quality assurance programme (Freudenthaler et al., 2018) and lidar data evaluation algorithms (Böckmann et al., 2004) have been developed and assessed at each lidar station, as well as during lidar intercomparison campaigns (e.g. Wandinger et al., 2016), to meet the accuracy standards required for calculations of aerosol radiative forcing. The unique dataset of lidar observations conducted over Europe allows for the classification of the aerosol type (e.g. Nicolae et al., 2018; Papagiannopoulos et al., 2018). The EARLINET network is an integral part of the Aerosol, Clouds, and Trace gases Research Infrastructure (ACTRIS; https://www.actris.eu, last access: 29 August 2019) – a pan-European initiative consolidating actions from European partners producing high quality observations of aerosol, clouds, and trace gases. As different atmospheric processes are increasingly becoming the focus of many societal and environmental challenges, such as air quality, health, sustainability, and climate change, ACTRIS initiatives aim at contributing to resolving these challenges by providing a platform for researchers to more effectively combine their efforts, and by making observational data of aerosol, clouds, and trace gases openly available to other external users.

The aerosol optical properties derived for the boundary layer from lidar have been studied using a statistical approach at several EARLINET sites in Europe (e.g. Matthias et al., 2004; Mattis et al., 2004; Amiridis et al., 2005; Sicard et al., 2011; Siomos et al., 2018). However, most of these studies have been restricted to the analysis of either AOD and/or LR values in the ABL (e.g. Matthias et al. 2004; Amiridis et al. 2005, 2009; Sicard et al., 2011), or relations between LR_{ABL} and AE_{ABL} (Giannakaki et al., 2010). Comprehensive investigations of interrelations of various aerosol optical properties have not been reported thus far. Therefore, the current study is the first to report on these interrelations (or lack of) for different times of day (nocturnal, sunrise and sunset, daytime) in summer (July and August) and early autumn (September) over Warsaw. The relations of surface $PM_{2.5}$, PM_{10}, and AOD_{CL} have been reported by e.g. Guo et al. (2009), Filip and Stefan (2011), Zang et al. (2017), and Szczepanik and Markowicz (2018), and the relations of AOD_{CL} and ambient RH were reported by e.g. Bergin et al. (2000) and Altaratz et al. (2013). Stachlewska et al. (2017b, 2018), investigated the relations of $PM_{2.5}$, PM_{10}, RH, LR_{ABL}, AOD_{ABL}, AE_{ABL}, and δ_{ABL}, based on case studies. In this paper, we analyse and report on those sets of properties based on long-term observations. The combination of such study with hygroscopic growth monitoring is the next step in the future (Navas Guzmán et al., 2019). The results reported in the current paper will enrich the state of knowledge on boundary layer aerosol optical properties by building a seasonal climatology over Warsaw (even if it is limited to July–September of the 3-year period – 2013, 2015, and 2016) and, thus, providing a reference for comparative studies with the other EARLINET (e.g. Papayannins et al., 2008) and AERONET sites (e.g. Siomos et al., 2018). The dataset obtained has excellent potential for aerosol microphysical parameter inversion (e.g. Veselovskii et al., 2002; Böckmann et al., 2005) and can also be used to test aerosol typing algorithms (e.g. Nicolae et al., 2018; Papagiannopoulos et al., 2018). This research provides parameters for studies of boundary layer meteorology, and the derived aerosol optical properties can serve to verify aerosol transport models (e.g. Binietoglou et al., 2015); furthermore, these properties can be used in the estimation of the aerosol radiative forcing effect in radiative transfer modelling (e.g. Lisok et al., 2018; Lolli et al., 2018) as well as for the validation of spaceborne lidar (e.g. Illingworth et al., 2015; Papagiannopoulos et al., 2016; Proestakis et al., 2019).

In the framework of EARLINET, extensive observations at a continental, urban site in Warsaw at the Remote Sensing Laboratory (RS-Lab) of the Institute of Geophysics at the Faculty of Physics of the University of Warsaw have been performed since July 2013. Within the current paper the data products from the Warsaw site published in the EARLINET/ACTRIS database were utilized (The EARLINET Publishing Group, 2018). The study was dedicated to the calculation and analysis of the aerosol optical properties derived within the atmospheric boundary layer, at various times of the day, during summer (July and August) and early autumn (September) of 2013, 2015, and 2016, over a continental urban site in Warsaw. The following three specific goals were addressed: (i) investigation of interrelations between the different aerosol optical properties; (ii) investigation of relations between the aerosol optical properties, particulate matter ($PM_{2.5}$ and PM_{10}), and the relative humidity; and (iii) assessment of the quantitative contribution of the boundary aerosol optical depth to the columnar aerosol optical depth. In Sect. 2, the instrumentation and datasets are described. Section 3 presents the methodology regarding the boundary layer height derivation and the aerosol optical property retrieval approaches. Section 4 focuses on compar-

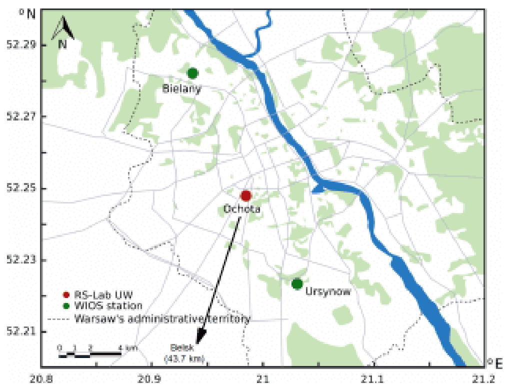

Figure 1. The location of the Remote Sensing Laboratory (RS-Lab) at UW Ochota Campus in Warsaw, Poland (in red), the WIOS monitoring stations in Ursynow and Bielany (in green), and the Institute of Geophysics at the Polish Academy of Sciences (IGF-PAS) Observatory in Belsk (arrow).

isons of different types of mean optical properties as derived within the boundary layer and in the atmospheric column: PMs, ABLHs, and near-surface relative humidity. Conclusions are given in Sect. 5.

2 Instrumentation and dataset

The Raman polarization and water vapour lidar (52.2109° N, 20.9826° E, 112 m a.s.l.) is located at the Remote Sensing Laboratory (RS-Lab, https://www.igf.fuw.edu.pl/en/instruments, last access: 1 May 2019) of the Institute of Geophysics at the Faculty of Physics of the University of Warsaw, Poland. The location of the RS-Lab is shown in Fig. 1. The RS-Lab conducts observations as a part of the European Aerosol Research Lidar Network (EARLINET, https://www.earlinet.org, last access: 15 October 2019, Pappalardo et al., 2014) and provides regular measurements within the worldwide Polly.NET lidar network (http://polly.tropos.de/, last access: 23 September 2019, Baars et al., 2016) and within the National Aerosol Research Network PolandAOD-NET (http://www.polandaod.pl, last access: 15 October 2019, Supplement in Markowicz et al., 2016). The so-called "next generation PollyXT" lidar deployed in Warsaw was described in a great detail in Engelmann et al. (2016).

Since July 2013, the PollyXT lidar has performed quasi-continuous 24/7 observations. Powerful laser pulses (180, 110, and 60 mJ) at 1064, 532, and 355 nm are emitted coaxially and vertically, with a 20 Hz repetition frequency, into the atmosphere. Detection is performed with a Newtonian telescope at eight channels (so-called $2\alpha + 3\beta + 2\delta +$ WV), which enables the determination of the particle extinction coefficient profiles (α) at 532 and 355 nm, the particle backscatter coefficient profiles (β) at 1064, 532, and 355 nm, the linear particle depolarization ratio profiles (δ) at 532 and 355 nm, and the water vapour mixing ratio (WV). The signals at all channels are recorded up to 48 km with a standard 7.5 m vertical and 30 s temporal resolution. Measured signals are affected by an incomplete geometrical overlap between the emitted laser beam and the receiving telescope; therefore, the signals in the range below an altitude of 400 m are rejected from further evaluation. The overlap-range issue posed a first constraint on the selected dataset, i.e. constraining analyses to the summer and early-autumn (July–September) data. In winter, the atmospheric boundary layer height derived at noon and midnight from the radiosounding profiles was found often enough below the complete lidar's overlap range. Hence, in winter, within the range in which the divergent lidar laser beam is not fully received by the full field of view of the lidar telescope, the detection of the boundary layer height by lidar is limited. In contrast, in summer and early autumn, the boundary layer height is always above the complete lidar's overlap range; thus, it does not affect the derived profiles. Therefore, we restricted the analyses of the optical properties within the boundary layer to the latter period. Moreover, the analysis was restricted to the complete sets of profiles of aerosol properties (i.e. $2\alpha+3\beta+2\delta+$ WV) derived in 2013, 2015, and 2016, as for the above-mentioned period, for this site, it was feasible to obtain the highest number of quality controlled lidar profiles. They were then calculated and stored in the EARLINET/ACTRIS database.

Although the PollyXT lidar in Warsaw performs quasi-continuous 24/7 observations, the data cannot be obtained every single day. Unfavourable weather conditions (e.g. precipitation or thick low-level clouds) significantly limit the number of observations in spring and late autumn, and practically prevent observations in winter. Instrumental issues occur (e.g. technical failures), which are season independent but in some periods lasted several weeks or months. Finally, even if observations were performed, it was not always feasible to derive the aforementioned full sets of aerosol properties, e.g. due to overly strong background light at daytime or an overly low (high) aerosol load. Note that, for the July–September period of 2013, 2015, and 2016, no other site provided such a high number of complete sets of measurements within the EARLINET/ACTRIS database.

Quality-controlled profiles of optical properties are stored in the EARLINET/ACTRIS database (http://www.earlinet.org, last access: 15 October 2019). The statistical analysis covers profiles derived for EARLINET regular measurements (Mondays and Thursdays, ±2 h from zenith and sunset) and for dedicated measurements (e.g. diurnal cycles, special alert events). From the Warsaw site, only cloud-screened profiles evaluated using the classical Raman approach are feed into the database. The profiles obtained for lidar observations in July, August, and September of 2013, 2015, and 2016 were analysed (2014 was excluded from analyses due to that fact that the data availability was too sparse).

In total, 246 lidar profiles were collected for this study (denoted as contributing to "entire time"), 113 profiles were obtained for the "nocturnal time" (21:00–02:00 UTC), and 37 profiles were derived at sunrise (03:00–08:00 UTC) and 63 profiles at sunset (16:00–20:00 UTC), here defined as the "sunrise/sunset or transition time". The precise sunrise and sunset times are available at http://www.timeanddate.com/sun/poland/warsaw (last access: 5 May 2019). The analysis period is separated into three periods, because the change in atmospheric conditions is driven by different processes during the designated times; this allows for change in the aerosol optical properties to be investigated. Note, that only 29 profiles were available under daytime conditions (08:00–16:00 UTC), which was considered to be too low to consider the daytime category separately – thus, these profiles joined the entire time category. However, comparisons of the optical properties derived from the lidar and photometer measurements were carried out for a subset of daytime profiles (03:00–19:00 UTC).

A multi-filter rotating shadowband radiometer (MFR-7; Yankee Environmental Systems) was used for continuous passive measurements at the RS-Lab in the frame of the PolandAOD-NET network activities. The instrument operates at six narrow-band channels (415, 500, 615, 673, 870, and 940 nm) and one broadband channel. It measures direct, diffuse, and total solar radiation, from which the spectrally resolved aerosol optical depth is obtained. In situ calibration using the classic Langley approach is applied on a regular basis. Details on the instrument design and uncertainty analyses are reported in Harrison et al. (1994). Cloud-screened products used in this study are the $AOD_{CL}(415)$ and $AOD_{CL}(500)$, with uncertainty at the ± 0.025 level, and $ÅE_{CL}(415/500)$, with uncertainty at the ± 0.04 level. AOD_{CL} values less than 0.03 were excluded from the analyses.

A sun photometer (CE318; CIMEL Electronique) is operated at the Institute of Geophysics at the Polish Academy of Sciences (IGF-PAS) in the Observatory in Belsk (51.8366° N, 20.7916° E, 190 m a.s.l.), which is located 43.7 km south-west of the RS-Lab in Warsaw and provides the longest record of passive measurements in Poland. The same instrument was recently installed in the RS-Lab in Warsaw, and since January 2018 it has provided data to the AERONET database. Passive measurements of direct and diffuse solar irradiance and sky radiance at the Earth's surface at nine wavelengths in a spectral range from 340 to 1640 nm are used for retrieval of the AOD and ÅE. The data are calibrated once a year at the PHOTONS/AERONET-EUROPE calibration centre (http://loaphotons.univ-lille1.fr, last access: 3 September 2019) and processed by the Aerosol Robotic NETwork (AERONET, http://aeronet.gsfc.nasa.gov, last access: 15 October 2019, Holben et al., 1998). The Version 3 products (Giles et al., 2019) of AERONET Level 2.0 cloud-screened $AOD_{CL}(380)$ and $AOD_{CL}(500)$, with uncertainty at the ± 0.01 level, and $ÅE_{CL}(380/500)$, with uncertainty at the ± 0.03 level, were used. AOD_{CL} values less than 0.03 were excluded from the analyses. Note that, the AOD_{CL} data from MFR-7 and CE318 are scaled using the Ångström power law (Ångström, 1929; Iqbal, 1983) to match either one another or the lidar wavelength.

The sun photometer is located about 2 km from the village of Belsk, in a typical agricultural region with fertile soil and trees. Note that the AERONET data in Belsk were only used in the current study to check data consistency and only as an indicator that the free-tropospheric aerosol load existed above Warsaw and in its vicinity; therefore, sun-photometer data from Belsk do not contribute to the core results. Note that, the AERONET CE318 sun photometer is also operated (since January 2018) at the RS-Lab of the University of Warsaw. The data from the latter instrument, specifically the data for the intercomparison of AODs obtained with the co-located CE318 and MFR-7 instruments at the RS-Lab, constitute a vital part of the results.

Particulate matter concentrations for particles with an aerodynamic diameter of less than 2.5 and 10 µm (referred to as $PM_{2.5}$ and PM_{10} respectively) were measured at the air quality monitoring site of the Warsaw Regional Inspectorate for Environmental Protection (WIOS) in Ursynow, Warsaw, located 6.5 km from the RS-Lab. The daily and hourly averaged $PM_{2.5}$ and PM_{10} data are available at http://sojp.wios.warszawa.pl/raport-dobowy-i-roczny (last access: 15 October 2019). The data measurements conducted at the State Environmental Monitoring stations are gathered in the JPOAT 2.0 air quality database of the National Chief Inspectorate for Environmental Protection (GIOS). These official, calibrated datasets of $PM_{2.5}$ and PM_{10} are accessible at http://powietrze.gios.gov.pl/pjp/archive (last access: 15 October 2019). The measurement uncertainty is below 30 % for the hourly concentrations. Products used in this study are as follows: surface daily and hourly mean particulate matter concentrations for $PM_{2.5}$ and PM_{10}, and the fine-to-coarse mass ratio (FCMR) defined as $PM_{2.5} / (PM_{10} - PM_{2.5})$ (Zawadzka et al., 2013). A FCMR greater than 1.5 denotes "fine particle" domination (diameter < 2.5 µm); a FCMR less than 0.5 means "coarse particle" domination (diameter between 2.5 to 10 µm). FCMR values between 0.5 and 1.5 indicate that fine and coarse particles are distributed approximately equally.

The temperature, pressure, relative humidity, wind speed, and wind direction at the surface (p, T, RH, V, and Vdir), were measured by the WXT510 (Vaisala) weather transmitter mounted on the roof platform of the RS-Lab at 21 m above the ground's surface. The atmospheric pressure, temperature, and relative humidity profiles were obtained from the RS92 (Vaisala) radiosonde launched at two World Meteorological Organization sites located in Poland: WMO 12374 station in Legionowo (52.40° N, 20.96° E, 96 m a.s.l., 25 km north of Warsaw) and WMO 12425 station in Wroclaw (51.78° N, 16.88° E, 122 m a.s.l., 300 km south-west of Warsaw). The noon and midnight radiosounding profiles (launch at 11:15 and 23:15 UTC respectively, with a duration of circa 1.5 h) were visualized and downloaded from the University of Wyoming Upperair Air Data website (http://weather.uwyo.edu/upperair/sounding.html, last access: 27 August 2019).

Note that the shadowband radiometer-derived and the sun-photometer-derived AOD and the in situ measured PM concentration values are averaged so as to correspond to the time of the lidar-derived optical profiles available for given period for the Warsaw site in the EARLINET/ACTRIS database. Moreover, the MFR-7 and CE318 instruments only collected data at daytime. The measurement sites are shown in Fig. 1. The PM site is located in the residential suburb of Ursynow. The RS-Lab is located at the university campus in the suburb of Ochota, which is shrouded by green parks. Between the three sites Ochota and Ursynow (in Warsaw) and Belsk, there are no industrial pollution sources and the anthropogenic pollution in summertime is related to traffic (Zawadzka et al., 2013).

3 Methodology of lidar product retrieval

The atmospheric boundary layer is regarded as the lowest layer of the troposphere; it is directly influenced by the Earth's surface and reacts quickly to the surface forcing (Stull, 1988). The atmospheric boundary layer height (ABLH) can be derived from the lidar elastic-scattering aerosol backscatter signal, which relies on a higher aerosol load within the boundary layer than in the free troposphere. Dang et al. (2019) recently summarized the available methods for ABLH retrievals. The limitations and capabilities of mixing height retrieval algorithms for different lidar and ceilometer systems were investigated by Haeffelin et al. (2012). Comerón et al. (2013) discussed the wavelet correlation transform method and the gradient method for the determination of the ABLH by lidar. Stachlewska et al. (2012) used the latter method for the first retrievals of the ABLH in Warsaw. Wang et al. (2019) reported that the wavelet covariance transform method (WCT) is the most optimal technique for ABLH retrieval for the PollyXT lidar data in Warsaw. As for the WCT method applied in our study, the covariance transform W_f of the Haar wavelet function h, is defined as in Eq. (1):

$$W_f(a,b) = \frac{1}{a}\int_{z_1}^{z_2} P(z)\cdot h\left(\frac{z-b}{a}\right)\mathrm{d}z,$$

$$h\left(\frac{z-b}{a}\right) = \begin{cases} +1 & b-\frac{a}{2} \le z \le b \\ -1 & b \le z \le b+\frac{a}{2} \\ 0 & \text{elsewhere} \end{cases}, \tag{1}$$

where $P(z)$ is the lidar elastic signal, z_1 and z_2 are the respective lower and upper limits of the signal, z is the altitude, and a and b are the dilation and the centre of the Haar wavelet function respectively. The WCT calculations were carried out with the dilation of 30 range bins applied on signals averaged over 7.5 m and 30 min, and the ABLH was derived at all three elastic wavelength signals (355, 532, and 1064 nm) and then averaged for a final result.

Aerosol optical properties can be derived in different ways. The Cloud-Aerosol Lidar and Infrared Pathfinder Satellite Observation (CALIPSO) can provide the range-resolved profiles of aerosol and clouds (Winker et al., 2007). The combined ground-based lidar and cloud radar is capable of obtaining the vertical structure of cloud and aerosol properties (e.g. Delanoë and Hogan, 2008). The high spectral resolution lidar technique allows for the separation of molecular and aerosol signals (e.g. Grund and Eloranta, 1991; Burton et al., 2012). The aerosol and cloud information can be retrieved by multi-wavelength Raman lidars (e.g. Müller et al., 2007; Giannakaki et al., 2010; Alados-Arboledas et al., 2011; Baars et al., 2016; Lolli et al., 2018; Ansmann et al., 2018). The latter lidar technique was used for this study.

Lidar signals stored in the EARLINET/ACTRIS database were evaluated using the classical Raman retrieval approach. The particle extinction coefficient profiles at 355 and 532 nm were calculated from the so-called Raman lidar equation using the Rayleigh law for molecules and the Ångström power law (usually with ÅE = 1) for aerosol particles. The particle extinction coefficient (α_p) was derived as in Eq. (2):

$$\alpha_p = \frac{\frac{\mathrm{d}}{\mathrm{d}z}\left(\ln\left(\frac{N}{P_N z^2}\right)\right) - \alpha^m_{\lambda_0} - \alpha^m_{\lambda_N}}{1+\left(\frac{\lambda_0}{\lambda_N}\right)^k}, \tag{2}$$

where N denotes the molecular number density of the nitrogen, λ_0 is the emitted wavelength (355 or 532 nm), λ_N is the wavelength of the nitrogen channel (387 or 607 nm), P_N is the Raman signal at the nitrogen channel, z is the distance from the lidar, $\alpha^m_{\lambda i}$ ($i = 0, N$) is the molecular extinction coefficient at the emitted or the nitrogen wavelength, and k is the wavelength dependence of particle.

The particle backscatter coefficient profiles (β_p) at 355, 532, and 1064 nm are derived with the use of the obtained particle extinction coefficient profiles at 355 and 532 nm (utilized for both larger wavelengths) and calibrated at the height range free of aerosol. More details on the exact procedure are given in Baars et al. (2016).

The linear particle depolarization ratio (δ_p) was derived as the ratio of the cross channel and the corresponding total channel at the same wavelength, using Eq. (3):

$$\delta_p = \frac{(1+\delta_m)\,\delta_v\left(1+\frac{\beta_p}{\beta_m}\right) - (1+\delta_v)\,\delta_m}{(1+\delta_m)\left(1+\frac{\beta_p}{\beta_m}\right) - (1+\delta_v)}, \tag{3}$$

where δ_v is the linear volume depolarization ratio, δ_m is the linear depolarization ratio of air molecules, and β_m is the molecule backscatter coefficient. The procedure for the ±45 depolarization calibration is used as in Engelmann et al. (2016).

The water vapour mixing ratio (WV) was obtained as the ratio of the Raman water vapour channel and the Raman nitrogen channel, as described in Stachlewska et al. (2017a), using Eq. (4):

$$\mathrm{WV} = C\frac{P_{\lambda_{\mathrm{H_2O}}}}{P_{\lambda N}}\exp\left(-\left(\alpha\left(\lambda_{\mathrm{H_2O}}\right)-\alpha\left(\lambda_{\mathrm{N}}\right)\right)\right), \tag{4}$$

where $P_{\lambda N}$ is the Raman backscatter signal of the nitrogen channel wavelength $\lambda_{\mathrm{N}} = 387$ nm, $P_{\lambda_{\mathrm{H_2O}}}$ is the Raman backscatter signal of water vapour channel wavelength $\lambda_{\mathrm{N}} =$ 407 nm, and C is the calibration constant.

For all analysed data products, low- and mid-altitude clouds are screened prior to the retrieval. The sets of profiles (α_{p}, β_{p}, and σ_{p}) were averaged over the same time interval, which was either 60 min (60 %), 45 min (23 %), or 30 min (17 % of profiles used), depending on the variability of the atmospheric conditions and the signal-to-noise ratio. Iarlori et al. (2015) reported that smoothing procedures can affect the features of the lidar signal profile. For the EARLINET/ACTRIS database, we store the files with profiles smoothed with the running mean over 49 (b-file) and 101 (e-file) range bins (length of a single range bin is 7.5 m), which were found to be optimal for the PollyXT lidar data products derived at the Warsaw site. Typically, the α_{p} profiles need higher smoothing than β_{p} and δ_{p} profiles. However, we keep two versions of the smoothed profiles in the database. In this paper, the profiles smoothed over 49 range bins were used. Keeping the smoothing at the same level is not only advantageous for the error estimations and the profile comparisons but also for the microphysical parameter inversion (Janicka et al., 2017). The profiles of the WV were averaged over 30–60 min and 60 m with no smoothing applied. With respect to the lidar retrieval, the atmospheric profiles obtained by radiosounding at Legionowo or Wroclaw were used depending on the approaching direction of the air mass transport.

After the ABLH was determined, the mean values of different optical properties within the boundary layer were derived. For the incomplete overlap region, data in the lowermost altitude range required special treatment. The lowest value of the available particle extinction coefficient was assumed to be representative down to the ground surface, which is the commonly accepted approach in lidar studies, e.g. Matthias et al. (2004). Therefore, the mean extinction coefficient of the entire ABL was obtained by extrapolating the extinction profile using this value down to the ground. Similarly, the mean backscattering coefficient and the particle depolarization ratio of the ABL were extrapolated. Although the δ profiles can be derived almost to the ground, for the EARLINET/ACTRIS database profiles are only stored down to 400 m, so that extrapolation was also required here. The water vapour mixing ratio profiles were also extrapolated, from 100 m down to the ground. The WV profiles were calculated using the ratio of two signals at the 407 and 387 nm Raman channels. The overlap term of those two channels (which is close in spectral range – only 20 nm) practically cancels when calculating their ratio. Similarly, for the particle depolarization ratio (the cross and total ratio at the same wavelength), the overlap term also cancels. Therefore, the water vapour (and the depolarization ratio profile) can be obtained almost down to the ground. The water vapour nighttime detection in July–September is typically performed from 20:00 to 04:00 UTC; thus, only the data corresponding to the nocturnal time (21:00 to 02:00 UTC) were analysed.

Within the ABL, the vertical distribution of the lidar ratio ($\mathrm{LR_{ABL}}$) was derived as a ratio of the aerosol extinction to backscatter coefficient profiles at 355 and 532 nm ($\mathrm{LR} = \alpha_{\mathrm{p}}/\beta_{\mathrm{p}}$), and then the mean $\mathrm{LR_{ABL}}$ was calculated.

The vertical distribution of the Ångström exponent $\mathrm{ÅE_{ABL}}$(355/532) was computed by using the profiles of the aerosol extinction coefficient (not AOD) at 355 and 532 nm; the mean $\mathrm{ÅE_{ABL}}$ was then calculated using Eq. (5):

$$\mathrm{ÅE} = -\frac{\ln\left(\frac{\alpha_{\mathrm{p}}(\lambda_1)}{\alpha_{\mathrm{p}}(\lambda_2)}\right)}{\ln\left(\frac{\lambda_1}{\lambda_2}\right)}. \tag{5}$$

The aerosol optical depth within the boundary layer ($\mathrm{AOD_{ABL}}$) was calculated by integrating the extrapolated (to the ground) aerosol extinction profile at 355 and 532 nm from the height of $z_1 = 0$ to the height of the top of the boundary layer $z_2 = \mathrm{ABLH}$, as in Eq. (6):

$$\mathrm{AOD} = \int_{z_1}^{z_2} \alpha_{\mathrm{p}} \mathrm{d}z. \tag{6}$$

There is a threshold set on the mean values of an $\mathrm{AOD_{ABL}}$(355) of less than 0.05 and an $\mathrm{AOD_{ABL}}$(532) of less than 0.03 within the lowermost 1 km, i.e. the aerosol extinction coefficient profiles are extrapolated according to the AOD threshold for each wavelength. If the AOD within 1 km is below the threshold, re-extrapolation is applied from a range bin just above the initially chosen one down to the ground in an iterative manner until the AOD values within 1 km meet the above-mentioned thresholds.

Stachlewska et al. (2018) reported the uncertainty of the $\mathrm{AOD_{ABL}}$ at 355 and 532 nm derived from the Raman extinction coefficient profiles as being less than 20 %, the uncertainty of $\mathrm{LR_{ABL}}$ derived by extinction-to-backscattering coefficient ratios at 355 and 532 nm as less than 35 %, and the uncertainty of δ_{ABL} at 355 and 532 nm as less than 20 % of the derived value. The uncertainty of extinction-derived $\mathrm{ÅE_{ABL}}$(355/532) is less than 30 %. The uncertainty of the ABLH retrieval from PollyXT lidar is ±70 m (Wang et al., 2019).

Finally, we attempt to interpret the aerosol measured within the boundary layer during the specified observational period over Warsaw. A number of publications have highlighted aerosol studies that use backward trajectories to interpret the possible aerosol source/type based on optical properties of observed aerosol and on the origin of air masses containing aerosol (e.g. Dörnbrack et al., 2010; Mona et al.,

Table 1. Literature review based on the values of the lidar-derived particle optical properties used for the interpretation of aerosol measured over the RS-Lab in Warsaw. The listed properties are assessed in each aerosol layer based on a manual approach in combination with case-to-case air mass transport analyses.

	LR (sr)		δ (%)		ÅE	RH	Air mass	No. of cases
	355	532	355	532	(355/532)	(%)	transport*	(in the ABL) (%)
Anthropogenic pollution	50–65	33–72	3–6	3–11	0.7–1.8	50–90	Local (Warsaw), advective (western Europe)	151 (61 %)
Biomass burning	50–95	60–90	2–6	4–12	0.8–2.0	60–80	Advective (eastern Europe, North America)	34 (14 %)
Pollen	50–75	46–69	5–17	6–20	–	< 50	Local	16 (7 %)
Arctic marine	16–30	18–26	1–7	1–11	−0.6–0.7	–	Advective (Arctic, subarctic)	14 (5 %)
Dust	50–70	45–65	24–29	25–43	0.1–1.5	20–40	Advective (Africa)	0
Undefined Mixtures								31 (13 %)

* Calculations of up to 10-day backward trajectories for aerosol layers in the free troposphere and in the boundary layer, and the assessment of possible sources of aerosol by interpreting them against satellite data (MODIS, MSG, and CALIPSO) and model outputs (NAAPS).

2012; Nemuc et al., 2014; Burton et al., 2015; Granados-Muñoz et al., 2015; Jung et al., 2016; Papagiannopoulos et al., 2016; Schmeisser et al., 2017; Szkop and Pietruczuk 2017; Ansmann et al., 2018; Di Biagio et al., 2018; Horvath et al., 2018; Foth et al., 2019). In this paper, the analysis was undertaken in a standard manner, case by case, based on the comparison of aerosol optical properties (LR, δ, ÅE, and RH) with the values reported in the literature (an excellent review of these values is provided by e.g. Nicolae et al., 2018), as well as by using the HYbrid Single-Particle Lagrangian Integrated Trajectory (HYSPLIT) model to calculate trajectories (Stein et al., 2015). The 246 profiles analysed were checked against the 3–10 day backward trajectories obtained in the boundary layer and the free troposphere, starting at altitudes of 0.5, 1.2, and 3 km, applied on the Global Data Assimilation System (GDAS) and CDC1 meteorological data (trajectories are available via the PolandAOD-NET website). We assessed possible aerosol sources by inspecting the trajectories and the aerosol optical properties against the satellite data, i.e. from the Moderate Resolution Imaging Spectroradiometer (MODIS), the Spinning Enhanced Visible and Infrared Imager (SEVIRI), and the Cloud-Aerosol Lidar and Infrared Pathfinder Satellite Observations (CALIPSO), and model outputs, i.e. the Navy Aerosol Analysis and Prediction System (NAAPS), http://www.nrlmry.navy.mil/aerosol, last access: 4 May 2019), as described by Stachlewska et al. (2018).

Roughly speaking, a LR greater than 75 sr can indicate the existence of aerosol particles related to biomass burning, values between 40 and 50 sr can indicate mineral dust, values between 50 and 60 sr can indicate anthropogenic pollution, and values between 20 and 30 sr can indicate Arctic marine particles, although these values depict an ideal case (a pure aerosol type rarely exists) and the values overlap for the different aerosol species, as indicated in Table 1.

The particle linear depolarization ratio (δ_p) can be used as a tracer of spherical and non-spherical particles: the low values ($\delta < 0.01$) can be regarded as being due to very small spherical particles (e.g. pollution); δ values between 0.2 and 0.35 can be regarded as beng due to dust (polluted dust values are lower – even as low as 0.1); δ values between 0.04 and 0.08 can be regarded as characteristic of biomass burning aerosol, values of approximately 0.1 indicate pollen, and a value less than 0.2 indicates urban pollution. Also here, values can overlap for the different aerosol species, as indicated in Table 1.

The Ångström exponent (ÅE) can be used as an indicator of the size of atmospheric aerosol particles. ÅE values of less than or equal to 1 indicate particle size distribution dominated by the coarse-mode aerosol (radii ≥ 0.5 µm, here referred to as "large particles") that are typically associated with dust and sea salt particles (Perrone et al., 2014). ÅE values greater than or equal to 1.5 indicate size distributions dominated by the fine-mode aerosol (radii < 0.5 µm, here referred to as "small particles") that are associated with urban pollution (Perrone et al., 2014). ÅE values between 1 and 1.5 belong to the accumulation mode (here referred to as "medium-size particles") and are associated with biomass-burning aerosol (Janicka et al., 2017). The use of the ÅE nomenclature with respect to small, medium, and large particles is for clarity, as not to confuse them with the fine-to-coarse mass ratio (FCMR).

For brevity, hereafter the α_p, β_p, and δ_p are denoted as α, β, and δ.

Table 2. Mean values of the aerosol optical properties with standard deviations derived within the atmospheric boundary layer (ABL) from the PollyXT lidar at the EARLINET site, Warsaw, for measurements at 355 and 532 nm conducted for the July–September period of 2013, 2015, and 2016. Symbols denote the particle extinction coefficient (α), the particle backscatter coefficient (β), the aerosol optical depth (AOD), the lidar ratio (LR), the linear particle depolarization ratio (δ), the Ångström exponent (ÅE), and the atmospheric boundary layer height (ABLH). Mean values are obtained for different times of the day with respect to the boundary layer type.

	λ (nm)	α_{ABL} (Mm^{-1})	β_{ABL} ($Mm^{-1}sr^{-1}$)	AOD_{ABL}	LR_{ABL} (sr)	δ_{ABL}	$ÅE_{ABL}$	ABLH (km)
Entire time (ET)								
WML, RL, MTL (246 cases)	355 532	142 ± 68 83 ± 43	3.1 ± 1.2 2.2 ± 0.7	0.20 ± 0.10 0.11 ± 0.06	48 ± 17 41 ± 15	0.02 ± 0.01 0.05 ± 0.01	1.54 ± 0.37	1.33 ± 0.36
Nocturnal time (NT) (21:00–02:00 UTC)								
NL (113 cases)	355 532	129 ± 56 69 ± 39	3.0 ± 1.1 1.9 ± 0.7	0.11 ± 0.04 0.07 ± 0.02	44 ± 12 38 ± 12	0.02 ± 0.01 0.05 ± 0.01	1.58 ± 0.36	0.76 ± 0.12
RL (105 cases)	355 532	137 ± 53 75 ± 37	3.1 ± 1.0 2.3 ± 1.0	0.18 ± 0.08 0.11 ± 0.05	47 ± 15 40 ± 13	0.02 ± 0.01 0.04 ± 0.01	1.61 ± 0.38	1.34 ± 0.17
Transition time (TT) during sunrise (03:00–08:00 UTC) and sunset (16:00–20:00 UTC)								
MTL (37 cases)	355 532	128 ± 54 73 ± 35	3.8 ± 1.1 2.3 ± 0.6	0.11 ± 0.03 0.06 ± 0.02	37 ± 14 32 ± 13	0.02 ± 0.01 0.04 ± 0.01	1.53 ± 0.30	0.70 ± 0.10
WML (63 cases)	355 532	163 ± 63 96 ± 49	2.8 ± 1.1 1.9 ± 0.8	0.24 ± 0.01 0.14 ± 0.05	55 ± 18 49 ± 16	0.02 ± 0.01 0.05 ± 0.02	1.37 ± 0.34	1.60 ± 0.38

4 Results and discussion

Table 2 shows the mean particle extinction coefficient (α), the particle backscatter coefficient (β), the aerosol optical depth (AOD), the lidar ratio (LR), the linear particle depolarization ratio (δ), and the Ångström exponent (ÅE) derived at the 355 and 532 nm channels within the atmospheric boundary layer (ABL) for the entire (ET), nocturnal (NT), and transition (TT) times obtained for the July–September measurement period of 2013, 2015, and 2016. Different mechanisms govern the sunrise and sunset conditions; the first is driven by the development of the convective boundary layer; the latter lessens the convection which causes more stratification within the residual layer (RL). Thus, the ABLH algorithm developed determines the atmospheric boundary layer top as a morning transition layer (MTL), a well-mixed layer (WML), a nocturnal layer (NL), and/or a residual layer (RL).

The mean entire time (24 h) ABLH was 1.33 ± 0.36 km for July–September of 2013, 2015, and 2016. Wang et al. (2019) reported that the decadal mean ABLH over Warsaw in summer was 1.34 ± 0.15 km based on the 10-year dataset. This indicates that, in terms of the ABLH, the dataset analysed can be regarded as representative of the long-term analysis. The mean values of the α_{ABL}, AOD_{ABL}, and LR_{ABL} calculated at the two wavelengths in the transition time are higher during the sunset period (WML) and lower during the sunrise period (MTL), the latter being similar to the NL. The mean $ÅE_{ABL}$ in the given periods was high (1.37–1.61, in Table 2), indicating small particles. (Later on, we will show that the $ÅE_{ABL}$ values ranged between 0.7 and 2.9 for the nocturnal period, whereas the range narrowed to 0.8–2.2 in the sunrise/sunset period.)

The frequency distribution plots for the AOD_{ABL}, LR_{ABL}, and $ÅE_{ABL}$ derived at 355 and 532 nm, and the FCMR derived for $PM_{2.5}$ and PM_{10} for the entire, nocturnal, and sunrise/sunset periods are shown in Fig. 2. The mean AOD_{ABL} mainly ranges from 0.1 to 0.3: 80 % of the occurrences are attributed to $AOD_{ABL}(355)$ in the 0.1–0.3 range and $AOD_{ABL}(532)$ of below 0.2. The mean $LR_{ABL}(355)$ and $LR_{ABL}(532)$ values mainly range from 30 to 70 sr, which accounts for more than 75 % of total data. The majority of the $ÅE_{ABL}(355/532)$ values are between 1.0 and 2.0 (more than 90 % of the total data), which indicates mid-sized and small particles (≤ 500 nm) within the boundary layer. The FCMR values between 0.5 and 1.5 constitute around 70 % of the total data, indicating a more or less equal distribution of fine and coarse particles with a size between 2.5 and 10 µm at the surface. Most of the AOD_{ABL} in the MTL is below 0.2, and the LR_{ABL} in the MTL ranges from 25 to 50 sr at both wavelengths. The δ_{ABL} in the MTL between 0.04 and 0.06 accounts for around 50 % of occurrences. The fine particles are expected in the MTL, as the majority of the FCMR values are above 1.5.

Amiridis et al. (2005) reported a 4-year mean AOD_{ABL} of 0.44 ± 0.16 at 355 nm and a mean LR_{ABL} of 49 ± 25 at 355 nm in summer at Thessaloniki, Greece. According to Papayannis et al. (2008), this much higher value of $AOD_{ABL}(355)$ can be attributed to a significantly stronger impact from the

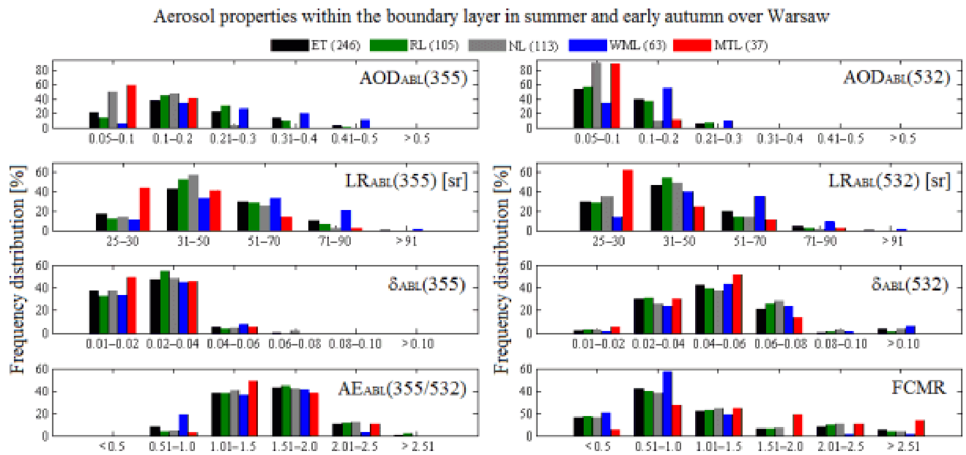

Figure 2. Frequency distribution of the aerosol optical depth (AOD), the lidar ratio (LR), the linear particle depolarization ratio (δ), and the Ångström exponent (ÅE) at 355 and 532 nm derived within the atmospheric boundary layer at the EARLINET/ACTRIS lidar site, Warsaw, for the July–September period of 2013, 2015, and 2016. The corresponding fine-to-coarse mass ratio (FCMR) derived from measurements of surface particulate matter with an aerodynamic diameter below 10 µm (PM_{10}) and below 2.5 µm ($PM_{2.5}$) at the WIOS site in Ursynow, Warsaw. The period of measurement is divided into the following time spans: the entire time (ET; 24 h); the nocturnal time (NT), between 22:00 and 02:00 UTC – including the residual boundary layer (RL) and the nocturnal boundary layer (NL); and the transition time (TT), after sunrise between 03:00 and 08:00 for the morning transition layer (MTL) and before sunset between 16:00 and 20:00 UTC for the well-mixed boundary layer (WML).

summertime Saharan dust events on Thessaloniki than on Warsaw. Sicard et al. (2011) reported a low AOD_{ABL} of 0.07 ± 0.02 at 532 nm in north-eastern Spain, and attributed it to the influence of the sea breeze on the Barcelona area. Mattis et al. (2004) reported a 3-year mean $AOD_{ABL}(355)$ of 0.38 and a $AOD_{ABL}(532)$ of 0.18 for Leipzig, with a mean $LR_{ABL}(355)$ of 58 sr and a $LR_{ABL}(532)$ of 53 sr, and a mean $ÅE_{ABL}(355/532)$ of 1.4. However, the $ÅE_{ABL}$ was between 1.8 and 2.2 in the upper boundary layer during summer in Leipzig (Matthias et al., 2004); thus, only slightly larger particles are observed in the ABL in Warsaw during summer compared with Leipzig. Using Raman lidar observations at 10 EARLINET stations, Matthias et al. (2004) derived the lowest AOD_{ABL} values in northwestern Europe (Aberystwyth) and the highest values in southeastern Europe (Athens), which was again attributed to the impact of Saharan dust events on the aerosol distribution in southern Europe.

The lidar ratio was used for the aerosol type characterization in various aerosol typing algorithms (e.g. Papagiannopoulos et al., 2018; Nicolae et al., 2018). Alados-Arboledas et al. (2011) reported lidar ratios for a fresh biomass-burning pollution plume of 60–65 sr at 355 and 532 nm at Granada. Müller et al. (2007) reported lidar ratios of 45–60 sr with a mean value of 53 sr at 532 nm, and a particle depolarization ratio at 532 nm of below 0.05 for Leipzig, under local and regional urban and anthropogenic haze conditions. Amiridis et al. (2005) reported a continental aerosol 4-year mean lidar ratio of 40–47 sr at 355 nm for Thessaloniki, and Giannakaki et al. (2010) reported a biomass-burning aerosol 7-year mean lidar ratio of 70 sr at 355 nm. Optical properties of eight aerosol types were derived by Burton et al. (2012) over North America for urban aerosol (lidar ratio of 53–70 sr at 532 nm with a particle depolarization ratio of 0.03–0.07) and for smoke particles (lidar ratio of 33–46 sr with a particle depolarization ratio of 0.04–0.09). A lidar ratio of marine particles of 20–26 sr at 532 nm was found in North Atlantic and the tropical Indian Ocean by Müller et al. (2007), and Masonis et al. (2003) reported a value of 25 ± 4 sr at 532 nm in Hawaii. Dawson et al. (2015) presented a global mean lidar ratio for marine aerosol of 26 sr, with a range from 22 ± 7 to 32 ± 17 sr, depending on variation of the mean ocean surface wind speed. Haarig et al. (2017) reported lidar ratios varying from 19 to 27 sr at 355 nm and 23 to 25 sr at 532 nm for marine particles, and a particle depolarization ratio of between 0.05 and 0.12 sr at 355 nm and 0.07 and 0.15 sr at 532 nm. A review of aerosol types reported by Groß et al. (2013, 2015) includes a classification scheme based on the following values: the lidar ratio for the marine particles varies from 16 to 30 sr at 355 nm and 18 to 26 sr at 532 nm; biomass burning aerosol ranges from 50 to 95 sr at 355 nm and 60 to 90 sr at 532 nm; mineral dust ranges from 50 to 70 sr at 355 nm and 45 to 65 sr at 532 nm; and anthropogenic pollution ranges from 50 to 65 sr at 355 nm and 50 to 60 sr at 532 nm. In the current study, LR_{ABL} values in the range of 25–30 sr at both wavelengths were obtained in several cases (Fig. 2), and were interpreted as likely being due to the transport of a clean air mass of Arctic marine particles injected into the boundary layer in Warsaw during the analysis period. Such cold air masses can be transported from the Arctic to eastern Europe (Costa-Surós et al., 2015).

The linear particle depolarization ratio is an indicator of non-spherical particles (Ansmann et al., 2009; Sakai et al., 2010; Gasteiger and Freudenthaler, 2014). The total depolarization ratio in dust episodes have been reported to be above 0.2, whereas anthropogenic pollution aerosol have a total depolarization ratio below 0.1 (Xie et al., 2008; Nemuc et al., 2013). Heese and Wiegner (2008) reported a particle depolarization ratio for dust (~ 0.25) and biomass-burning aerosol (< 0.1) over Sahel (West Africa). Particle depolarization ratios of dust particles in the range of 0.1–0.25 were reported in Leipzig (Matthias et al., 2004), whereas values of 0.3–0.35 were found at Ouarzazate, Morocco (Freudenthaler et al., 2009). The particle depolarization ratios of urban haze and fire smoke have been reported to be less than 0.05 at different sites (Müller et al., 2007). A linear particle depolarization ratio for marine aerosol, in the range from 0.01 to 0.03, was reported by Groß et al. (2011). In the current study, the δ_{ABL} values obtained (shown in Fig. 2) are within the range of the values listed above, characterizing different aerosol types. As δ is sensitive to the size of the sensed non-spherical particles, small particles (< 300 nm) sensed with a wavelength that is twice as large (532 nm) can be under the limit of detection (as seen in Fig. 2). The dust cases detected in the free troposphere during the given measurement period in Warsaw (e.g. Janicka et al., 2017) were excluded from the current analyses (four cases); however, the derived δ values of the entire observation time are less than 0.1, which means that there were no cases of dust particles being deposited or advected into the ABL, although the existence of polluted dust cannot be entirely excluded.

Overall, during the July to September period of 2013, 2015, and 2016 in Warsaw, the aerosol within the ABL consisted mainly of the following: (i) urban anthropogenic pollution of local origin or pollution transported from areas below or above of the Czech Republic via Silesia and/or Germany (61 %), and its mixtures with (ii) grass and peatland biomass-burning aerosol transported from Russia, the Ukraine, and Belarus (14 %), (iii) pollen emissions of strictly local origin from Warsaw's semi-natural green parks (7 %), and (iv) Arctic marine particles transported mainly from the Arctic over the Baltic Sea (5 %). For the remaining cases, the aerosol composition was regarded as being due to a mixture of more than two subcomponents (13 %), and was consequently not interpreted. The percentages given were derived by relating the number of profiles with an estimated origin to the total number of profiles, and are therefore given without uncertainties. No significant contribution of mineral dust into the boundary layer was found for the 246 profiles analysed, although transport pathways from the Sahara over the Iberian Peninsula or via Italy were identified for the upper troposphere.

For the co-located, simultaneous Raman lidar measurements and the shadowband radiometer measurements, we assessed the AOD_{ABL} contribution within the boundary layer to the AOD_{CL} within the column of air, keeping in mind that such co-located measurements never sample an identical section of air (lidar sampling in the zenith position vs. radiometer sampling at angles related to sun's elevation over the horizon). To make sure that the columnar measurements with the less commonly used (in the lidar community) shadowband radiometer do provide high quality data products, an intercomparison of the MFR-7 shadowband radiometer (PolandAOD-NET, Level 1.5 data, 415 nm and 500 nm) and the CE318 sun photometer (AERONET, Version 3, Level 2.0 data, 380 and 500 nm) was performed. The use of the above-mentioned level of data for both networks refers to clear-sky, manually cloud screened data products that have been calibrated within the past 12 months. One month of co-located daytime (03:00–19:00 UTC) measurements in July 2018 at the RS-Lab in Warsaw was chosen for the intercomparison and confirmed the high quality of the measurements performed using both instruments. Figure 3 shows high correlation coefficients ($R = 0.98$) and low standard deviations ($STD = 0.02$) for 144 data points obtained at 380 and 500 nm for the intercomparison of the CE318 and the MFR-7. Note that the AOD_{CL} value at 415 nm from the MFR-7 was scaled to the value at 380 nm (corresponding to CE318 wavelength) using the Ångström power law (Fig. 3).

Figure 4 shows the daytime mean 30–60 min average of the aerosol optical depth within the atmospheric boundary layer, AOD_{ABL}, at 355 and 532 nm, calculated from the mean extinction coefficient profiles of the EARLINET PollyXT lidar in Warsaw and the columnar daytime mean 1 h average (with a threshold of at least five data points) of the AOD_{CL} at 415 and 500 nm (scaled to lidar wavelengths) derived from the PolandAOD-NET MFR-7 shadowband radiometer measurements in Warsaw. Note that the AOD_{CL} values of the CE318 in Belsk were in good agreement with Warsaw results, with Belsk values being slightly lower than those in Warsaw (compare values in Table 3). Figure 4 also depicts the extinction-derived $ÅE_{ABL}$(355/532) of the lidar and the $ÅE_{CL}$(355/532) computed from the (scaled) shadowband radiometer AOD_{CL}. Products presented in Fig. 4 were derived for the July–September period of 2013, 2015, and 2016, for a subsample of cases when all three instruments were conducting observations at the same time (i.e. 41 cases).

In Table 3, the CE318-derived mean AOD is 0.41 ± 0.17 at 355 nm and 0.23 ± 0.09 at 532 nm, the MFR-7-derived mean AOD is 0.45 ± 0.17 at 355 and 0.25 ± 0.11 at 532 nm, and the PollyXT-derived mean AOD_{ABL} is 0.20 ± 0.06 at 355 and 0.13 ± 0.03 at 532 nm, for the 41 points. The columnar AOD_{CL} values of the two instruments are the same within

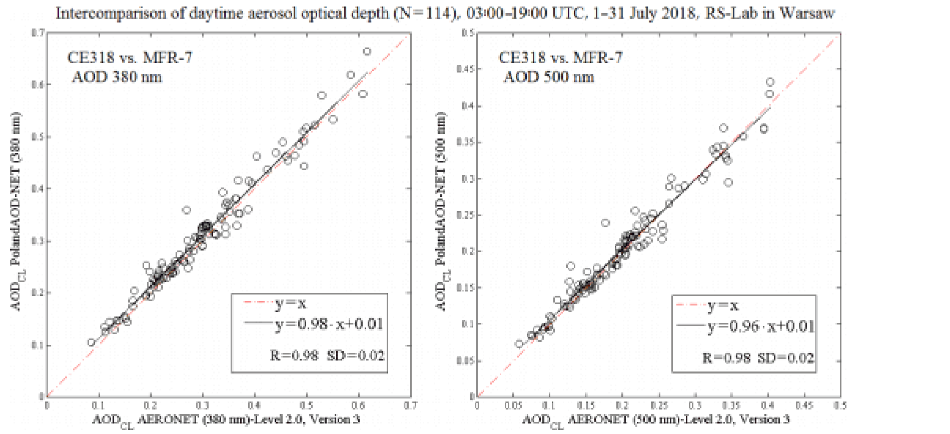

Figure 3. Intercomparison of hourly averaged clear-sky daytime aerosol optical depth measured within the atmospheric column (AOD_{CL}) with the CE318 instrument at the AERONET site in Warsaw (Version 3 Level 2.0 data) and the MFR-7 shadowband radiometer at the PolandAOD-NET site in Warsaw (Level 1.5 data). Note the high agreement obtained for both wavelengths for a month (July 2018) of co-located measurements (instruments at a distance of 3 m and at the same altitude) at the RS-Lab in Warsaw. The AOD_{CL} at 415 nm from the MFR-7 was scaled to 380 nm using the Ångström power law.

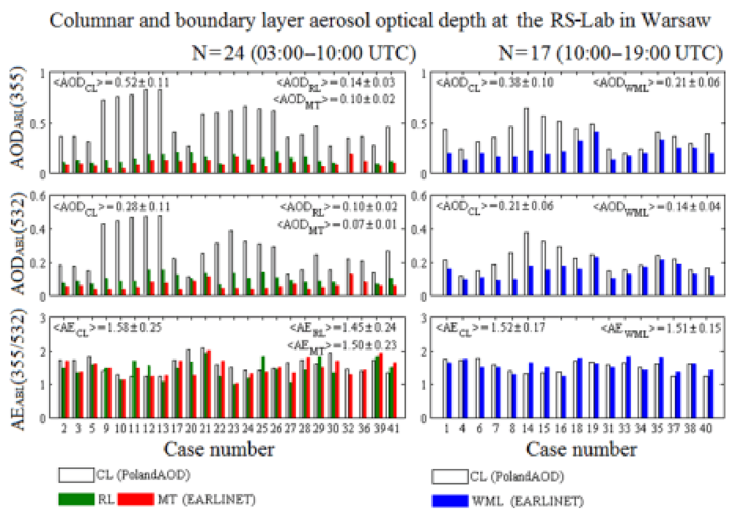

Figure 4. Hourly averages of the aerosol optical depth (AOD) and the Ångström exponent (ÅE) derived within the atmospheric boundary layer at 355 and 532 nm from the PollyXT lidar at the EARLINET/ACTRIS site, Warsaw, plotted along with the corresponding MFR-7 shadowband radiometer values from the PolandAOD-NET site, Warsaw, for July–September 2013, 2015, and 2016 (leap year). These were co-located measurements at the RS-Lab in Warsaw. The AOD_{CL} from the MFR-7 measurements at 415 and 500 nm were scaled to 355 and 532 nm using the Ångström power law.

the given uncertainty range, despite the 43.7 km distance between the two sites (Warsaw and Belsk). It can be expected that the AOD_{ABL} is less than the AOD_{CL} (e.g. Sicard et al., 2011; Szczepanik and Markowicz, 2018). The results obtained indicate that the mean values of the AOD_{ABL} are twice as large as the mean values of the AOD_{CL}. The high contribution of the aerosol load in the free troposphere can be related to the summertime long-range transport of the

Table 3. The mean daytime (03:00–19:00 UTC) aerosol optical depth (AOD) and Ångström exponent (ÅE) with standard deviations derived within the atmospheric boundary layer at 355 and 532 nm from the PollyXT lidar at the EARLINET site, Warsaw, and in atmospheric column measured by the MFR-7 shadowband radiometer (415 and 500 nm) at the PolandAOD-NET site, Warsaw. For reference, the mean values derived from Version 3 Level 2.0 CE318 CIMEL (380 and 500 nm) at the AERONET site in Belsk are given. The AOD_{CL} of the CE318 and the MFR-7 were scaled to the lidar wavelength (355 and 532 nm respectively) using the Ångström power law. The mean values were obtained for July–September of 2013, 2015, and 2016, when instruments operated simultaneously (41 cases). The mean values derived for cases with no aerosol in the free troposphere (12 cases), as given in EARLINET/ACTRIS database, are shown in parentheses and emphasized using italic font.

	AOD	AOD	ÅE (355/532)	ÅE (380/500)	ÅE (415/500)
AERONET Belsk (columnar) reference site CE318 photometer					
	355 nm	532 nm			
	0.41 ± 0.17	0.23 ± 0.09	1.49 ± 0.23		
All cases	*(0.28 ± 0.12)*	*(0.16 ± 0.06)*	*(1.57 ± 0.10)*		
(no FT aerosol)	380 nm	500 nm			
	0.36 ± 0.16	0.24 ± 0.12		1.51 ± 0.23	
	(0.26 ± 0.10)	*(0.19 ± 0.08)*		*(1.60 ± 0.13)*	
PolandAOD Warsaw (columnar) MFR-7 shadowband radiometer					
	355 nm	532 nm			
	0.45 ± 0.17	0.25 ± 0.11	1.56 ± 0.21		
All cases	*(0.30 ± 0.09)*	*(0.15 ± 0.06)*	*(1.71 ± 0.17)*		
(no FT aerosol)	415 nm	500 nm			
	0.36 ± 0.15	0.27 ± 0.12			1.50 ± 0.31
	(0.26 ± 0.08)	*(0.17 ± 0.07)*			*(1.66 ± 0.35)*
EARLINET Warsaw (within the aerosol boundary) PollyXT-UW Raman lidar					
	355 nm	532 nm			
All cases	0.20 ± 0.06	0.13 ± 0.03	1.53 ± 0.23		
(no FT aerosol)	*(0.16 ± 0.08)*	*(0.10 ± 0.03)*	*(1.60 ± 0.15)*		

biomass-burning aerosol to Warsaw (e.g. Markowicz et al. 2016; Szkop and Pietruczuk, 2017; Janicka et al., 2017; Stachlewska et al., 2017a, 2018). This is why the mean values derived for the cases with no long-range transport in the free troposphere are listed in parentheses in Table 3 (i.e. no allocation to categories such as forest-fire or dust in the EARLINET/ACTRIS database). Excluding those cases from the mean results in an AOD_{CL} that is roughly 30 to 40 % lower in Warsaw and ∼ 30 % lower in Belsk. At the same time, the mean values of the AOD_{ABL} do not decrease as much, i.e. the AOD_{ABL} is less than 20 % lower. For conditions with no aerosol layers in the free troposphere, Szczepanik and Markowicz (2018) proposed the following approximation of the daytime boundary layer aerosol load for a rural mountainous site (Strzyzow, Poland, elevation 899 m a.s.l.): the $AOD_{ABL}(500)$ equals approximately 80 % of the $AOD_{CL}(500)$. Based on the values listed in the Table 3, such approximation for the urban continental site in Warsaw (elevation 112 m a.s.l.) would indicate $AOD_{ABL}(532) \approx 53\,\%\ AOD_{CL}(532)$ and $AOD_{ABL}(355) \approx 67\,\%\ AOD_{CL}(355)$.

A closer look at Fig. 4 shows that the lidar-derived AOD_{ABL} values are less than 0.2 on a few days (e.g. case numbers 9–13), although corresponding values of the radiometer-derived AOD_{CL} are more than 0.7. This is not an error. On 10 July 2013, biomass-burning aerosol from Canadian wildfires was detected by lidar in Warsaw, with an apparent optically thick aerosol layer suspended in the lower troposphere just above the top of the boundary layer, as reported by Janicka et al. (2017) and Ortiz-Amezcua et al. (2017). Due to the low ABLH (< 1000 m) on this day, not unusual under high-pressure system conditions over Poland e.g. Stachlewska et al. (2018), the optical depth contribution of the aerosol smoke layer in the free troposphere dominated over the optical depth contribution of the aerosol within the boundary layer, which explains the much higher columnar values compared with the boundary layer AOD. Markowicz et al. (2016) reported aerosol layers in the free troposphere having a significant (up to 55 %) contribution to the total optical depth, which is consistent with the results obtained in the current paper.

The results in Fig. 4, obtained for the ÅE with relation to the particle size, show that retrievals from different instruments have a similar trend of variation with time. The mean $ÅE_{CL}$ values given in Table 3 are the same with respect to the given variability range for all 41 cases, despite the differences in the measurement wavelengths. The values in parentheses (no long-range transport of aerosol in free troposphere) show consistent results, i.e. higher $Å E_{ABL}$ values than $Å E_{CL}$ values were obtained, which indicates pollution dominating within the boundary layer.

4.1 Relation of the ABLH with optical properties and surface PM in summer and early autumn over Warsaw

The comparison of the AOD_{CL} and AOD_{ABL} with the ABLH for 41 cases of temporally co-located measurements conducted with the MFR-7 and the PollyXT shows a positive correlation (0.74 at both wavelengths) of AOD_{ABL} and ABLH, which is even higher than the correlation coefficient of 0.55 between AOD_{ABL} and ABLH reported for Leipzig by Mattis et al. (2004). Similar results were reported for Warsaw by Stachlewska et al. (2017b, 2018), i.e. when there is no aerosol in the free troposphere above Warsaw; however, Stachlewska et al. (2017b, 2018) found that both the AOD_{CL} and AOD_{ABL} increased with increasing ABLH. In the current study, no significant correlation was observed for the AOD_{CL} and ABLH, which is related to differences in the load and type of aerosol in the free troposphere and within the boundary layer. When an aerosol layer containing particles of dust, smoke, pollution, or a mixture of the above is suspended in the free troposphere, an increase in the columnar AOD_{CL} values can be observed. Marinou et al. (2017) reported that dust particles can be transported far from their source of origin and are frequently observed over central and northern Europe, with higher occurrences during summer. Dust particles can occur over Warsaw, mainly in the free troposphere (at a height above 2–3 km) during the spring and summer period (Chilinski et al., 2016; Janicka et al., 2017; Szczepanik et al., 2019). Biomass-burning particles and smoke layers were detected over central Europe in the summers of 2013 (Janicka et al., 2017; Ortiz-Amezcua et al., 2017; Trickl et al., 2015), 2015 (Stachlewska et al., 2017b; Szkop and Pietruczuk, 2017), and 2016 (Stachlewska et al., 2018). Biomass burning and dust were detected and analysed in southern Europe using a 10 year lidar dataset (Siomos et al., 2017, 2018). Canadian wildfire smoke detected in the troposphere and the stratosphere in summer 2017 over central Europe was also reported by Haarig et al. (2018), Ansmann et al. (2018), Hu et al. (2019), and Baars et al. (2019).

In cases where there is a lack of clouds (as in this study), the less sufficient growth of the ABLH could be explained as being partly due to the aerosol suspended in the free troposphere; this aerosol reduces the solar radiation reaching the surface and, thus, suppresses the thermal turbulence, leading to a lower boundary layer height. Hence, for certain conditions, the relation of AOD_{CL} and the ABLH can be expected to exhibit a negative correlation.

The majority of the 41 cases of daytime, clear-sky, summertime measurements analysed were related to observations of biomass-burning aerosol in the free troposphere. Over an urban site, the AOD_{ABL} can increase due to pollution in the boundary layer, which adds to the growth of the ABLH due to the sun-driven turbulence. At the same time, the AOD_{CL} can decrease when free-tropospheric aerosol (e.g. absorbing particles) causes negative radiative effects at the surface. Another aspect that has to be accounted for is the presence of aerosol particles in the troposphere directly above the top of the boundary layer, which may follow from the dynamics of turbulent eddy structures in the layer. Even in the absence of convection, a typical feature of turbulent boundary layer flows is the presence of abrupt bursting and sweeping events (Pope, 2000). Bursts can eject aerosol particles to the upper regions of the boundary layer. The interactions between vortical structures are responsible for the balances of the particle concentration in the boundary layer flows (Béghein et al., 2014).

The AOD_{ABL} is calculated as an integral of the extinction coefficient within the ABLH, and the ABLH is a variable of AOD_{ABL}; therefore, the ABLH is not expected to be strongly related to the aerosol conditions above in the free troposphere. The aerosol optical depth is a unique parameter to determine the atmospheric aerosol load, and the ABLH derived by lidar relies on a higher aerosol concentration within the boundary layer than in the free troposphere. Therefore, a positive correlation between the AOD_{ABL} and the ABLH can be expected. Note that although an intrusion of biomass-burning smoke into the boundary layer can contribute strongly to the suppression of the growth of the ABLH, as reported by Stachlewska et al. (2018), it still did not result in a negative correlation.

The relations of lidar-derived AOD_{ABL}, $Å E_{ABL}$, and the ABLH at different times of the day for the July–September period of 2013, 2015, and 2016 (246 cases) are depicted in Fig. 5. As the AOD_{ABL} is related to the ABLH, there is a higher aerosol load in the ABL than in the free troposphere – thus, a positive correlation can be observed. A relatively high correlation coefficient (0.76 at 355 nm and 0.75 at 532 nm) between the ABLH and the AOD_{ABL} occurred in the MTL, whereas their correlation coefficients were slightly weaker (0.66 and 0.61 respectively) during the nocturnal time (residual layer effect), when aerosol load within the ABL basically remained stable due to much weaker vertical mixing at night.

The mean $Å E_{ABL}$ is 1.54 ± 0.37, indicating the dominance of relatively small particles during the observation period. No obvious relation between $Å E_{ABL}$ and the ABLH was obtained, but the highest values ($Å E_{ABL} > 2$) were only observed at night, i.e. there was either more pollution or less humidity. Indeed, a higher concentration of $PM_{2.5}$ was measured during the nocturnal period ($16.75 \pm 6.86\,\mu g\,m^{-3}$) compared with the other time spans ($15.74 \pm 7.24\,\mu g\,m^{-3}$ during sunrise and $10.94 \pm 4.13\,\mu g\,m^{-3}$ during sunset). Note that the

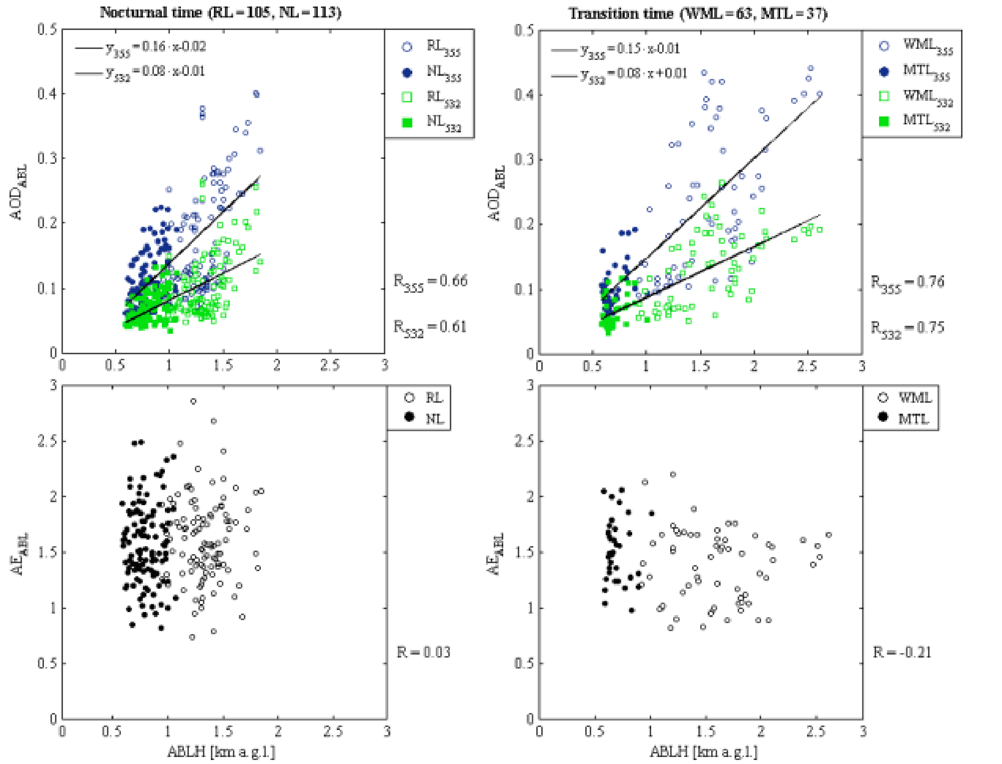

Figure 5. Hourly averaged aerosol optical depth (AOD) and Ångström exponent (ÅE) derived within the boundary layer at 355 and 532 nm vs. the atmospheric boundary layer height (ABLH), all derived from the PollyXT lidar at the EARLINET/ACTRIS site of the RS-Lab,Warsaw, for July–September of 2013, 2015, and 2016. A linear fit to data points is shown for correlation coefficients (R) greater than 0.6.

standard deviations given indicate high variability in the values obtained.

Figure 6 illustrates the relations between the ABLH, $PM_{2.5}$, PM_{10}, and the FCMR. A slightly negative trend between the FCMR and the ABLH can be observed for the well-mixed layer, which may suggest an increase in coarse particles (number or/and size) at the surface with an ascending ABLH. The fact that adiabatic effects have partly influenced the growth of particle size cannot be excluded. Schäfer et al. (2006) found a high negative correlation between PM_{10} and the ABLH in Hanover and Munich in winter. Rost et al. (2009) reported a strong negative relation between PM_{10} and the ABLH in Stuttgart. Similarly, Du et al. (2013) found that $PM_{2.5}$ and the ABLH exhibited a negative correlation in Delhi and Xi'an. Geiß et al. (2017) reported that the link between PM and the ABLH can be attributed to several different reasons, such as meteorological conditions, terrain, local particle sources, and even the ABLH retrieval method itself. This was also the case for Warsaw during aerosol injections into the boundary layer that had undergone long-range transport (Stachlewska et al., 2017b, 2018). However, in general, no pronounced relationship between PM_{10} and the ABLH are expected for Warsaw, as also shown in Zawadzka et al. (2013). Furthermore, in the current study, no significant link between particulate matter (PM_{10} and $PM_{2.5}$) and the ABLH was found for Warsaw during summer and early autumn (Fig. 6), which can be partly attributed to relatively low records of PM_{10} emissions (hourly values $< 60\,\mu g\,m^{-3}$) and relatively high summer ABLH values (up to 1.6 km, Table 2). The highest PM_{10} and $PM_{2.5}$ values are observed at night (NL and RL), lower values are found for the MTL, and the lowest values are noted for the WML. Reizer and Juda-Rezler (2015) reported that either regional background pollution or local emission sources are mainly responsible for the high PM_{10} and $PM_{2.5}$ concentrations in Polish urban areas. Clearly, the ABLH is not the main factor controlling the surface pollution in summer in Warsaw, which is consistent

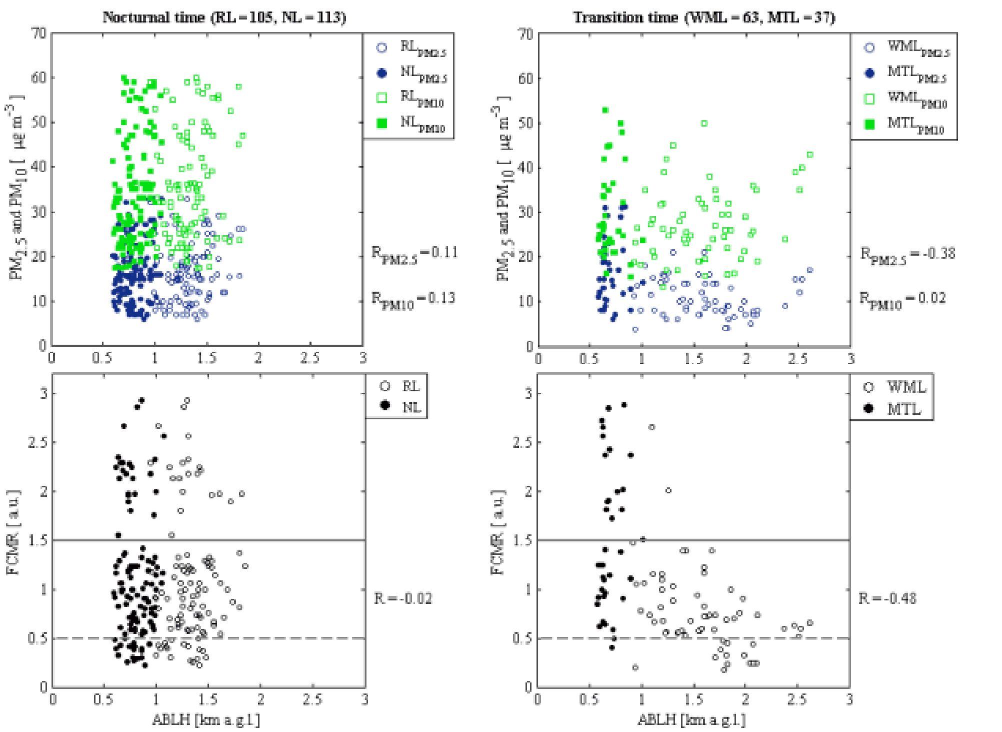

Figure 6. Hourly averages of the surface fine-to-coarse mass ratio (FCMR) and particulate matter ($PM_{2.5}$ and PM_{10}) measured at the WIOS site in Ursynow, Warsaw, vs. the atmospheric boundary layer height (ABLH) derived from the PollyXT lidar at the EARLINET/ACTRIS site at the RS-Lab, Warsaw, for the July–September period of 2013, 2015, and 2016. Thresholds of the FCMR are marked using horizontal lines.

with reports by Bonn et al. (2016), Stachlewska et al. (2017b, 2018), and Geiß et al. (2017).

4.2 Interrelations between different optical properties and with surface PM in summer and early autumn over Warsaw

Figure 7 presents the relationship of AOD_{ABL}, $ÅE_{ABL}$, LR_{ABL}, δ_{ABL}, and the surface FCMR for the nocturnal and transition times during July, August, and September of 2013, 2015, and 2016. The separation thresholds for the FCMR are defined as follows: an FCMR greater than 1.5 (vertical line) means that fine particles (< 2.5 µm) dominated and an FCMR less than 0.5 (vertical dashed line) means that coarse particles dominated (2.5–10 µm). The given thresholds for the ÅE roughly indicate the dominant particle size distribution mode, with separation thresholds of for small particles ÅE > 1.5 (horizontal line) and large particles ÅE < 1 (horizontal dashed line). However, the relation between the ÅE and the aerosol size distribution is complicated, as is the relationship with the FCMR.

For all time periods, FCMR values between 0.5 and 1.5 constitute the largest proportion in total. During the nocturnal period there are more fine particles than during sunrise (MTL) or sunset (WML). There is clear separation mark at a FCMR of 1.5 regardless the time period, and no clear correlation of $ÅE_{ABL}$ with FCMR; however, for an $ÅE_{ABL}$ between 1 and 2 during the nocturnal period and at sunrise, there is a higher $PM_{2.5}$ contribution at the surface.

Because of weak vertical air motion (no convective mixing) and a lower ABLH during nighttime, relatively large aerosol particles are deposited in the ABL and most of small aerosol particles stack below the inversion of the top of the boundary layer (or residual layer). This can lead to an increase in the number of small particles accumulated within the nocturnal ABL, which manifests as a fine particles increase at the surface. In general, urban pollution, regarded as road traffic, industrial emissions, and the chemical reaction of gases (SO_2, NO_2, NO_x), causes an increase in both PM_{10} and $PM_{2.5}$ (He et al., 2008). The sunrise period in July–September (05:00–09:00 local time) corresponds to ur-

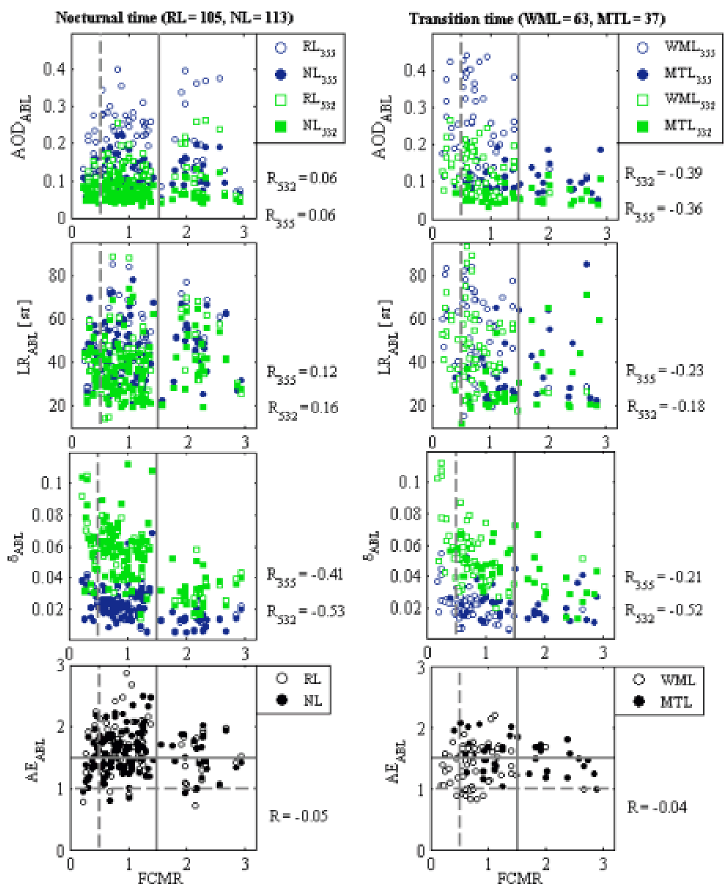

Figure 7. Hourly averaged aerosol optical depth (AOD), lidar ratio (LR), linear particle depolarization ratio (δ), and Ångström exponent (ÅE) derived within the atmospheric boundary layer at 355 and 532 nm by the PollyXT lidar at the RS-Lab, EARLINET/ACTRIS site in Warsaw, for the July–September period of 2013, 2015, and 2016 vs. the surface fine-to-coarse mass ratio (FCMR) derived from particulate matter ($PM_{2.5}$ and PM_{10}) measured at the WIOS site in Ursynow, Warsaw. Thresholds of the ÅE and FCMR are marked using horizontal and vertical lines respectively.

ban traffic emission, which can cause the lifting of particles from the ground (Zawadzka et al., 2013). The relationship of LR_{ABL} and the FCMR in Fig. 7 shows a clear separation of data, which is mainly the result of a higher abundance of fine particles in the MTL. On the contrary, more coarse particles (PM_{10} with a higher LR_{ABL} of 40–80 sr) occur in the WML.

The relationship of δ_{ABL} and the FCMR in Fig. 7 indicates possible negative trends (stronger at 532 nm) for all time periods. The abundance of the fine (coarse) particles at the surface is related to the abundance of the spherical particles within the ABL.

Bennouna et al. (2016) reported that a significant positive correlation of PM_{10} and AOD_{CL}, and an increasing correlation coefficient for daily, monthly, and yearly averages, relays on the aerosol characteristics of the site. Zawadzka et al. (2013) reported a negative correlation between PM_{10} and AOD_{CL} for long-term monthly mean values in winter in Belsk and Warsaw, and a positive relation for unstable (meaning strong turbulent vertical mixing in summer) atmospheric conditions in Warsaw. The relation between optical properties and the surface aerosol mass concentration depends on boundary layer processes, chemical composition, source regions, weather conditions, and aerosol type,

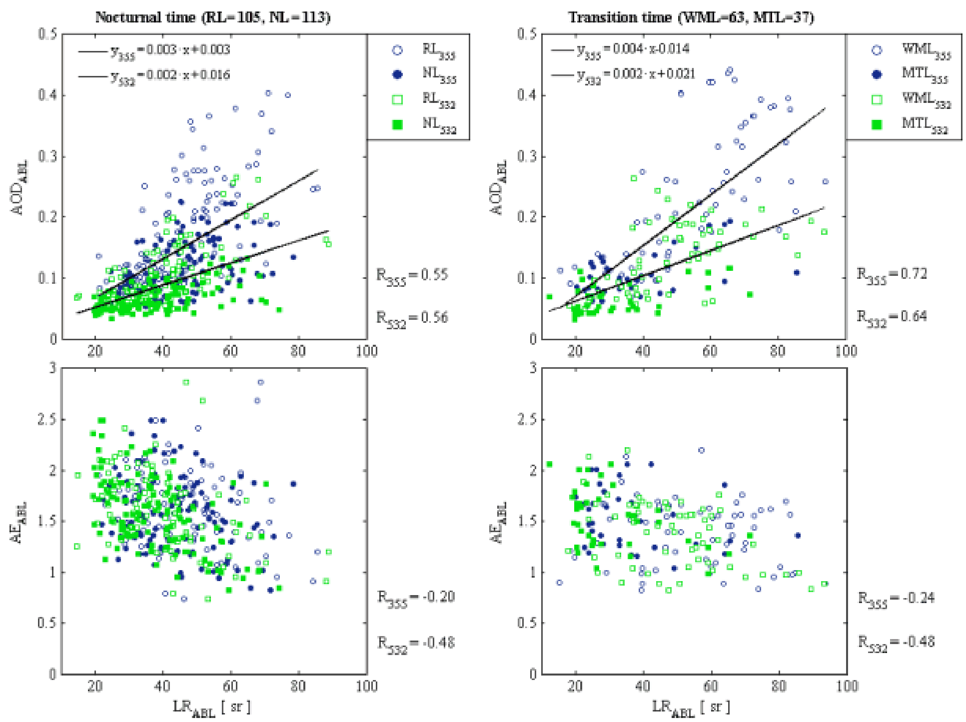

Figure 8. Hourly averaged aerosol optical depth (AOD), Ångström exponent (ÅE), and lidar ratio (LR) derived within the atmospheric boundary layer at 355 and 532 nm from the PollyXT lidar at the RS-Lab, at the EARLINET/ACTRIS site in Warsaw, for the July–September period of 2013, 2015, and 2016. The lack of a correlation between the linear particle depolarization ratio (δ) and the lidar ratio (LR) is not shown for brevity. The linear fit to data points is shown for correlation coefficients (R) greater than 0.6.

which are challenging to characterize well with the columnar AOD_{ABL} and the surface PM concentrations alone. As depicted in Fig. 7, the AOD_{ABL} and FCMR indicate a higher AOD_{ABL} for coarse particles (PM_{10}) in the WML and a lower AOD_{ABL} for fine particles ($PM_{2.5}$) in the MTL; however, no significant correlations of AOD_{ABL} with PM_{10} or $PM_{2.5}$ are reported in the current study.

Significant correlations ($R > 0.5$) of AOD_{CL} and $PM_{2.5}$ were reported mainly for the eastern cities of China (Guo et al., 2009; Zheng et al., 2015; Zang et al., 2017) and the United States (Liu et al., 2007; Hutchison et al., 2008; Wang and Christopher, 2003), where the main industrial regions with extreme pollution are located. In these cases, the majority of aerosol was expected to be present within the boundary layer. The anthropogenic pollution in Warsaw is much lower compared with the above-mentioned regions: Zawadzka et al. (2013) reported an R value of 0.42 between AOD_{CL} and $PM_{2.5}$ in Warsaw, which was attributed to a significant load in the free troposphere affecting the relationship. The current study shows that there is also no significant correlation for AOD_{ABL} and $PM_{2.5}$, which can be explained by the low values of AOD_{ABL} and $PM_{2.5}$ measured during the investigated period; these low values of AOD_{ABL} and $PM_{2.5}$ are, in turn, attributed to the lack of high pollution events in summer and early autumn in Warsaw. Stachlewska et al. (2017b, 2018) showed that AOD_{ABL} and $PM_{2.5}$ in Warsaw can be correlated, under high aerosol load conditions, during events involving an injection of pollution or biomass burning that has undergone long-range transport into the boundary layers (but with no aerosol in the free troposphere).

As for the relation between AOD_{ABL} and PM_{10}, in the current study no significant linear correlation was found for the nocturnal time (similar to Filip and Stefan, 2011), and a weak positive relation was observed for the sunrise/sunset period (similar to Zawadzka et al. 2013). The ABL in summer is primarily driven by intensive convective mixing, resulting in a significantly higher ABLH than in other seasons (Wang et al., 2019). In summer, the ABL aerosol can be elevated by effective convection into the free troposphere, and this can lead to a decrease in the aerosol loading within the ABL, as reported by e.g. He et al. (2008) and Tian et al. (2017). The emission of PM_{10} in summer is lower than in other seasons in Warsaw (Zawadzka et al., 2013). Even lower urban emissions at night reduce the mass concentrations of surface PM_{10}, and the aerosol properties within ABL are concurrently relatively stable due to the stable boundary layer at nighttime. Therefore, no apparent relationship can be observed during the nocturnal period.

Interrelations of optical properties within the ABL are given in Fig. 8. A positive correlation between the AOD_{ABL} and LR_{ABL} is observed for all times, which is higher for sunrise and sunset (0.64–0.72) and lower for the nocturnal time (~ 0.56). The AOD_{ABL} and LR_{ABL} depend on the extinction coefficient derived within the ABL; thus, both values will increase when the fine particle contribution increases and/or when there is an increase in the absorption capability of the particles within the ABL, and vice versa. This may be partly due to the presence of biomass-burning particles inside the ABL, as reported e.g. in Stachlewska et al. (2018).

The relation between the $ÅE_{ABL}$ and LR_{ABL} shows a weak negative trend during the analysed period, which may be due to larger size particles being injected into the ABL, particles growing in the ABL, or the smoke contribution in the composition of the ABL aerosol. As for the latter, the presence of smoke particles results in high negative correlations, e.g. correlations between LR_{ABL} and $ÅE_{ABL}$ of −0.79 (Giannakaki et al., 2010) and −0.84 (Amiridis et al., 2009) were found for smoke particles. Moreover, Stachlewska et al. (2018) showed negative correlation of $ÅE_{ABL}$ and LR_{ABL} for smoke particles. An alternative explanation could be the condensation of large organic molecules and particle coagulation from the upper atmosphere into the ABL, as reported by e.g. Pósfai et al. (2004) and Fiebig et al (2003). Giannakaki et al. (2010), showed no significant correlation between $ÅE_{ABL}$ and LR_{ABL} for continental and urban aerosol related to anthropogenic pollution. Moreover, Mattis et al. (2004) reported no relationship between $ÅE_{ABL}$ and LR_{ABL} when anthropogenic particles dominated in Leipzig. The results obtained in the current paper suggest that a mixture of local urban anthropogenic aerosol with a natural source aerosol (local or long-range transported into ABL) during summer and early autumn in Warsaw, might be a reasonable explanation for the weak negative tendency of $ÅE_{ABL}$ and LR_{ABL} observed.

4.3 Relations of optical properties, surface PM, and relative humidity in summer and early autumn over Warsaw

Relations between the near-surface relative humidity (RH) and surface PM_{10} and $PM_{2.5}$ and FCMR, and relations between the near-surface RH and the lidar-derived aerosol properties (AOD_{ABL} $ÅE_{ABL}$, LR_{ABL} and δ_{ABL}) were investigated for the entire, nocturnal, and sunrise/sunset times. Additionally, the nighttime relations between the lidar-derived water vapour mixing ratios (WV_{ABL}) and the aforementioned quantities were investigated.

Generally, as seen in Fig. 9, a weak positive trend of RH and $PM_{2.5}$ is in agreement with the results of Sharma et al. (2017). The RH and FCMR exhibit a positive correlation, with correlation coefficients of 0.6 for the NT, 0.63 for the WML, and 0.71 for the MTL. Zhang et al. (2015) reported that high RH values can led to high $PM_{2.5}$ in Beijing. In the summer urban environment, Li et al. (2017) showed that an increase of the RH can lead to growth of fine particles ($PM_{2.5}$), but not to a growth of PM_{10} due to the hygroscopic effect on aerosol, and mainly attributed this to the effects of the wet scavenging under the high summer rainfall. The mean RH obtained in the current study was highest for the MTL at 63 ± 10 %, was 57 ± 12 % for the NL, and was lowest for the WML at 43±10 %. Small particles have a greater possibility to aggregate into relatively large particles at nighttime; thus, the lower correlation coefficients for RH and $PM_{2.5}$ (and FCMR) are found for the nocturnal time.

Figure 10 presents no clear relation of WV_{ABL} with surface $PM_{2.5}$, PM_{10}, and FCMR at nighttime in Warsaw. The correlation coefficient of WV_{ABL} and $PM_{2.5}$ is a little higher than WV_{ABL} and PM_{10}, indicating that the water vapour in the ABL can affect the surface fine particles more than the surface coarse particles at night. This could be due to the presence of anthropogenic particles in the ABL, as these hygroscopic particles can absorb water vapour and gradually increase in size, although the growth of particles due to particle coagulation within the ABL cannot be excluded (Fiebig et al., 2003).

Figure 10 also does not depict a clear relation between WV_{ABL} and AOD_{ABL} or $ÅE_{ABL}$ and LR_{ABL} – only δ_{ABL} and WV_{ABL} show a negative trend. The hygroscopicity of particles increases with decreasing particle size (Petters et al., 2009). At the same time, the more fine particles the lower the depolarization (see Fig. 7). Hence, an increase in water vapour and the presence of hygroscopic particles leads to a decrease in depolarization. When biomass-burning aerosol that has undergone long-range transport occurs over Warsaw, hygroscopic effects can be well captured with quasi-continuous profiling of the water vapour (Stachlewska et al., 2017a). Note that the relation of the AOD_{ABL}, $ÅE_{ABL}$, and LR_{ABL} with the surface RH also does not show much of a trend for the NL, although for the WML the negative trends and property groupings becomes more visible (Fig. 11).

The AOD_{CL} was reported to increase with an increase in the ambient relative humidity for the hygroscopic particles due to hygroscopic growth (Bergin et al., 2000; Altaratz et al., 2013). In Fig. 11, a negative relation between AOD_{ABL} and surface RH is found (with a higher surface RH, a lower AOD_{ABL} is observed), except for during the nocturnal period (no trend in Fig. 11, similar to Fig. 10 for AOD_{ABL} and WV_{ABL}). The size and optical properties can change as aerosol particles take up water and a higher RH is more favourable for hygroscopic growth of pollution parti-

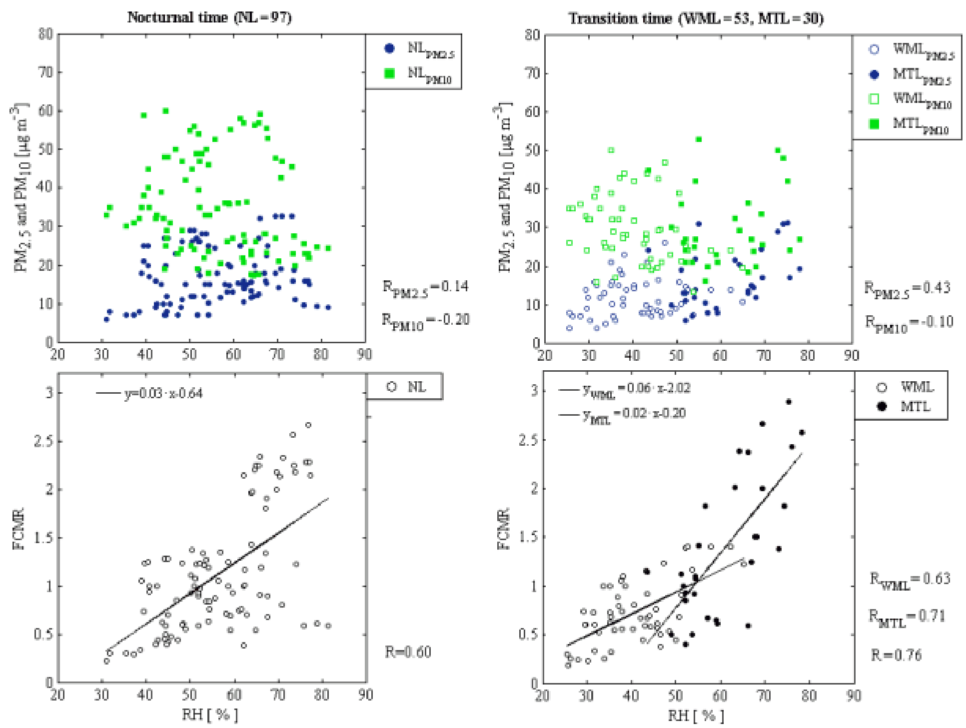

Figure 9. Hourly averaged near-surface relative humidity (RH) measured by the WXT510 (Vaisala) weather transmitter at the RS-Lab in Warsaw for the July–September period of 2013, 2015, and 2016 vs. surface particulate matter ($PM_{2.5}$ and PM_{10}) measured at the WIOS site in Ursynow, Warsaw. The linear fit to data points is shown for correlation coefficients (R) greater than 0.6.

cles (Tang, 1996). During the observational period, urban anthropogenic aerosol was observed most frequently within the boundary layer. An increase in RH led to an increase in the pollution particle size, which was visible at nighttime (ÅE and RH show slight negative trend). A slight positive trend between $ÅE_{ABL}$ and RH is seen at transition times (different grouping in the moister MTL and drier WML), which is in accordance with the FCMR and ÅE scatterplots (more coarse particles in the MTL and more fine particles in the WML). Pollution particles within the boundary layer, due to a weaker convective mixing at nighttime, are prone to water uptake, which contributes to an increase in the aerosol particle size Cheng et al. (2008). The relation between LR_{ABL} and RH shows practically no correlation during the nocturnal time, but it is well separated in the transition time (a lower LR for the MTL). At nighttime, an increasing LR due to the accumulation of hygroscopic smoke particles was reported by Giannkaki et al. (2010). The convection and the energy exchange is stronger in the transition time (Stull, 1988), leading to anthropogenic aerosol being dominant in the atmospheric boundary layer. Increasing the surface RH results in a rise in the aerosol particles' size, and thus contributes to a decrease in the LR_{ABL}. The negative trend in the relation between δ_{ABL} and the surface RH (clearly visible during the nocturnal time) is in agreement with the trend obtained for WV_{ABL} and δ_{ABL}.

5 Conclusions

This study focuses on the optical properties derived within the atmospheric boundary layer, based on a dataset comprising measurements from July to September in 2013, 2015, and 2016 from the EARLINET/ACTRIS site in Warsaw. Interrelations between the different optical properties within ABL as well as relations between the optical properties and the surface PM concentrations and RH measurements were studied by conducting comparisons of various parameters during different periods: the entire time (24 h, ABL), nighttime (21:00–02:00 UTC; NL and RL), sunrise (03:00–08:00 UTC; MTL), and sunset (16:00–20:00 UTC; WML).

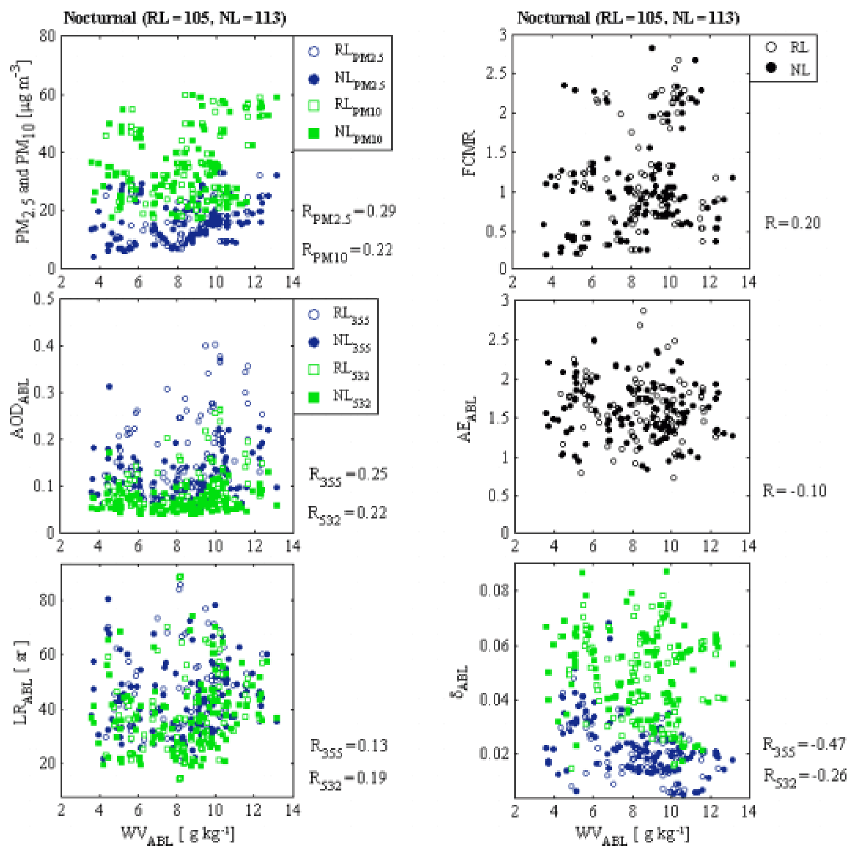

Figure 10. Nighttime hourly averaged water vapour mixing ratio (WV) vs. aerosol optical depth (AOD), lidar ratio (LR), Ångström exponent (ÅE), and linear particle depolarization ratio (δ), all derived within the atmospheric boundary layer from the PollyXT lidar at the RS-Lab, at the EARLINET/ACTRIS site in Warsaw, and vs. the fine-to-coarse mass ratio (FCMR) and surface particulate matter ($PM_{2.5}$ and PM_{10}) measured at the WIOS site in Ursynow, Warsaw, during the July–September period of 2013, 2015, and 2016. Note that the lidar-derived WV is only available at nighttime.

At both wavelengths, AOD_{ABL} and LR_{ABL} at sunset were found to be higher (0.14–0.24 for AOD_{ABL} and 49–55 sr for LR_{ABL}) than for the other two periods (0.06–0.18 for AOD_{ABL} and 32–47 sr for LR_{ABL}). During the nocturnal period, $ÅE_{ABL}$ values were higher (1.58 ± 0.36 for NL, 1.61 ± 0.37 for RL) than for the two remaining periods (1.53 ± 0.30 for MTL, 1.37 ± 0.34 for WML). For the entire dataset, the AE_{ABL} was distributed between 1 and 2 (> 90 % of data points) and the surface FCMR ranged between 0.5 and 1.5 (∼ 70 % of data points). The aerosol composition within the ABL in summer and early autumn in Warsaw consisted of urban anthropogenic pollution and its mixtures with local pollen and long-range transported biomass-burning aerosol and Arctic marine particles.

The boundary layer AOD_{ABL} contribution to the columnar AOD_{CL} was assessed. The latter was more than twice as high when optically thick aerosol layers were observed above the ABL, and less than twice as high for cases with no aerosol layers in the free troposphere but with the presence of pollution aloft due to convection.

The AOD_{ABL} and ABLH exhibit a positive correlation (∼0.75) during the observation period, which is highest for the WML and MTL. When the ABLH increases, a declining trend of the FCMR is observed for the WML, indicating an increase in the coarse particle fraction. However, there is no clearly apparent link between PM_{10} or $PM_{2.5}$ and the ABLH. For the MTL, the ranges of $ÅE_{ABL}$ and FCMR values obtained are higher than for the WML. A negative correlation

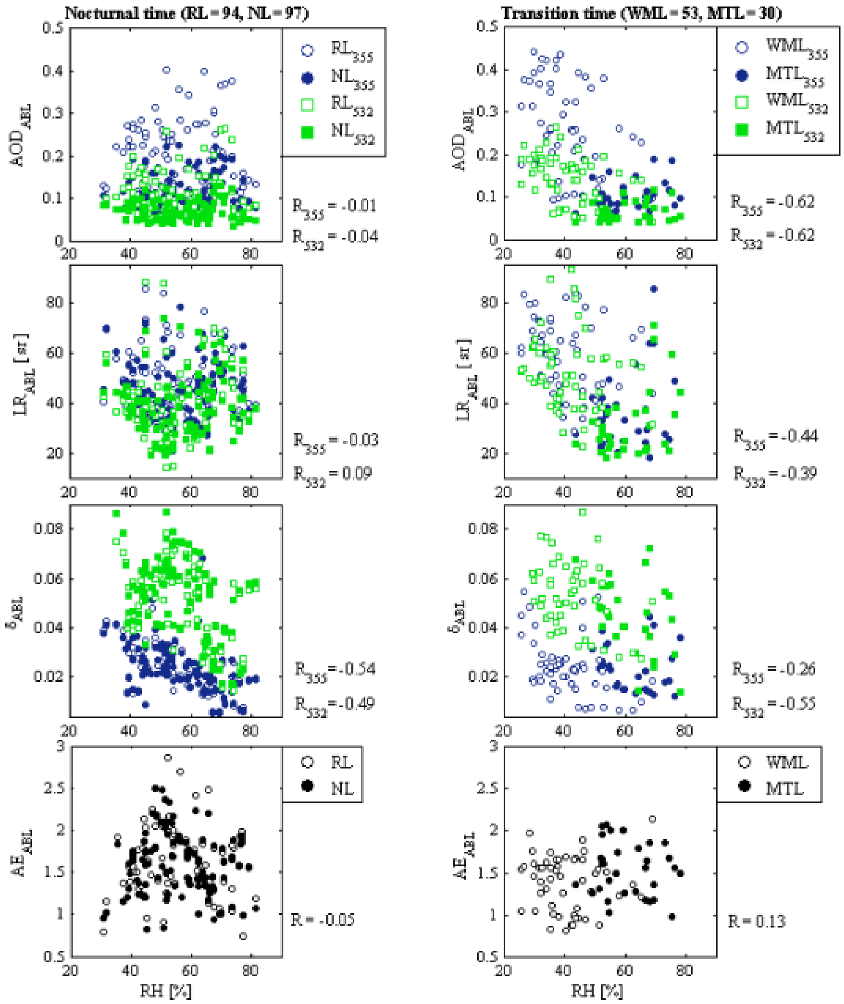

Figure 11. Hourly averaged near-surface relative humidity (RH) measured by the WXT510 (Vaisala) weather transmitter at the RS-Lab, Warsaw, vs. the aerosol optical depth (AOD), the lidar ratio (LR), the linear particle depolarization ratio (δ), and the Ångström exponent (ÅE) derived within the boundary layer at 355 and 532 nm from the PollyXT lidar at the RS-Lab, at the EARLINET/ACTRIS site in Warsaw, for the July–September period of 2013, 2015, and 2016.

of δ_{ABL} and the FCMR was found for all time periods, which indicates the higher sphericity of fine particles. As reported in literature, different correlations obtained for AOD_{ABL} and PM_{10} are attributed to complicated atmospheric and weather conditions. In summer and early autumn in Warsaw, high-pressure systems generally govern the dynamics of the atmosphere, there is significantly less traffic pollution (people on holidays, on bicycles), and the pollination of plants also plays a role.

The relation between AOD_{ABL} and FCMR reported here displays a negative correlation at sunrise and sunset, which can be related to the traffic peaks. Due to lower urban emissions (no traffic nor domestic heating in summer) and a stable boundary layer, no apparent relationship between AOD_{ABL} and the FCMR was observed at night. The AOD_{ABL} and

LR_{ABL} depend on the extinction coefficient within the ABL – thus, a positive correlation is observed. The relation of $ÅE_{ABL}$ and LR_{ABL} reveals a weak negative trend. The positive trends of the RH and FCMR were found at night and for sunrise and sunset, although the sunrise trend was most pronounced.

The weak positive relation at night for WV_{ABL} and $PM_{2.5}$ is higher than for PM_{10}, indicating that the water vapour in the NL and RL affects surface fine particles more than surface coarse particles. The increasing WV_{ABL} (and RH at the surface) can lead to a decrease in depolarization (both relations are very similar at night) in the presence of hygroscopic particles. For high near-surface RH, lower AOD_{ABL} values were derived in the MTL and WML, which was not seen in the NL and RL. A negative trend of δ_{ABL} and WV_{ABL} and of δ_{ABL} and RH is due to the hygroscopicity of particles. A negative relation between AOD_{ABL} and surface RH is found for the transition time (in both the MTL and WML), which is followed by a weak negative correlation of LR_{ABL} and RH observed only during sunset (in the WML).

The co-located measurements conducted in Warsaw with the MFR-7 shadowband radiometer (PolandAOD-NET) and the CE318 sun photometer (AERONET) showed strong agreement with a correlation coefficient (R) of 0.98 and a standard deviation of 0.02 at both 380 and 500 nm.

The results obtained increase the current knowledge on the variability of optical properties within the summer and early-autumn atmospheric boundary layer at a continental urban site in central Europe. The relations found in previously published research, obtained using a case-study approach, do not necessarily apply and are not necessarily seen in the long-term study. Therefore, special care should be taken when interpreting and comparing the different results.

The bottom line is that regular, automated observations of the next generation PollyXT lidar conducted at the EARLINET site in the framework of the ACTRIS infrastructure activities allow for such studies. The excellent capabilities of this lidar enabled the combination of the results derived within this study with other data sources (e.g. AERONET, WIOS, and PolandAOD networks). Hypotheses regarding boundary layer aerosol properties interrelations were proposed and will be further verified using additional lidar data from regular observations in Warsaw. The expansion of the existing high quality lidar data sample would allow for an improvement in the investigation of the subgrouping of aerosol properties, which could provide statistically significant correlations. Moreover, more observations would allow for an extension of the investigation of differences to other seasons, would enable daytime analyses, and would aid with better distinguishing between sunset and sunrise aerosol property relationships; furthermore, a separation of aerosol properties accordingly to aerosol content, i.e. urban aerosol vs. urban aerosol mixtures with other aerosol types, would be possible (currently too few data exist in the mixed categories), followed by an estimation of their radiative effect.

Data availability. The lidar data used in this study are available upon registration from http://data.earlinet.org (last access: 15 October 2019). The $PM_{2.5}$ and PM_{10} data are publicly accessible via the data archive of the National Chief Inspectorate for Environmental Protection (GIOS) at http://powietrze.gios.gov.pl/pjp/archive (last access: 15 October 2019). The sun photometer AOD data are publicly available via the AERONET data website at https://AERONETl.gsfc.nasa.gov (last access: 15 October 2019). The shadowband radiometer AOD data and the surface RH data are available via the Polish aerosol Research Network PolandAOD-NET website at https://polandaod.pl (last access: 15 October 2019). The radiosounding profiles are available via the University of Wyoming Upperair Air Data website at http://weather.uwyo.edu/upperair/sounding.htm (last access: 15 October 2019).

Appendix A: Lists of symbols and physical quantities

Entire time	ET
Nocturnal time	NT
Transition rime	TT
Atmospheric boundary layer (derived by lidar)	ABL
Atmospheric boundary layer height (derived by lidar)	ABLH
Residual layer (derived by lidar)	RL
Nocturnal layer (derived by lidar)	NL
Morning transition layer (derived by lidar)	MTL
Well-mixed layer (derived by lidar)	WML
Particle extinction coefficient (within the atmospheric boundary layer)	α_{ABL}
Particle backscatter coefficient (within the atmospheric boundary layer)	β_{ABL}
Aerosol optical depth (within the atmospheric boundary layer, derived by lidar)	$AOD_{ABL}(\lambda)$
Aerosol optical depth (columnar, derived by sun photometer or radiometer)	$AOD_{CL}(\lambda)$
Lidar ratio (within the atmospheric boundary layer)	$LR_{ABL}(\lambda)$
Linear particle depolarization ratio (within the atmospheric boundary layer)	$\delta_{ABL}(\lambda)$
Ångström exponent (within the atmospheric boundary layer, derived by lidar)	$ÅE_{ABL}(\lambda_1/\lambda_2)$
Ångström exponent (columnar, derived by sun photometer or radiometer)	$ÅE_{CL}(\lambda_1/\lambda_2)$
Water vapour mixing ratio (within the atmospheric boundary layer)	WV_{ABL}
Relative humidity (at the near-surface)	RH
Particulate matter with diameter $< 10\,\mu m$; $< 2.5\,\mu m$	PM_{10}; $PM_{2.5}$
Fine to coarse mass ratio	FCMR
Wavelength	λ

Author contributions. ISS wrote the paper, obtained funding for the research, came up with the study approach, designed the methodology, performed the experiment, contributed to the development of the PollyXT lidar (Warsaw) and the lidar evaluation algorithms, took care of the quality assurance of lidar measurements and data products, and holistically interpreted the lidar results with respect to other data sources' results (AERONET, PolandAOD-NET, and WIOS Monitoring Network). DS was responsible for the calculation of the aerosol optical property profiles (α, β, and δ) and their categorization for the EARLINET/ACTRIS database. DW was responsible for an extensive literature review, wrote the codes for the ABLH and the WV retrieval algorithms, and performed statistical analysis of the optical properties (ÅE, LR, δ, and WV). All authors contributed to revisions of the paper.

Competing interests. The authors declare that they have no conflict of interest.

Special issue statement. This article is part of the special issue "EARLINET aerosol profiling: contributions to atmospheric and climate research". It is not associated with a conference.

Acknowledgements. This research was mainly carried out in the frame of the Technical assistance for Polish Radar and Lidar Mobile Observation System (POLIMOS) project funded by ESA-ESTEC. The PollyXT lidar (Warsaw) was developed via a scientific collaboration between the Faculty of Physics at the University of Warsaw (FUW) and the Institute of Tropospheric Research (TROPOS). The development was financed by the Polish Foundation of Science and Technology (FNTP). We especially acknowledge members of the PollyXT lidar group lead by Dietrich Althausen. The authors acknowledge the Warsaw Regional Inspectorate for Environmental Protection (WIOS) of the National Chief Inspectorate for Environmental Protection (GIOS) for the provision of the processed and quality assured $PM_{2.5}$ and PM_{10} data. We acknowledge Brent Holben for processing the AERONET data; Aleksander Pietruczuk and Piotr Sobolewski of the Institute of Geophysics at the Polish Academy of Sciences for performing the AERONET measurements in Belsk; Wojciech Kumala of the Faculty of Physics at the University of Warsaw (FUW) for performing the AERONET measurements in Warsaw; Phillippe Golub for performing instrument calibrations at the PHOTONS/AERONET-EUROPE calibration centre. The AERONET sun photometer at the RS-Lab site in Warsaw is the property of the National Institute of Research and Development for Optoelectronics (INOE 2000) in Romania, and was kindly lent by the research group led by Doina Nicolae, within the framework of the SAtellite based Monitoring Initiative for Regional Air quality (SAMIRA) funded by ESA-ESRIN. We acknowledge Krzysztof Markowicz for processing the MFR-7 data within the Polish aerosol Research Network PolandAOD-NET. The purchase of the MFR-7 instrument was funded by the Polish Ministry of Science and High Education. The EARLINET/AERONET site in Warsaw established at RS-Lab at Faculty of Physics, University of Warsaw (FUW) acknowledges the vital support of the ACTRIS Research Infrastructure in developing the site.

Financial support. This research has been supported by the European Space Agency ESA-ESTEC (grant no. 4000119961/16/NL/FF/mg), the Polish Foundation of Science and Technology (grant no. 519/FNITP/115/2010), the Polish Ministry of Science and High Education (grant no. 1283/B/P01/2010/38), and the European Space Agency ESA-ESRIN (grant no. 4000117393/16/INB). The EARLINET activities have been supported by the ACTRIS project, funded within the European Commission Seventh Framework Programme under the research infrastructures for atmospheric research (grant agreement no. 262254); the ACTRIS-2 project, funded by the European Union Research Infrastructures action under the H2020 specific programme for integrating and opening existing national and regional research infrastructures of European interest (grant agreement no. 654109); and the ACTRIS PPP 65 project supported by the European Commission under the Horizon 2020 – Research and Innovation Framework Programme, H2020INFRADEV-2016-2017 (grant agreement no. 739530).

Review statement. This paper was edited by Lucia Mona and reviewed by three anonymous referees.

References

Altaratz, O., Bar-Or, R. Z., Wollner, U., and Koren, I.: Relative humidity and its effect on aerosol optical depth in the vicinity of convective clouds, Environ. Res. Lett., 8, 034025, https://doi.org/10.1088/1748-9326/8/3/034025, 2013.

Alados-Arboledas, L., Müller, D., Guerrero-Rascado, J., Navas-Guzmán, F., Pérez-Ramírez, D., and Olmo, F.: Optical and microphysical properties of fresh biomass burning aerosol retrieved by Raman lidar, and star- and sun-photometry, Geophys. Res. Lett., 38, L01807, https://doi.org/10.1029/2010GL045999, 2011.

Amiridis, V., Balis, D., Kazadzis, S., Bais, A., Giannakaki, E., Papayannis, A., and Zerefos, C.: Four-year aerosol observations with a Raman lidar at Thessaloniki, Greece, in the framework of European Aerosol Research Lidar Network (EARLINET), J. Geophys. Res., 110, D21203,https://doi.org/10.1029/2005JD006190, 2005.

Amiridis, V., Balis, D. S., Giannakaki, E., Stohl, A., Kazadzis, S., Koukouli, M. E., and Zanis, P.: Optical characteristics of biomass burning aerosols over Southeastern Europe determined from UV-Raman lidar measurements, Atmos. Chem. Phys., 9, 2431–2440, https://doi.org/10.5194/acp-9-2431-2009, 2009.

Ångström, A.: On the atmospheric transmission of sun radiation and on dust in the air, Geogr. Ann., 12, 156–166, https://doi.org/10.1080/20014422.1929.11880498, 1929.

Ansmann, A., Tesche, M., Knippertz, P., Bierwirth, E., Althausen, D., Mueller, D., and Schulz, O.: Vertical profiling of convective dust plumes in Southern Morocco during SAMUM, Tellus B, 61, 340–353, https://doi.org/10.1111/j.1600-0889.2008.00384.x, 2009.

Ansmann, A., Baars, H., Chudnovsky, A., Mattis, I., Veselovskii, I., Haarig, M., Seifert, P., Engelmann, R., and Wandinger, U.: Extreme levels of Canadian wildfire smoke in the stratosphere over central Europe on 21–22 August 2017, Atmos. Chem.

Phys., 18, 11831–11845, https://doi.org/10.5194/acp-18-11831-2018, 2018.

Baars, H., Kanitz, T., Engelmann, R., Althausen, D., Heese, B., Komppula, M., Preißler, J., Tesche, M., Ansmann, A., Wandinger, U., Lim, J.-H., Ahn, J. Y., Stachlewska, I. S., Amiridis, V., Marinou, E., Seifert, P., Hofer, J., Skupin, A., Schneider, F., Bohlmann, S., Foth, A., Bley, S., Pfüller, A., Giannakaki, E., Lihavainen, H., Viisanen, Y., Hooda, R. K., Pereira, S. N., Bortoli, D., Wagner, F., Mattis, I., Janicka, L., Markowicz, K. M., Achtert, P., Artaxo, P., Pauliquevis, T., Souza, R. A. F., Sharma, V. P., van Zyl, P. G., Beukes, J. P., Sun, J., Rohwer, E. G., Deng, R., Mamouri, R.-E., and Zamorano, F.: An overview of the first decade of PollyNET: an emerging network of automated Raman-polarization lidars for continuous aerosol profiling, Atmos. Chem. Phys., 16, 5111–5137, https://doi.org/10.5194/acp-16-5111-2016, 2016.

Baars, H., Ansmann, A., Ohneiser, K., Haarig, M., Engelmann, R., Althausen, D., Hanssen, I., Gausa, M., Pietruczuk, A., Szkop, A., Stachlewska, I. S., Wang, D., Reichhardt, J., Skupin, A., Mattis, I., Trickl, T., Vogelmann, H., Navas-Guzmán, F., Haefele, A., Acheson, K., Ruth, A. A., Tatarov, B., Müller, D., Hu, Q., Podvin, T., Goloub, P., Vesselovski, I., Pietras, C., Haeffelin, M., Fréville, P., Sicard, M., Comerón, A., Fernández García, A. J., Molero Menéndez, F., Córdoba-Jabonero, C., Guerrero-Rascado, J. L., Alados-Arboledas, L., Bortoli, D., Costa, M. J., Dionisi, D., Liberti, G. L., Wang, X., Sannino, A., Papagiannopoulos, N., Boselli, A., Mona, L., D'Amico, G., Romano, S., Perrone, M. R., Belegante, L., Nicolae, D., Grigorov, I., Gialitaki, A., Amiridis, V., Soupiona, O., Papayannis, A., Mamouri, R.-E., Nisantzi, A., Heese, B., Hofer, J., Schechner, Y. Y., Wandinger, U., and Pappalardo, G.: The unprecedented 2017–2018 stratospheric smoke event: Decay phase and aerosol properties observed with EARLINET, Atmos. Chem. Phys. Discuss., https://doi.org/10.5194/acp-2019-615, in review, 2019.

Barlage, M., Miao, S., and Chen, F.: Impact of physics parameterizations on high-resolution weather prediction over two Chinese megacities, J. Geophys. Res., 121, 4487–4498, https://doi.org/10.1002/2015JD024450, 2016.

Bennouna, Y., Cachorro, V. E., Mateos, D., Burgos, M. A., Toledano, C., Torres, B., and de Frutos, A.: Long-term comparative study of columnar and surface mass concentration aerosol properties in a background environment, Atmos. Environ., 140, 261–272, https://doi.org/10.1016/j.atmosenv.2016.05.061, 2016.

Béghein C., Allery C., Wacławczyk C., and Pozorski J.: Application of POD-based dynamical systems to dispersion and deposition of particles in turbulent channel flow, Int. J. Multiphase Flow, 58, 97–113, https://doi.org/10.1016/j.ijmultiphaseflow.2013.09.001, 2014.

Bergin, M. H., Schwartz, S. E., Halthore, R. N., Ogren, J. A., and Hlavka, D. L.: Comparison of aerosol optical depth inferred surface measurements with that determined by Sun photometry for cloud-free conditions at a continental US site, J. Geophys. Res., 105, 6807–6816, https://doi.org/10.1029/1999JD900454, 2000.

Binietoglou, I., Basart, S., Alados-Arboledas, L., Amiridis, V., Argyrouli, A., Baars, H., Baldasano, J. M., Balis, D., Belegante, L., Bravo-Aranda, J. A., Burlizzi, P., Carrasco, V., Chaikovsky, A., Comerón, A., D'Amico, G., Filioglou, M., Granados-Muñoz, M. J., Guerrero-Rascado, J. L., Ilic, L., Kokkalis, P., Maurizi, A., Mona, L., Monti, F., Muñoz-Porcar, C., Nicolae, D., Papayannis, A., Pappalardo, G., Pejanovic, G., Pereira, S. N., Perrone, M. R., Pietruczuk, A., Posyniak, M., Rocadenbosch, F., Rodríguez-Gómez, A., Sicard, M., Siomos, N., Szkop, A., Terradellas, E., Tsekeri, A., Vukovic, A., Wandinger, U., and Wagner, J.: A methodology for investigating dust model performance using synergistic EARLINET/AERONET dust concentration retrievals, Atmos. Meas. Tech., 8, 3577–3600, https://doi.org/10.5194/amt-8-3577-2015, 2015.

Böckmann, C., Wandinger, U., Ansmann, A., Bösenberg, J., Amiridis, V., Boselli, A., Delaval, A., De Tomasi, F., Frioud, M., and Grigorov, I. V.: Aerosol lidar intercomparison in the framework of the EARLINET project. 2. Aerosol backscatter algorithms, Appl. Opt., 43, 977–989, https://doi.org/10.1364/AO.43.000977, 2004.

Böckmann, C., Mironova, I., Müller, D., Schneidenbach, L., and Nessler, R.: Microphysical aerosol parameters from multiwavelength lidar, J. Opt. Soc. Am. A, 22, 518–528, https://doi.org/10.1364/JOSAA.22.000518, 2005.

Bonn, B., von Schneidemesser, E., Andrich, D., Quedenau, J., Gerwig, H., Lüdecke, A., Kura, J., Pietsch, A., Ehlers, C., Klemp, D., Kofahl, C., Nothard, R., Kerschbaumer, A., Junkermann, W., Grote, R., Pohl, T., Weber, K., Lode, B., Schönberger, P., Churkina, G., Butler, T. M., and Lawrence, M. G.: BAERLIN2014 – the influence of land surface types on and the horizontal heterogeneity of air pollutant levels in Berlin, Atmos. Chem. Phys., 16, 7785–7811, https://doi.org/10.5194/acp-16-7785-2016, 2016.

Burton, S. P., Ferrare, R. A., Hostetler, C. A., Hair, J. W., Rogers, R. R., Obland, M. D., Butler, C. F., Cook, A. L., Harper, D. B., and Froyd, K. D.: Aerosol classification using airborne High Spectral Resolution Lidar measurements – methodology and examples, Atmos. Meas. Tech., 5, 73–98, https://doi.org/10.5194/amt-5-73-2012, 2012.

Burton, S. P., Hair, J. W., Kahnert, M., Ferrare, R. A., Hostetler, C. A., Cook, A. L., Harper, D. B., Berkoff, T. A., Seaman, S. T., Collins, J. E., Fenn, M. A., and Rogers, R. R.: Observations of the spectral dependence of linear particle depolarization ratio of aerosols using NASA Langley airborne High Spectral Resolution Lidar, Atmos. Chem. Phys., 15, 13453–13473, https://doi.org/10.5194/acp-15-13453-2015, 2015.

Chen, B. and Kan, H.: Air pollution and population health: A global challenge, Environ. Health Prev. Med., 13, 94–101, https://doi.org/10.1007/s12199-007-0018-5, 2008.

Cheng, Y. F., Wiedensohler, A., Eichler, H., Heintzenberg, J., Tesche, M., Ansmann, A., Wendisch, M., Su, H., Althausen, D., Herrmann, H., Gnauk, T., Brüggemann, E., Hu, M., and Zhang, Y. H.: Relative humidity dependence of aerosol optical properties and direct radiative forcing in the surface boundary layer at Xinken in Pearl River Delta of China: An observation based numerical study, Atmos. Environ., 42, 6373–6397, https://doi.org/10.1016/j.atmosenv.2008.04.009, 2008.

Chilinski, M. T., Markowicz, K. M., Zawadzka, O., Stachlewska, I. S., Kumala, W., Petelski, T., Makuch, P., Westphal, D. L., and Zagajewski, B.: Modelling and Observation of Mineral Dust Optical Properties over Central Europe, Acta Geophys., 64, 2550–2590, https://doi.org/10.1515/acgeo-2016-0069, 2016.

Comerón, A., Sicard, M., and Rocadenbosch, F.: Wavelet Correlation Transform Method and Gradient Method to Determine Aerosol Layering from Lidar Returns: Some

Comments, J. Atmos. Ocean. Tech., 30, 1189–1193, https://doi.org/10.1175/JTECH-D-12-00233.1, 2013.

Costa-Surós, M., Stachlewska, I. S., Nemuc, A., Talianu, C., Heese, B., and Engelmann, R.: Study case of air-mass modification over Poland and Romania observed by the means of multiwavelength Raman depolarization lidars, 27th International Laser Radar Conference, New York, USA, 5–10 July 2015, 1–4, 2015.

Dang, R., Yang, Y., Hu, X.-M., Wang, Z., and Zhang, S.: A Review of Techniques for Diagnosing the Atmospheric Boundary Layer Height (ABLH) Using Aerosol Lidar Data, Remote Sens., 11, 1590, https://doi.org/10.3390/rs11131590, 2019.

Dawson, K. W., Meskhidze, N., Josset, D., and Gassó, S.: Spaceborne observations of the lidar ratio of marine aerosols, Atmos. Chem. Phys., 15, 3241–3255, https://doi.org/10.5194/acp-15-3241-2015, 2015.

Delanoë, J. and Hogan, R. J.: A variational scheme for retrieving ice cloud properties from combined radar, lidar, and infrared radiometer, J. Geophys. Res., 113, D07204, https://doi.org/10.1029/2007JD009000, 2008.

De Leeuw, F., Sluyter, R., van Breugel, P., and Bogman, F.: Air Pollution by ozone in Europe in 1999 and the summer of 2000, European Environmental Agency Topic Report number 1/2001, EEA, Copenhagen, Denmark, 2001.

Di Biagio, C., Pelon, J., Ancellet, G., Bazureau, A., and Mariage, V.: Sources, load, vertical distribution, and fate of wintertime aerosol north of Svalbard from combined V4 CALIOP data, ground-based IAOOS lidar observations and trajectory analysis, J. Geophys. Res.-Atmos., 123, 1363–1383, https://doi.org/10.1002/2017JD027530, 2018.

Dörnbrack, A., Stachlewska, I. S., Ritter, C., and Neuber, R.: Aerosol distribution around Svalbard during intense easterly winds, Atmos. Chem. Phys., 10, 1473–1490, https://doi.org/10.5194/acp-10-1473-2010, 2010.

Du, C., Liu, S., Yu, X., Li, X., Chen, C., Peng, Y., Dong, Y., Dong, Z., and Wang, F.: Urban boundary layer height characteristics and relationship with particulate matter mass concentrations in Xi'an, Central China, aerosol, Air Qual. Res., 13, 1598–1607, https://https://doi.org/10.4209/aaqr.2012.10.0274, 2013.

Engelmann, R., Kanitz, T., Baars, H., Heese, B., Althausen, D., Skupin, A., Wandinger, U., Komppula, M., Stachlewska, I. S., Amiridis, V., Marinou, E., Mattis, I., Linné, H., and Ansmann, A.: The automated multiwavelength Raman polarization and water-vapor lidar PollyXT: the neXT generation, Atmos. Meas. Tech., 9, 1767–1784, https://doi.org/10.5194/amt-9-1767-2016, 2016.

Fan, J., Wang, Y., Rosenfeld, D., and Liu, X.: Review of aerosol cloud interactions: Mechanisms, significance, and challenges, J. Atmos. Sci., 73, 4221–4252, https://doi.org/10.1175/JAS-D-16-0037.1, 2016.

Feingold, G., McComiskey, A., Yamaguchi, T., Johnson, J., Carslaw, K., and Schmidt, K. S.: New approaches to quantifying aerosol influence on the cloud radiative effect, P. Nat. Acad. Sci. USA, 113, 5812–5819, https://doi.org/10.1073/pnas.1514035112, 2016.

Fiebig, M., Stohl, A., Wendisch, M., Eckhardt, S., and Petzold, A.: Dependence of solar radiative forcing of forest fire aerosol on ageing and state of mixture, Atmos. Chem. Phys., 3, 881–891, https://doi.org/10.5194/acp-3-881-2003, 2003.

Filip, L. and Stefan, S.: Study of the correlation between the near-ground PM10 mass concentration and the aerosol optical Depth, J. Atmos. Sol.-Terr. Phys., 73, 1883–1889, https://doi.org/10.1016/j.jastp.2011.04.027, 2011.

Flentje, H., Heese, B., Reichardt, J., and Thomas, W.: Aerosol profiling using the ceilometer network of the German Meteorological Service, Atmos. Meas. Tech. Discuss., 3, 3643–3673, https://doi.org/10.5194/amtd-3-3643-2010, 2010.

Freudenthaler, V., Esselborn, M., Wiegner, M., Heese, B., Tesche, M., Ansmann, A., Müller, D., Althausen, D., Wirth, M., Fix, A., Ehret, G., Knippertz, P., Toledano, C., Gasteiger, J., Garhammer, M., and Seefeldner, M.: Depolarization ratio profiling at several wavelengths in pure Saharan dust during SAMUM 2006, Tellus B, 61, 165–179, https://https://doi.org/10.1111/j.1600-0889.2008.00396.x, 2009.

Freudenthaler, V., Linné, H., Chaikovski, A., Rabus, D., and Groß, S.: EARLINET lidar quality assurance tools, Atmos. Meas. Tech. Discuss., https://doi.org/10.5194/amt-2017-395, in review, 2018.

Foth, A., Kanitz, T., Engelmann, R., Baars, H., Radenz, M., Seifert, P., Barja, B., Fromm, M., Kalesse, H., and Ansmann, A.: Vertical aerosol distribution in the southern hemispheric midlatitudes as observed with lidar in Punta Arenas, Chile (53.2° S and 70.9° W), during ALPACA, Atmos. Chem. Phys., 19, 6217–6233, https://doi.org/10.5194/acp-19-6217-2019, 2019.

Fuzzi, S., Baltensperger, U., Carslaw, K., Decesari, S., Denier van der Gon, H., Facchini, M. C., Fowler, D., Koren, I., Langford, B., Lohmann, U., Nemitz, E., Pandis, S., Riipinen, I., Rudich, Y., Schaap, M., Slowik, J. G., Spracklen, D. V., Vignati, E., Wild, M., Williams, M., and Gilardoni, S.: Particulate matter, air quality and climate: lessons learned and future needs, Atmos. Chem. Phys., 15, 8217–8299, https://doi.org/10.5194/acp-15-8217-2015, 2015.

Gasteiger, J. and Freudenthaler, V.: Benefit of depolarization ratio at $\lambda = 1064$ nm for the retrieval of the aerosol microphysics from lidar measurements, Atmos. Meas. Tech., 7, 3773–3781, https://doi.org/10.5194/amt-7-3773-2014, 2014.

Gayatri, K., Patade, S., and Prabha, T. V.: Aerosol–Cloud interaction in deep convective clouds over the Indian Peninsula using spectral (bin) microphysics, J. Atmos. Sci., 74, 3145–3166, https://doi.org/10.1175/JAS-D-17-0034.1, 2017.

Geiß, A., Wiegner, M., Bonn, B., Schäfer, K., Forkel, R., von Schneidemesser, E., Münkel, C., Chan, K. L., and Nothard, R.: Mixing layer height as an indicator for urban air quality?, Atmos. Meas. Tech., 10, 2969–2988, https://doi.org/10.5194/amt-10-2969-2017, 2017.

Giannakaki, E., Balis, D. S., Amiridis, V., and Zerefos, C.: Optical properties of different aerosol types: seven years of combined Raman-elastic backscatter lidar measurements in Thessaloniki, Greece, Atmos. Meas. Tech., 3, 569–578, https://doi.org/10.5194/amt-3-569-2010, 2010.

Ghan, S. J., Wang, M., Zhang, S., Ferrachat, S., Gettleman, A., Griesfeller, J., Kipling, Z., Lohmann, U., Morrison, H., Neubauer, D., Partridge, D. G., Stier, P., Takemura, T., Wang, H., and Zhang, K.: Challenges in constraining anthropogenic aerosol effects on cloud radiative forcing using present-day spatiotemporal variability, P. Natl. Acad. Sci. USA, 113, 5804–5811, https://doi.org/10.1073/pnas.1514036113, 2016.

Giles, D. M., Sinyuk, A., Sorokin, M. G., Schafer, J. S., Smirnov, A., Slutsker, I., Eck, T. F., Holben, B. N., Lewis, J. R., Campbell,

J. R., Welton, E. J., Korkin, S. V., and Lyapustin, A. I.: Advancements in the Aerosol Robotic Network (AERONET) Version 3 database – automated near-real-time quality control algorithm with improved cloud screening for Sun photometer aerosol optical depth (AOD) measurements, Atmos. Meas. Tech., 12, 169–209, https://doi.org/10.5194/amt-12-169-2019, 2019.

Granados-Muñoz, M. J., Navas-Guzmán, F., Bravo-Aranda, J. A., Guerrero-Rascado, J. L., Lyamani, H., Valenzuela, A., Titos, G., Fernández-Gálvez, J., and Alados-Arboledas, L.: Hygroscopic growth of atmospheric aerosol particles based on active remote sensing and radiosounding measurements: selected cases in southeastern Spain, Atmos. Meas. Tech., 8, 705–718, https://doi.org/10.5194/amt-8-705-2015, 2015.

Groß, S., Tesche, M., Freudenthaler, V., Toledano, C., Wiegner, M., Ansmann, A., Althausen, D., and Seefeldner, M.: Characterization of Saharan dust, marine aerosol and mixtures of biomass-burning aerosol and dust by means of multi-wavelength depolarization and Raman lidar measurements during SAMUM 2, Tellus B, 63, 706–724, https://doi.org/10.1111/j.1600-0889.2011.00556.x, 2011.

Groß, S., Esselborn, M., Weinzierl, B., Wirth, M., Fix, A., and Petzold, A.: Aerosol classification by airborne high spectral resolution lidar observations, Atmos. Chem. Phys., 13, 2487–2505, https://doi.org/10.5194/acp-13-2487-2013, 2013.

Groß, S., Freudenthaler, V., Schepanski, K., Toledano, C., Schäfler, A., Ansmann, A., and Weinzierl, B.: Optical properties of long-range transported Saharan dust over Barbados as measured by dual-wavelength depolarization Raman lidar measurements, Atmos. Chem. Phys., 15, 11067–11080, https://doi.org/10.5194/acp-15-11067-2015, 2015.

Grund, C. J. and Eloranta, E. W.: University of Wisconsin High Spectral Resolution Lidar, Opt. Eng., 30, 6–12, 1991.

Guo, H., Wang, Y., and Zhang, H.: Characterization of criteria air pollutants in Beijing during 2014–2015, Environ. Res., 154, 334–344, https://doi.org/10.1016/j.envres.2017.01.029, 2017.

Guo, J.-P., Zhang, X.-Y., Che, H.-Z., Gong, S.-L., An, X., Cao, C.-X., Guang, J., Zhang, H., Wang, Y.-Q., Zhang, X.-C., Xue, M., and Li, X.-W.: Correlation between PM concentrations and aerosol optical depth in eastern China, Atmos. Environ., 43, 5876–5886, https://doi.org/10.1016/j.atmosenv.2009.08.026, 2009.

Haarig, M., Ansmann, A., Gasteiger, J., Kandler, K., Althausen, D., Baars, H., Radenz, M., and Farrell, D. A.: Dry versus wet marine particle optical properties: RH dependence of depolarization ratio, backscatter, and extinction from multiwavelength lidar measurements during SALTRACE, Atmos. Chem. Phys., 17, 14199–14217, https://doi.org/10.5194/acp-17-14199-2017, 2017.

Haarig, M., Ansmann, A., Baars, H., Jimenez, C., Veselovskii, I., Engelmann, R., and Althausen, D.: Depolarization and lidar ratios at 355, 532, and 1064 nm and microphysical properties of aged tropospheric and stratospheric Canadian wildfire smoke, Atmos. Chem. Phys., 18, 11847–11861, https://doi.org/10.5194/acp-18-11847-2018, 2018.

Haeffelin, M., Angelini, F., Morille, Y., Martucci, G., Frey, S., Gobbi, G. P., Lolli, S., O'Dowd, C. D., Sauvage, L., XuerefRémy, I., Wastine, B., and Feist, D. G: Evaluation of mixing height retrievals from automatic profiling lidars and ceilometers in view of future integrated networks in Europe, Bound.-Lay. Meteorol., 143, 49–75, https://doi.org/10.1007/s10546-011-9643-z, 2012.

Harrison, L., Michalsky, J., and Berndt, J.: Automated multifilter rotating shadow-band radiometer: An instrument for optical depth and radiation measurements, Appl. Opt., 33, 5118–5125, https://doi.org/10.1364/AO.33.005118, 1994.

He, Q., Li, C., Mao, J., Lau, A. K. H., and Chu, D.: Analysis of aerosol vertical distribution and variability in Hong Kong, J. Geophys. Res., 113, D14211, https://doi.org/10.1029/2008JD009778, 2008.

Heese, B. and Wiegner, M.: Vertical aerosol profiles from Raman polarization lidar observations during the dry season AMMA field campaign, J. Geophys. Res., 113, D00C11, https://doi.org/10.1029/2007JD009487, 2008.

Holben, B. N., Eck, T. F., Slutsker, I., Tanre, D., Buis, J. P., Setzer, A., Vermote, E., Reagan, J. A., Kaufman, Y. J., Nakjima, T., Lavenu, F., Jankowiak, I., and Smirnov, A.: AERONET – A federated instrument network and data archive for aerosol characterization, Remote Sens. Environ., 66, 1–16, https://doi.org/10.1016/S0034-4257(98)00031-5, 1998.

Horvath, H., Alados Arboledas, L., and Olmo Reyes, F. J.: Angular scattering of the Sahara dust aerosol, Atmos. Chem. Phys., 18, 17735–17744, https://doi.org/10.5194/acp-18-17735-2018, 2018.

Hu, Q., Goloub, P., Veselovskii, I., Bravo-Aranda, J.-A., Popovici, I. E., Podvin, T., Haeffelin, M., Lopatin, A., Dubovik, O., Pietras, C., Huang, X., Torres, B., and Chen, C.: Long-range-transported Canadian smoke plumes in the lower stratosphere over northern France, Atmos. Chem. Phys., 19, 1173–1193, https://doi.org/10.5194/acp-19-1173-2019, 2019.

Hutchison, K. D., Faruqui, S. J., and Smith, S.: Improving correlations between MODIS aerosol optical thickness and ground-based $PM_{2.5}$ observations through 3D spatial analyses, Atmos. Environ., 42, 530–543, https://doi.org/10.1016/j.atmosenv.2007.09.050, 2008.

Iarlori, M., Madonna, F., Rizi, V., Trickl, T., and Amodeo, A.: Effective resolution concepts for lidar observations, Atmos. Meas. Tech., 8, 5157–5176, https://doi.org/10.5194/amt-8-5157-2015, 2015.

Illingworth, A. J., Barker, H. W., Beljaars, A., Ceccaldi, M., Chepfer, H., Clerbaux, N., Cole, J., Delanoë, J., Domenech, C., Donovan, D. P., Fukuda, S., Hirakata, M., Hogan, R. J., Huenerbein, A., Kollias, P., Kubota, T., Nakajima, T., Nakajima, T.Y., Nishizawa, T., Ohno, Y., Okamoto, H., Oki, R., Sato, K., Satoh, M., Shephard, M., Velázquez-Blázquez, A., Wandinger, U., Wehr, T., and van Zadelhoff, G.-J.: The EarthCARE Satellite: The next step forward in global measurements of clouds, aerosol, precipitation and radiation, B. Am. Meteorol. Soc., 96, 1311–1332, https://doi.org/10.1175/BAMS-D-12-00227.1, 2015.

Iqbal, M.: An introduction to solar radiation, Acadamec Press, Ontario, 1983.

Janicka, L., Stachlewska, I. S., Veselovskii, I., and Baars, H.: Temporal variations in optical and microphysical properties of mineral dust and biomass burning aerosol derived from daytime Raman lidar observations over Warsaw, Poland, Atmos. Environ., 169, 162–174, https://doi.org/10.1016/j.atmosenv.2017.09.022, 2017.

Juda-Rezler, K., Reizer, M., and Oudinet, J. P.: Determination and analysis of PM10 source apportionment during episodes of air pollution in Central Eastern European urban areas: The case of wintertime 2006, Atmos. Environ., 45, 6557–6566, https://doi.org/10.1016/j.atmosenv.2011.08.020, 2011.

Juda-Rezler, K., Reizer, M., Huszar, P., Krueger, B., Zanis, P., Syrakov, D., Katragkou, E., Trapp, W., Melas, D., Chervenkov, H., Tegoulias, I., and Halenka, T.: Modelling the effects of climate change on air quality over central and Eastern Europe: concept, evaluation and projections, Clim. Res., 53, 179–203, https://doi.org/10.3354/cr01072, 2012.

Jung, E., Albrecht, B. A., Feingold, G., Jonsson, H. H., Chuang, P., and Donaher, S. L.: Aerosols, clouds, and precipitation in the North Atlantic trades observed during the Barbados aerosol cloud experiment – Part 1: Distributions and variability, Atmos. Chem. Phys., 16, 8643–8666, https://doi.org/10.5194/acp-16-8643-2016, 2016.

Kaufman, Y. J., Tanré, D., and Boucher, O.: A satellite view of aerosol in the climate system, Nature, 419, 215–223, https://doi.org/10.1038/nature01091, 2002.

Kipling, Z., Stier, P., Johnson, C. E., Mann, G. W., Bellouin, N., Bauer, S. E., Bergman, T., Chin, M., Diehl, T., Ghan, S. J., Iversen, T., Kirkevåg, A., Kokkola, H., Liu, X., Luo, G., van Noije, T., Pringle, K. J., von Salzen, K., Schulz, M., Seland, Ø., Skeie, R. B., Takemura, T., Tsigaridis, K., and Zhang, K.: What controls the vertical distribution of aerosol? Relationships between process sensitivity in HadGEM3–UKCA and inter-model variation from AeroCom Phase II, Atmos. Chem. Phys., 16, 2221–2241, https://doi.org/10.5194/acp-16-2221-2016, 2016.

Koffi, B., Schulz, M., Breon, F. M., Dentener, F., Steensen, B. M., Griesfeller, J., Winker, D., Balkanski, Y., Bauer, S. E., Bellouin, N., Berntsen, T., Bian, H. S., Chin, M., Diehl, T., Easter, R., Ghan, S., Hauglustaine, D. A., Iversen, T., Kirkevag, A., Liu, X. H., Lohmann, U., Myhre, G., Rasch, P., Seland, O., Skeie, R. B., Steenrod, S. D., Stier, P., Tackett, J., Takemura, T., Tsigaridis, K., Vuolo, M. R., Yoon, J., and Zhang, K.: Evaluation of the aerosol vertical distribution in global aerosol models through comparison against CALIOP measurements: AeroCom phase II results, J. Geophys. Res.-Atmos., 121, 7254–7283, https://doi.org/10.1002/2015JD024639, 2016.

Lelieveld, J., Evans, J. S., Fnais, M., Giannadaki, D., and Pozzer, A.: The contribution of outdoor air pollution sources to premature mortality on a global scale, Nature, 525, 367–371, https://doi.org/10.1038/nature15371, 2015.

Li, X., Ma, Y., Wang, Y., Liu, N., and Hong, Y.: Temporal and spatial analyses of particulate matter (PM_{10} and $PM_{2.5}$) and its relationship with meteorological parameters over an urban city in Northeast China, Atmos. Res., 198, 185–193, https://doi.org/10.1016/j.atmosres.2017.08.023, 2017.

Lisok, J., Rozwadowska, A., Pedersen, J. G., Markowicz, K. M., Ritter, C., Kaminski, J. W., Struzewska, J., Mazzola, M., Udisti, R., Becagli, S., and Gorecka, I.: Radiative impact of an extreme Arctic biomass-burning event, Atmos. Chem. Phys., 18, 8829–8848, https://doi.org/10.5194/acp-18-8829-2018, 2018.

Liu, Y., Franklin, M., Kahn, R., and Koutrakis, P.: Using aerosol optical thickness to predict ground-level $PM_{2.5}$ concentrations in the St. Louis area: A comparison between MISR and MODIS, Remote Sens. Environ., 107, 33–44, https://doi.org/10.1016/j.rse.2006.05.022, 2007.

Lolli, S. and Di Girolamo, P.: Principal Component Analysis Approach to Evaluate Instrument Performances in Developing a Cost-Effective Reliable Instrument Network for Atmospheric Measurements, J. Atmos. Ocean. Tech., 32, 1642–1649, https://doi.org/10.1175/JTECH-D-15-0085.1

Lolli, S., Madonna, F., Rosoldi, M., Campbell, J. R., Welton, E. J., Lewis, J. R., Gu, Y., and Pappalardo, G.: Impact of varying lidar measurement and data processing techniques in evaluating cirrus cloud and aerosol direct radiative effects, Atmos. Meas. Tech., 11, 1639–1651, https://doi.org/10.5194/amt-11-1639-2018, 2018.

Marinou, E., Amiridis, V., Binietoglou, I., Tsikerdekis, A., Solomos, S., Proestakis, E., Konsta, D., Papagiannopoulos, N., Tsekeri, A., Vlastou, G., Zanis, P., Balis, D., Wandinger, U., and Ansmann, A.: Three-dimensional evolution of Saharan dust transport towards Europe based on a 9-year EARLINET-optimized CALIPSO dataset, Atmos. Chem. Phys., 17, 5893–5919, https://doi.org/10.5194/acp-17-5893-2017, 2017.

Markowicz, K., Chilinski, M. T., Lisok, J., Zawadzka, O., Stachlewska, I. S., Janicka, L., Rozwadowska, A., Makuch, P., Pakszys, P., Zielinski, T., Petelski, T., Posyniak, M., Pietruczuk, A., Szkop, A., and Westphal, D. L.: Study of aerosol optical properties during long-range transport of biomass burning from Canada to Central Europe in July 2013, J. Aeros. Sci., 101, 156–173, https://doi.org/10.1016/j.jaerosci.2016.08.006, 2016.

Masonis, S. J., Anderson, T. L., Covert, D. S., Kapustin, V., Clarke, A. D., Howell, S., and Moore, K.: A study of the extinction-to-backscatter ratio of marine aerosol during the shoreline environment aerosol study, J. Atmos. Ocean. Tech., 20, 1388–1402, https://doi.org/10.1175/1520-0426(2003)020<1388:ASOTER>2.0.CO;2, 2003.

Masson-Delmotte, V., Zhai, P., Pörtner, H.-O., Roberts, D., Skea, J., Shukla, P. R., Pirani, A., Moufouma-Okia, W., Péan, C., Pidcock, R., Connors, S., Matthews, J. B. R., Chen, Y., Zhou, X., Gomis, M. I., Lonnoy, E., Maycock, T., Tignor, M., and Waterfield, T.: Global Warming of 1.5 °C, An IPCC Special Report on the impacts of global warming of 1.5 °C above pre-industrial levels and related global greenhouse gas emission pathways, in the context of strengthening the global response to the threat of climate change, sustainable development, and efforts to eradicate poverty, IPCC, 2018.

Matthias, V., Balis, D., Bösenberg, J., Eixmann, R., Iarlori, M., Komguem, L., Mattis, I., Papayannis, A., Pappalardo, G., and Perrone, M.: Vertical aerosol distribution over Europe: Statistical analysis of Raman lidar data from 10 European aerosol research lidar network (EARLINET) stations, J. Geophys. Res., 109, D18201, https://doi.org/10.1029/2004JD004638, 2004.

Mattis, I., Ansmann, A., Müller, D., Wandinger, U., and Althausen, D.: Multiyear aerosol observations with dual-wavelength Raman lidar in the framework of EARLINET, J. Geophys. Res., 109, D13203, https://doi.org/10.1029/2004JD004600, 2004.

Mona, L., Amodeo, A., D'Amico, G., Giunta, A., Madonna, F., and Pappalardo, G.: Multi-wavelength Raman lidar observations of the Eyjafjallajökull volcanic cloud over Potenza, southern Italy, Atmos. Chem. Phys., 12, 2229–2244, https://doi.org/10.5194/acp-12-2229-2012, 2012.

Müller, D., Ansmann, A., Mattis, I., Tesche, M., Wandinger, U., Althausen, D., and Pisani, G.: Aerosol-type-dependent lidar ratios observed with Raman lidar, J. Geophys. Res., 112, D16202, https://doi.org/10.1029/2006JD008292, 2007.

Navas-Guzmán, F., Martucci, G., Collaud Coen, M., Granados-Muñoz, M. J., Hervo, M., Sicard, M., and Haefele, A.: Characterization of aerosol hygroscopicity using Raman lidar measurements at the EARLINET station of Payerne, Atmos. Chem. Phys., 19, 11651–11668, https://doi.org/10.5194/acp-19-11651-2019, 2019.

Nemuc, A., Vasilescu, J., Talianu, C., Belegante, L., and Nicolae, D.: Assessment of aerosol's mass concentrations from measured linear particle depolarization ratio (vertically resolved) and simulations, Atmos. Meas. Tech., 6, 3243–3255, https://doi.org/10.5194/amt-6-3243-2013, 2013.

Nemuc, A., Stachlewska, I. S., Valilescu, J., Górska, A., Nicolae, D., and Talianu, C.: Optical Properties of Long-Range Transported Volcanic Ash over Romania and Poland During Eyjafjallajökull Eruption in 2010, Acta Geophys., 62, 350–366 https://doi.org/10.2478/s11600-013-0180-7, 2014.

Nicolae, D., Vasilescu, J., Talianu, C., Binietoglou, I., Nicolae, V., Andrei, S., and Antonescu, B.: A neural network aerosol-typing algorithm based on lidar data, Atmos. Chem. Phys., 18, 14511–14537, https://doi.org/10.5194/acp-18-14511-2018, 2018.

Ortiz-Amezcua, P., Guerrero-Rascado, J. L., Granados-Muñoz, M. J., Benavent-Oltra, J. A., Böckmann, C., Samaras, S., Stachlewska, I. S., Janicka, Ł., Baars, H., Bohlmann, S., and Alados-Arboledas, L.: Microphysical characterization of long-range transported biomass burning particles from North America at three EARLINET stations, Atmos. Chem. Phys., 17, 5931–5946, https://doi.org/10.5194/acp-17-5931-2017, 2017.

Pan, X., Chin, M., Gautam, R., Bian, H., Kim, D., Colarco, P. R., Diehl, T. L., Takemura, T., Pozzoli, L., Tsigaridis, K., Bauer, S., and Bellouin, N.: A multi-model evaluation of aerosols over South Asia: common problems and possible causes, Atmos. Chem. Phys., 15, 5903–5928, https://doi.org/10.5194/acp-15-5903-2015, 2015.

Papagiannopoulos, N., Mona, L., Alados-Arboledas, L., Amiridis, V., Baars, H., Binietoglou, I., Bortoli, D., D'Amico, G., Giunta, A., Guerrero-Rascado, J. L., Schwarz, A., Pereira, S., Spinelli, N., Wandinger, U., Wang, X., and Pappalardo, G.: CALIPSO climatological products: evaluation and suggestions from EARLINET, Atmos. Chem. Phys., 16, 2341–2357, https://doi.org/10.5194/acp-16-2341-2016, 2016.

Papagiannopoulos, N., Mona, L., Amodeo, A., D'Amico, G., Gumà Claramunt, P., Pappalardo, G., Alados-Arboledas, L., Guerrero-Rascado, J. L., Amiridis, V., Kokkalis, P., Apituley, A., Baars, H., Schwarz, A., Wandinger, U., Binietoglou, I., Nicolae, D., Bortoli, D., Comerón, A., Rodríguez-Gómez, A., Sicard, M., Papayannis, A., and Wiegner, M.: An automatic observation-based aerosol typing method for EARLINET, Atmos. Chem. Phys., 18, 15879–15901, https://doi.org/10.5194/acp-18-15879-2018, 2018.

Papayannis, A., Amiridis, V., Mona, L., Tsaknakis, G., Balis, D., Bosenberg, J., Chaikovski, A., De Tomasi, F., Grigorov, I., Mattis, I., Mitev, V., Muller, D., Nickovic, S., Perez, C., Pietruczuk, A., Pisani, G., Ravetta, F., Rizi, V., Sicard, M., Trickl, T., Wiegner, M., Gerding, M., Mamouri, R. E., D'Amico, G., and Pappalardo, G.: Systematic lidar observations of Saharan dust over Europe in the frame of EARLINET (2000–2002), J. Geophys. Res., 113, D10204, https://doi.org/10.1029/2007JD009028, 2008.

Pappalardo, G., Amodeo, A., Apituley, A., Comeron, A., Freudenthaler, V., Linné, H., Ansmann, A., Bösenberg, J., D'Amico, G., Mattis, I., Mona, L., Wandinger, U., Amiridis, V., Alados-Arboledas, L., Nicolae, D., and Wiegner, M.: EARLINET: towards an advanced sustainable European aerosol lidar network, Atmos. Meas. Tech., 7, 2389–2409, https://doi.org/10.5194/amt-7-2389-2014, 2014.

Perrone, M. R., De Tomasi, F., and Gobbi, G. P.: Vertically resolved aerosol properties by multi-wavelength lidar measurements, Atmos. Chem. Phys., 14, 1185–1204, https://doi.org/10.5194/acp-14-1185-2014, 2014.

Petters, M. D., Carrico, C. M., Kreidenweis, S. M., Prenni, A. J., DeMott, P. J., Collett, J. L., and Moosmüller, H.: Cloud condensation nucleation activity of biomass burning aerosol, J. Geophys. Res., 114, D22205, https://doi.org/10.1029/2009JD012353, 2009.

Pope, S. B.: Turbulent Flows. Cambridge University Press, UK, 771 pp., 2000.

Popovici, I. E., Goloub, P., Podvin, T., Blarel, L., Loisil, R., Unga, F., Mortier, A., Deroo, C., Victori, S., Ducos, F., Torres, B., Delegove, C., Choël, M., Pujol-Söhne, N., and Pietras, C.: Description and applications of a mobile system performing on-road aerosol remote sensing and in situ measurements, Atmos. Meas. Tech., 11, 4671–4691, https://doi.org/10.5194/amt-11-4671-2018, 2018.

Pósfai, M., Gelencsér, A., Simonics, R., Arató, K., Li, J., Hobbs, P. V., and Buseck, P. R.: Atmospheric tar balls: Particles from biomass and biofuel burning, J. Geophys. Res., 109, D06213, https://doi.org/10.1029/2003JD004169, 2004.

Proestakis, E., Amiridis, V., Marinou, E., Binietoglou, I., Ansmann, A., Wandinger, U., Hofer, J., Yorks, J., Nowottnick, E., Makhmudov, A., Papayannis, A., Pietruczuk, A., Gialitaki, A., Apituley, A., Szkop, A., Muñoz Porcar, C., Bortoli, D., Dionisi, D., Althausen, D., Mamali, D., Balis, D., Nicolae, D., Tetoni, E., Liberti, G. L., Baars, H., Mattis, I., Stachlewska, I. S., Voudouri, K. A., Mona, L., Mylonaki, M., Perrone, M. R., Costa, M. J., Sicard, M., Papagiannopoulos, N., Siomos, N., Burlizzi, P., Pauly, R., Engelmann, R., Abdullaev, S., and Pappalardo, G.: EARLINET evaluation of the CATS Level 2 aerosol backscatter coefficient product, Atmos. Chem. Phys., 19, 11743–11764, https://doi.org/10.5194/acp-19-11743-2019, 2019.

Qin, K., Zou, J., Guo, J., Lu, M., Bilal, M., Zhang, K., Ma, F., and Zhang, Y.: Estimating PM1 concentrations from MODIS over Yangtze River Delta of China during 2014–2017. Atmos. Environ., 195, 149–158, https://doi.org/10.1016/j.atmosenv.2018.09.054, 2018.

Reizer, M. and Juda-Rezler, K.: Explaining the high PM_{10} concentrations observed in Polish urban areas, Air Qual. Atmos Health., 9, 517–531, https://doi.org/10.1007/s11869-015-0358-z, 2015.

Rost, J., Holst, T., Sähn, E., Klingner, M., Anke, K., Ahrens, D., and Mayer, H.: Variability of PM10 concentrations dependent on meteorological conditions, Intern. J. Environ. Poll., 36, 3–18, https://doi.org/10.1504/IJEP.2009.021813, 2009.

Sakai, T., Nagai, T., Zaizen, Y., and Mano, Y.: Backscattering linear depolarization ratio measurements of mineral, sea-salt, and ammonium sulfate particles simulated in a laboratory chamber, Appl. Opt., 49, 4441–4449, https://doi.org/10.1364/AO.49.004441, 2010.

Schaap, M., Apituley, A., Timmermans, R. M. A., Koelemeijer, R. B. A., and de Leeuw, G.: Exploring the relation between aerosol optical depth and PM2.5 at Cabauw, the Netherlands, Atmos. Chem. Phys., 9, 909–925, https://doi.org/10.5194/acp-9-909-2009, 2009.

Schäfer, K., Emeis, S., Hoffmann, H., and Jahn, C.: Influence of mixing layer height upon air pollution in urban and sub-urban areas, Meteorol. Z., 15, 647–658, https://doi.org/10.1127/0941-2948/2006/0164, 2006.

Schmeisser, L., Andrews, E., Ogren, J. A., Sheridan, P., Jefferson, A., Sharma, S., Kim, J. E., Sherman, J. P., Sorribas, M., Kalapov, I., Arsov, T., Angelov, C., Mayol-Bracero, O. L., Labuschagne, C., Kim, S.-W., Hoffer, A., Lin, N.-H., Chia, H.-P., Bergin, M., Sun, J., Liu, P., and Wu, H.: Classifying aerosol type using in situ surface spectral aerosol optical properties, Atmos. Chem. Phys., 17, 12097–12120, https://doi.org/10.5194/acp-17-12097-2017, 2017.

Seinfeld, J. H., Bretherton, C., Carslaw, K. S., Coe, H., DeMott, P. J., Dunlea, E. J., Feingold, G., Ghan, S., Guenther, A. B., Kahn, R., Kraucunas, I., Kreidenweis, S. M., Molina, M. J., Nenes, A., Penner, J. E., Prather, K. A., Ramanathan, V., Ramaswamy, V., Rasch, P. J., Ravishankara, A. R., Rosenfeld, D., Stephens, G., and Wood, R.: Improving our fundamental understanding of the role of aerosol–cloud interactions in the climate system, P. Natl. Acad. Sci. USA, 113, 5781–5790, https://doi.org/10.1073/pnas.1514043113, 2016.

Sicard, M., Rocadenbosch, F., Reba, M. N. M., Comerón, A., Tomás, S., García-Vízcaino, D., Batet, O., Barrios, R., Kumar, D., and Baldasano, J. M.: Seasonal variability of aerosol optical properties observed by means of a Raman lidar at an EARLINET site over Northeastern Spain, Atmos. Chem. Phys., 11, 175–190, https://doi.org/10.5194/acp-11-175-2011, 2011.

Siomos, N., Balis, D. S., Poupkou, A., Liora, N., Dimopoulos, S., Melas, D., Giannakaki, E., Filioglou, M., Basart, S., and Chaikovsky, A.: Investigating the quality of modeled aerosol profiles based on combined lidar and sunphotometer data, Atmos. Chem. Phys., 17, 7003–7023, https://doi.org/10.5194/acp-17-7003-2017, 2017.

Siomos, N., Balis, D. S., Voudouri, K. A., Giannakaki, E., Filioglou, M., Amiridis, V., Papayannis, A., and Fragkos, K.: Are EARLINET and AERONET climatologies consistent? The case of Thessaloniki, Greece, Atmos. Chem. Phys., 18, 11885–11903, https://doi.org/10.5194/acp-18-11885-2018, 2018.

Sharma, A., Mandal, T., Sharma, S., Shukla, D., and Singh, S.: Relationships of surface ozone with its precursors, particulate matter and meteorology over Delhi, J. Atmos. Chem., 74, 451–474, https://doi.org/10.1007/s10874-016-9351-7, 2017.

Stachlewska, I., Piądłowski, M., Migacz, S., Szkop, A., Zielińska, A., and Swaczyna, P.: Ceilometer observations of the boundary layer over Warsaw, Poland, Acta Geophys., 60, 1386–1412, https://doi.org/10.2478/s11600-012-0054-4, 2012.

Stachlewska, I. S., Costa-Surós, M., and Althausen, D.: Raman lidar water vapour profiling over Warsaw, Poland, Atmos. Res., 194, 258–267, https://doi.org/10.1016/j.atmosres.2017.05.004, 2017a.

Stachlewska, I. S., Zawadzka, O., and Engelmann, R.: Effect of heat wave conditions on aerosol optical properties derived from satellite and ground-based remote sensing over Poland, Remote Sens., 9, 1199, https://doi.org/10.3390/rs9111199, 2017b.

Stachlewska, I. S., Samson, M., Zawadzka, O., Harenda, K. M., Janicka, L., Poczta, P., Szczepanik, D., Heese, B., Wang, D., and Borek, K. Tetoni, E., Proestakis, E., Siomos, N., Nemuc, A., Chojnicki, B. H., Markowicz, K. M., Pietruczuk, A., Szkop, A., Althausen, D., Stebel, K., Schuettemeyer, D., and Zehner, C.: Modification of local urban aerosol properties by long-range transport of biomass burning aerosol, Remote Sens., 10, 412, https://doi.org/10.3390/rs10030412, 2018.

Stein, A. F., Draxler, R. R., Rolph, G. D., Stunder, B. J. B., Cohen, M. D., and Ngan, F.: NOAA's HYSPLIT Atmospheric Transport and Dispersion Modeling System, B. Am. Meteorol. Soc., 96, 2059–2077, https://doi.org/10.1175/BAMS-D-14-00110.1, 2015.

Stocker, T., Qin, D., Plattner, G., Tignor, M., Allen, S., Boschung, J., Nauels, A., Xia, Y., Bex, V., and Midgley, P.: IPCC, 2013: Climate Change 2013: The Physical Science Basis, Contribution of Working Group I to the Fifth Assessment Report of the Intergovernmental Panel on Climate Change, Cambridge Univ. Press, Cambridge, UK, and New York, 1535 pp., 2013.

Stull, R. B.: An Introduction to Boundary Layer Meteorology, Kluwer Academic Publishers, Dordrecht, the Netherlands, 1988.

Szczepanik, D. and Markowicz, K.: The relation between columnar and surface aerosol optical properties in a background environment, Atmos. Poll. Res., 9, 246–256, https://doi.org/10.1016/j.apr.2017.10.001, 2018.

Szczepanik, D., Tetoni, E., Wang, D., and Stachlewska, I.: Lidar Based Separation of Polluted Dust Observed over Warsaw (Case Study on 09 August 2013), the 29th International Laser Radar Conference, Hefei, China, 24–28 June 2019, 1–5, 2019.

Szkop, A. and Pietruczuk, A.: Analysis of aerosol transport over southern Poland in August 2015 based on a synergy of remote sensing and backward trajectory techniques, J. Appl. Remote. Sens., 11, 016039, https://doi.org/10.1117/1.JRS.11.016039, 2017.

Tang, I. N.: Chemical and size effects of hygroscopic aerosol on light scattering coefficients, J. Geophys. Res., 101, 19245–19250, https://doi.org/10.1029/96JD03003, 1996.

The EARLINET publishing group 2000–2015: EARLINET All 2000–2015, World Data Center for Climate (WDCC) at DKRZ, https://doi.org/10.1594/WDCC/EARLINET_All_2000-2015, 2018.

Tian, P., Cao, X., Zhang, L., Sun, N., Sun, L., Logan, T., Shi, J., Wang, Y., Ji, Y., Lin, Y., Huang, Z., Zhou, T., Shi, Y., and Zhang, R.: Aerosol vertical distribution and optical properties over China from long-term satellite and ground-based remote sensing, Atmos. Chem. Phys., 17, 2509–2523, https://doi.org/10.5194/acp-17-2509-2017, 2017.

Trickl, T., Vogelmann, H., Flentje, H., and Ries, L.: Stratospheric ozone in boreal fire plumes – the 2013 smoke season over central Europe, Atmos. Chem. Phys., 15, 9631–9649, https://doi.org/10.5194/acp-15-9631-2015, 2015.

Trippetta, S., Sabia, S., and Caggiano, R.: Fine aerosol particles (PM_1): Natural and anthropogenic contributions and health risk assessment, Air Qual. Atmos. Hlth., 9, 621–629, https://doi.org/10.1007/s11869-015-0373-0, 2016.

Veselovskii, I., Kolgotin, A., Griaznov, V., Müller, D., Wandinger, U., and Whiteman, D. N.: Inversion with regularization for the retrieval of tropospheric aerosol parameters from multiwavelength lidar sounding, Appl. Opt., 41, 3685–3699, https://doi.org/10.1364/AO.41.003685, 2002.

Wałaszek, K., Kryza, M., and Werner, M.: The role of precursor emissions on ground level ozone concentration during summer season in Poland, J. Atmos. Chem., 75, 181–204, https://doi.org/10.1007/s10874-017-9371-y, 2018.

Wandinger, U., Freudenthaler, V., Baars, H., Amodeo, A., Engelmann, R., Mattis, I., Groß, S., Pappalardo, G., Giunta, A., D'Amico, G., Chaikovsky, A., Osipenko, F., Slesar, A., Nicolae, D., Belegante, L., Talianu, C., Serikov, I., Linné, H., Jansen, F., Apituley, A., Wilson, K. M., de Graaf, M., Trickl, T., Giehl, H., Adam, M., Comerón, A., Muñoz-Porcar, C., Rocadenbosch, F., Sicard, M., Tomás, S., Lange, D., Kumar, D., Pujadas, M., Molero, F., Fernández, A. J., Alados-Arboledas, L., Bravo-Aranda, J. A., Navas-Guzmán, F., Guerrero-Rascado, J. L., Granados-Muñoz, M. J., Preißler, J., Wagner, F., Gausa, M., Grigorov, I., Stoyanov, D., Iarlori, M., Rizi, V., Spinelli, N., Boselli, A., Wang, X., Lo Feudo, T., Perrone, M. R., De Tomasi, F., and Burlizzi, P.: EARLINET instrument intercomparison campaigns: overview on strategy and results, Atmos. Meas. Tech., 9, 1001–1023, https://doi.org/10.5194/amt-9-1001-2016, 2016.

Wang, D., Stachlewska, I. S., Song, X., Heese, B., and Nemuc, A.: Variability of boundary layer over an urban continental site based on 10 years of active remote sensing observations in Warsaw, Remote Sens., in review, 2019.

Wang, J. and Christopher, S. A.: Intercomparison between satellite-derived aerosol optical thickness and $PM_{2.5}$ mass: Implications for air quality studies, Geophys. Res. Lett., 30, 2095, https://doi.org/10.1029/2003GL018174, 2003.

Winker, D. M., Hunt, W. H., and McGill, M. J.: Initial performance assessment of CALIOP, Geophys. Res. Lett., 34, L19803, https://doi.org/10.1029/2007GL030135, 2007.

Wolff, H. and Perry, L.: Policy monitor: Trends in clean air legislation in Europe: Particulate matter and low emission zones, Rev. Environ. Econ. Policy, 4, 293–308, https://doi.org/10.1093/reep/req008, 2010.

Xie, C., Nishizawa, T., Sugimoto, N., Matsui, I., and Wang, Z.: Characteristics of aerosol optical properties in pollution and Asian dust episodes over Beijing, China, Appl. Opt., 47, 4945–4951, https://doi.org/10.1364/AO.47.004945, 2008.

Zang, Z. L., Wang, W. Q., You, W., Li, Y., Ye, F., and Wang, C. M.: Estimating ground-level $PM_{2.5}$ concentrations in Beijing, China using aerosol optical depth and parameters of the temperature inversion layer, Sci. Total Environ., 575, 1219–1227, https://doi.org/10.1016/j.scitotenv.2016.09.186, 2017.

Zawadzka, O., Markowicz, K., Pietruczuk, A., Zielinski, T., and Jaroslawski, J.: Impact of urban pollution emitted in Warsaw on aerosol properties, Atmos. Environ., 69, 15–28, https://doi.org/10.1016/j.atmosenv.2012.11.065, 2013.

Zhang, H., Wang, Y., Hu, J., Ying, Q., and Hu, X.-M.: Relationships between meteorological parameters and criteria air pollutants in three megacities in China, Environ. Res., 140, 242–254, https://doi.org/10.1016/j.envres.2015.04.004, 2015.

Zheng, S., Pozzer, A., Cao, C. X., and Lelieveld, J.: Long-term (2001–2012) concentrations of fine particulate matter ($PM_{2.5}$) and the impact on human health in Beijing, China, Atmos. Chem. Phys., 15, 5715–5725, https://doi.org/10.5194/acp-15-5715-2015, 2015.

Chapter 6 Target classification using a combination of lidar, cloud radar and microwave radiometer

6.1 Value-added of the PhD research

The atmospheric target classification is essential for studying aerosol and cloud properties. In general, target classification is a challenging task. Several groups developed target classification schemes using different techniques and methods. However, the majority of developments in this field were done in relation to satellite or airborne observations.

In the existing studies, atmosphere was classified using thresholds on the lidar products, such as: particle backscatter coefficient, and/or particle depolarization ratio and/or Ångström exponent. In my work, quantities used for classification were the scattering ratio (SR) to separate molecular, aerosol and cloud scattering regions and the backscatter colour ratio (CR) to discriminate an aerosol particle size. This is the first algorithm that uses thresholds on lidar-derived SR and CR products to be applied in the classification scheme (Wang et al., 2020b).

The new target classification algorithm combines different capabilities of three ground-based remote sensors – lidar, cloud radar, and microwave radiometer and can perform separation even in a meteorologically complicated situation. The workflow is in Figure 3.

Validated, state-of-the-art calibration and retrieval methods are applied to each instrument signals. Then the physical quantities are used in classification, so as

(i) obtained from the lidar: profiles of scattering ratio, backscatter colour ratio, particle depolarization ratio,
(ii) obtained from cloud radar: profiles of reflectivity and Doppler velocity, and
(iii) obtained from microwave radiometer: profiles of temperature and relative humidity.

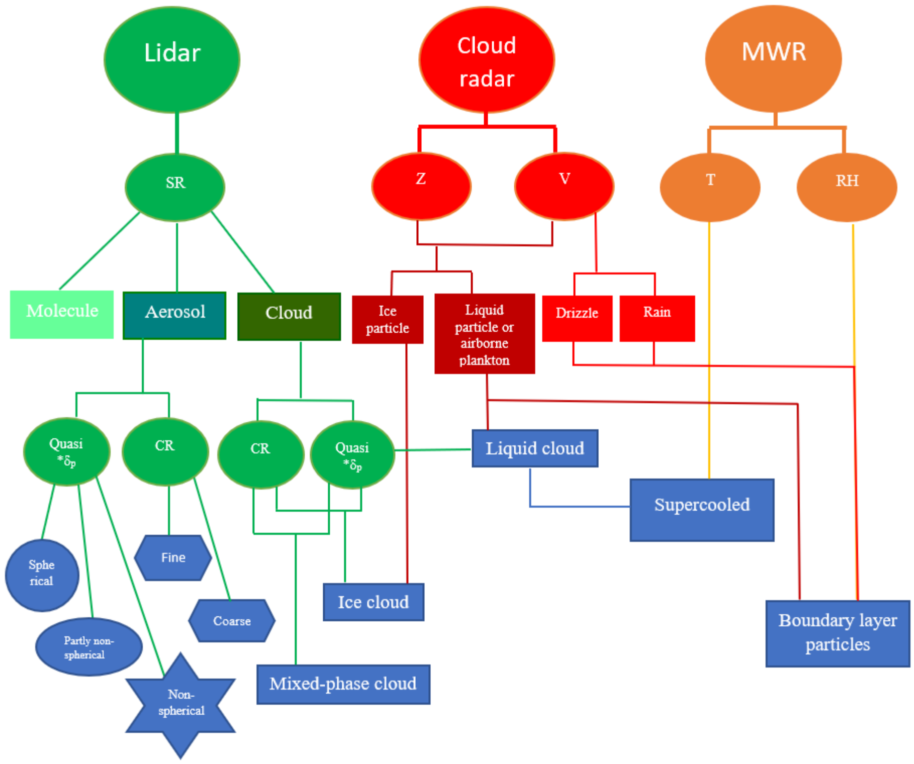

Figure 3. The flowchart of the target classification procedure using the combination of data from the lidar, cloud radar, and microwave radiometer; *adapted after Wang et al. 2020b.*

The new discrimination algorithm was established based on the thresholds that combine the existing knowledge for the individual sensors (results published in literature) with certain modifications assessed by conducting sensitivity studies of different parameters. Finally, a classification mask with different target types was achieved. The main advantage of this approach is that each instrument overcomes the limitations of the other ones in terms of detected targets. This makes it possible to thoroughly detect, characterize and discriminate very diversified (in sizes, shapes and phases) atmospheric aerosol, clouds and molecules, which would not be possible with a single-instrument approach.

Figure 4 shows 24 h measurement on 10 June 2019 in Rzecin (peatland environment) using the classification algorithm applied on the combined data of the three instruments. The atmosphere on that day was composed of very different aerosol and cloud types, rain and drizzle, whereby even melting layer phenomena was captured. The obtained retrieval for this case shows the excellent potential of the proposed method.

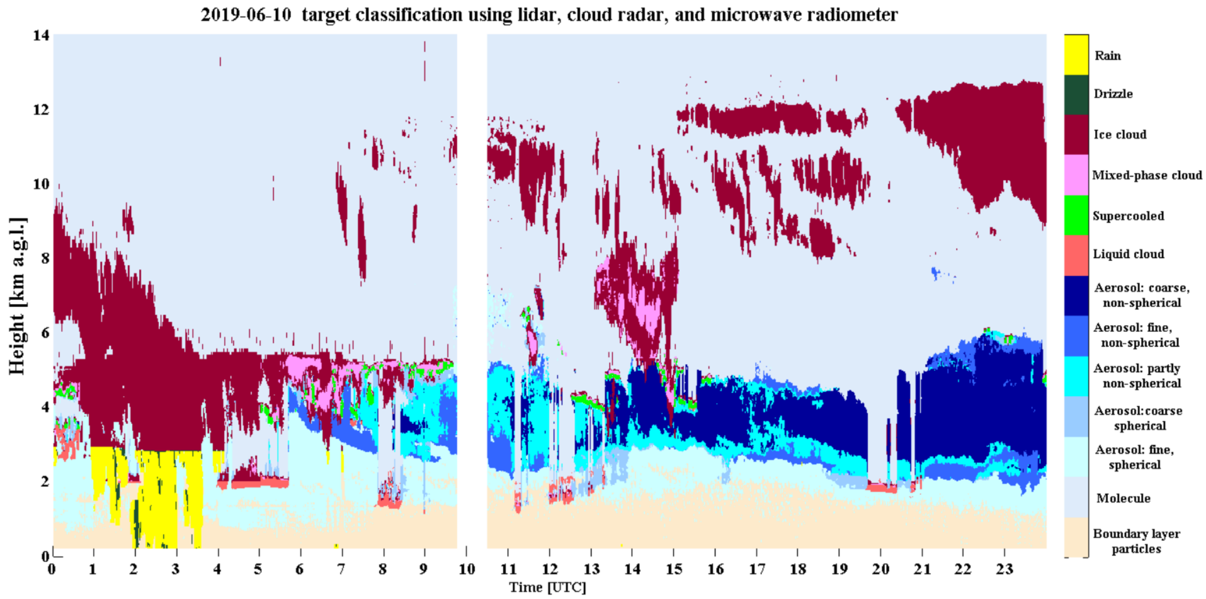

Figure 4. Synergy for molecule, aerosol and cloud identification derived from a combination of EMORAL Raman -polarization lidar, BASTA Doppler cloud radar, and HATPRO-G2 microwave radiometer over the PolWET site in Rzecin on 10 June 2019.

The new combined target classification created by the synergy of observations from three sensors is well demonstrated in Figure 4. The advantage of a synergetic use of ground-based instruments, together with the application of fully continuous measurements makes this methodology ideal to build in future detailed databases of aerosol and clouds observations and further studies of aerosol and cloud properties and types. It is crucial to use it in climatology research as a high-quality model input. The results obtained with such complex target classification scheme can also be used in research on the aerosol-cloud-ecosystem interaction process over wetland.

Currently, I am involved in a research related to long-term analyses of aerosol and cloud types over the Rzecin peatland.

6.2 Paper 3

Published paper title: Spatio-temporal discrimination of molecular, aerosol and cloud scattering and polarization using a combination of Raman lidar, Doppler cloud radar and microwave radiometer.

Authors: Dongxiang Wang, Iwona S. Stachlewska, Julien Delanoë, Dragos Ene, Xiaoquan Song, and Dirk Schüttemeyer.

Bibliographic record: Optics Express, 28 (14), 20117-20134, 2020.

Link: https://doi.org/10.1364/OE.393625.

Author Contributions (Stated explicitly in the published paper):

D.W. and I.S.S. wrote the paper, designed the study concept, conducted formal analyses, made an extensive literature review, and holistically interpreted the results. D.W. coded all algorithms and performed sensitivity tests to assess their performance. I.S.S. and D.S. contributed to the lidar development, setting up and conducting the experiment, as well as taking care of the quality assurance of lidar data. J.D. contributed with the cloud radar system development, the target classification for cloud radar, and its data interpretation. D.E. provided the microwave radiometer and contributed with the interpretation of its data. I.S.S. and X.S. developed a synergetic algorithm for target classification and contributed to the assessment of classification quality. I.S.S., D.W., D.E. and X.S. obtained funding to conduct the research. All authors contributed to the interpretation and discussion of the results and conducted revisions of the paper.

Research Article Vol. 28, No. 14 / 6 July 2020 / *Optics Express* 20117

Optics EXPRESS

Spatio-temporal discrimination of molecular, aerosol and cloud scattering and polarization using a combination of a Raman lidar, Doppler cloud radar and microwave radiometer

DONGXIANG WANG,[1] IWONA S. STACHLEWSKA,[1,*] JULIEN DELANOË,[2] DRAGOS ENE,[3] XIAOQUAN SONG,[4] AND DIRK SCHÜTTEMEYER[5]

[1] *Faculty of Physics, University of Warsaw (FUW), Warsaw 00-927, Poland*
[2] *LATMOS/IPSL, UVSQ Université Paris-Saclay, Sorbonne Université, CNRS, Guyancourt 78280, France*
[3] *National Institute of R&D for Optoelectronics (INOE), Magurele-Bucharest 07712, Romania*
[4] *College of Information Science and Engineering, Ocean University of China (OUC), Qingdao 266100, China*
[5] *European Space Research and Technology Centre, European Space Agency (ESA), Noordwijk 2201, The Netherlands*
[*] *iwona.stachlewska@fuw.edu.pl*

Abstract: The combined data from the ESA Mobile Raman Polarization and Water Vapor Lidar (EMORAL), the LATMOS Bistatic Doppler Cloud Radar System for Atmospheric Studies (BASTA), and the INOE Microwave Radiometer (HATPRO-G2) have been used to explore the synergy for the spatio-temporal discrimination of polarization and molecular, aerosol and cloud scattering. The threshold-based methodology is proposed to perform an aerosol-cloud typing using the three instruments. It is demonstrated for 24 hours of observations on 10 June 2019 in Rzecin, Poland. A new scheme for target classification, developed collaboratively by the FUW and the OUC, can help determine molecules, aerosol (spherical, non-spherical, fine, coarse), cloud phase (liquid, ice, supercooled droplets) and precipitation (drizzle, rain). For molecular, aerosol, and cloud discrimination, the thresholds are set on the backward scattering ratio, the linear particle depolarization ratio and the backscatter colour ratio, all calculated from lidar signals. For the cloud phase and precipitation categorization, the thresholds are set on the reflectivity and the Doppler velocity derived from cloud radar signals. For boundary layer particles, precipitation, and supercooled droplets separation, the thresholds are set on the profiles of temperature and relative humidity obtained by the microwave radiometer. The algorithm is able to perform separation even under complicated meteorological situation, as in the presented case study.

1. Introduction

The 24/7 ground-based remote sensing measurements of aerosol and clouds are an important source of information, as they can obtain high resolution, long-term data in well-defined areas on a continuous basis [e.g. 1–3]. Their data products are closer to target particles than satellite observations and have a better spatio-temporal resolution and accuracy [1]. Knowledge about aerosol and clouds on such a scale can help better assess their direct and indirect effects on radiation transfer and the balance of the Earth-atmosphere system [4–7]. As the effects of aerosol and clouds can differ significantly, depending on their optical thickness and altitude [5,6,8], they should be observed, if possible, at the same time, using instruments that are well suited for this purpose.

#393625 https://doi.org/10.1364/OE.393625
Journal © 2020 Received 24 Mar 2020; revised 6 Jun 2020; accepted 15 Jun 2020; published 24 Jun 2020

Research Article Vol. 28, No. 14 / 6 July 2020 / *Optics Express* 20118
Optics EXPRESS

In many studies, aerosol and/or cloud properties are derived from measurements conducted with airborne sensors [e.g. 9–11] and space-borne sensors [e.g. 12–15]. Space-borne sensors can also provide a good temporal coverage. However, in this case the major challenge is to obtain information on aerosol and clouds with a high vertical resolution [e.g. 12,14]. Another drawback is that satellite sensors cannot conduct observations over the site of interest continuously. Thus, both active and passive ground-based remote sensing observations are necessary to complement airborne and satellite observations.

Doppler cloud radars provide information on cloud and precipitation particles, as well as on cloud dynamics [e.g. 16–19]. Cloud radars are active remote sensors, and they are more sensitive to large particles, compared with lidar. They are able to penetrate optically thick clouds, but fail to detect aerosol and clouds composed of small-sized particles [9,20]. Lidars are capable of measuring aerosol, and almost all cloud types, as long as they are the first encountered layer and their optical depth is low [e.g. 21–24]. Lidars are also active remote sensors, but their backscatter signal is proportional to the second moment of the particle size distribution, hence compared with cloud radars, lidar signals are sensitive to optically thin clouds [e.g. 12], Cirrus and contrails [e.g. 25], as well as supercooled water layers [e.g. 9,26], but cannot penetrate optically thick clouds, because of strong signal attenuation [e.g. 27]. Scanning microwave radiometers are passive remote sensors that can provide integrated-column measurements of integrated water vapor (IWV) and liquid water path (LWP), as well as profiles of relative humidity and temperature [28,29].

The target classification schemes can be applied either solely to the cloud radar (e.g. cloud droplets, ice, and precipitating particles) [30,31] or to lidar data (e.g. aerosol typing [32]). Combining lidar and cloud radar measurements can result in more complete information on aerosol and cloud properties, their vertical structure and occurrence [e.g. 33,34]. Microwave radiometer products can support target classification in combination with lidar/radar (e.g. [12,19]). The synergy between cloud radar, lidar, and microwave radiometers has proved effective for retrieving cloud properties such as ice/liquid water content and effective radius [10,12].

The aim of this paper is to propose a new threshold based methodology that can be used for studies of aerosol and cloud properties and types, including the cloud phase, using the synergy of lidar, cloud radar and microwave radiometer to provide better forecasting and climate models [18,35].

The paper is organized as follows. In section 2, instrumentation and typical data products are described. The methodology and the data products that are used for the molecules-aerosol-cloud classification are described in section 3. The current classification methodology is discussed in section 4. Section 5 gives details on the new thresholds proposed for the target classification. The results and their repercussions are provided for in section 6. The paper is summarized in section 7.

2. Instrumentation and derived data products

The three remote sensing instruments, the Raman-polarization lidar, the Doppler cloud radar and the microwave radiometer were installed in a close proximity on 10 June 2019 in Rzecin (52°45'N, 16°18'E, 54 m a.s.l.), Poland. The distance between them was fewer than 15 m. The instruments do not measure the same volume: the lidar footprint is the smallest, next is the cloud radar (half beam width 0.4°), and the microwave radiometer is the largest, which has an impact on retrievals. All instruments operated in a 24/7 detection mode, providing profiles covering almost the entire troposphere, whereby the spatial and temporal resolution of the profiles provided by each instrument was different. Each instrument is described below.

The ESA Mobile Raman Lidar (EMORAL) uses as a radiation source the Nd-YAG laser (SpitLight 400, InnoLas, Germany), operating at 1064 nm (112 mJ), 532 nm (103 mJ) and 355 nm (128 mJ). The laser emits all three wavelengths to the atmosphere simultaneously and collinearly,

Research Article Vol. 28, No. 14 / 6 July 2020 / *Optics Express* 20119
Optics EXPRESS

with a repetition rate of 10 Hz and pulse lengths of 5-7 ns. The backward scattered radiation is collected with a Cassegrain telescope (primary mirror of 300 mm, adjustable field of view of 2-3.6 mrad), then separated and filtered to detect 8 channels: 3 elastic channels (1064 nm, 532 nm, and 355 nm), 3 vibrational Raman channels (for nitrogen at 387 nm, 607 nm and for water vapour at 407 nm), and 2 depolarization channels at 532 nm and 355 nm. All signals are recorded with an analogue and photon-counting mode, using the 16-bits transient recorders (TR40-160, Licel, Germany), except for 1064 nm (only analogue). The raw signal height resolution is 3.75 m and the time resolution is adjustable (from 2 s to 1 min). The full overlap height is at 400 m, the effect of overlap below this altitude is neglected, no overlap correction function is applied. The level-1 products comprise attenuated backscatter signals and the volume depolarization ratio. The level-2 products are the water vapour mixing ratio [36], the atmospheric boundary layer height [37], the range of aerosol optical properties [3,38–40], and the backward scattering ratio (this paper). The level-3 products comprise microphysical parameters [41]. The combination of the different level products obtained at different wavelengths can be used for aerosol and cloud typing in terms of particle size and shape, i.e. to assess aerosol-free molecular atmosphere, fine/coarse particles, spherical/non-spherical particles, water droplets, ice crystals or their mixtures. The profiles of the lidar-derived atmospheric properties used in this paper are obtained for a vertical resolution of 3.75 m and the time of 2 s. A lidar evaluation scheme applied for the data evaluation is compliant with the Quality Assurance recommendations of the European Aerosol Research Lidar Network (EARLINET) developed within the Aerosol, Clouds, and Trace Gases Research Infrastructure (ACTRIS), i.e. the full quality assure (QA) tests are applied (tele cover test, dark measurement, depolarization calibration, trigger delay [42]). The tools for the high quality lidar data evaluation are described in [e.g. 43,44].

The Bistatic Radar System for Atmospheric Studies (BASTA) is a semi-operational 95 GHz Doppler cloud radar, which uses the frequency-modulated continuous wave (FMCW) technique. The technique can be highly sensitive with much less power than traditional pulsed systems, there are some advantages and some disadvantages of using it [45]. It was installed next to the EMORAL lidar (circa 15 m away). It provides real time 24/7 vertical observations of the cloud structure and properties (such as cloud fraction, cloud phase, cloud water content, etc). It uses a specific signal processing technique in such a way that the radar can provide high-quality measurements of cloud and fog. The main products are reflectivity and Doppler velocity (level-1), obtained successively with 12.5 m, 25 m and 100 m vertical resolution and 3 s time resolution. The lower limit is 125 m for all modes. The 12.5 m mode is limited to 12 km. The 25 m and 100 m modes cover the range up to 18 km. A merged product is derived making the most of the sensitivity and resolution of each mode, i.e. a combination of different vertical resolutions is applied at different altitude ranges. The resulting vertical resolution of the merged product is height-dependent and it is of 12.5 m below 0.5 km, 25 m between 0.5 and 5 km, and 100 m above 5 km. The integration time is 9 s for the merged product. The level-2 products (rain, drizzle, ice cloud and liquid particles and droplets) and the level-3 products (microphysical cloud properties) can also be obtained. The three successive modes are used for specific applications: the 12.5 m vertical resolution mode is dedicated to fog and low clouds, the 25 m mode is for liquid and ice mid-tropospheric clouds, and the 100 m is ideal for optically thin, high-level ice clouds. The radar comes with a set of products dedicated to cloud and fog studies. For instance, a cloud mask, corrected Doppler velocity and multi-mode products combining a high sensitivity mode and high-resolution mode are provided. More details can be found in [10,45] and http://basta.projet.latmos.ipsl.fr, last access: 28 February 2020. The cloud radar has been calibrated based on the methodology given in [45,46,47], which is typically applied for high-quality data retrieval in the Cloud Observation Network (CLOUDNET) within the ACTRIS.

The microwave radiometer (HATPRO-G2, Radiometer Physics GmbH) was installed in a proximity of the BASTA cloud radar (circa 2 m away). The microwave radiometer consists of two

Research Article Vol. 28, No. 14 / 6 July 2020 / Optics Express 20120
Optics EXPRESS

working bands at 22–31 and 51–58 GHz, each with seven channels [48]. The vertical resolution of this instrument is much coarser than that for the other two instruments. Measurements with a temporal resolution of 15 s and a height-dependent vertical resolution: 200 m from 0 to 2 km, 400 m from 2 to 5 km, and > 500 m for the heights above 5 km [49]. The level-1 products are brightness temperatures. The level-2 products are integrated water vapour (IWV), liquid water path (LWP), and the vertical profiles of absolute humidity (AH), relative humidity (RH), water vapor (WV), temperature (T) and boundary layer height (ABL). The profiles of temperature and water vapour are calculated from the brightness temperatures using statistical regression algorithms [50]. To ensure high quality of the observation, the absolute calibration is done using liquid nitrogen, according to the details in [51]. The data quality control was done compliant with the methodology described in [48].

3. Methodology

Different optical properties of aerosol and cloud can be obtained from lidar signals [e.g. 22,24,52]. The backscatter signal P can be described with the classical elastic lidar equation:

$$P = C\frac{O}{R^2}(\beta_p + \beta_m)\exp\left\{-2\int_0^R(\alpha_p + \alpha_m)dr\right\} \tag{1}$$

where C is the instrumental constant (system factor), R is the range of the lidar signal, O is the overlap function that equals 1 at the complete overlap between the laser beam and the full field of view of the telescope, β_p is the particle backscatter coefficient, β_m is the molecular backscatter coefficient, α_p is the particle extinction coefficient, α_m is the molecular extinction coefficient.

When the lidar system is equipped with the Raman channels, the extinction coefficient profiles can be derived using the Raman method. It has its limitations related to a relatively weak Raman scattering cross-section at the detected wavelength in comparison to the elastic scattering cross-section at the initial wavelength. This matters especially if the Raman method is applied during the daytime. Sunlight radiation affects the signal to noise ratio, which can be improved at the cost of reducing temporal and spatial resolutions. This limits the retrieval to 2 km in the daytime for a 30-minute averaged profile and 120 m height resolution. At night, profiles reach 3.5 km for the same averaging. Hence, the Raman method was considered as not sufficiently consistent in terms of quality and performance to provide products for use in the 24/7 classification scheme. Therefore, the Klett-Fernald method was chosen [53,54].

The particle backscatter (β_p) and extinction (α_p) coefficient profiles in the Klett-Fernald method are obtained using elastic lidar signals [Eq. (1)] by solving the Bernoulli differential equation with the assumption of the height independent particle lidar ratio ($LR_p = \alpha_p / \beta_p$), calibrated at a certain height-range of the atmosphere, where only molecular scattering occurs [53,54]. There is an obvious difficulty to choose the appropriate lidar ratio and the calibration range in the presence of low-level clouds or when aerosol load is high. Therefore, the attenuated backscatter coefficient (β_a) is often used instead, as described in [24], defined in Eq. (2):

$$\beta_a = \frac{PR^2}{C} \tag{2}$$

The C can be calculated as in Eq. (3):

$$C = \frac{PR^2}{(\beta_p + \beta_m)\,O}\exp\left\{2\int_0^R(\alpha_p + \alpha_m)dr\right\} \tag{3}$$

The C is generally stable in a daytime scale [24], thus it can be calculated once per day for the clear sky observation period. If there is no clear sky on the observational day, the C can be calculated for adjacent days with a clear sky period. The β_p profiles used for the C calculation

Research Article Vol. 28, No. 14 / 6 July 2020 / Optics Express 20121
Optics EXPRESS

can be computed with the aforementioned approach [53,54] and the β_m can be calculated using the atmospheric profiles of the 1976 US standard atmosphere (note that rawinsondes can be used, if available close to the observational site). The particle lidar ratio (LR_p) of 55 sr can be used as a reference, as such it is applied at several European continental sites for long-term statistical studies [e.g. 3]. The final system factor C is calculated as the mean value of the height between 1 and 2 km in Eq. (3).

The determination of the quasi-particle backscatter coefficient (${}^{quasi}\beta_p$) is in accordance with to the reference [24], i.e. it is done as a 2-step process, where the Eq. (4) gives the first guess of ${}^{quasi*}\beta_p$ (indicated with *) that is used to obtain the quasi-particle extinction coefficient (${}^{quasi}\alpha_p$), as in the Eq. (5). Then the Eq. (6) is used to calculate the final quasi-particle backscatter coefficient value.

$$ {}^{quasi*}\beta_p = \beta_a\, exp\left\{2\int_0^R \alpha_m dr\right\} - \beta_m \tag{4}$$

$$ {}^{quasi}\alpha_p = {}^{quasi*}\beta_p\, LR_p \tag{5}$$

$$ \beta_p \approx {}^{quasi}\beta_p = \beta_a\, exp\left\{2\int_0^R ({}^{quasi}\alpha_p + \alpha_m) dr\right\} - \beta_m \tag{6}$$

The linear volume depolarization ratio (δ_v) can be derived from the lidar data as the ratio of the backscatter signal from the vertically-polarized signal channel (P_v) and the corresponding parallel-polarized signal channel (P_p), as in Eq. (7).

The linear particle depolarization ratio (δ_p) is nearly equal to the linear quasi-particle depolarization ratio (${}^{quasi}\delta_p$), derived as in Eq. (8). Note that the β_p is replaced by the ${}^{quasi}\beta_p$ (defined as in Eq. (6)) for this calculation:

$$ \delta_v = \frac{P_v}{P_p} \tag{7}$$

$$ \delta_p \approx {}^{quasi}\delta_p = \frac{(1+\delta_m)\delta_v\left(1+\frac{{}^{quasi}\beta_p}{\beta_m}\right) - (1+\delta_v)\delta_m}{(1+\delta_m)\left(1+\frac{{}^{quasi}\beta_p}{\beta_m}\right) - (1+\delta_v)} \tag{8}$$

where δ_v is the linear volume depolarization ratio, δ_m is the linear depolarization ratio of air molecules. The δ_v and δ_p quantities in Eqs. (7) and (8), are obtained using the $\Delta 90$ depolarization calibration [55,56]. These quantities proved to be very useful to distinguish between spherical (low depolarization ratios) and non-spherical particles (high depolarization ratios) [e.g. 57,58].

The properties of cloud and precipitation can be obtained from the Doppler cloud radar [e.g. 10,16]. The cloud radar target classification (rain, drizzle, ice cloud and liquid) is retrieved from the level-1 products (i.e. the reflectivity and the Doppler velocity). In a first approximation, assuming small particles and therefore in Rayleigh regime, the reflectivity (Z) can be represented as in Eq. (9) for the number of reflective particle diameters $N(D)$ and the size of reflective particles D.

$$ Z = \int_0^\infty N(D) D^6 dD \tag{9}$$

When it comes to the microwave radiometer (MWR), temperature profiles can be used to provide an important reference for the separation of aerosol layers (e.g. supercool layer, liquid cloud) and cloud types (liquid, ice or mixed phase). The relative humidity can be used as an important reference for separation of a dry and wet environment.

Research Article Vol. 28, No. 14 / 6 July 2020 / Optics Express 20122
Optics EXPRESS

4. Current classification methodology

An atmospheric constituent/target classification is, in general, a challenging task. It has been developed by several groups [e.g. 9,12,24,32], using different techniques and methods applied for the separation of different targets throughout the atmosphere. The majority of developments in this field were done in relation to satellite observations with Cloud-Aerosol Lidar and Infrared Pathfinder Satellite Observations CALIPSO (National Aeronautics and Space Administration, NASA, USA, and National Centre for Space Studies, CNES, France) and CloudSat (NASA). A methodology for the classification of aerosol, rain, liquid, supercooled and ice clouds using datasets from the Cloud Profiling Radar onboard CloudSat and the Cloud-Aerosol Lidar with Orthogonal Polarization (CALIOP) onboard CALIPSO, collocated in time and space is extensively discussed in [9]. Categorization of molecular, aerosol, rain, supercooled and ice clouds using the A-Train satellite constellation data – spaceborne lidar, radar and infrared radiometers was proposed by [12]. Another scheme for classification of ice cloud, mixed-phase cloud, and supercooled layers in Arctic region using airborne cloud radar and lidar data is discussed in [23]. In the study of [23], the lidar was mainly used for identifying supercooled layers, while in [12] the lidar was also used to separate molecular and aerosol in addition to identifying the supercooled layers. In none of these papers a further classification with regards to the aerosol type nor the aerosol shape was attempted. Categorizations of aerosol and cloud types using the thresholds on the ground-based lidar, but with no rain/drizzle and thick clouds typing due to the usage of a single instrument was proposed by [24].

In existing studies, atmosphere was classified using thresholds on the lidar products, such as: particle backscatter coefficient [e.g. 22,24], and/or particle depolarization ratio [e.g. 24,59], and/or Ångström exponent [e.g. 24,60]. The different thresholds are described below.

The particle backscatter coefficient (β_p) was used to discriminate molecular, aerosol, and cloud scattering based on space-borne [e.g. 22,61] and ground-based observations [24]. For aerosol and clouds classification of CALIPSO lidar, the study in [61] considered clear-sky atmosphere for $\beta_p(1064\,\mathrm{nm}) < 1\times10^{-8}\,\mathrm{m^{-1}sr^{-1}}$, clouds for $\beta_p\,(1064\,\mathrm{nm}) > 2\times10^{-5}\,\mathrm{m^{-1}sr^{-1}}$, and aerosol for values in between. For the CALIPSO lidar in the study of [59], a threshold of $\beta_p\,(1064\,\mathrm{nm}) > 1\times10^{-5}\,\mathrm{m^{-1}sr^{-1}}$ was used for discrimination of clouds from aerosol. In the study of [24], for ${}^{quasi}\beta_p\,(1064\,\mathrm{nm}) > 2\times10^{-7}\,\mathrm{m^{-1}sr^{-1}}$ ice clouds were separated from aerosol for the ground-based lidar. The latter threshold was considered as an equivalent to the one used in the CALIPSO feature mask, i.e. the attenuated backscatter $\beta_a\,(532\,\mathrm{nm}) > 5\times10^{-7}\,\mathrm{m^{-1}sr^{-1}}$ separating ice clouds from aerosol [22].

The particle depolarization ratio (δ_p) was used to discriminate spherical and non-spherical particles [22,24]. The particle was regarded as non-spherical with the $\delta_p\,(532\,\mathrm{nm}) > 0.2$ and as spherical when $\delta_p\,(532\,\mathrm{nm}) < 0.05$ [22]. Particles were considered as non-spherical for the quasi-particle depolarization ratio ${}^{quasi}\delta_p\,(532\,\mathrm{nm}) > 0.2$ and spherical for ${}^{quasi}\delta_p\,(532\,\mathrm{nm}) < 0.07$ and a mixture for values in between [24].

The Ångström exponent ($\AA E$) was used to discriminate aerosol particles size and aerosol type [e.g. 24]. The ÅE can be calculated using e.g. particle extinction coefficients, particle backscatter coefficients, aerosol optical depths (the obtained values are not directly comparable). The threshold of $\AA E\,(532/1064\,\mathrm{nm}) \geq 0.75$ was used for separating small particles from the large ones in the aerosol classification scheme [24].

In the current paper, other quantities are proposed to be used for classification, namely the scattering ratio (SR) to separate molecular, aerosol and cloud scattering regions and the backscatter colour ratio (CR) to discriminate an aerosol particle size. This is the first algorithm that uses thresholds on lidar-derived SR and CR products to be applied in the classification scheme based on the lidar, cloud radar, and microwave radiometer.

Research Article Vol. 28, No. 14 / 6 July 2020 / Optics Express 20123

Optics EXPRESS

5. Improved target classification

A new classification scheme is proposed. It can be currently considered as the most advanced in terms of discrimination of molecular, aerosol, and cloud scattering and polarization properties. The proposed categorization relies on physical features (e.g. scattering properties, depolarizing properties, particle size) and it is based on a literature review and a sensitivity study on how the change in the threshold affects the consistency of the results. Currently, there are no operational algorithms that use the proposed combination of instruments, whereby this combination has some significant advantages. Target classification workflow based on SR, ${}^{quasi}\delta_p$, CR, Z, V, T and RH profiles is illustrated in Fig. 1. The data product profiles from the cloud radar (12.5, 25, and 100 m vertical and 9 s time resolutions), the microwave radiometer (200, 400, 500 m of vertical and 15 s time resolutions) are the lidar (30 m vertical and 30 s time resolutions) are combined to ensure that all observe a similar column of the atmosphere. Many classification schemes prefer not to use threshold values on their own, unless the threshold value provides a clear separation between two classes [e.g. 9,22,24]. This is also in our case.

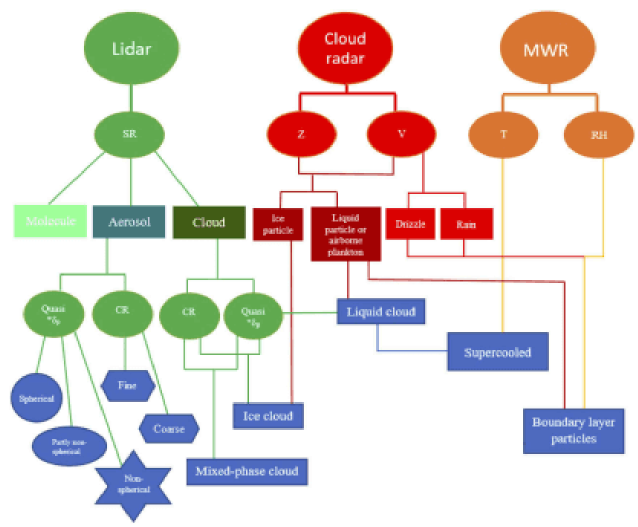

Fig. 1. The flowchart of the target classification procedure using the combination of data from the Raman-polarization lidar, Doppler cloud radar, and microwave radiometer (MWR).

5.1. *Target classification of lidar with new threshold types*

A new method, based on the thresholds on the scattering ratio (SR), is applied in this study, whereby the SR is defined as the ratio of the quasi-total backscatter coefficient (${}^{quasi}\beta$) and the molecular backscatter coefficient (β_m), as Eq. (10):

$$SR = \frac{{}^{quasi}\beta}{\beta_m} = \frac{({}^{quasi}\beta_p + \beta_m)}{\beta_m} \tag{10}$$

The SR of 1 represents no scattering on aerosol particles in the atmosphere. The SR (532 nm) values for tropospheric aerosol are within the range of 1.2–1.33 over North India and Western

Research Article Vol. 28, No. 14 / 6 July 2020 / Optics Express 20124
Optics EXPRESS

China, obtained based on the CALIOP lidar [62]. Over the United States of America, the *SR* (532 nm) of dust and smoke in the troposphere is of 2.3 and 2.9, based on the NASA Langley airborne High Spectral Resolution Lidar (HSRL) measurements [63]. The *SR* (532 nm) of volcanic ash aerosol ranges from 1.1 to 3.5 using lidar observations in Russia [64]. The *SR* (532 nm) of aerosol under dust conditions is distributed between 3 and 9 in the central Himalayas [65]. The *SR* (532 nm) > 5 was observed by [66] using airborne lidar when the mineral dust appeared in the Arctic. In most cases reported in literature, the threshold of the lidar derived *SR* at 532 nm used for the separation of molecule from aerosol is within 1.1-1.3. In this study, we set the *SR* (532 nm) < 1.4 ± 9% for molecule. The *SR* (532 nm) > 10 was considered as cloud [66], thus we set the *SR* (532 nm) > 10 ± 20% to discriminate clouds. The values between the two thresholds denote aerosol (Table 1).

Table 1. The new classification thresholds applied on the backscatter scattering ratio (SR), quasi-particle depolarization ratio ($^{quasi}\delta_p$), and backscatter colour ratio (CR) used for molecules, aerosol and cloud typing based on lidar observations.

Raman-polarization lidar measurements			
	New method	Standard method	New method
	Scattering ratio (*SR*)	Quasi-particle depolarization ratio ($^{quasi}\delta_p$)	Colour ratio (*CR*)
Molecules	SR < 1.4 ± 9%	-	-
Aerosol	1.4 ± 9% ≤ SR < 10 ± 20%		
fine			CR > 2.5 ± 5%
coarse			CR < 1.6 ± 5%
spherical		$^{quasi}\delta_p$ < 0.08 ± 13%	
non-spherical		$^{quasi}\delta_p$ ≥ 0.18 ± 11%	
partly non-spherical		0.08 ± 13% ≤ $^{quasi}\delta_p$ < 0.18 ± 11%	1.6 ± 5% ≤ CR ≤ 2.5 ± 5%
Cloud	SR ≥ 10 ± 20%		
liquid		$^{quasi}\delta_p$ < 0.10 ± 13%	-
ice		$^{quasi}\delta_p$ ≥ 0.35 ± 11%	CR < 0.5 ± 5%
mixed-phase		0.10 ± 13% ≤ $^{quasi}\delta_p$ < 0.35 ± 11%	CR < 1 ± 5%

The sensitivity constitutes a reference for the selected threshold. Taking *SR* < 1.4 ± 9% as an example, means that *SR* within 1.3-1.5 can be used as a threshold for separating molecules and aerosol. The % denotes the actual sensitivity range, in this example, the threshold was fixed initially at 1.4 and a solution (categorization) was obtained. The sensitivity of the solution was assessed by introducing a small change, applied in an iterative way. The new result (obtained after the change was introduced) was compared with the initial solution. If the profiles (categories) were not significantly different (< 5%), further change was introduced. When the initial and changed profiles differed above this limit, it was considered an actual limit (listed in the Table 1). In this example, introduction of ± 9% change of the initial threshold value brought no significant change in the derived classification. Thus the sensitivity relating to all thresholds applied on lidar products established uncertainty in terms of %. Sensitivity related to instruments is not discussed.

A new methodology, based on the thresholds on the backscatter colour ratio (*CR*), is applied in this study, whereby the *CR*, which is related to aerosol size, is defined as the ratio of the quasi particle backscatter coefficient at 532nm and 1064 nm, as Eq. (11):

$$CR\,(532/1064) = \frac{^{quasi}\beta_{p\,532}}{^{quasi}\beta_{p\,1064}} \tag{11}$$

Research Article Vol. 28, No. 14 / 6 July 2020 / Optics Express 20125

Optics EXPRESS

The reported range of *CR* (532/1064) was 1.7-3 for pollution, 0.5-1.5 for pure dust, 1.16-1.96 for mixed dust, > 2.6 for smoke, and < 1.7 for marine particle, based on airborne HSRL observations over four field sites in Europe and Africa [67]. The range of *CR* (532/1064) for anthropogenic pollution 1.5-2.5, pure dust 0.5-1.5, mixed dust 1.0-2.0, smoke 1.8-2.8, and marine particle 1.2-1.6 were reported based on airborne HSRL observations over North America from 2006 until 2010 [60]. Moreover, the mean value of *CR* (532/1064) was determined, for pollution it was 1.8 ± 0.1, for dust 0.70 ± 0.07, for smoke 1.7 ± 0.1, and for marine 1.1 ± 0.1 [68]. In literature, values of *CR* (532/1064) > 2.6 are typically associated with fine particles (pollution, smoke) and *CR* (532/1064) < 1.6 with coarse particles (dust, marine particle). The *CR* (532/1064) < 0.8 is reported for ice particles [69]. In order to make a more precise classification on fine and coarse particles, in the current study, fine particles are considered for *CR* (532/1064) > $2.5 \pm 5\%$, while coarse particles for *CR* (532/1064) < $1.6 \pm 5\%$. In addition, ice particles are considered for *CR* (532/1064) < $0.5 \pm 5\%$ (Table 1).

The low values of δ_p (532) < 0.01 were considered as due to very small spherical particles (e.g. [70,71]), values between 0.04-0.1 as spherical particles [72,73], 0.2-0.35 as non-spherical particles (e.g. [72]). A mixture of non-spherical and spherical particles was considered for) between $0.07 < \delta_p$ (532 nm) < 0.2, while above 0.2 the particles are categorized as large and non-spherical [58,74]. In most cases reported in literature, lidar derived δ_p (532 nm) is < 0.1 for spherical particles (e.g. smoke, marine, pollution) and δ_p (532nm) > 0.2 for non-spherical particles (e.g. dust, ice particles). The values in between are seen for partly non-spherical particles (e.g. small pollen grains, mixture of anthropogenic pollution with dust and/or biomass burning smoke). In order to make a more precise classification on spherical and non-spherical particles, in the current study, aerosol particles characterized by ${}^{quasi}\delta_p$ (532 nm) > $0.18 \pm 11\%$ are regarded as non-spherical particles and ${}^{quasi}\delta_p$ (532 nm) < $0.08 \pm 13\%$ as spherical ones, and partly non-spherical in between (Table 1).

The new threshold types/values used for the separation of molecule, aerosol and cloud spatio-temporal ranges from the lidar observations are listed in Table 1. The *SR* was used for identifying and discriminating molecule, aerosol and clouds. The shape of an aerosol particle was classified by ${}^{quasi}\delta_p$ that consist of spherical, partly non-spherical and non-spherical particles discrimination. The particle size was assessed based on the *CR*. An example of the profiling in terms of these properties is shown in Fig. 2.

5.2. Target classification of cloud radar

The target classification of the cloud radar is based on the existing scheme [e.g. 9,10,12,45] and consists of the following five classes: ice particle, liquid particle or airborne plankton (during summer), drizzle, rain, and no cloud. The liquid area (liquid cloud, drizzle and rain) is defined by the threshold on the Doppler velocity and reflectivity, as in [12,75]. The typical thresholds, as in other studies, were used for the radar-alone classification scheme, which are listed in Table 2. One can also identify melting layers, e.g. by searching in the Doppler velocity for the altitude where particles start to fall [9] or in the reflectivity for the step-wise increase at the altitude where ice particles start to get coated in liquid water [10]. In our study, the melting layer is defined as below 6km, for the Doppler velocity gradient $dV/dr \geq 0.021 s^{-1}$ and reflectivity gradient $dZ/dr \leq 0.025$ dBz^{-1}. An example of the profiling in terms of these properties is shown in Fig. 3.

5.3. Target classification of the microwave radiometer with new threshold types

The microwave radiometer data proved to be useful in the target classification based on space-borne [e.g. 12], airborne [e.g. 9] and ground-based measurements [e.g. 18]. The profiles of temperature (*T*) indicate warm (> 0°C) and cold areas (< 0°C) throughout the troposphere. Liquid, ice and mixed-phase clouds can be detected by the lidar. The liquid cloud layer can contain warm liquid water or supercooled water particles. The lidar alone is not able to discriminate

Research Article Vol. 28, No. 14 / 6 July 2020 / Optics Express 20126
Optics EXPRESS

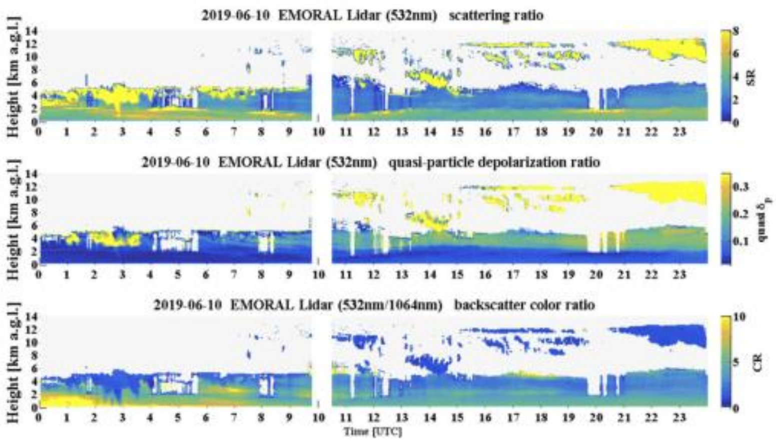

Fig. 2. The EMORAL lidar observations at the PolWET site in Rzecin, Poland, on 10 June 2019. The scattering ratio (top), quasi-particle depolarization ratio (middle), and backscatter colour ratio (bottom) derived at 532 nm with 30 m spatial and 30 s temporal resolutions.

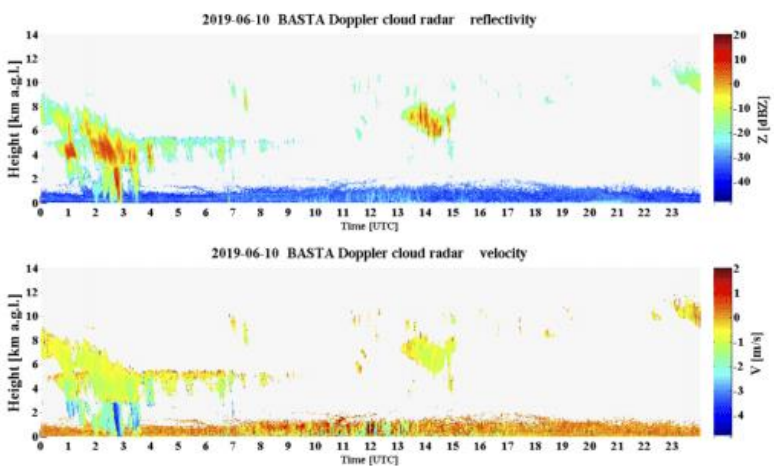

Fig. 3. BASTA cloud radar observations at the PolWET site in Rzecin on 10 June 2019. The reflectivity (top) and Doppler velocity (bottom) at merged vertical resolution (12.5, 25 and 100 m) and 9 s time integration.

Research Article Vol. 28, No. 14 / 6 July 2020 / Optics Express 20127
Optics EXPRESS

Table 2. Target classification applied on reflectivity (Z) and Doppler velocity (V) using cloud radar.

Doppler cloud radar measurements		
	Standard method	Standard method
	Doppler velocity (*V*)	Reflectivity (*Z*)
Ice particle	$V \geq -0.5$ m/s	-
Liquid particle or airborne plankton	$V \geq -0.5$ m/s	$Z < 17$ dBz
Drizzle	$-1.5 < V < -0.5$ m/s	-
Rain	$V \leq -1.5$ m/s	-

between them. Therefore, temperature profiles are needed and serve as an important parameter for judging the probability of existence of supercooled particles layers [e.g. 19]. The liquid water clouds with the temperature between -40 °C and 0 °C measured by microwave radiometer are regarded as supercooled layers.

In the boundary layer, the precipitation particles/droplets and other very large-size scatter targets (airborne plankton in summer) can be separated using a combination of the cloud radar (rain/drizzle) and the microwave radiometer relative humidity (*RH*). The *RH* values indicate wetter (≥ 65%) and drier areas (< 65%) in the atmosphere. Rain and drizzle detected at first by the cloud radar is confirmed with the threshold on $RH \geq 65\%$. When $RH < 65\%$, the rain/drizzle detected by the cloud radar within the boundary layer is defined as unknown boundary layer particles. The thresholds used are listed in Table 3. An example of the profiling in terms of these properties is shown in Fig. 4.

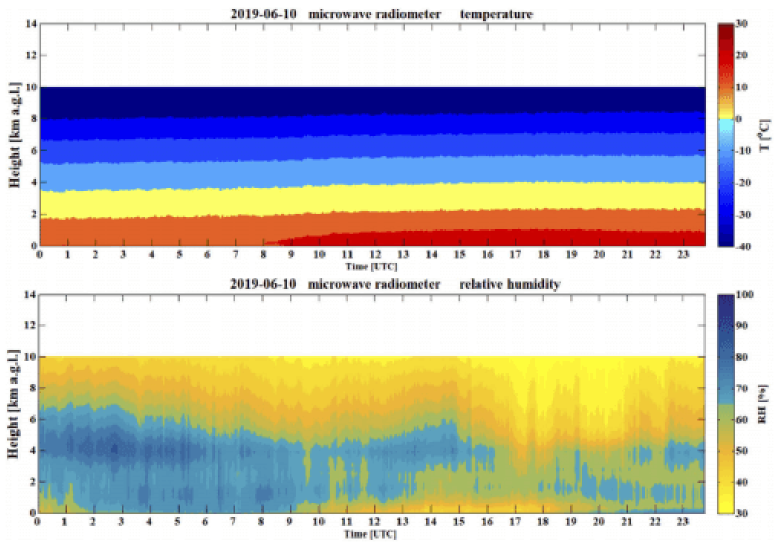

Fig. 4. The profiles of temperature (T) and relative humidity (RH) obtained from HATPRO-G2 microwave radiometer at the PolWET site in Rzecin on 10 June 2019.

Research Article Vol. 28, No. 14 / 6 July 2020 / Optics Express 20128
Optics EXPRESS

Table 3. Target classification applied on temperature (T) and relative humidity (RH) using microwave radiometer (MWR).

Microwave radiometer measurements		
	Standard method	New method
	Temperature (*T*)	Relative humidity (*RH*)
Supercooled	Liquid cloud & -40°C < T < 0°C	-
Ice particle	Ice or Liquid cloud & T ≤ -40°C	-
Rain/drizzle in boundary layer	-	precipitation & RH ≥ 65%
Unknown particles in boundary layer	-	precipitation & RH < 65%

6. Results and discussions

The measurements used in this paper were obtained during a joint field campaign as part of two European Space Agency (ESA) activities: The Technical Assistance for the Polish Radar and Lidar Mobile Observation System (POLIMOS) and the Technical Assistance for a Romanian Atmospheric Mobile Observation System (RAMOS).

The proposed methodology is demonstrated in a case study for 24 h observations conducted with the Raman-polarization lidar, Doppler cloud radar and microwave radiometer on 10 June 2019. On that day, characterized by different aerosol and cloud types and precipitation over the site, the fine quality of the proposed method can clearly be demonstrated.

The lidar-derived *SR*, ${}^{quasi}\delta_p$ and *CR* at 532 nm and the cloud radar *Z* and *V* on 10 June 2019 are shown in Figs. 2 and 3, respectively.

Microphysical characteristics (size and shape) of the particles lead to clearly seen differences in lidar and radar observations. At the lidar wavelength of 532 nm, cloud particles scatter in the geometric optics regime, where the backscattered intensity is proportional to the square of the particle diameter (D^2), and consequently dominated by liquid droplets, due to their large number concentration [75]. On the other hand, radar reflectivity is, in the Rayleigh regime approximation, proportional to a much higher moment (D^6), and hence, it is dominated by ice particles, because of their large diameter [12].

The day started with a stratocumulus cloud with the base at around 4.5 km (captured by the lidar) and the top at around 9 km (captured by the cloud radar). Note that the altitude marking the top of the cloud shows a slow declining trend for 9 to 5 km until 04:00 UTC. The Doppler velocity shows negative values between 01:00 and 04:00 UTC, which indicates precipitation during this period. The lidar derives the cloud base well, but it cannot penetrate deeply into the thick cloud, while the radar can, and thus, it is able to detect its top. Using a combination of both is a good way to obtain the base and the top of liquid, mixed-phase and thick ice clouds.

For optically thin ice-clouds, this combination is not always available, as the radar has difficulty detecting them. Thus, above 10 km, optically thin Cirrus was observed mainly by the lidar, which is manifested also by high (for ice-clouds) ${}^{quasi}\delta_p > 0.35$. Cirrus was detected by the radar only occasionally, which confirms their low optical thickness. The temperature above 6 km is below -30°C, which shows that Cirrus is mainly composed of ice crystals.

A supercooled layer from 12:30 to 13:30 UTC at the altitude of 4.8 km is likely to be found where lidar echo is strong (Fig. 2) but no radar echo was detected (Fig. 3). The profiles of temperature and relative humidity obtained by the microwave radiometer (Fig. 4) show the 0°C line at the height of 3.5 km this day. Below 0°C, there is a cold area where supercooled droplets and ice particles are likely to exist. Above 0°C, there is a warm area where liquid particles are likely to exist.

Figure 5 shows the new combined target classification created by the synergy of the lidar, cloud radar and microwave radiometer utilizing all thresholds. The categorization of molecule,

Research Article Vol. 28, No. 14 / 6 July 2020 / Optics Express 20129
Optics EXPRESS

aerosol (spherical, partly non-spherical, and non-spherical, fine, and coarse) and cloud (liquid and ice) according to the new thresholds of SR, ${}^{quasi}\delta_p$, and CR (Table 1) was derived for the lidar. Rain, drizzle and ice and liquid particles, relying on the threshold of Z and V (Table 2), were classified using the cloud radar.

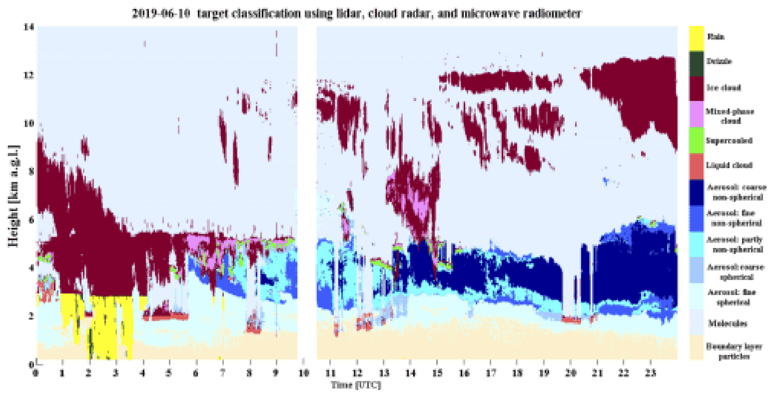

Fig. 5. Synergy for molecule, aerosol and cloud identification derived from a combination of EMORAL Raman-polarization lidar, BASTA Doppler cloud radar, and HATPRO-G2 microwave radiometer over the PolWET site in Rzecin on 10 June 2019.

On 10 June 2019, from 06:00 to 13:00 UTC, the mixed aerosol layer with spherical and non-spherical particles is observed at 2-6 km by the lidar (cyan colour in Fig. 5), then from 13:00 to 24:00 UTC as a thin layer at 2 km. The aerosol directly above it, at 3-6 km has non-spherical particles visible (dark blue in Fig. 5). The backward trajectories, calculated using the Hybrid Single-Particle Lagrangian Integrated Trajectory (HYSPLIT) model with the Global Data Assimilation System (GDAS) and CDC1 meteorological reanalyses, indicated a dust transport from the Sahara region towards the observational site at that time/height (not shown for the sake of brevity).

The rain (yellow colour in Fig. 5) and drizzle (dark green in Fig. 5) appeared with a connection to the ice cloud (dark red in Fig. 5) between 01:00 and 04:00 UTC. Between 10:30 and 20:30 UTC, the radar indicated some rain and drizzle at the height below 2.2 km, but the relative humidity (RH) was below 65% (dry environment) at this part of the day. There was also no signature of liquid clouds in lidar data directly above the radar derived rain/drizzle. That means that undefined large particles (detected by the radar but too sparse for lidar) existed inside the atmospheric boundary layer (beige colour in Fig. 5). Note that the class called boundary layer particles corresponds to the areas where cloud radar detect liquid cloud or airborne plankton and the lidar does not detect any liquid layer. The airborne plankton (pollens or insects) is made of particles too sparsely present in the air and often also too large to be detected with the lidar but large enough to be detected by the radar. Before that, between 6:00 and 9:00 UTC, the RH was > 65%, so they are categorized as drizzle or rain below 2.2 km (yellow, green in Fig. 5).

The change in the Doppler velocity (in Fig. 3) at around 3 km altitude from 01:00 to 3:30 UTC (dark red and yellow/dark green in Fig. 5) indicates the existence of a melting layer, where ice crystals melt into raindrops, which constitutes a cold rain system (originating in ice).

Liquid cloud layers (light red in Fig. 5) and a mixed cloud phase (pink in Fig. 5) are observed below 5 km, while ice clouds are mainly distributed above 5 km (dark red colour in Fig. 5).

Research Article Vol. 28, No. 14 / 6 July 2020 / Optics Express 20130
Optics EXPRESS

Strong backscatter regions in the lidar are composed either of warm liquid water, supercooled water (light green in Fig. 5), ice in high concentration (dark red), or a mixture of them (pink).

Locating supercooled water layers is crucial, as they represent a major weather hazard in aeronautics and can cause fatalities [76] and radiative transfer calculations [77]. The method to identify supercooled water layers was described before [e.g. 9,12,19]. Supercooled layers are usually physically thin (no more than 300 m) and observed in regions, where the temperature is between $-40 < T < 0$°C [12,19]. Note that supercooled or liquid clouds have the same signature in lidar signals if there is no drizzle below them. According to the temperature plots in Fig. 4, (a) cold area ($T < 0$°C, ice or supercooled layers) is above 3.5 km. Therefore, several supercooled droplets mixed with ice particles are detected above 4 km this day (light green in Fig. 5). In addition, the values of liquid water path (not shown for the sake of brevity) between 00:00 and 07:00 UTC were clearly higher than values between 08:00 and 24:00 UTC, which can be explained by rain and a liquid cloud between 00:00 and 07:00 UTC.

7. Conclusion

A target classification based on the case study of 10 June 2019 in Rzecin, Poland, conducted using a combination of the EMORAL Raman lidar, BASTA Doppler cloud radar, and HATPRO-G2 microwave radiometer was presented. The thresholds on the particle backward scattering ratio and the linear particle depolarization ratio calculated from lidar signals are used for the separation of molecular, aerosol, and cloud signatures. Apart from that, the colour ratio computed from lidar-derived particle backscatter coefficients is utilized to discern aerosol size. The thresholds on Doppler velocity and reflectivity of the cloud radar are used for categorizing drizzle, rain, ice and liquid particles. Supercooled droplets are estimated using temperature profiles from the microwave radiometer and relative humidity profiles are used for separating rain/drizzle within the boundary layer. Different types of scatter targets (from the boundary layer particles, through rain, drizzle, supercooled layer, ice cloud, liquid cloud, aerosol, to molecules) are classified using the synergy of lidar, cloud radar, and microwave radiometer, so that our work fits very well within the core tasks of the European Cooperation in Science and Technology (COST) Action for the Profiling of the atmospheric Boundary layer on a European scale (PROBE) [78].

Funding

European Cooperation in Science and Technology (PROBE, CA18235); European Space Agency (POLIMOS 4000119961/16/NL/FF/mg, RAMOS 4000118115/16/NL/FF/gp); Narodowe Centrum Nauki (Preludium-15 UMO-2018/29/N/ST10/02628); National Key Research and Development Program of China (2018YFC0213101, 2016YFC1400905).

Acknowledgments

We acknowledge Bogdan Chojnicki, the PI of the PolWET site, for granting an access to the experimental site of the Poznan University of Life Sciences (PULS). Patryk Poczta (PULS) for conducting lidar measurement. Damian Józwiak (PULS), Rafal Fortuna (University of Warsaw, UW), George Georgoussis, Alex Louridas and Christos Evangelatos (Raymetrics, Greece), Bernhard Stein and Bernd Mielke (LiCEL GmbH, Germany), Matthias Resch (Innolas Laser GmbH, Germany) and Georgios Tzeremes (ESA-ESTEC, The Netherlands), for their technical support. The EMORAL lidar is a property of the European Space Agency (ESA). It was developed by Raymetrics in a collaborative R&D effort with the University of Warsaw (UW), the Ludwig-Maximilians-Universität München (LMU), the National Observatory of Athens (NOA), and the European Space Agency (ESA). The BASTA cloud radar was developed by the Laboratoire Atmosphères, Milieux, Observations Spatiales (LATMOS). The HATPRO-G2

Research Article Vol. 28, No. 14 / 6 July 2020 / Optics Express 20131
Optics EXPRESS

microwave radiometer (Radiometer Physics GmbH, Germany) is a property of the Romanian National Institute of R&D for Optoelectronics (INOE).

D.W. and I.S.S. wrote the paper, designed the study concept, conducted formal analyses, made an extensive literature review, and holistically interpreted the results. D.W. coded all algorithms and performed sensitivity tests to assess their performance. I.S.S. and D.S. contributed to the lidar development, setting up and conducting the experiment, as well as taking care of the quality assurance of lidar data. J.D. contributed with the cloud radar system development, the target classification for cloud radar, and its data interpretation. D.E. provided the microwave radiometer and contributed with the interpretation of its data. I.S.S. and X.S. developed a synergetic algorithm for target classification and contributed to the assessment of classification quality. I.S.S., D.W., D.E. and X.S. obtained funding to conduct the research. All authors contributed to the interpretation and discussion of the results and conducted revisions of the paper.

Disclosures

The authors declare no conflict of interest.

References

1. M. D. Fielding, J. C. Chiu, R. J. Hogan, G. Feingold, E. Eloranta, E. J. O'Connor, and M. P. Cadeddu, "Joint retrievals of cloud and drizzle in marine boundary layer clouds using ground-based radar, lidar and zenith radiances," Atmos. Meas. Tech. **8**(7), 2663–2683 (2015).
2. K. Sarna and H. W. J. Russchenberg, "Ground-based remote sensing scheme for monitoring aerosol–cloud interactions," Atmos. Meas. Tech. **9**(3), 1039–1050 (2016).
3. H. Baars, T. Kanitz, R. Engelmann, D. Althausen, B. Heese, M. Komppula, J. Preißler, M. Tesche, A. Ansmann, U. Wandinger, J. H. Lim, J. Y. Ahn, I. S. Stachlewska, V. Amiridis, E. Marinou, P. Seifert, J. Hofer, A. Skupin, F. Schneider, S. Bohlmann, A. Foth, S. Bley, A. Pfüller, E. Giannakaki, H. Lihavainen, Y. Viisanen, R. K. Hooda, S. N. Pereira, D. Bortoli, F. Wagner, I. Mattis, L. Janicka, K. M. Markowicz, P. Achtert, P. Artaxo, T. Pauliquevis, R. A. F. Souza, V. P. Sharma, P. G. van Zyl, J. P. Beukes, J. Sun, E. G. Rohwer, R. Deng, R. E. Mamouri, and F. Zamorano, "An overview of the first decade of PollyNET: an emerging network of automated Raman-polarization lidars for continuous aerosol profiling," Atmos. Chem. Phys. **16**(8), 5111–5137 (2016).
4. E. Marinou, M. Tesche, A. Nenes, A. Ansmann, J. Schrod, D. Mamali, A. Tsekeri, M. Pikridas, H. Baars, R. Engelmann, K. A. Voudouri, S. Solomos, J. Sciare, S. Groß, F. Ewald, and V. Amiridis, "Retrieval of ice-nucleating particle concentrations from lidar observations and comparison with UAV in situ measurements," Atmos. Chem. Phys. **19**(17), 11315–11342 (2019).
5. J. H. Seinfeld, C. Bretherton, K. S. Carslaw, H. Coe, P. J. DeMott, E. J. Dunlea, G. Feingold, S. Ghan, A. B. Guenther, R. Kahn, and I. Kraucunas, "Improving our fundamental understanding of the role of aerosol−cloud interactions in the climate system," Proc. Natl. Acad. Sci. U. S. A. **113**(21), 5781–5790 (2016).
6. K. Markowicz, M. T. Chilinski, J. Lisok, O. Zawadzka, I. S. Stachlewska, L. Janicka, A. Rozwadowska, P. Makuch, P. Pakszys, T. Zielinski, T. Petelski, M. Posyniak, A. Pietruczuk, A. Szkop, and D. L. Westphal, "Study of aerosol optical properties during long-range transport of biomass burning from Canada to Central Europe in July 2013," J. Aeros. Sci. **101**, 156–173 (2016).
7. Z. Li, F. Niu, J. Fan, Y. Liu, D. Rosenfeld, and Y. Ding, "Long-term impacts of aerosol on the vertical development of clouds and precipitation," Nat. Geosci. **4**(12), 888–894 (2011).
8. P. Hasekamp, "Capability of multi-viewing-angle photo-polarimetric measurements for the simultaneous retrieval of aerosol and cloud properties," Atmos. Meas. Tech. **3**(4), 839–851 (2010).
9. M. Ceccaldi, J. Delanoë, R. J. Hogan, N. L. Pounder, A. Protat, and J. Pelon, "From CloudSat-CALIPSO to EarthCare: Evolution of the DARDAR cloud classification and its comparison to airborne radar-lidar observations," J. Geophys. Res. **118**(14), 7962–7981 (2013).
10. J. Delanoë and R. J. Hogan, "A variational scheme for retrieving ice cloud properties from combined radar, lidar and infrared radiometer," J. Geophys. Res. **113**(D7), D07204 (2008).
11. H. Pawlowska and J.L. Brenguier, "Microphysical properties of stratocumulus clouds during ACE–2," Tellus B **52**(2), 868–887 (2000).
12. J. Delanoë and R. J. Hogan, "Combined CloudSat–CALIPSO–MODIS retrievals of the properties of ice clouds," J. Geophys. Res. **115**, D00H29 (2010).
13. J. L. Brenguier, H. Pawlowska, and L. Schüller, "Cloud microphysical and radiative properties for parameterization and satellite monitoring of the indirect effect of aerosol on climate," J. Geophys. Res. **108**(D15), 8632 (2003).
14. E. Gryspeerdt, O. Sourdeval, J. Quaas, J. Delanoë, M. Krämer, and P. Kühne, "Ice crystal number concentration estimates from lidar–radar satellite remote sensing – Part 2: Controls on the ice crystal number concentration," Atmos. Chem. Phys. **18**(19), 14351–14370 (2018).

Research Article Vol. 28, No. 14 / 6 July 2020 / *Optics Express* 20132

Optics EXPRESS

15. C. Listowski, J. Delanoë, A. Kirchgaessner, T. Lachlan-Cope, and J. King, "Antarctic clouds, supercooled liquid water and mixed phase, investigated with DARDAR: geographical and seasonal variations," Atmos. Chem. Phys. **19**(10), 6771–6808 (2019).
16. G. L. Stephens, D. G. Vane, R. J. Boain, G. G. Mace, K. Sassen, Z. Wang, A. J. Illingworth, E. J. O'Connor, W. B. Rossow, S. L. Durden, S. D. Miller, R. T. Austin, A. Benedetti, C. Mitrescu, and T. C. S. Team, "The Cloudsat mission and the A–train: A new dimension of space-based observations of clouds and precipitation," B. Am. Meteorol. Soc. **83**(12), 1771–1790 (2002).
17. Z. B. Zhang, A. S. Ackerman, G. Feingold, S. Platnick, R. Pincus, and H. W. Xue, "Effects of cloud horizontal inhomogeneity and drizzle on remote sensing of cloud droplet effective radius: case studies based on large-eddy simulations," J. Geophys. Res. **117**(D19), D19208 (2012).
18. J. Illingworth, R. J. Hogan, E. J. O'Connor, D. Bouniol, M. E. Brooks, J. Delanoe, D. P. Donovan, J. D. Eastment, N. Gaussiat, J. W. F. Goddard, M. Haeffelin, H. K. Baltink, O. A. Krasnov, J. Pelon, J. M. Piriou, A. Protat, H. W. J. Russchenberg, A. Seifert, A. M. Tompkins, G. J. van Zadelhoff, F. Vinit, U. Willen, and D. R. Wilson,, and C. L. Wrench, "Cloudnet – continuous evaluation of cloud profiles in seven operational models using ground-based observations," B. Am. Meteorol. Soc. **88**(6), 883–898 (2007).
19. D. Zhang, Z. Wang, and D. Liu, "A global view of midlevel liquid-layer topped stratiform cloud distribution and phase partition from CALIPSO and CloudSat measurements," J. Geophys. Res. **115**, D00K30 (2010).
20. E. J. O'Connor, R. J. Hogan, and A. J. Illingworth, "Retrieving Stratocumulus Drizzle Parameters Using Doppler Radar and Lidar," J. Appl. Meteorol. **44**(1), 14–27 (2005).
21. M. J. McGill, D. Hlavka, W. Hart, V. S. Scott, J. Spinhirne, and B. Schmid, "Cloud physics lidar: Instrument description and initial measurement results," Appl. Opt. **41**(18), 3725–3734 (2002).
22. H. Omar, D. M. Winker, C. Kittaka, M. A. Vaughan, Z. Liu, Y. Hu, C. R. Trepte, R. R. Rogers, R. A. Ferrare, K. P. Lee, R. E. Kuehn, and C. A. Hostetler, "The CALIPSO automated aerosol classification and lidar ratio selection algorithm," J. Atmos. Oceanic Technol. **26**(10), 1994–2014 (2009).
23. J. Delanoë, A. Protat, O. Jourdan, J. Pelon, M. Papazzoni, R. Dupuy, J. F. Gayet, and C. Jouan, "Comparison of airborne in situ, airborne radar-lidar, and spaceborne radar-lidar retrievals of polar ice cloud properties sampled during the POLARCAT campaign," J. Atmos. Oceanic Technol. **30**(1), 57–73 (2013).
24. H. Baars, P. Seifert, R. Engelmann, and U. Wandinger, "Target categorization of aerosol and clouds by continuous multiwavelength-polarization lidar measurements," Atmos. Meas. Tech. **10**(9), 3175–3201 (2017).
25. F. Immler, R. Treffeisen, D. Engelbart, K. Kruger, and O. Schrems, "Cirrus, contrails, and ice supersaturated regions in high pressure systems at northern mid latitudes," Atmos. Chem. Phys. **8**(6), 1689–1699 (2008).
26. I. S. Stachlewska and C. Ritter, "On retrieval of lidar extinction profiles using Two-Stream and Raman techniques," Atmos. Chem. Phys. **10**(6), 2813–2824 (2010).
27. Z. Wang and K. Sassen, "Cirrus cloud microphysical property retrieval using lidar and radar measurements. Part I: Algorithm description and comparison with in situ data," J. Appl. Meteorol. **41**(3), 218–229 (2002).
28. C. Mätzler, P. W. Rosenkranz, and J. Cermak, "Microwave absorption measurements of supercooled clouds and implications for the dielectric properties of water," IAP Res. Rep. 2010–02–MW, Institute for Applied Physics, University of Bern, Bern, Switzerland. 2010.
29. C. Mätzler, P.W. Rosenkranz, and J. Cermak, "Microwave absorption of supercooled clouds and implications for the dielectric properties of water," J. Geophys. Res. **115**(D23), D23208 (2010).
30. Z. Sokol, J. Minářová, and P. Novák, "Classification of Hydrometeors Using Measurements of the Ka-Band Cloud Radar Installed at the Milešovka Mountain (Central Europe)," Remote Sens. **10**(11), 1674 (2018).
31. S. K. Das, M. Konwar, K. Chakravarty, and S. M. Deshpande, "Raindrop size distribution of different cloud types over the Western Ghats using simultaneous measurements from micro–rain radar and disdrometer," Atmos. Res. **186**, 72–82 (2017).
32. D. Nicolae, J. Vasilescu, C. Talianu, I. Binietoglou, V. Nicolae, S. Andrei, and B. Antonescu, "A neural network aerosol-typing algorithm based on lidar data," Atmos. Chem. Phys. **18**(19), 14511–14537 (2018).
33. Z. Wang and K. Sassen, "Cloud type and macrophysical property retrieval using multiple remote sensors," J. Appl. Meteorol. **40**(10), 1665–1682 (2001).
34. J. Heymsfield, A. Protat, D. Bouniol, R.T. Austin, R.J. Hogan, J. Delanoë, H. Okamoto, K. Sato, G. J. van Zadelhoff, D. P. Donovan, and Z. Wang, "Testing IWC retrieval methods using radar and ancillary measurements with in situ data," J. Appl. Meteorol. Climatol. **47**(1), 135–163 (2008).
35. D. Bouniol, A. Protat, J. Delanoé, J. Pelon, J. M. Piriou, F. Bouyssel, A. Tompkins, D. R. Wilson, Y. Morille, M. Haeffelin, E. J. O'Connor, R. Hogan, A. J. Illingworth, D. P. Donovan, and H. K. Baltink, "Using continuous ground-based radar and lidar measurements for evaluating the representation of clouds in four operational models," J. Appl. Meteorol. Climatol. **49**(9), 1971–1991 (2010).
36. I. S. Stachlewska, M. Costa-Surós, and D. Althausen, "Raman lidar water vapour profiling over Warsaw, Poland," Atmos. Res. **194**, 258–267 (2017).
37. D. Wang, I. S. Stachlewska, X. Song, B. Heese, and A. Nemuc, "Variability of boundary layer over an urban continental site based on 10 years of active remote sensing observations in Warsaw," Remote Sens. **12**(2), 340 (2020).
38. I. S. Stachlewska, O. Zawadzka, and R. Engelmann, "Effect of heat wave conditions on aerosol optical properties derived from satellite and ground-based remote sensing over Poland," Remote Sens. **9**(11), 1199 (2017).

Research Article Vol. 28, No. 14 / 6 July 2020 / *Optics Express* 20133

Optics EXPRESS

39. I. S. Stachlewska, M. Samson, O. Zawadzka, K. M. Harenda, L. Janicka, P. Poczta, D. Szczepanik, B. Heese, D. Wang, K. Borek, E. Tetoni, E. Proestakis, N. Siomos, A. Nemuc, B. H. Chojnicki, K. M. Markowicz, A. Pietruczuk, A. Szkop, D. Althausen, K. Stebel, D. Schuettemeyer, and C. Zehner, "Modification of Local Urban Aerosol Properties by Long-Range Transport of Biomass Burning Aerosol," Remote Sens. **10**(3), 412 (2018).
40. D. Wang, D. Szczepanik, and I. S. Stachlewska, "Interrelations between surface, boundary layer, and columnar aerosol properties derived in summer and early autumn over a continental urban site in Warsaw, Poland," Atmos. Chem. Phys. **19**(20), 13097–13128 (2019).
41. L. Janicka, I. S. Stachlewska, I. Veselovskii, and H. Baars, "Temporal variations in optical and microphysical properties of mineral dust and biomass burning aerosol derived from daytime Raman lidar observations over Warsaw, Poland," Atmos. Environ. **169**, 162–174 (2017).
42. V. Freudenthaler, H. Linné, A. Chaikovski, D. Rabus, and S. and Groß, "EARLINET lidar quality assurance tools," Atmos. Meas. Tech. Discuss, in review, 2018.
43. C. Böckmann, U. Wandinger, A. Ansmann, J. Bösenberg, V. Amiridis, A. Boselli, A. Delaval, F. De Tomasi, M. Frioud, and I. V. Grigorov, "Aerosol lidar intercomparison in the framework of the EARLINET project. 2.Aerosol backscatter algorithms," Appl. Opt. **43**(4), 977–989 (2004).
44. G. Pappalardo, A. Amodeo, A. Apituley, A. Comeron, V. Freudenthaler, H. Linné, A. Ansmann, J. Bösenberg, G. D'Amico, I. Mattis, L. Mona, U. Wandinger, V. Amiridis, L. AladosArboledas, D. Nicolae, and M. Wiegner, "EARLINET: towards an advanced sustainable European aerosol lidar network towards an advanced sustainable European aerosol lidar network," Atmos. Meas. Tech. **7**(8), 2389–2409 (2014).
45. J. Delanoë, A. Protat, J. P. Vinson, W. Brett, C. Caudoux, F. Bertrand, J. Parent du Chatelet, R. Hallali, L. Barthes, M. Haeffelin, and J. C. Dupont, "BASTA: A 95-GHz FMCW Doppler radar for cloud and fog studies," J. Atmos. Oceanic Technol. **33**(5), 1023–1038 (2016).
46. R. J. Hogan, D. Bouniol, D. N. Ladd, E. J. O'Connor, and A. J. Illingworth, "Absolute calibration of 94/95-GHz radars using rain," J. Atmos. Oceanic Technol. **20**(4), 572–580 (2003).
47. F. Toledo, J. Delanoë, M. Haeffelin, and J.-C. Dupont, "Absolute Calibration method for FMCW Cloud Radars," Atmos. Meas. Tech. Discuss., in review, 2020
48. K. Fragkos, B. Antonescu, D. M. Giles, D. Ene, M. Boldeanu, G. A. Efstathiou, L. Belegante, and D. Nicolae, "Assessment of the total precipitable water from a sun photometer, microwave radiometer and radiosondes at a continental site in southeastern Europe," Atmos. Meas. Tech. **12**(3), 1979–1997 (2019).
49. T. Rose, S. Crewell, U. Löhnert, and C. Simmer, "A network suitable microwave radiometer for operational monitoring of the cloudy atmosphere," Atmos. Res. **75**(3), 183–200 (2005).
50. L. D. Labzovskii, A. Papayannis, I. Binietoglou, R. F. Banks, J. M. Baldasano, F. Toanca, C. G. Tzanis, and J. Christodoulakis, "Relative humidity vertical profiling using lidar-based synergistic methods in the framework of the Hygra-CD campaign," Ann. Geophys. **36**(1), 213–229 (2018).
51. L. Liljegren, "Microwave Radiometer Profiles Handbook, Manual," Argonne National Laboratory, Washington D.C., 2002.
52. H. M. Cho, P. Yang, G. W. Kattawar, S. L. Nasiri, Y. Hu, P. Minnis, C. Trepte, and D. Winker, "Depolarization ratio and attenuated backscatter for nine cloud types: analyses based on collocated CALIPSO lidar and MODIS measurements," Opt. Express **16**(6), 3931–3948 (2008).
53. J. D. Klett, "Stable analytical inversion solution for processing lidar returns," Appl. Opt. **20**(2), 211–220 (1981).
54. G. Fernald, "Analysis of atmospheric lidar observations – some comments," Appl. Opt. **23**(5), 652–653 (1984).
55. V. Freudenthaler, M. Esselborn, M. Wiegner, B. Heese, M. Tesche, A. Ansmann, D. Müller, D. Althausen, M. Wirth, A. Fix, G. Ehret, P. Knippertz, C. Toledano, J. Gasteiger, M. Garhammer, and M. Seefeldner, "Depolarization ratio profiling at several wavelengths in pure Saharan dust during SAMUM 2006," Tellus B **61**(1), 165–179 (2009).
56. V. Freudenthaler, "About the effects of polarising optics on lidar signals and the Δ90 calibration," Atmos. Meas. Tech. **9**(9), 4181–4255 (2016).
57. K. Sassen, "Polarization in Lidar," *Lidar*, C. Weitkam, eds., Springer Press: New York. 19–42 (2005).
58. A. Ansmann, P. Seifert, M. Tesche, and U. Wandinger, "Profiling of fine and coarse particle mass: case studies of Saharan dust and Eyjafjallajökull/Grimsvötn volcanic plumes," Atmos. Chem. Phys. **12**(20), 9399–9415 (2012).
59. Z. Liu, M. Vaughan, D. Winker, C. Kittaka, B. Getzewich, R. Kuehn, A. Omar, K. Powell, C. Trepte, and C. Hostetler, "The CALIPSO lidar cloud and aerosol discrimination: Version 2 algorithm and initial assessment of performance," J. Atmos. Oceanic Technol. **26**(7), 1198–1213 (2009).
60. S. P. Burton, R. A. Ferrare, C. A. Hostetler, J. W. Hair, R. R. Rogers, M. D. Obland, C. F. Butler, A. L. Cook, D. B. Harper, and K. D. Froyd, "Aerosol classification using airborne High Spectral Resolution Lidar measurements – methodology and examples," Atmos. Meas. Tech. **5**(1), 73–98 (2012).
61. D. M. Winker, M. A. Vaughan, A. Omar, Y. Hu, K. A. Powell, Z. Liu, W. H. Hunt, and S. A. Young, "Overview of the CALIPSO mission and CALIOP data processing algorithms," J. Atmos. Ocean. Tech **26**(11), 2310–2323 (2009).
62. J. P. Vernier, T. D. Fairlie, M. Natarajan, F. G. Wienhold, J. Bian, B. G. Martinsson, S. Crumeyrolle, L. W. Thomason, and K. M. Bedka, "Increase in upper tropospheric and lower stratospheric aerosol levels and its potential connection with Asian pollution," J. Geophys. Res. **120**(4), 1608–1619 (2015).
63. S. P. Burton, J. W. Hair, M. Kahnert, R. A. Ferrare, C. A. Hostetler, A. L. Cook, D. B. Harper, T. A. Berkoff, S. T. Seaman, J. E. Collins, M. A. Fenn, and R. R. Rogers, "Observations of the spectral dependence of linear particle

Research Article Vol. 28, No. 14 / 6 July 2020 / *Optics Express* 20134

Optics EXPRESS

depolarization ratio of aerosol using NASA Langley airborne High Spectral Resolution Lidar," Atmos. Chem. Phys. **15**(23), 13453–13473 (2015).
64. V. V. Zuev, V. D. Burlakov, A. V. Nevzorov, V. L. Pravdin, E. S. Savelieva, and V. V. Gerasimov, "30-year lidar observations of the stratospheric aerosol layer state over Tomsk (Western Siberia, Russia)," Atmos. Chem. Phys. **17**(4), 3067–3081 (2017).
65. K. Srivastava, P. Pant, P. Hegde, S. Singh, U. C. Dumka, M. Naja, N. Singh, and Y. Bhavanikumar, "The Influence of a South Asian Dust Storm on Aerosol Radiative Forcing at a High-Altitude Station in Central Himalayas," Int. J. Remote. Sens. **32**(22), 7827–7845 (2011).
66. A. Dörnbrack, I. S. Stachlewska, C. Ritter, and R. Neuber, "Aerosol distribution around Svalbard during intense easterly winds," Atmos. Chem. Phys. **10**(4), 1473–1490 (2010).
67. S. Groß, M. Esselborn, B. Weinzierl, M. Wirth, A. Fix, and A. Petzold, "Aerosol classification by airborne high spectral resolution lidar observations," Atmos. Chem. Phys. **13**(5), 2487–2505 (2013).
68. S. P. Burton, M. A. Vaughan, R. A. Ferrare, and C. A. Hostetler, "Separating mixtures of aerosol types in airborne High Spectral Resolution Lidar data," Atmos. Meas. Tech. **7**(2), 419–436 (2014).
69. A. Borovoi, Y. Balin, G. Kokhanenko, I. Penner, A. Konoshonkin, and N. Kustova, "Layers of quasi-horizontally oriented ice crystals in cirrus clouds observed by a two-wavelength polarization lidar," Opt. Express **22**(20), 24566–24573 (2014).
70. A. Nemuc, J. Vasilescu, C. Talianu, L. Belegante, and D. Nicolae, "Assessment of aerosol's mass concentrations from measured linear particle depolarization ratio (vertically resolved) and simulations," Atmos. Meas. Tech. **6**(11), 3243–3255 (2013).
71. D. Müller, A. Ansmann, I. Mattis, M. Tesche, U. Wandinger, D. Althausen, and G. Pisani, "Aerosol-type-dependent lidar ratios observed with Raman lidar," J. Geophys. Res. **112**(D16), D16202 (2007).
72. B. Heese and M. Wiegner, "Vertical aerosol profiles from Raman polarization lidar observations during the dry season AMMA field campaign," J. Geophys. Res. **113**, D00C11 (2008).
73. C. Córdoba-Jabonero, M. Sicard, A. Ansmann, A. del Águila, and H. Baars, "Separation of the optical and mass features of particle components in different aerosol mixtures by using POLIPHON retrievals in synergy with continuous polarized Micro-Pulse Lidar (P-MPL) measurements," Atmos. Meas. Tech. **11**(8), 4775–4795 (2018).
74. A. Ansmann, M. Tesche, P. Knippertz, E. Bierwirth, D. Althausen, D. Mueller, and O. Schulz, "Vertical profiling of convective dust plumes in Southern Morocco during SAMUM," Tellus B **61**(1), 340–353 (2009).
75. R. J. Hogan and E. J. O'Connor, "Facilitating cloud radar and lidar algorithms: The Cloudnet Instrument Synergy/Target Categorization product," Cloudnet documentation. 2004.
76. A. Reehorst, D. Brinker, M. Politovich, D. Serke, C. Ryerson, A. Pazmany, and F. Solheim, "Progress towards the remote sensing of aircraft icing hazards, in Remote Sensing Applications for Aviation Weather Hazard Detection and Decision Support," Proc. SPIE **7088**, 70880J (2008).
77. R. J. Hogan, M. D. Behera, E. J. O'Connor, and A. J. Illingworth, "Estimate of the global distribution of stratiform supercooled liquid water clouds using the lite lidar," Geophys. Res. Lett. **31**(5), L05106 (2004).
78. D. Cimini, M. Haeffelin, S. Kotthaus, U. Löhnert, P. Martinet, E. O'Connor, C. Walden, M. Collaud Coen, and J. Preissler, "Towards the profiling of the atmospheric boundary layer at European scale – Introducing the COST Action PROBE," B. Atmos. Sci. Tech. **1**(1), 1–11 (2020).

Outlook and future plans

During my PhD studies, I conducted research which culminated in the three above-described papers constituting an integral part of my doctoral dissertation. During this process, several new questions were posed, new hypotheses arose, and new research topics opened to me and other members of the RS-Lab team. Those are already being investigated or shall be approached in the very near future:

1. Interplay of clouds and the ABL, as connected to research regarding the characteristics of the ABL differences at the urban and peatland site in terms of structure and top height but also aerosol optical properties. Specifically, the effect of clouds on ABL evolution and structure in different seasons is to be studied, as well as the characteristics of ABL under different underlying conditions are to be compared and discussed.

2. Interrelations regarding boundary layer aerosol properties were derived for summertime season (highest data availability). They will be further extended using long-term regular lidar observations in Warsaw. More observations shall allow to broaden the investigation of differences to other seasons. This will also allow for deeper research on distinguishing between sunset and sunrise aerosol properties relationships.

3. Different characterizations of aerosol and cloud above the urban and peatland site in a statistical analyses approach will be possible using the developed lidar, cloud radar and microwave radiometer classification scheme. Aerosol and cloud properties from long-term measurements over the wetland environment will serve as an input for aerosol-cloud-ecosystem modelling.

Although to continue my research career, I will return back to China this year, I am looking forward to further deepen my collaboration with colleagues in the Remote Sensing Laboratory lead by Dr. hab. Iwona S. Stachlewska.

Appendixes

Appendix 1.1 Lists of symbols and physical quantities

Atmospheric boundary layer	-- ABL
Atmospheric boundary layer height	-- ABLH
Aerosol optical depth	-- AOD(λ)
Ångström exponent	-- ÅE(λ_1/λ_2)
Backscatter colour ratio	-- CR(λ_1/λ_2)
Entire time	-- ET
Free troposphere	-- FT
Fine to coarse mass ratio	-- FCMR
Lidar ratio	-- LR(λ)
Lidar instrumental constant	-- C
Linear particle depolarization ratio	-- δ (λ)
Morning transition layer	-- MTL
Molecule	-- m
Nocturnal layer	-- NL
Particle extinction coefficient	-- α
Particle backscatter coefficient	-- β
Particle	-- p
Particulate matter with diameter <10 μm; <2.5 μm	-- PM_{10}; $PM_{2.5}$
Residual layer	-- RL
Relative humidity	-- RH
Scattering ratio	-- SR
Temperature	-- T
Water vapor mixing ratio	-- WV
Well-mixed layer	-- WML
Wavelet covariance transform method	-- WCT
Wavelength	-- λ

Appendix 1.2 Lists of acronyms

Aerosol, Clouds, and Trace gases Research Infrastructure	-- ACTRIS
Bistatic Radar System for Atmospheric Studies	-- BASTA
European Space Agency	-- ESA
ESA Mobile Raman Lidar	-- EMORAL
European Aerosol Research Lidar Network	-- EARLINET
University of Warsaw	-- UW
Laboratoire Atmosphères, Milieux, Observations Spatiales	-- LATMOS
Leibniz Institute of Tropospheric Research	-- TROPOS
Microwave radiometer	-- MWR
National Chief Inspectorate for Environmental Protection	-- GIOS
Near real time	-- NRT
Polish Radar and Lidar Mobile Observation System	-- POLIMOS
Romanian Atmospheric Mobile Observation System	-- RAMOS
Remote Sensing Laboratory	-- RS-Lab
Romanian National Institute of R&D for Optoelectronics	-- INOE
Warsaw Regional Inspectorate for Environmental Protection	-- WIOS

Appendix 2 Co-authored publications (during PhD study)

A 2.1 Publications in IF journals (Metrics: ResearchGate, H-index 3, citations 28)

(1) **<u>Wang, D</u>**., Stachlewska, I. S., Delanoë, J., Ene, D., Song, X., Schüttemeyer, D.: *Spatio-temporal discrimination of molecular, aerosol and cloud scattering and polarization using a combination of Raman lidar, Doppler cloud radar and microwave radiometer*. ***Optics Express***, 28 (14), 20117-20134. doi.org/10.1364/OE.393625. ***2020b.***
(IF=3.561, 0 Citations, Ranking list of MNISW: 140 pkt. physics)

(2) **<u>Wang, D</u>**., Stachlewska, I. S., Song, X., Heese, B., and Nemuc, A.: *Variability of the boundary layer over an urban continental site based on 10 years of active remote sensing observations in Warsaw*. ***Remote Sensing***, 12(2), 340. doi.org/10.3390/ rs12020340. ***2020a***.
(IF=4.118, 3 Citations, Ranking list of MNISW: 140 pkt. earth sciences)

(3) **<u>Wang, D</u>**., Szczepanik, D., and Stachlewska, I. S.: *Interrelations between surface, boundary layer, and columnar aerosol properties derived in summer and early autumn over a continental urban site in Warsaw, Poland*. ***Atmospheric Chemistry and Physics***, 19, 13097–13128. doi.org/10.5194/acp-19-13097-2019. ***2019***.
(IF=5.668, 4 Citations, Ranking list of MNISW: 140 pkt. physics/earth sciences)

(4) Baars, H., Ansmann, A., Ohneiser, K., Haarig, M., Engelmann, R., Althausen, D., Hanssen, I., Gausa, M., Pietruczuk, A., Szkop, A., Stachlewska, I. S., **<u>Wang, D</u>**., Reichardt, J., Skupin, A., Mattis, I., Trickl, T., Vogelmann, H., Navas-Guzmán, F., Haefele, A., Acheson, K., Ruth, A. A., Tatarov, B., Müller, D., Hu, Q., Podvin, T., Goloub, P., Veselovskii, I., Pietras, C., Haeffelin, M., Fréville, P., Sicard, M., Comerón, A., Fernández García, A. J., Molero Menéndez, F., Córdoba-Jabonero, C., Guerrero-Rascado, J. L., Alados-Arboledas, L., Bortoli, D., Costa, M. J., Dionisi, D., Liberti, G. L., Wang, X., Sannino, A., Papagiannopoulos, N., Boselli, A., Mona, L., D'Amico, G., Romano, S., Perrone, M. R., Belegante, L., Nicolae, D., Grigorov, I., Gialitaki, A., Amiridis, V., Soupiona, O., Papayannis, A. Mamouri, R.-E., Nisantzi, A., Heese, B., Hofer, J., Schechner, Y. Y., Wandinger, U., and Pappalardo, G.: *The unprecedented 2017–2018 stratospheric smoke event: Decay phase and aerosol properties observed with EARLINET*. ***Atmospheric Chemistry and Physics***, 19, 15183–15198. doi.org/10.5194/ acp-19-15183-2019. ***2019***.
(IF=5.668, 3 Citations, Ranking list of MNISW: 140 pkt. physics/earth sciences)

(5) Stachlewska, I.S., Samson, M., Zawadzka, O., Harenda, K.M., Janicka, L., Poczta, P., Szczepanik, D., Heese, B., **<u>Wang, D</u>**., Borek, K., Tetoni, E., Proestakis, E., Siomos, N., Nemuc, A., Chojnicki, B.H., Markowicz, K.M., Pietruczuk, A., Szkop, A., Althausen, D., Stebel, K., Schüttemeyer, D., Zehner, C.: *Modification of Local Urban Aerosol Properties by Long-Range Transport of Biomass Burning Aerosol*. ***Remote Sensing***, 10(3), 412. doi.org/10.3390/rs10030412. ***2018***.
(IF=4.118, 18 Citations, Ranking list of MNISW: 140 pkt. earth sciences)

A 2.2 Scientific reports

Nicolae, D. and 74 authors a.o. Stachlewska, I.S., Szczepanik D., **Wang, D**., Fortuna, R., **2020**: *EARLINET/ACTRIS analysis of aerosol profiles during the COVID-19 lock-down and relaxation period. A preliminary study on aerosol properties in the low and high troposphere*. https://www.earlinet.org/index.php?id=covid-19-reports.

A 2.3 Conference proceedings with first author

(1) 23, April 2020, the POLIMOS progress meeting, ***oral presentation*** (online, Warsaw)
Dongxiang Wang, Iwona S. Stachlewska, Julien Delanoe, Dragos Ene, Bogdan Chojnicki, Xiaoquan Song, Dirk Schuettemeyer.: The aerosol and cloud retrieval from the synergy of lidar, radar and microwave radiometer measurements.

(2) 18-22, November 2019, the ACTRIS Remote Sensing meeting, ***poster presentation*** (Rome, Italy)
Dongxiang Wang, Julien Delanoe, Florica Toanca, Xiaoquan Song, Iwona S. Stachlewska.: Aerosol and cloud classification using lidar and radar observations at a peatland site.

(3) June 24-28, 2019, the 29th International Laser Radar Conference (ILRC29), ***oral presentation*** (Hefei, China).
Dongxiang Wang & Iwona S. Stachlewska: Stratospheric smoke properties based on lidar observations in August 2017 over Warsaw.

(4) April 1-3, 2019, final ACTRIS Workshop, ***poster presentation*** (Darmstadt, Germany)
Dongxiang Wang., Dominika Szczepanik., Iwona S. Stachlewska.: Interrelations between surface, boundary layer and columnar aerosol properties over a continental urban site.

(5) March 12-14, 2019, the POLIMOS Workshop, ***poster presentation*** (Poznan, Poland)
Dongxiang Wang., Kamila Harenda., Patryk Poczta., Julien Delanoe., Iwona S. Stachlewska.: Preliminary analysis of ground-based lidar and cloud lidar observation at Rzecin peatland - a case study.

(6) July 3-5, 2018, the 1st European Lidar Conference (ELC), ***poster presentation*** (Thessaloniki, Greece)
Dongxiang Wang, Iwona S. Stachlewska, Xiaoquan Song, Birgit Heese.: Seasonal changes in diurnal boundary layer cycle over Warsaw.

(7) May 22-25, 2018, the 19th International Symposium for the Advancement of Boundary-Layer Remote Sensing (ISARS), ***oral presentation*** (Cologne, Germany)
Dongxiang Wang, Iwona S. Stachlewska, Xiaoquan Song, Birgit Heese.: Variability of boundary layer evolution over an urban continental site based on 10 years of remote sensing observations in Warsaw, Poland.

Appendix 3 Activities in projects (during PhD study)

A 3.1 Participation in projects

Combined lidar-radar technique for studies of aerosol-cloud interaction in troposphere.
https://www.ncn.gov.pl/sites/default/files/listy-rankingowe/2018-03-15/streszczenia/410514-en.pdf

Role: Project leader.
National project with international scientific collaboration with LATMOS, France.
Source of financing: National Science Centre - Poland, PRELUDIUM.
Period: January 15, 2019 – January 14, 2021.

Technical assistance for Polish Radar and Lidar Mobile Observation System (POLIMOS).

Role: Investigator / PhD student
International R&D project with several partners, PULS Poland, LMU Germany, and LATMOS France, and private sector Raymertics Greece.
Source of financing: European Space Agency, ESTEC.
Period: April 10, 2017 – August 31, 2020.

A 3.2 Participation in field campaigns

June 2018 - participated in the Carbon Dioxide and Methane Mission for HALO (CoMET) campaign organized by German Aerospace Center (Germany) and AGH University of Science and Technology (Poland).
May 2018 - participated in the POLIMOS 2018 campaign organized by University of Warsaw (Poland) and Poznan University of Life Sciences (Poland).
August 2019 - participated in the POLIMOS-RAMOS 2019 campaign organized by University of Warsaw (Poland), Poznan University of Life Sciences (Poland), and Romanian National Institute of R&D for Optoelectronics-2000 (Romania).

A 3.3 Scientific visits abroad

June 2019, I visited the Laboratoire Atmosphères, Milieux, Observations Spatiales (LATMOS) in France with purpose of acquiring sufficient knowledge on working with cloud radar instrument and data products.

Appendix 4 Agreements from publishers and co-authors

All three papers comprising this PhD thesis are published under the Creative Commons Attribution License 4.0 (https://creativecommons.org/licenses/by/4.0/) that is allowing to use them as a part of this thesis.

All co-authors agreed to use of published papers in PhD thesis of Dongxiang Wang (agreements on 29/06/2020).

Paper 1

Published paper title: Variability of the boundary layer over an urban continental site based on 10 years of active remote sensing observations in Warsaw.
Authors: Dongxiang Wang, Iwona S. Stachlewska, Xiaoquan Song, Birgit Heese, and Anca Nemuc.
Bibliographic record: Remote Sensing, 12(2), 340, 2020.
Link to paper: https://doi.org/10.3390/rs12020340.

Agreement information on 30/06/2020 by Rachel Zhang, Assistant Editor.

License Link:
https://www.mdpi.com/about/terms-and-conditions.

Paper 2

Published paper title: Interrelations between surface, boundary layer, and columnar aerosol properties derived in summer and early autumn over a continental urban site in Warsaw, Poland.
Authors: Dongxiang Wang, Dominika Szczepanik, and Iwona S. Stachlewska.
Bibliographic record: Atmospheric Chemistry and Physics, 19, 13097–13128, 2019.
Link to paper: https://doi.org/10.5194/acp-19-13097-2019.

Agreement information on 29/06/2020 by Anja Rasmussen, Editor.

License Link:
https://www.atmospheric-chemistry-and-physics.net/about/licence_and_copyright.html

Paper 3

Published paper title: Spatio-temporal discrimination of molecular, aerosol and cloud scattering and polarization using a combination of Raman lidar, Doppler cloud radar and microwave radiometer.
Authors: Dongxiang Wang, Iwona S. Stachlewska, Julien Delanoë, Dragos Ene, Xiaoquan Song, and Dirk Schüttemeyer.
Bibliographic record: Optics Express, 28 (14), 20117-20134, 2020.
Link to paper: https://doi.org/10.1364/OE.393625.

Agreement information on 29/06/2020 by Marco Dizon, Journal Staff.

License Link:
https://www.osapublishing.org/submit/review/copyright_permissions.cfm#posting.